1219

TRANSPORTATION RESEARCH RECORD

Geotechnical Engineering 1989

TRANSPORTATION RESEARCH BOARD
NATIONAL RESEARCH COUNCIL
WASHINGTON, D.C. 1989

Transportation Research Record 1219
Price: $25.00

mode
1 highway transportation

subject areas
17 energy and environment
24 pavement design and performance
25 structures design and performance
62 soil foundations
63 soil and rock mechanics
64 soil science

TRB Publications Staff
Director of Publications: Nancy A. Ackerman
Senior Editor: Edythe T. Crump
Associate Editors: Naomi C. Kassabian
Ruth S. Pitt
Alison G. Tobias
Production Editor: Kieran P. O'Leary
Graphics Coordinator: Karen L. White
Office Manager: Phyllis D. Barber
Production Assistant: Betty L. Hawkins

Printed in the United States of America

Library of Congress Cataloging-in-Publication Data
National Research Council. Transportation Research Board.

Geotechnical engineering 1989.
p. cm.—(Transportation research record, ISSN 0361-1981 ; 1219)
Reports prepared for the 68th annual meeting of the Transportation Research Board.
ISBN 0-309-04815-X
1. Soil stabilization. I. National Research Council (U.S.). Transportation Research Board. II. Series.
TE7.H5 no. 1219
[TE210.4]
380 s—dc20
[624.1'51] 90-5427
CIP

Sponsorship of Transportation Research Record 1219

GROUP 2—DESIGN AND CONSTRUCTION OF TRANSPORTATION FACILITIES
Chairman: Raymond A. Forsyth, California Department of Transportation

Stabilization Section
Chairman: J. M. Hoover, Iowa State University

Committee on Soil–Portland Cement Stabilization
Chairman: Lynne H. Irwin, Strategic Highway Research Program
Secretary: Dallas N. Little, Texas A&M University
Ara Arman, Henry H. Duval, Jr., Donald G. Fohs, K. P. George, Amir N. Hanna, Myron L. Hayden, J. M. Hoover, Robert W. Israel, John B. Lynch, Raymond K. Moore, Robert G. Packard, Lutfi Raad, Sam I. Thornton, Daniel R. Turner, Mumtaz A. Usmen, Anwar E. Z. Wissa, David C. Wyant

Committee on Lime and Lime–Fly Ash Stabilization
Chairman: Raymond K. Moore, University of Kansas
Mehmet C. Anday, James R. Blacklock, Humberto Castedo, James L. Eades, Donald G. Fohs, Kenneth A. Gutschick, Neil F. Hawks, J. M. Hoover, Robert W. Israel, Thomas W. Kennedy, Robert O. Lamb, Harold W. Landrum, Dallas N. Little, Larry Lockett, B. Dan Marks, W. C. Ormsby, Thomas M. Petry, Christopher David Foss Rogers, Donald R. Snethen, Marshall R. Thompson, Mumtaz A. Usmen, Laverne Weber, Paul J. Wright

Soil Mechanics Section
Chairman: Michael G. Katona, TRW, Inc.

Committee on Soils and Rock Instrumentation
Chairman: John L. Walkinshaw, Federal Highway Administration
Loren R. Anderson, Harold E. Beeston, Barry R. Christopher, Brian J. Dawes, Charles N. Easton, John B. Gilmore, Gordon E. Green, William H. Hansmire, Neil F. Hawks, John L. Henkes III, Kenneth A. Jackura, Richard H. Ledbetter, Dewayne L. Misterek, Gary W. Rhodes, A. J. Simmonds, Anwar E. Z. Wissa, Duncan C. Wyllie

Committee on Transportation Earthworks
Chairman: Richard P. Long, University of Connecticut
Loren R. Anderson, Thomas A. Bellatty, Jerome A. DiMaggio, Raymond L. Gemme, Robert D. Holtz, J. M. Hoover, Ilan Juran, James E. Kelly, Philip C. Lambe, Richard E. Landau, Robert M. Leary, C. William Lovell, David P. McKittrick, Victor A. Modeer, Jr., K. Jeff Nelson, Walter C. Waidelich, David E. Weatherby, Gary C. Whited

Committee on Foundations of Bridges and Other Structures
Chairman: Richard S. Cheney, Federal Highway Administration
Secretary: Richard P. Long, University of Connecticut
Francois J. Baguelin, Jean-Louis Briaud, Bernard E. Butler, Murty S. Devata, Albert F. DiMillio, Victor Elias, Richard L. Engel, Bengt H. Fellenius, George G. Goble, Richard J. Goettle III, James S. Graham, Robert C. Houghton, Alan P. Kilian, Hugh S. Lacy, Robert M. Leary, John F. Ledbetter, Jr., Larry Lockett, Randolph W. Losch, Lyle K. Moulton, Peter J. Nicholson, Michael Wayne O'Neill, Harvey E. Wahls, John L. Walkinshaw, Gdalyah Wiseman

Committee on Subsurface Soil–Structure Interaction
Chairman: J. M. Duncan, Virginia Polytechnic Institute
George Abdel-Sayed, Baidar Bakht, Sangchul Bang, Timothy J. Beach, Mike Bealey, C. S. Desai, Lester H. Gabriel, James B. Goddard, John Owen Hurd, Michael G. Katona, J. Neil Kay, Kenneth K. Kienow, Raymond J. Krizek, Richard W. Lautensleger, L. R. Lawrence, G. A. Leonards, Donald Ray McNeal, Michael C. McVay, A. P. Moser, Samuel C. Musser, Thomas D. O'Rourke, Raymond B. Seed, Ernest T. Selig, H. J. Siriwardane, Mehdi S. Zarghamee

Geology and Properties of Earth Materials Section
Chairman: C. William Lovell, Purdue University

Committee on Soil and Rock Properties
Chairman: James J. Schnabel, Schnabel Engineering Associates
Robert C. Bachus, S. S. Bandy, Roy H. Borden, Timothy D. Bowen, William H. Highter, Robert D. Holtz, Richard H. Howe, An-Bin Huang, Steven L. Kramer, C. William Lovell, Priscilla P. Nelson, Sibel Pamukcu, Gerald P. Raymond, J. Allan Tice, Mehmet T. Tumay, Recep Yilmaz

Committee on Physicochemical Phenomena in Soils
Chairman: Thomas F. Zimmie, Rensselaer Polytechnic Institute
John J. Bowders, Jr., Myron L. Hayden, John B. Heagler, Jr., Richard H. Howe, Robert Johnson, Joakim G. Laguros, Milton W. Meyer, Anwar E. Z. Wissa

Committee on Environmental Factors Except Frost
Chairman: Robert L. Lytton, Texas A&M University System
S. S. Bandy, Warren T. Bennett, Michael L. Bunting, Fu Hua Chen, Barry J. Dempsey, Donald G. Fohs, Donald J. Janssen, Badru M. Kiggundu, Amos Komornik, C. William Lovell, Said Ossama Mazen, R. Gordon McKeen, James B. Nevels, Jr., Zvi Ofer, Thomas M. Petry, Rogel H. Prysock, Albert C. Ruckman, Larry A. Scofield, Joe P. Sheffield, Malcolm L. Steinberg, Shiraz D. Tayabji, John L. Walkinshaw, William G. Weber, Jr., Gdalyah Wiseman

G. P. Jayaprakash, Transportation Research Board staff

Sponsorship is indicated by a footnote at the end of each paper. The organizational units, officers, and members are as of December 31, 1988.

Transportation Research Board publications are available by ordering directly from TRB. They may also be obtained on a regular basis through organizational or individual affiliation with TRB; affiliates or library subscribers are eligible for substantial discounts. For further information, write to the Transportation Research Board, National Research Council, 2101 Constitution Avenue, N.W., Washington, D.C. 20418.

Transportation Research Record 1219

Contents

Foreword

This Record contains 16 papers that are of interest to geotechnical engineers. The content of these papers includes reports on investigations of pile foundations; methods of determination of soil properties; use of fly ash, lime, and cement for soil stabilization and the effects of these additives on soil properties; and interaction of chemical wastes and soils.

Comparison of Formula Predictions with Pile Load Tests

RICHARD J. FRAGASZY, DOUGLAS ARGO, AND JERRY D. HIGGINS

To determine whether the Washington State Department of Transportation should replace the *Engineering News* (EN) formula with another dynamic formula for estimating pile capacity, the relative performance of 10 pile-driving formulas was studied. Data were collected from 63 pile load tests conducted in western Washington and northwest Oregon. The predicted capacity of each pile was calculated using several formulas: Danish, EN, modified EN, Eytelwein, Hiley, Gates, Janbu, Navy-McKay, Pacific Coast Uniform Building Code, and Weisbach. The Gates formula provided the most consistent prediction of pile capacity for each pile type and soil condition analyzed. The average predicted pile capacity was compared using the Gates and the EN formulas for different levels of safety. For each level of safety chosen, the Gates formula produced a higher average pile capacity. As the level of required safety increased, so did the difference between the two formula predictions.

Despite the development of wave equation techniques and pile analyzers, the use of pile-driving formulas continues. Earlier publications (*1,2*) reported that the *Engineering News* (EN) formula was the preferred method of the majority of state highway departments for estimating pile capacity. A growing number of states use wave equation and pile analyzer methods to evaluate pile foundation installations for relatively large projects. The literature included in those early publications describes several studies that compared pile load test results and formula predictions.

These comparisons brought out three important points. First, the EN formula generally is a poor estimator of pile capacity when compared with other formulas. The second point is that, although a few formulas were consistently among the best, no one formula stood out as the formula of choice for every situation. Last, local soil conditions and pile type affect the accuracy of each formula greatly.

Because the Washington State Department of Transportation (WSDOT) uses the EN formula along with wave equation and pile analyzer methods, WSDOT and the Federal Highway Administration (FHWA) funded a study to compare formula predictions with the results of pile load tests performed in the Pacific Northwest. The objective of this study was to recommend changes in WSDOT's methods of estimating pile capacity to improve the safety and economy of pile-supported structures.

R. J. Fragaszy, Department of Civil and Environmental Engineering, Washington State University, Pullman, Wash. 99162-2910. D. Argo, GeoEngineers, Inc., Bellevue, Wash. 98005. J. D. Higgins, Department of Geological Engineering, Colorado School of Mines, Golden, Colo. 80401.

To achieve this objective, data were collected from pile load tests conducted in western Washington and northwest Oregon. For those tests in which complete data were obtained, capacity was calculated on the basis of pile load tests. The capacity of each pile was also calculated using 10 common pile-driving formulas. These predictions were then compared with the pile load test results to determine the accuracy of each formula. This paper presents the results of the study.

PILE LOAD TESTS

Data Collection

Data for this research were gathered from the records of various consulting firms in the Seattle-Portland area and from the Oregon and Washington state departments of transportation. Forty-one reports, describing 103 pile load tests performed in the Puget Sound and lower Columbia River areas, were obtained. Of the 103 tests, 38 were not usable because of incomplete data. Two other load tests were rejected because the piles were damaged during driving.

The remaining 63 usable tests included 6 timber, 20 prestressed concrete, 5 H-section, 4 pipe (open and closed), 7 concrete-filled pipe, 5 hollow concrete, and 16 Raymond step taper piles. Included in these tests were 41 piles driven in cohesionless soil, 11 in cohesive soil, and 11 where the subsurface conditions consisted of layers of both cohesive and cohesionless soil. Further details of the pile load tests are given by Argo (*3*).

Sufficient documentation to allow wave equation analysis was available for only four of the pile load tests. Rather than assume values for missing data, only dynamic formulas were studied.

Calculation of Pile Capacity

To determine pile capacity for each pile load test, WSDOT engineers chose the following three methods: D-over-30, elastic tangent, and double tangent. In the D-over-30 method, the elastic compression line for the pile is plotted on the load-settlement graph, assuming that all the load is transferred to the tip. A second line parallel to the elastic compression line, with a y-axis (settlement axis) intercept equal to the pile diameter divided by 30, is also drawn on the load-settlement graph. The interception of this line with the load-settlement curve gives the predicted pile capacity (Q_{D30}).

In the elastic tangent method, a line is drawn parallel to

the elastic compression line and tangent to the load-settlement curve. A second line with a slope of 0.05 in./ton is drawn tangent to the plunging portion of the load-settlement curve. The point where these two lines meet is the predicted pile capacity (Q_{ET}).

In the double tangent method, two lines are drawn—one parallel to the initial portion and one parallel to the plunging portion of the load-settlement curve. The intersection of these two lines is the predicted pile capacity (Q_{DT}).

Pile capacity was calculated for every pile by each method and the results are presented in Table 1. The methods were compared to determine which method to use to evaluate formula predictions. Only small differences were found in the average pile capacity—the mean pile capacities were 188.1, 182.2, and 178.3 tons for the D-over-30, elastic tangent, and double tangent methods, respectively. The average maximum difference among the three methods was 13.2 tons—only 7.2 percent of the average capacity.

The D-over-30 method predicted the highest capacity 88 percent of the time and resulted in an average of 3.2 percent and 5.5 percent higher capacities than the elastic tangent and double tangent methods, respectively. The D-over-30 method was the most objective of the three, and the relatively small differences in capacity were not considered significant. Therefore, the D-over-30 method was used to compare formula predictions.

TABLE 1 MEASURED ULTIMATE PILE CAPACITIES

Pile Number	Q_{D30} (tons)	Q_{ET} (tons)	Q_{DT} (tons)	Pile Number	Q_{D30} (tons)	Q_{ET} (tons)	Q_{DT} (tons)
HP-3	142	140	137	OC-10	127	124	124
HP-4	79	73	71	OC-11	124	119	121
HP-5	122	119	118	OC-14	152	144	144
HP-6	182	178	172	OC-16	85	73	73
HP-7	149	153	148	HC-1	256	234	236
CP-4	247	237	236	HC-2	296	292	288
CP-6	123	116	116	HC-4	300	265	220
OP-3	212	201	200	HC-5	300	285	240
OP-4	225	219	209	HC-6	310	274	255
FP-1	145	135	130	ST-1	151	147	146
FP-2	79	80	79	ST-2	148	143	143
FP-3	300	313	318	ST-3	155	153	152
FP-6	122	113	110	ST-4	142	138	135
FP-7	221	204	198	ST-5	140	133	132
FP-8	261	252	243	ST-6	144	142	140
FP-9	169	154	148	ST-7	240	231	227
SC-3	105	98	100	ST-8	163	161	163
SC-4	102	99	100	ST-9	300	290	288
SC-5	88	80	78	ST-10	290	279	269
SC-6	55	49	51	ST-11	213	208	208
SC-8	140	128	126	ST-12	209	203	201
SC-10	130	122	120	ST-15	169	204	209
SC-13	188	180	180	ST-17	162	179	179
SC-14	241	231	229	ST-22	155	153	152
SC-15	255	246	245	ST-23	168	182	181
SC-16	85	73	73	T-1	168	163	160
SC-17	195	200	203	T-6	70	66	63
OC-1	518	512	473	T-7	66	62	58
OC-2	450	440	440	T-8	49	42	40
OC-3	620	610	610	T-10	48	47	46
OC-6	243	237	233	T-11	57	51	51
OC-9	248	241	237				

FORMULA PREDICTIONS

On the basis of the recommendations contained in an earlier study (*1*), the following formulas were selected for comparison: EN, modified EN, Hiley, Gates, Janbu, Danish, Pacific Coast Uniform Building Code (PCUBC), Eytelwein, Weisbach, and Navy-McKay. All inherent safety factors were removed, so the ultimate load is assumed to be predicted by each equation. The specific form of each equation used is given in Table 2. Using these formulas, the predicted capacities presented in Table 3 were calculated along with the capacities based on the D-over-30 method.

To illustrate the range of predicted-versus-measured capacity for each formula, scatter graphs were plotted. Two examples are presented in Figures 1 and 2, which show the predicted capacity based on the EN and Gates formulas, respectively, versus the measured capacity as determined by the D-over-30 method. A 45° line, representing the points at which the predicted and measured ultimate capacities are equal, is also shown on each graph.

In the example shown in Figure 1, it can be seen that the EN formula, without including any safety factor, significantly overpredicts pile capacity in most cases. More importantly, the data clearly are quite scattered; and it would be difficult, if not impractical, to adjust the formula to make the data fit near the 45° line. In contrast, it can be seen in Figure 2 that the predicted capacity, based on the Gates formula, is generally lower than the measured capacity and the data fall much more closely to a straight line. Applying a multiplying factor to the predicted capacity could bring the data more closely in line with the 45° line.

To allow statistical evaluations, the predicted capacities from each formula were divided by the measured capacities. Histograms of these ratios were plotted to determine whether the data are normally distributed, a necessary requirement for the statistical methods employed. The histograms, shown in Figures 3a and 4a for the EN and Gates formulas, respectively, reveal that the data are skewed. In order to perform statistical tests, the ratios were transformed by calculating the common logarithm of each. Histograms were again plotted, as shown in Figures 3b and 4b, and the transformed data were found to be normally distributed by a chi-square goodness-of-fit test. The transformed data set was then used as the basis for statistical comparisons.

The first method used to quantify the scatter of each equa-

TABLE 2 DYNAMIC FORMULAS

ENR	$Q_u = \dfrac{e_h E_h}{s + z}$
Mod. ENR	$Q_u = \dfrac{e_h E_h}{s + z} \cdot \dfrac{W + n^2 w}{W + w}$
Hiley	$Q_u = \dfrac{e_h E_h}{s+(C_1+C_2+C_3)/2} \cdot \dfrac{W + n^2 w}{W + w}$
Gates	$Q_u = 27 \sqrt{e_h E_h}(1-\log s)$ e_h = 0.75 for drop hammers E_h = 0.85 for other hammers Q_u (kips), s (in), E_h (ft-kips)
Janbu	$Q_u = \dfrac{e_h E_h}{K_u s}$ $K_u = C_d \left[1 + \sqrt{1 + \dfrac{\lambda}{C_d}} \right]$ $C_d = 0.75 + 0.15 \dfrac{w}{W}$ $\lambda = \dfrac{e_h E_h}{AEs^2}$
Danish	$Q_u = \dfrac{e_h E_h}{s + \sqrt{\dfrac{e_h E_h L}{2AE}}}$
PCUBC piles	$Q_u = \dfrac{e_h E_h \cdot \dfrac{W + Kw}{W + w}}{S + \dfrac{Q_u L}{AE}}$ K = 0.25 for steel piles = 0.10 for all other

TABLE 2 (*continued on next page*)

TABLE 2 (*continued*)

Eytelwein	$Q_u = \dfrac{e_h E_h}{s\left(1 + \dfrac{w}{W}\right)}$ (drop hammers)
	$Q_u = \dfrac{e_h E_h}{s + \left[0.1\dfrac{w}{W}\right]}$ (steam hammers)
Weisbach	$Q_u = \dfrac{-sAE}{L} + \sqrt{\dfrac{2e_h E_h AE}{L} + \dfrac{sAE}{L}}$
Navy-McKay	$Q_u = \dfrac{e_h E_h}{s\left[1 + 0.3\dfrac{w}{W}\right]}$

tion was the coefficient of variation (standard deviation divided by the mean) of the transformed data. Because the data for this study are log-normally distributed, the coefficients of variation were computed for the logarithms of the data; thus, the term CV_{log} is used to refer to these values. The closer CV_{log} is to zero, the more consistent the formula prediction.

The second method of comparison was taken from Agerschou (*4*), in which a divisor is calculated for each formula. This divisor is based on a statistical analysis of the ratio between formula predictions and load test results, such that its application to the formula results in a specific percentage (usually 98 percent) of all formula predictions having actual safety factors above 1.0 (i.e., a predicted capacity less than the measured capacity). The use of this divisor results in a wide range of actual safety factors. The upper limit of actual safety factors that would result is also computed. This value shows the extent of overdesign that must be accepted to ensure 98 percent safety. Use of a formula with a high upper limit would result in significant overdesign for many piles.

Although the divisor might appear to be a safety factor (it replaces the safety factor in the formula), it is not. A safety factor is an (almost) arbitrary factor used to account for variation in the parameters used in the calculation. The divisor is a statistically derived factor that allows the restriction of failure to a small, specified level.

Agerschou chose a 98-percent confidence level in his work (*4*). This, perhaps, represents the strictest tolerance that might be required for situations in which extreme safety is required. A more reasonable level for bridge foundations and similar transportation structures where excessive loading of a single pile does not have catastrophic consequences might be 95 percent. The divisors for both these confidence levels were used in this research.

RESULTS OF STATISTICAL ANALYSES

A qualitative feel for the data can be obtained by examining the scatter graphs and histograms of the data shown in Figures 1 through 4. On the basis of these figures and those for the other eight formulas presented by Argo (*3*), it is clear that none of the formulas can be considered accurate predictors of pile capacity, although some are significantly better than others. A comparison of the Gates and EN formulas should leave little doubt as to which is the better formula.

The Gates scatter graph shows a reasonably good fit to a straight line relationship, with a tendency to slightly underpredict the measured capacity. The EN formula, in contrast, significantly overpredicts pile capacity in the 160- to 260-ton-capacity range. However, if a reduction of safety factor is applied to lower the predicted capacities in this range, the formula would significantly underpredict the capacity of many piles.

Several equations show a trend of curving upward farther away from the 45° line for piles with increasing measured capacity. These formulas are EN, modified EN, Danish, and Weisbach. The Janbu, PCUBC, and Eytelwein formulas appear to plot near the 45° line on the average, but the graphs indicate significant scatter (*3*).

To determine which formulas are most accurate for different piles and soil types, the values of CV_{log} were calculated for several groupings according to these parameters. The values for eight groups are presented in Table 4. In all but one of the groupings, the Gates formula is ranked first and is a close second for piles in cohesive soils. The PCUBC, Hiley, Weisbach, and Danish formulas group closely together, but they have larger values of CV_{log} than does the Gates formula. The Janbu formula is also in this group, except for piles in

TABLE 3 PILE CAPACITIES PREDICTED BY DYNAMIC FORMULAS (tons)

Pile Number	Q_{D30}	ENR	Mod. ENR	Hiley	Gates	Janbu	Danish	PCUBC	Eytel-wein	Weis-bach	Navy-McKay
HP-3	142	366	313	200	97	140	167	115	438	192	497
HP-4	79	65	61	62	47	45	59	57	71	69	68
HP-5	122	306	273	186	93	134	155	120	363	184	366
HP-6	182	247	211	112	83	100	118	84	280	139	288
HP-7	149	231	200	147	81	116	136	105	263	166	264
CP-4	247	1070	969	390	162	300	357	250	1604	389	1880
CP-6	123	476	445	336	110	197	223	181	714	257	742
OP-3	212	448	405	250	115	214	244	201	520	297	513
OP-4	225	886	716	295	154	176	223	131	915	243	1001
FP-1	145	429	358	262	106	215	258	180	480	309	542
FP-2	79	113	83	77	62	67	92	66	116	112	101
FP-3	300	774	678	341	137	254	304	206	1074	335	1367
FP-6	122	368	335	175	100	113	132	98	466	149	480
FP-7	221	617	554	278	135	132	156	110	718	173	710
FP-8	261	1536	1371	430	193	144	179	114	2314	184	2913
FP-9	169	632	568	312	136	134	159	112	739	175	734
SC-3	105	421	359	226	105	218	254	190	506	305	552
SC-4	102	159	103	84	72	78	106	64	151	132	128
SC-5	88	98	64	54	57	55	82	52	97	98	78
SC-6	55	98	62	61	57	54	81	49	96	97	76
SC-8	140	208	136	115	82	112	149	98	206	186	181
SC-10	130	109	71	70	60	61	90	57	108	108	88
SC-13	188	267	189	120	85	143	174	121	285	213	303
SC-14	241	306	206	173	101	158	205	140	307	257	265
SC-15	255	362	230	183	108	167	218	136	353	270	303
SC-16	139	267	170	136	94	133	179	113	262	224	215
SC-17	195	838	520	282	151	246	319	179	765	364	838
OC-1	518	2790	985	362	259	371	664	258	1004	695	3453
OC-2	450	1633	611	303	205	361	606	256	880	680	1302
OC-3	620	3730	1619	522	313	560	915	404	1822	935	12648
OC-6	243	812	262	94	142	117	178	74	337	183	1636
OC-9	248	436	169	131	115	121	182	82	321	213	286

TABLE 3 (*continued on next page*)

TABLE 3 (*continued*)

Pile Number	Q_{D30}	ENR	Mod. ENR	Hiley	Gates	Janbu	Danish	PCUBC	Eytel-wein	Weis-bach	Navy-McKay
OC-10	1271	1855	957	302	217	346	487	229	1128	500	5641
OC-11	124	1821	770	202	214	273	408	174	809	418	4487
OC-14	152	194	122	97	79	104	145	90	188	180	161
OC-16	85	98	60	59	57	53	83	47	95	98	74
HC-1	256	1499	452	214	193	294	521	183	341	545	2188
HC-2	296	1086	268	202	162	234	434	149	277	476	803
HC-4	300	1280	600	509	176	366	558	238	611	621	1309
HC-5	300	1152	532	353	171	344	531	225	591	608	954
HC-6	310	1800	788	442	208	444	671	284	800	719	2526
ST-1	151	457	245	143	106	243	333	176	324	400	539
ST-2	148	398	232	235	100	270	381	213	312	476	440
ST-3	155	360	196	160	96	210	293	160	279	364	366
ST-4	142	366	178	108	97	161	229	113	249	274	345
ST-5	140	398	213	170	100	223	309	165	293	379	423
ST-6	144	332	175	126	93	171	242	127	250	298	312
ST-7	240	428	224	241	106	208	292	151	313	357	403
ST-8	163	344	165	160	97	137	198	96	249	239	278
ST-9	300	840	364	231	142	128	193	82	379	200	1408
ST-10	290	855	437	406	144	165	238	107	463	248	1638
ST-11	213	188	101	98	75	106	168	87	162	206	149
ST-12	209	342	184	174	95	198	281	151	264	350	335
ST-15	169	522	370	344	114	320	400	258	517	487	689
ST-17	162	470	333	319	110	301	380	250	466	470	578
ST-22	155	288	172	175	91	153	212	122	255	265	21
ST-23	168	301	143	138	87	161	239	116	192	294	24
T-1	168	302	284	160	88	77	90	67	455	98	40
T-6	70	140	128	79	65	67	75	64	165	91	14
T-7	66	103	95	73	57	57	64	58	116	80	9
T-8	49	45	42	42	39	29	36	35	47	44	4
T-10	48	112	105	72	59	56	63	57	128	78	10
T-11	57	18	17	17	19	1	16	16	18	18	1

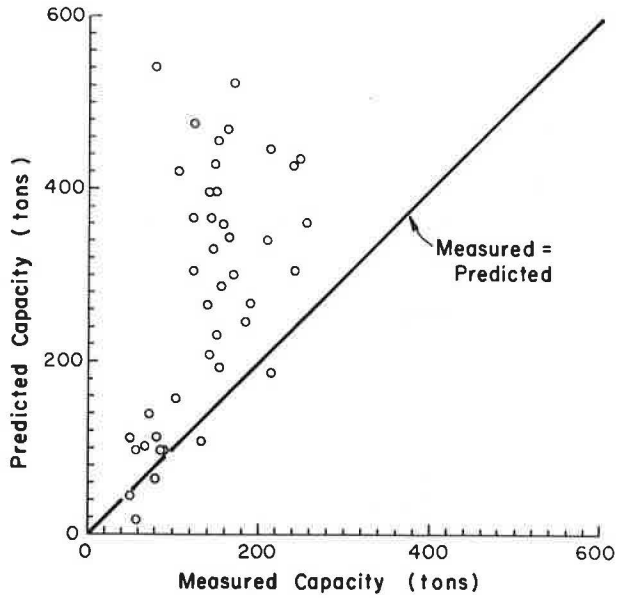

FIGURE 1 Predicted versus measured pile capacity for the EN formula.

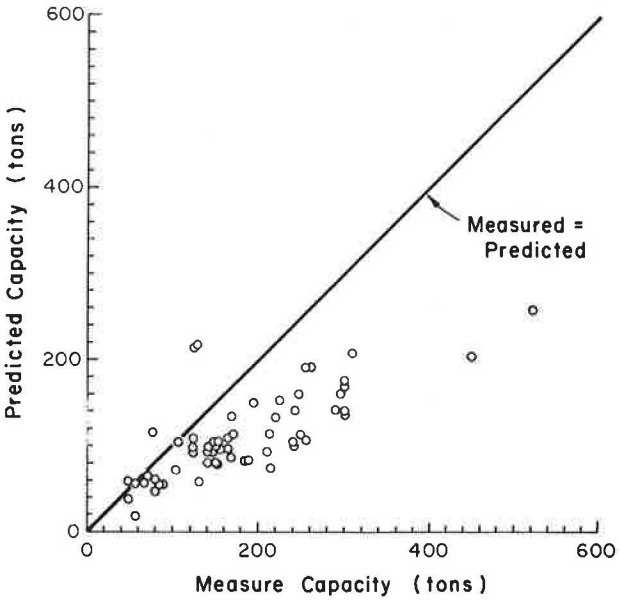

FIGURE 2 Predicted versus measured pile capacity for the Gates formula.

cohesionless soils. The EN, modified EN, and Eytelwein formulas have consistently larger values of $CV_{\log}$ than the above formulas. The Navy-McKay formula is consistently last by a large margin.

The divisors required for 98 percent and 95 percent assurance that the actual safety factor will be greater than or equal to 1.0 are shown in Table 5. For example, if it is required that 98 percent of the time the actual capacity will be greater than the allowable capacity, then the pile capacity predicted by the EN formula should be divided by 9.06 to obtain allowable capacity. If this divisor (9.06) is used, the resulting actual safety factors will range as high as 14.36. In contrast, the

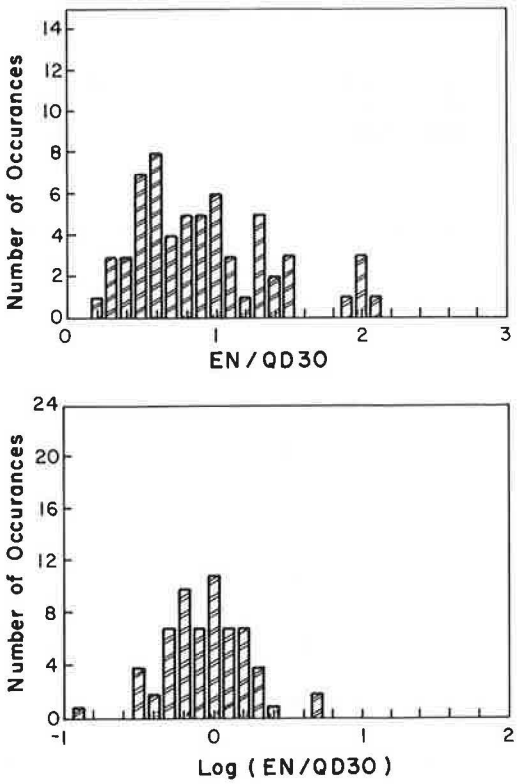

FIGURE 3 Histograms for raw and logarithm-transformed data for the EN formula.

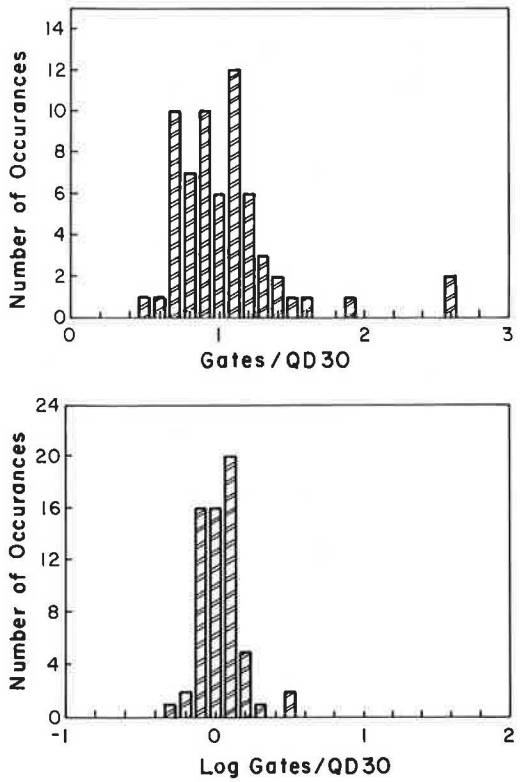

FIGURE 4 Histograms for raw and logarithm-transformed data for the Gates formula.

TABLE 4 CV_{LOG} VALUES FOR SELECTED PILE TYPES AND SOIL CONDITIONS

ALL PILES (N=63)			ALL EXCEPT TIMBER (N=57)		
RANK	FORMULA	CV_{LOG}	RANK	FORMULA	CV_{LOG}
1	Gates	0.14	1	Gates	0.13
2	Hiley	0.20	2	Danish	0.19
2	PCUBC	0.20	2	Hiley	0.19
4	Danish	0.21	2	Janbu	0.19
4	Weisbach	0.21	2	PCUBC	0.19
6	Janbu	0.29	2	Weisbach	0.19
7	Modified ENR	0.30	7	ENR	0.28
7	Eytelwein	0.30	7	Eytelwein	0.28
9	ENR	0.32	9	Modified ENR	0.29
10	Navy-McKay	0.91	10	Navy-McKay	0.58

All PILES IN COHESIONLESS SOILS (N=41)			ALL PILES IN COHESIVE SOILS (N=11*)		
RANK	FORMULA	CV_{LOG}	RANK	FORMULA	CV_{LOG}
1	Gates	0.11	1	PCUBC	0.18
2	Danish	0.21	2	Gates	0.19
2	Hiley	0.21	3	Weisbach	0.20
2	PCUBC	0.21	4	Hiley	0.21
5	Weisbach	0.22	4	Janbu	0.21
6	Modified ENR	0.27	6	Danish	0.22
7	Eytelwein	0.29	7	Eytelwein	0.31
8	ENR	0.30	8	Modified ENR	0.35
9	Janbu	0.33	9	ENR	0.38
10	Navy-McKay	0.92	10	Navy-McKay	0.65

TABLE 4 (*continued on next page*)

TABLE 4 (*continued*)

H-SECTION (N=5*)			SQUARE AND OCTAGONAL CONCRETE (N=20)		
RANK	FORMULA	CV_{LOG}	RANK	FORMULA	CV_{LOG}
1	Gates	0.08	1	Gates	0.18
2	PCUBC	0.11	2	Weisbach	0.20
3	Danish	0.13	3	Danish	0.21
3	Weisbach	0.13	4	Janbu	0.22
5	Janbu	0.14	4	PCUBC	0.22
6	Hiley	0.16	6	Hiley	0.23
7	Modified ENR	0.20	7	Eytelwein	0.31
8	Eytelwein	0.24	8	Modified ENR	0.36
9	ENR	0.25	9	ENR	0.39
10	Navy-McKay	0.34	10	Navy-McKay	0.68
RAYMOND STEP TAPER (N=16)			TIMBER (N=6*)		
RANK	FORMULA	CV_{LOG}	RANK	FORMULA	CV_{LOG}
1	Gates	0.09	1	Gates	0.18
2	ENR	0.16	2	PCUBC	0.23
2	Hiley	0.16	3	Hiley	0.25
4	Danish	0.17	4	Danish	0.30
5	Weisbach	0.18	5	Weisbach	0.32
6	Eytelwein	0.19	6	Modified ENR	0.37
6	Janbu	0.19	7	Eytelwein	0.46
8	Modified ENR	0.20	8	ENR	0.49
9	PCUBC	0.22	9	Navy-McKay	0.60
10	Navy-McKay	0.77	10	Janbu	0.90

*Sample size is too small to provide reliable results

TABLE 5 DIVISOR FOR 98% AND 95% LEVELS OF SAFETY CALCULATED USING ALL DATA

FORMULA	98% Assurance Divisor	Upper Limit of Actual Safety Factors
Gates	1.21	3.61
PCUBC	1.78	5.99
Hiley	2.53	6.17
Danish	3.16	6.76
Weisbach	3.72	6.93
Eytelwein	7.03	12.19
Modified ENR	5.29	12.37
Janbu	3.11	12.86
ENR	9.06	14.36
Navy-McKay	33.08	278.54

FORMULA	95% Assurance Divisor	Upper Limit of Actual Safety Factors
Gates	1.06	2.80
PCUBC	1.49	4.19
Hiley	2.11	4.29
Danish	2.61	4.62
Weisbach	3.07	4.71
Eytelwein	5.48	7.40
Modified ENR	4.12	7.49
Janbu	2.41	7.73
ENR	6.95	8.44
Navy-McKay	18.87	90.59

Gates formula prediction should be divided by 1.21, resulting in actual safety factors up to 3.61.

To evaluate the economic effects of changing to the Gates formula, comparisons were made of allowable load using several different assumptions. The average allowable load for all piles ($N = 63$) based on the Gates formula was calculated using the divisor for 98 percent and 95 percent assurance (1.21 and 1.06, respectively). This was also done using the EN formula (9.06 and 6.95, respectively). The average allowable load based on the EN formula was also calculated using the customary safety factor of 6.0, as well as the allowable load for the Gates formula using the same level of safety, 92.7 percent. In this

TABLE 6 COMPARISON OF AVERAGE ALLOWABLE LOADS BASED ON GATES AND EN FORMULAS

	Divisor Used			Average Allowable Load (tons)		
	98%	95%	Current[a]	98%	95%	Current
EN	9.06	6.95	6.0	69.2	90.2	104.5
Gates	1.21	1.06	1.01	95.4	108.9	113.9

[a]Typical safety factor used for EN formula, equivalent to 92.5 percent.

way, a comparison can be made using the same measures of safety for both formulas. The results of these analyses are presented in Table 6.

When both formulas are used with a 98 percent assurance that the allowable load will be lower than the actual capacity, the Gates formula gives an average allowable capacity of 95.4 tons versus 69.2 tons using the EN formula. This is an average increase of 38 percent, with no additional risk. The allowable capacity is higher using the Gates formula for 55 out of 63 piles. Using the known pile capacities based on the pile load tests, an average actual safety factor can be calculated. For the Gates formula, that safety factor is 1.97 and for EN it is 2.72. When 95 percent assurance is used (a more realistic value), the Gates formula gives an average allowable capacity of 108.9 tons versus 90.2 tons using EN—an increase of 21 percent. These average capacities reflect average actual safety factors of 1.73 and 2.09.

Using the current safety factor of 6.0 for EN, the average allowable load is 104.5 tons, approximately 4 percent less than that obtained with the Gates formula using 95 percent assurance. Using the same level of safety (92.7 percent), the Gates formula predicts an average capacity of 113.9 tons, 9 percent higher than EN. The average actual safety factor using the EN formula in this case is 1.8 compared with 1.65 for the Gates formula.

The economic benefits of switching to the Gates formula clearly depend on the choices made in selecting the desired assurance level (safety factor). If the comparison is made between the EN formula (as it is currently used) and the Gates formula with the same level of safety, the economic benefits are small, but positive. If the comparison is made using higher levels of safety, the economic benefit of switching to the Gates formula will be substantial.

DISCUSSION OF RESULTS

The results of this study follow the trend of similar comparative studies reported elsewhere. Those formulas that fared well in other comparisons (Danish, Gates, Hiley, Janbu, PCUBC, and Weisbach) also ranked high in this study. Of these, the Gates formula clearly is the best—ranking first in all but one comparison (cohesive soils), where it was a close second. The EN, modified EN, Eytelwein, and Navy-McKay formulas are clearly unreliable.

Using the EN Formula

This study points out two important aspects of the question of whether the EN formula should be used in western Washington and northwest Oregon. The first is that other formulas clearly do a better job of predicting pile capacity, in particular the Gates formula. The second is that the typical safety factor (6.0) used with the EN formula may not provide the level of safety desired. On the basis of the data obtained from all pile load tests, the EN calculation of pile capacity should be divided by 6.95 to ensure that the allowable load is less than the actual capacity 95 percent of the time, and a divisor of 9.06 is necessary for 98 percent assurance. Although the data set for some of the subgroups, such as timber piles, is small, the authors believe that use of the data from all piles provides a large enough sample to produce confidence in the validity of the results.

From this study, it seems apparent that the EN formula should not be used in western Washington and northwest Oregon. If use of a formula is desirable, the Gates formula provides the most consistent estimation of pile capacity of those investigated and should be preferred over all others. The Gates formula is not significantly more difficult to use than the EN formula and requires only a calculator with common logarithm and square root functions. The data required are the same: the set in inches and the energy of the hammer in foot-pounds. It should be emphasized, however, that the Gates formula will not always result in higher pile capacities. It is possible that, for a given project, the Gates formula may require more or deeper piles, or both.

Implementation

The implementation of the recommendations from this paper raises some interesting questions. The first question involves the use of a divisor of 1.06 or 1.21 with the Gates formula, depending on the level of safety required. This is much lower than the safety factor recommended in standard references (*5*). Bowles recommends the use of 3.0, and safety factors of 2 to 3 are commonly used by engineers in the United States.

Understandably, individuals who design pile foundations may be hesitant to make what might appear to be a significant change in safety factor. However, it should be emphasized that a different approach to the question of safety is suggested based on statistical analyses of real test data from a specific area of the country. The divisor recommended is not a safety factor but rather an adjustment factor based on a group of pile load tests and the level of safety desired. The resulting average actual safety factors for the piles analyzed in this study range from 1.65 to 1.97, depending on the degree of safety required. These are quite reasonable values for design.

A major purpose of a study such as this is to allow safe but less conservative design. When sufficient statistical data are available, such a design is possible as long as the results are applied *only in the region of the country and for the types of piles covered by the study*. In other locations, the divisor used

should be based on similar statistical analyses. If none are available, the use of a safety factor in the 2 to 3 range, rather than a divisor, is sensible.

A second question concerns the relationship between allowable load calculations based on pile load tests and formula predictions. Current WSDOT practice when pile load tests are conducted is to specify an allowable load equal to one-half the ultimate load determined by the pile load test. To be consistent with this practice, it can be argued that the formula prediction, either EN or Gates, should also be divided by 2 to obtain the allowable load. Such a practice would result in much lower allowable loads than are currently used. However, the current use of a safety factor of 6.0 to obtain an allowable load with EN has not resulted in serious failures.

How can one justify reducing the allowable loads by an additional factor of 2? The authors believe that two points should be made. First, the use of a safety factor of 2 when pile load tests are conducted appears overly conservative in most cases, unless the consequence of small settlement is severe. For the pile load tests used in this study, the average settlement at ultimate load (based on the D-over-30 method) is 4.8 percent of the pile diameter (less than ¾ in., on average). The magnitude of settlement at one-half the ultimate load is 1.2 percent of pile diameter (less than ⅛ in., on average). This results in almost negligible settlement. In situations where soil conditions are reasonably uniform throughout a site and settlement tolerances are not extreme, a lower safety factor on pile load test results for this study area can be justified, perhaps in the range of 1.5 to 1.75.

Second, the Gates and EN formulas with the appropriate divisor yield an allowable load, not the ultimate load as do the pile load tests. The actual ultimate capacity for the vast majority of piles is greater than the predicted capacity; hence, the actual safety factor is greater than 1.0, averaging between 1.65 and 2, depending on the safety level desired. The actual safety factor for a given pile cannot be known unless the pile is tested. Even in those cases where the loading is near the ultimate, it appears unlikely that settlement would be excessive. There is no real way to make the two methods comparable because one is based on an actual test result on a similar, nearby pile, and the other is based on a formula prediction of allowable load.

SUMMARY

To determine whether WSDOT should replace the EN formula with some other dynamic formula for estimating pile capacity, the relative performance of 10 pile-driving formulas was studied. Data were collected from 63 pile load tests conducted in western Washington and northwest Oregon. Included in this data set are open and closed steel pipes, steel HP sections, timber, concrete, hollow concrete, and Raymond step tapered piles. Three methods of calculating pile capacity based on pile load test results were used and the results compared. Relatively little difference was found and the most objective of the three (the D-over-30 method) was chosen to establish the capacities of the test piles.

The predicted capacity of each pile was calculated using the Danish, EN, modified EN, Eytelwein, Hiley, Gates, Janbu, Navy-McKay, PCUBC, and Weisbach formulas. Scatter graphs of the predicted versus the measured capacity were plotted for each formula. To perform statistical analyses of the data, the predicted capacity was normalized by dividing it by the measured capacity. Because these data are not normally distributed the logarithms of the normalized capacities, which are normally distributed, were used.

Analyses of the coefficient of variation for each formula show that the Gates formula is the most accurate of the 10 formulas compared and that the EN formula is among the worst. The coefficient of variation for the EN formula is approximately 2 to 3 times higher than that for the Gates formula.

In addition, a second method of comparison was used in which the measure of safety was determined by the percentage of piles for which the measured capacity was expected to be lower than the formula prediction. This method also provided the spread of actual safety factors resulting from the use of each formula for a given measure of safety. The Gates formula was again found to be the best, and the EN formula again ranked near the bottom.

Subsequent economic analyses showed that for the same level of safety, the Gates formula resulted, on average, in higher allowable capacities and therefore lower costs.

ACKNOWLEDGMENTS

The research described in this paper was supported by the Washington State Department of Transportation and the Federal Highway Administration, U.S. Department of Transportation. The authors are grateful to Alan Kilian for his review of the manuscript and his significant contributions to the discussion portion of the paper.

REFERENCES

1. R. J. Fragaszy, J. D. Higgins, and E. Lawton. *Development of Guidelines for Construction Control of Pile Driving and Estimation of Pile Capacity*. Report WA-RD 68.1. Washington State Transportation Center, Olympia, Wash., June 1985, 83 pp.
2. E. C. Lawton, R. J. Fragaszy, J. D. Higgins, A. P. Kilian, and A. J. Peters. Review of Methods for Estimating Pile Capacity. In *Transportation Research Record 1105*, TRB, National Research Council, Washington, D.C., 1986, pp. 32–40.
3. D. Argo. *Dynamic Formulas to Predict Driven Pile Capacity*. M.S. thesis. Washington State University, Pullman, Dec. 1987, 126 pp.
4. H. A. Agerschou. Analysis of the Engineering News Pile Formula. *Journal of the Soil Mechanics and Foundations Engineering Division—ASCE*, Vol. 88, No. SM5, Oct. 1962, pp. 1–11.
5. J. E. Bowles. *Foundation Analysis and Design*. 4th ed., McGraw-Hill, New York, 1988, 1,004 pp.

Publication of this paper sponsored by Committee on Foundations of Bridges and Other Structures.

Study of Dynamic Methods of Predicting Pile Axial Load Capacity by Louisiana Department of Transportation and Development

MICHAEL D. FOLSE, KENNETH L. MCMANIS, AND JANET S. ELIAS

The Louisiana Department of Transportation and Development (LADOTD) has undertaken the task of optimizing its use of dynamic prediction methods for pile axial load capacity. The immediate intention is to replace its current use of the *Engineering News Record* formula with a more reliable, yet comparably inexpensive dynamic method. Several alternative dynamic formulas and wave equation analyses are being considered. Through the University of New Orleans Civil Engineering Department, LADOTD is studying the ability of each method in predicting Louisiana load test results. After a replacement method has been selected, field implementation procedures and software will be developed. This paper presents a review of selected literature that has defined the current status of dynamic pile capacity prediction and influenced the direction of the LADOTD project. A description of the various components of the LADOTD project, which was completed in December 1989, is also presented.

Pile foundations are especially important for bridges in Louisiana, where the surface soils are often poor and the water table is high. Failure of piles under bridges can have disastrous consequences, but the high cost of piling makes extreme overdesign impractical. Therefore, in order to design economical bridge foundations, the capacity of virtually every pile must be estimated accurately.

Because of the critical nature of the problem, pile designers prefer to have several alternative methods of estimating pile capacity. On most projects, three sources of capacity estimates are available:

- Those based on analyses of soil-boring information or cone penetrometer testing,
- Those based on nearby load tests of similar piling, and
- Those based on the driving record and pile equipment characteristics for the particular pile (i.e., dynamic methods).

The Louisiana Department of Transportation and Development (LADOTD) is currently studying ways to optimize its use of dynamic methods of pile capacity prediction for bridges in Louisiana. Similar studies are under way in other parts of the country (*1,2*).

This paper describes the current status of dynamic prediction of pile axial load capacity by reviewing selected literature; it also describes the project completed by LADOTD.

Department of Civil Engineering, University of New Orleans, New Orleans, La. 70122.

NEED FOR DYNAMIC METHODS

Most pile designs evolve in the same way. Once the project has been conceived, soil borings are taken. Based on soil-boring analyses, appropriate pile type and length are selected. Typically, the pile design load is the predicted ultimate capacity from soil boring analyses, divided by a safety factor between 2.0 and 3.0. One or more of the selected piles is then driven and load tested to two or two and one-half times the desired design load. Blow counts and equipment characteristics pertinent to the test are recorded.

Most test piles survive the test loading without soil or structural failure and are used as part of the permanent foundation. The remaining (untested) piles are driven with the same equipment, and their blow counts are recorded. These piles are usually driven to similar depths and with similar blow counts as the test piles, and it is thus assumed that the untested piles also have the desired capacity.

Unfortunately, this model process does not always occur as previously described for various reasons. Soil-boring information may be insufficient, especially in some of the swamp areas of Louisiana where good samples cannot be recovered. Some projects are too small to justify a load test. For emergency repairs, there may not be enough time to conduct a load test. Also, production piles often do not receive the same number of blow counts as the test piles. A relatively low blow count at design penetration suggests a capacity lower than the test pile capacity. However, if the test pile resisted at least twice the design load without failure, it is uncertain whether this lower blow count indicates the need for additional pile length. A relatively high blow count before design penetration indicates the possibility of stopping the pile short. Continued driving may damage the pile or take an uneconomical length of time, but the reduced penetration may not result in adequate static capacity.

Because of these less-than-ideal situations, foundation engineers often must include the so-called *dynamic* methods when predicting pile axial load capacity. These methods currently range from the basic *Engineering News Record* (ENR) formula to the wave equation analysis with pile analyzer input.

The ENR, and most other formulas, is based on the principle of energy conservation (i.e., the energy imparted by the hammer ram, minus any losses, should equal the pile ultimate capacity, multiplied by the incremental penetration due to the latest hammer blow—this is oversimplified for most cases).

A wave equation analysis predicts the penetrations and corresponding blow counts for a given pile-hammer system and ultimate capacities by performing one-dimensional dynamic analyses of the hammer blow stress waves. Using the resulting curve inversely, one obtains the capacity corresponding to the known blow count. An allowable design load is obtained by dividing the ultimate capacity predicted (by whichever dynamic method is used) by a safety factor. The safety factor ranges from 2.0 to 6.0, for the current popular methods, and is generally loosely tied to the relation between the method's predictions and selected load test results.

When load tests have been performed and a given production pile drives similarly to the test pile, actual capacity predictions of the dynamic method are generally ignored in favor of test pile results. However, when load tests are not performed, or when a pile drives much differently than the test pile, dynamic predictions are very influential to design decisions.

Despite its proven inaccuracy, the ENR is still the most commonly used dynamic prediction method. This is due to its simplicity and the popular belief that none of the more complicated methods has yet been proven to be sufficiently superior to warrant its adoption. All of the dynamic methods, including the wave equation, have been criticized for use as pile static capacity predictors. One problem often cited is the possibility of large time-dependent gains or losses in capacity that cannot be quantified by analysis of end-of-driving conditions. However, the necessity for using dynamic methods in many instances has resulted in their continued use and development.

LITERATURE REVIEW

Pile Foundations by Chellis (*3*) presents extensive information relevant to predicting pile axial capacity using dynamic formulas. The time-dependent nature of pile axial capacity is discussed. Chellis suggests redriving the test piles after time delays in order to quantify time effects on capacity. Chellis also summarizes the soil conditions under which certain increases or decreases in capacity might be expected.

The history and use of dynamic formulas are presented, including detailed guidance on hammer efficiencies and coefficients of restitution, as well as information on driving hammers, piles, and other items pertinent to contemporary pile driving. Derivations for many of the formulas and comparisons between formula predictions and load tests are also presented. On the basis of these results, Chellis concluded:

> The scattering of results from the Engineering News and Eytelwein formulas is too wide to be comprehended within any one factor of safety, and even a factor of 6 would not be adequate for a number of the results.

In 1971, Poplin (*4*) examined and evaluated test pile data collected by LADOTD between 1950 and 1970. Among the many tasks undertaken during the project was a comparison of test loads to ENR formula predictions for 24 square precast concrete piles (14-in. and 16-in.). The ratio of ENR allowable load to test load ranged from 0.11 (safety factor = 9.0) to 1.00 (safety factor = 1.0). The average ratio was 0.506 (safety factor = 2.0), but the standard deviation of 0.183 was quite high. Poplin also examined a soil mechanics prediction of capacity for the same 24 piles and found only slighty better accuracy on the average. However, the range of safety factors was much smaller.

In 1962, Smith (*5*) described the use of the wave equation for estimating pile capacities and stresses. Smith presented mathematical models for the hammer-pile system and the soil resistance, and outlined a numerical solution to the pile displacements. Recommended values for most of the procedure inputs are given along with a detailed illustrative problem.

Critiques of Smith's paper by several well-known foundation experts were published with the paper in *ASCE Transactions*. Soderberg is generally supportive of the wave equation development and use. Marvin Gates, originator of the Gates formula, objects strongly to the implication that "the wave equation can be used to solve for the bearing capacity as well as the driving stresses." Cornfield acknowledges Smith's reference to the poor performance of dynamic formulas but suggested that correlations with load test results would be better if piles suspected to have large setups were eliminated from the comparison. Cornfield notes that load tests are the best method of determining pile capacity, but that their high cost precludes extensive use. He is hopeful that the wave equation solution will be a "reasonably accurate method of making use of the driving data" when load test results are not available or not applicable.

In 1980, Blessey and Lee (*6*) investigated the use of the wave equation for predicting pile capacities in the New Orleans area. The scope of their study was defined as follows:

> The investigation of the input soil parameters, and the development of the relationship of soil resistance from the Wave Equation to actual pile load capacities obtained from the pile load tests performed in the field for both friction and end-bearing piles.

Blessey and Lee studied 50 test pilings from the New Orleans area. R is the ratio of test-pile failure load to wave-equation-predicted failure load. The method of determining test-pile failure load was not stated, but the maximum load applied before pile plunging is probably intended. Classification of certain input was given and is reproduced in Table 1. Much of the input used, such as capblock and cushion stiffness, was not stated in the report.

For end-bearing prestressed concrete piles, the average R was 1.15 when minimum parameters were input to the wave equation. Mean R-values for average and maximum soil parameters were 0.9 and 0.5, respectively. The least variation between high and low R-values was obtained for minimum values. For end-bearing pipe piles, average R-values were 1.4, 1.1, and 0.9 for minimum, average, and maximum soil parameters, respectively. Again, the minimum parameters produced the most consistent results.

For friction piles, using the average blow count for the final 5 ft of penetration, average R-values for prestressed concrete piles were 6.0, 3.53, and 3.3 for minimum, average, and maximum soil parameters, respectively. For friction pipe piles, average R-values were 6.0, 4.5, and 3.3. For friction H-piles, average R-values were 5.0, 4.0, and 2.9. Minimum or average

TABLE 1 COMPUTER INPUT SOIL PARAMETERS (6)

Type of Input Parameters	Type of Soil	Quake(Q) (Inches)	Damping (J) (Sec/Ft) Side	Point	Hammer Efficiency
Minimum	Clay	0.30	0.20	0.01	0.65
Average	Clay	0.10	0.20	0.01	0.75
Maximum	Clay	0.05	0.10	0.01	0.85
Minimum	Sand	0.20	0.07	0.20	0.65
Average	Sand	0.10	0.05	0.15	0.75
Maximum	Sand	0.05	0.03	0.05	0.85

soil parameters produced the most consistent results in all cases.

In 1971, Rausche et al. (7) described the use of what is now commonly known as the *pile analyzer* to predict pile axial load capacities. Special instrumentation was used to measure actual pile force and acceleration due to the hammer blow. This information can be used directly or can be input to a wave-equation-type analysis for pile capacity prediction. The authors note that "the pile can be restruck a few days after driving to include strength changes of the pile-soil interface during set up." Dynamic records of 21 piles were analyzed. The dynamic data were obtained shortly (a few hours) before or after performing a static load test, thereby including the effects of set up in the dynamic method. The comparison between test pile failure load and pile analyzer prediction is reproduced in Table 2. The load test values given are those corresponding to the "largest pile displacement obtained under the [final?] hammer blow" and are substantially lower than actual maximum loads for many of the examples.

In 1982, Whited and Laughter (8) described the pile design process for the Arrowhead Bridge located between Superior, Wisconsin, and Duluth, Minnesota. Piles on this job were driven from 130 ft to 260 ft through loose sands and soft clays to a dense sand. Two pile types were considered: a 16-in. diameter cast-in-place (CIP) concrete pile driven closed end and an HP 14 × 73. Four H-piles and two pipe piles were load tested.

Whited and Laughter wrote that

> piles were to be driven to a minimum bearing of 172 tons-force as determined by the Wisconsin (modified EN) driving formula:
>
> $$P = 2WH/(S + 0.2) \quad (1)$$
>
> where
>
> P = bearing value (lb), (allowable)
> W = ram weight (lb),
> H = height of ram fall (ft), and
> S = penetration per blow (in).

Test piles were loaded to a maximum of 344 tons. Ultimate pile capacities were predicted from the resulting load-deflection curves using the methods of Davisson, Mazurkiewicz, Chin, the Swedish Pile Commission, and the American Association of State Highway and Transportation Officials (AASHTO). Davisson's method was selected as being most appropriate. The authors described this method as follows:

> Davisson's method defines the failure load as the load that corresponds to the movement that exceeds the elastic compression of the pile, when considered as a free column, by a value of 0.15 in plus a factor depending on the diameter of the pile. For the 16-in CIP piles and HP 14 × 73 this factor is approximately 0.1 inch. Thus, the pile reaches failure at a pile-head movement that exceeds the elastic compression by 0.25 in.

The Mazurkiewicz, Chin, and Swedish methods gave somewhat higher estimates of ultimate load, whereas the AASHTO limiting load, defined as the "load that, after a continuous application of 48 hours, produces a permanent settlement not greater than 0.25 inch," was significantly lower.

The performance of the pile analyzer in predicting load test results was described as "reliable" for the H-piles but not for the CIP piles. Errors for the CIP piles were attributed to larger setups together with the nonavailability of restrike data. The wave equation method (without pile analyzer input) was also used to predict load test results, but the predictions were poor.

On the basis of the test pile program, the HP 14 × 73 was selected for use on all foundations. The allowable load and assumed ultimate load were 150 and 300 tons, respectively. Most production piles were driven into the dense sand layer until the blow count indicated an allowable load of 150 tons by the Wisconsin formula. A blow count indicating an allowable load of 200 tons was required when penetration into the dense sand was not achieved. Hammers used to drive production piling were not the same as those used to drive test piling, but the rated energies were higher.

The pile analyzer was also used to monitor production piling by instrumenting one or two piles from each bent. A high instrument-damage rate led to reduced use of the analyzer only during pile restrikes after embedments were indicated to be adequate by the Wisconsin Department of Transportation formula. The analyzer was also found to be useful in identifying piles that were damaged by driving.

A 1985 report by Fragaszy et al. (1) to the Washington State Transportation Center presents a review of the literature

TABLE 2 PILE ANALYZER PREDICTIONS OF TEST PILE CAPACITIES (7)

Pile	Load Test,kips	Pile Analyzer,kips
1	151	159
2	97	91
3	107	136
4	172	163
5	200	233
6	176	210
7	174	180
8	137	166
9	183	204
10	60	69
11	93	119
12	32	56
13	75	122
14	165	173
15	90	151
16	125	151
17	152	163
18	40	45
19	64	84
20	176	184
21	174	187

with regard to the use of dynamic pile driving equations, wave equation methods, and pile analyzers. Approximately 200 technical references were reviewed, and the results were given of a survey of state transportation departments to determine what dynamic methods they were currently using.

With regard to the survey results, Fragaszy reported the following:

> The majority of the 34 states responding . . . indicated that they use the Engineering News formula in its original or modified form. No other dynamic equation was mentioned. Several states indicated a switch in recent years from the Engineering News formula to wave equation analyses with a resulting increase in accuracy. Only two states make regular use of the pile analyzer, but they are very satisfied with it.

Fragaszy's review of technical literature indicated that, among the simple formulas, the Hiley, Janbu, and Gates were generally superior, and he found the ENR formula and its modifications to be generally inferior. The wave equation was found to be equal to or better than the best formula. Fragaszy summarized the use of the pile analyzer as follows:

> A pile analyzer can produce very accurate estimations of pile capacity. However, a pile analyzer is relatively expensive to purchase and maintain and requires highly trained individuals to interpret the data it collects.

As a result, Fragaszy recommended increased use of, but by no means total reliance on, the wave equation and pile analyzer. Discontinued use of the ENR formula in favor of a more accurate one was also recommended. The best formula would be determined through statistical analyses of regional load test data and the ability of the formulas to predict those load test results.

DISCUSSION OF THE LITERATURE

Review of the above papers and reports leads to the conclusion that much is still to be achieved in the area of dynamic prediction of pile capacity. None of the simple formulas has been proven to be adequate, although several have not been proven totally inadequate. Furthermore, the simplicity of their

application makes their sudden and complete discard highly unlikely. Some have found the wave equation analysis to be accurate, but others have found it to be practically useless. The required availability of a computer and software for its execution generally is no longer a major obstacle; however, the uncertainty of proper input for many of its variables remains a problem for most potential users. The pile analyzer has been praised by most who have used it, but its requirement for additional instrumentation and experienced personnel makes most engineers unwilling to abandon all other alternatives. Furthermore, it is not a precise predictor in all cases.

One important issue in the use of any of the methods is the treatment of the time effects on pile capacity. The logical and seemingly simple solution to this problem is to use restrike blow counts or force-and-acceleration data, or both. However, restriking brings about several problems:

1. The restriking must be performed after an appropriate time delay. Pile accessibility is often impaired by installation of surrounding piling. Furthermore, resetting the pile driver over each pile can be quite expensive.
2. In soils of considerable setup, the pile hammer used for production driving may not be of adequate size to restart the pile. A suitable starter hammer or other device for obtaining an after-setup blow count or pile analyzer data may not be suitable for driving additional pile length, should it be required.
3. Very little restrike data have been gathered for test piles. Thus, it is impossible to check any method's ability to predict historic load test results by using restrike blow counts.
4. Significant increases or decreases in capacity may occur after restriking.

In the research described below, time effects are estimated by applying a setup factor to the end-of-driving side friction capacity.

LADOTD PROJECT

In common with many state transportation departments and other agencies, LADOTD currently uses the ENR formula or its modifications to some extent. Through an ongoing project with the University of New Orleans, LADOTD intends to replace its use of the ENR with a more reliable dynamic method. The project currently is focusing on evaluating alternative dynamic formulas and the wave equation. Pile failure load predictions of the various methods under study are being compared with pile load tests performed in Louisiana.

The pile analyzer has been proven relatively accurate, and LADOTD is already using it on some projects. However, its requirement for additional instrumentation and personnel eliminates the pile analyzer as an ENR replacement requiring roughly equivalent effort and expense. Furthermore, it is impossible to evaluate the ability of the pile analyzer to predict historical load test results, because pile force and acceleration data have rarely been taken.

The growing practice of restriking will contribute greatly to pile capacity prediction in Louisiana, where setup factors are often very high. However, the costs and access problems associated with restriking preclude its specification for every pile. Again, the lack of restrike data on historical load tests makes evaluation of its effectiveness difficult.

The following dynamic methods are currently being studied (*9*):

1. ENR,
2. Hiley,
3. Gates,
4. Janbu,
5. Pacific Coast Uniform Building Code (PCUBC), and
6. Wave equation.

Suitable Louisiana load test results have been, and are being, computerized as part of the effort. For each load test entered into the data base, six ratios involving test load and the prediction of each of these methods are calculated:

$R1$ = maximum test load/predicted ultimate load
$R2$ = maximum test load/adjusted predicted ultimate
$R3$ = estimated failure load at time of test/predicted ultimate load
$R4$ = estimated failure load at time of test/adjusted predicted ultimate
$R5$ = estimated failure load at end of driving/predicted ultimate load
$R6$ = estimated failure load at end of driving/adjusted predicted ultimate

The adjusted predicted ultimate is the predicted ultimate load divided by the applicable theoretical safety factor: ENR 6.0, Hiley 3.0, Gates 3.0, Janbu 4.5, PCUBC 4.0, WEAP (wave equation analysis of pile) 2.0; then multiplied by 2.0. This adjusts a method's ultimate prediction to be 2.0 times its customary allowable load.

The maximum test load is not always the failure load, because many load tests are not carried to failure. Furthermore, the failure load of a load test carried to failure varies according to the interpretation method. The estimated failure load at time of test is the maximum test load multiplied by a factor intended to account for this difference. The following methods were studied for possible use in deriving the failure load from test-pile-load versus deflection data: Van der Veen, Mazurkiewicz, Davisson, Chin, AASHTO, Swedish Pile Commission. The Van der Veen method was selected for this project because it was used previously with Louisiana test piles (*10*). Van der Veen proposed the following relation between a pile's ultimate capacity and its load-versus-deflection behavior:

$$Q = Q_u (1. - e^{-rz}) \tag{2}$$

where

Q = applied load causing butt deflection z,
Q_u = pile ultimate capacity, and
r = coefficient determined from load-deflection curve.

Using two (Q,z) points near the upper end of the load-deflection curve, Q_u and r can be determined.

The failure load at end of driving is not the same as the failure load at time of test if setup or relaxation occurs. The end-of-driving blow counts available for historical load tests can logically be expected only to indicate failure load at end of driving, even for the best of prediction methods. The estimated failure load at time of test is divided by an input setup factor to obtain the estimated failure load at end of driving. This setup factor, SUF, is computed as follows:

$$SUF = S(P_s) + 1.0(P_t) \tag{3}$$

where

P_s = fraction of total pile resistance coming from side friction,
P_t = fraction of total pile resistance coming from tip bearing,
S = 1.0 if predominant side soil has high permeability (sand or gravel),
= 2.0 if predominant side soil is medium to stiff clay,
= 3.0 if predominant side soil is soft to medium clay, and
= 4.0 if predominant side soil is very soft to soft clay.

The fraction, P_s, of total resistance coming from side friction refers to end-of-driving conditions and is computed as follows:

P_s = 0.95 if the final blow count is less than 3.5 times the average blow count,
= 0.75 if the final blow count is between 3.5 and 4.0 times the average blow count,
= 0.50 if the final blow count is more than 4.0 times the average blow count.

For the rare cases in which load tests are carried to failure as defined by Van Der Veen, without substantial setup, and the prediction method's theoretical safety factor is 2.0, all six ratios will be equal. If the method is also "perfect," all ratios will be 1.0. It is hoped and expected that by examining and analyzing these ratios for many load tests, the best prediction method for Louisiana will become evident.

To perform the above calculations, it was necessary to develop appropriate computer software and data-entry formats. A standard form was developed for manual extraction of applicable data from LADOTD's file of pile load tests. An interactive FORTRAN computer program was then written to accept keyboard data entry and to create an equivalent computer data file. Although each load test has its own file, a cumulative catalog file, containing key information from each test, is updated automatically with each additional load test entered.

A second FORTRAN program, PLCAP, was written to perform the comparisons between load test results and the predictions of the various dynamic methods. Formula methods were easily programmed. However, an early attempt to incorporate the WEAP program was abandoned in favor of running WEAP87 separately and simply inputting its prediction to the developed program for calculation of the described ratios.

Parameter studies were conducted with many of the input items for the WEAP87 program in order to determine the sensitivity of results to reasonable variations in those parameters that are not generally precisely known. These parameters include capblock stiffness, cushion stiffness, hammer efficiency, coefficients of restitution, pile internal damping, soil side and tip damping, soil side and tip quake, percentage skin friction, and skin friction distribution type. As expected, it was concluded that predicted blow count for a given pile ultimate capacity often varied greatly with changes in certain parameters within plausible limits. In practice, one or more key parameters, such as side damping, are often calibrated to site load test results, such that the wave equation precisely predicts the load test results when those calibrated values are used. These same parameter values are used for wave equation predictions of the production pile capacities. This calibration procedure, which can also be used with any of the dynamic prediction methods, is often successful. However, it is dependent on the availability of load test results and is obviously not appropriate for an evaluation of methods for independent use. In this research, two wave equation predictions per load test are determined. For the first prediction, the best information available is used for the WEAP87 input. This information is derived from the literature, the WEAP87 user's manual, and conversations with experienced individuals in the pile-driving industry. For the second prediction, referred to as WEAPDF, a set of default average parameters was input.

Summary statistics for several groupings of the compiled load test data base are given in Tables 3 through 7. These results should be regarded as preliminary because analysis of the results has not yet been completed.

TABLE 3 SUMMARY STATISTICS FOR 56 SQUARE CONCRETE PILES

	Mean		COV	Mean		COV
Method	R3	R4	R3 and R4	R5	R6	R5 and R6
ENR	0.599	1.797	0.61	0.348	1.044	0.60
Hiley	1.598	2.398	0.50	0.953	1.429	0.53
Gates	2.239	3.359	0.46	1.361	2.041	0.54
Janbu	2.186	4.918	0.55	1.264	2.844	0.51
PCUBC	2.972	5.944	0.52	1.730	3.460	0.50
WEAP87	2.605	2.605	0.64	1.461	1.461	0.58
WEAPDF	2.682	2.682	0.72	1.514	1.514	0.65

TABLE 4 SUMMARY STATISTICS FOR 12 TIMBER PILES

	Mean		COV	Mean		COV
Method	R3	R4	R3 and R4	R5	R6	R5 and R6
ENR	0.436	1.308	0.30	0.389	1.168	0.30
Hiley	1.429	2.143	0.24	1.280	1.920	0.24
Gates	1.643	2.464	0.24	1.471	2.206	0.24
Janbu	1.670	3.758	0.24	1.497	3.369	0.25
PCUBC	2.056	4.112	0.24	1.841	3.683	0.25
WEAP87	1.728	1.728	0.24	1.553	1.553	0.26
WEAPDF	1.704	1.704	0.25	1.527	1.527	0.26

TABLE 5 SUMMARY STATISTICS FOR 60 PILES DRIVEN WITH SINGLE-ACTING AIR/STEAM HAMMERS

	Mean		COV	Mean		COV
Method	R3	R4	R3 and R4	R5	R6	R5 and R6
ENR	0.650	1.949	0.60	0.391	1.172	0.50
Hiley	1.727	2.591	0.42	1.084	1.626	0.42
Gates	2.251	3.377	0.43	1.438	2.157	0.49
Janbu	2.278	5.126	0.52	1.381	3.106	0.44
PCUBC	2.954	5.908	0.50	1.805	3.609	0.44
WEAP87	2.685	2.685	0.63	1.573	1.573	0.49
WEAPDF	2.686	2.686	0.72	1.560	1.560	0.54

TABLE 6 SUMMARY STATISTICS FOR 43 PILES BEARING IN CLAY

	Mean		COV	Mean		COV
Method	R3	R4	R3 and R4	R5	R6	R5 and R6
ENR	0.619	1.858	0.60	0.360	1.079	0.53
Hiley	1.609	2.414	0.42	0.993	1.489	0.50
Gates	2.032	3.048	0.46	1.259	1.888	0.54
Janbu	2.204	4.959	0.49	1.298	2.921	0.48
PCUBC	2.828	5.657	0.47	1.678	3.355	0.49
WEAP87	2.728	2.728	0.60	1.529	1.529	0.48
WEAPDF	2.611	2.611	0.61	1.468	1.468	0.50

TABLE 7 SUMMARY STATISTICS FOR 12 PILES BEARING IN SAND

	Mean		COV	Mean		COV
Method	R3	R4	R3 and R4	R5	R6	R5 and R6
ENR	0.469	1.408	0.56	0.367	1.102	0.79
Hiley	1.498	2.247	0.58	1.091	1.636	0.59
Gates	2.450	3.676	0.63	1.925	2.887	0.85
Janbu	1.873	4.213	0.47	1.421	3.198	0.60
PCUBC	2.473	4.945	0.47	1.822	3.644	0.53
WEAP87	1.977	1.977	0.61	1.563	1.563	0.83
WEAPDF	2.087	2.087	0.57	1.643	1.643	0.78

CONCLUSIONS

1. Dynamic methods remain an important component in predicting pile axial load capacity.
2. Wave equation analysis with pile analyzer input and the practice of restriking are becoming recognized means of improving dynamic predictions. However, associated additional expenses and effort prevent their use on every pile.
3. Still needed are reliable dynamic prediction methods that can be used economically on every pile. The so-called best method may vary from location to location and should be selected by comparing the method's predictions to appropriate load test results.
4. Quantifying time effects on pile capacities remains a difficult component in the use of dynamic methods.

ACKNOWLEDGMENT

This ongoing study is being sponsored by the Louisiana Department of Transportation and Development and the Federal Highway Administration, U.S. Department of Transportation.

REFERENCES

1. R. Fragaszy, J. Higgins, and E. Lawton. *Development of Guidelines for Construction Control of Pile Driving and Estimation of Pile Capacity—Phase I.* Washington State Transportation Center, Pullman, June 1985.
2. J. F. Ledbetter, Jr. Use of the Wave Equation by the North Carolina Department of Transportation. In *Transportation Research Record 1169*, TRB, National Research Council, Washington, D.C., 1988, pp. 43–48.
3. R. Chellis. *Pile Foundations*. 2d ed. McGraw-Hill, New York, 1961.
4. J. Poplin. *Preliminary Evaluation of Test Pile Records for Highway Structures in Louisiana*. Louisiana Department of Highways, Baton Rouge, 1971.
5. E. Smith. Pile-Driving Analysis by the Wave Equation. *ASCE Transactions*, Vol. 127, Part 1, 1962, pp. 1145–1192.
6. W. E. Blessey and P. Y. Lee. *Report on Wave Equation Analysis of Pile Driving in the New Orleans Area*. Pile Driving Contractors Association of New Orleans, Inc., 1980.
7. F. Rausche, G. Goble, and F. Moses. A New Testing Procedure for Axial Pile Strength. Presented at Offshore Technology Conference, Houston, Tex., 1971.
8. G. Whited and C. Laughter. Pile Foundation—From Preliminary Borings to Production Driving. In *Transportation Research Record 884*, TRB, National Research Council, Washington, D.C., 1982, pp. 7–13.
9. J. E. Bowles. Single Piles—Dynamic Analysis. In *Foundation Analysis and Design*, 3rd ed., McGraw-Hill, New York, 1982.
10. M. Tumay and M. Fakhroo. *Friction Pile Capacity Prediction in Soft Louisiana Soils Using Electric Quasi-static Penetration Test*. Interim Research Report No. 1. Louisiana Highway Research, 1981.

Publication of this paper sponsored by Committee on Foundations of Bridges and Other Structures.

Analysis of Drilled Piers Used for Slope Stabilization

MICHAEL W. OAKLAND AND J.-L. CHAMEAU

This paper presents a technique to evaluate the effects of drilled piers on the stability of slopes. The model allows for construction sequences, interaction between pier displacements and soil movements, remolded areas around the piers, and weaker seams (if present) in the soil profile. Applications of the technique are presented, with emphasis on identifying and optimizing the factors that control the performance of piers used for slope stabilization. Three applications of the use of drilled piers for slope stabilization were investigated: surcharge loading, excavation from a horizontal ground surface, and cut slope stabilization. Several conclusions regarding slope-pier interaction can be drawn. Of prime importance is that the piers must be positioned at a point where relatively large displacements are expected to occur; the magnitude of these displacements determines how much stress will be mobilized against the pier. The balance between cohesive strength mobilized and frictional strength mobilized is important to the performance of the stabilizing piers. Where upward movement is a prime component, the support offered by the piers becomes very indirect, providing added support through retention of confinement. The entire soil-structure interaction that occurs between the piers and soil mass must be considered when evaluating drilled piers for slope stabilization—not simply the added shearing resistance provided by the piers. The redirection of stresses throughout the soil can be either beneficial or detrimental to the final stability. On the basis of the analyses performed to date, the best applications of the piers seem to be in purely cohesive materials under loading conditions that can use the vertical resistance of the piers.

During the past two decades, innovative soil-reinforcement techniques (such as reinforced earth, stone columns, soil anchors, piles, and cast-in-place piers) have been developed to solve many slope stability problems. These techniques use semirigid members that are capable of transferring loads through shear, tension, or compressional resistance from an unstable mass above the failure surface to more stable underlying layers. In Sweden, battered timber piles have been used to increase the stability of slopes in very soft clays by dowelling across potential failure surfaces. Inserting the piles at an angle allows them to act partially in compression rather than to rely totally on their resistance in shear. Steel pipe piles have been used for the same purpose in Japan (*1*). Broms and Wong (*2*) discussed similar applications for piles to support fills, bridge abutments, and deep excavations.

Systems of drilled-in minipiles (such as the reticulated root pile method, which consists of dense clusters of vertical and battered small-diameter piles) have been used in the United States. These systems take advantage of the soil strengthened by the piles to form a barrier that resists movement and transfers stresses downslope (*3*). Stone columns, although relatively new in the United States, have been proven to be quite effective in Europe (*4*, *5*). The relatively high shear strength of the columns increases the shearing resistance along the failure surface, whereas the high modulus of elasticity of the column transfers vertical loads from the surrounding moving soils to the more stable foundation layers. The vertical loads absorbed, in turn, increase the confining stress within the stone column, and thus its shearing resistance.

Large-diameter, cast-in-place, reinforced concrete piers have been used in Europe and the United States to stabilize active landslide areas in stiff clays and shales through dowel action (*6–12*). The diameters of these piers can be as large as 1.5 m (5 ft). In the United States, these piers have often been used side by side or slightly overlapped to form a continuous wall in highway and building foundations. Drilled piers can also be placed discretely (Figure 1) with clear space between the piers, which takes advantage of many of the strong points of

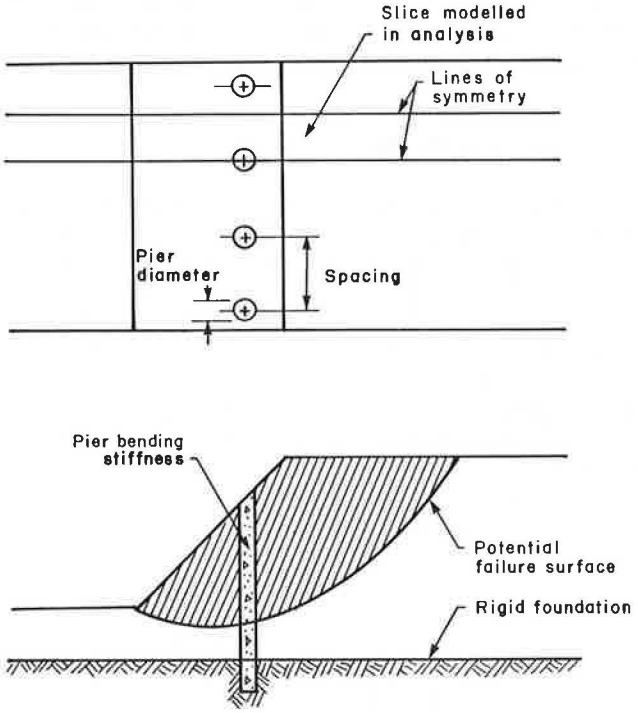

FIGURE 1 Discretely placed drilled piers for slope stabilization.

M. W. Oakland, Haley and Aldrich, Inc., Cambridge, Mass. 02141. J.-L. Chameau, School of Civil Engineering, Purdue University, West Lafayette, Ind. 47907.

previously described techniques. Drilled piers can be installed relatively quickly, at a moderate cost, and thus provide an ideal remedial measure to slow or halt the progress of failing slopes (*9*). Similar to drilled pier walls, the discretely placed piers add shearing resistance across potential failure surfaces. However, by proper positioning and spacing, the piers can also absorb vertical driving forces from the slope and transmit these forces directly to stable foundation layers below. This incorporates the design philosophy of transmitting the loads by compression rather than pure shear, as in the cases of stone columns and inclined timber piles. The discrete positioning, rather than continuous placement, provides an increased surface area that interacts with the soil and is more efficient in absorbing vertical forces. Soil arching develops between the piers, as is the case with the smaller root piles, and forms a continuous barrier that limits soil displacement between the piers.

Analysis techniques have been developed to predict lateral soil forces against piers used as reinforcement in slopes (*11–16*). The plastic deformation method developed by Ito and Matsui (*14*) to evaluate the lateral pressures acting on a row of passive piles has been incorporated in limiting equilibrium solutions for slope stability (*17*, *18*). Although these techniques are useful, especially for estimating the lateral loads on the drilled pier reinforcing system, they do not model the behavior of the slope itself and, most specifically, the changes in stress fields along potential failure surfaces. To improve the analysis of this problem, this paper presents a three-dimensional, finite element model of slopes stabilized by drilled piers that are socketed in bedrock. The technique provides displacement, strain, and stress fields within the reinforced slope. In addition, an analysis routine to estimate a limiting equilibrium factor of safety of the slope from the finite element-generated stresses has also been developed. The model and its numerical features are summarized first. Emphasis is then placed on applying the numerical method to relevant highway problems. Conclusions are drawn based on these applications and earlier examples (*19*).

PREVIOUS NUMERICAL ANALYSES

The problem of piers placed at discrete locations in a slope clearly involves three-dimensional effects; however, approximate two-dimensional analyses have proven useful. Rowe and Poulos (*20*) developed a two-dimensional model that makes allowances for the three-dimensional effect of soil flowing through the row of piers. This was accomplished by using separate solutions to analyze the soil movements and pier displacements, then comparing and adjusting their relative values. The study dealt primarily with the effect of the slope movement on the displacement and bending of the piers. A parametric study conducted for three rows of piers placed at the crest of a small slope led to the following conclusions (*20*):

1. Stability increased slowly with pier stiffness, and thus very rigid piers may have to be used to stabilize slopes.
2. Effectiveness was enhanced by restraining the pier tip. However, this restraint, combined with increased stiffness of the piers, greatly increased the bending moments in the piers.
3. Increasing soil stiffness and strength with depth had a positive effect on reducing the bending moments in the piers.

Oakland and Chameau (*19*) performed a simplified finite-element study of drilled piers (modeled as rectangular columns) used to stabilize a slope distressed by a surcharge loading at the crest. Following the recommendations made by Rowe and Poulos (*20*), the piers modeled in the study were of large diameter, very rigid, and firmly socketed into bedrock. The results were as follows:

1. To be most effective, piers should be located at the point of the expected maximum slope movement, as identified from an analysis without piers.
2. Both increasing the diameter and reducing the spacing of the piers had similar effects in reducing the surface displacements.
3. Increasing the stiffness of the pier generally decreased the displacements uniformly over the entire profile.

This simple model (rectangular piers, no slip elements, linear soil model, etc.) was used as a pilot study to establish the feasibility of drilled-pier reinforcing systems and led to the development of the technique discussed here.

PROPOSED MODELING TECHNIQUE

The finite-element program models the interaction between the slope and drilled piers used for stabilization by computing the resistance offered by passive, laterally loaded piers and applying that load to oppose soil movement. The principal features of the modeling procedure are summarized below, as well as the basic components of the associated computer program, SPILES. Additional details of the technique and program can be found elsewhere (*21*).

Finite Elements

Soil Elements

The basic soil element is a three-dimensional, linear strain eight-node isoparametric parallelepiped that is capable of adding a midside node to one or more of its sides, making it expandable to a quadratic strain 20-node isoparametric parallelepiped (Figure 2). The additional midside nodes are necessary to define the circular cross section of the piers and useful in subdividing the mesh in critical areas to improve numerical accuracy. The process of adding midside nodes is achieved by modifying and adding to the basic eight-node shape functions. Cook (*22*) described it for a two-dimensional case, and it is extended here to the three-dimensional case. Variable shape functions were developed to account for midside nodes (*21*). A second-order Gauss quadrature is used to integrate over the shape functions to determine the stiffness coefficients.

Pier Elements

The piers are represented by spar elements with four degrees of freedom, consisting of lateral translations and rotations at each end (Figure 3a). The three-dimensional behavior of the piers is developed by assigning the same node number to every

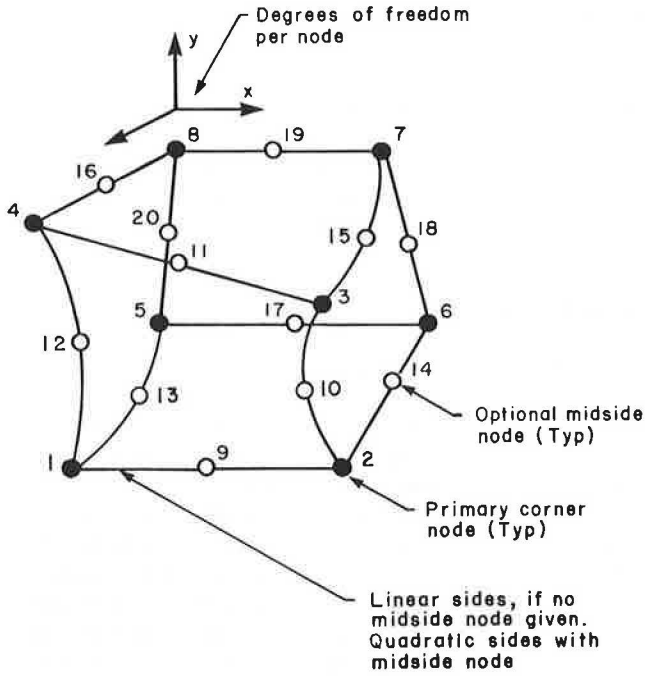

FIGURE 2 Three-dimensional, expandable, soil element.

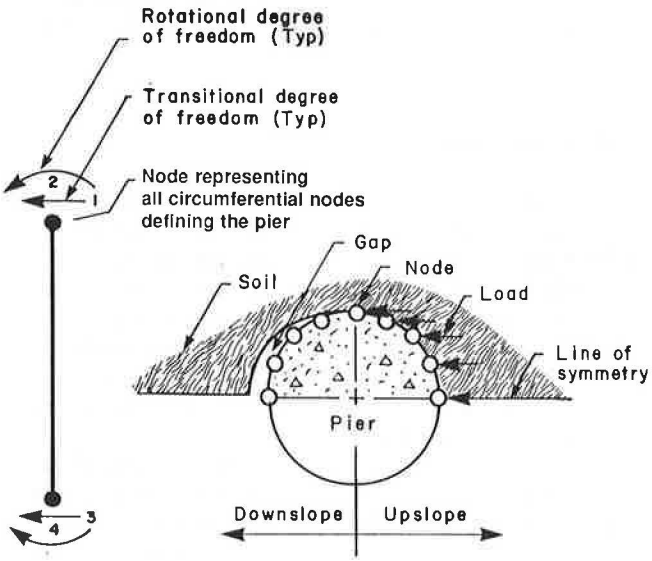

FIGURE 3 Pier elements: (*left*) pier spar element; (*right*) soil/pier nodal interaction.

soil node that defines the interface between pier and soil at a given elevation. The downslope side of the pier is not attached to the soil, which allows a gap to form as the soil separates from the piers (Figure 3b), thus preventing artificial tension forces from developing at the soil-pier interface. Bachus and Barksdale (*23*) noted such a gap when testing the lateral loading resistance of stone columns.

The spar elements chosen to represent the piers allow only for bending and translation of the piers in one direction; no deformation of the cross-sectional shape or length of the pier elements is allowed. The large difference in the elastic modulus between the soil and the concrete forming the piers makes this a realistic limitation that greatly simplifies the computational requirements and reduces the number of nodes required. In addition, the cubic bending characteristics of the spar elements provide a better representation of the pier deformations than could block elements. Furthermore, the aspect ratio of the elements (i.e., element length to width) is no longer a concern.

Slip Elements

Soil-pier interface or weak seams in the soil, or both, can be modeled by slip elements. The thin-layer elements used by Desai and Sargard (*24*) are easily incorporated in the finite element mesh. These thin elements are similar in construction to the soil elements, except that they are proportioned so that the ratio of the shortest to the longest side is between 0.01 and 0.1. They are assigned a small shearing modulus, whereas the modulus against normal displacement remains the same as that of the soil elements. These finite-thickness slip elements have several advantages over the traditional infinitely thin slip elements:

1. Because they have essentially the same characteristics as the soil elements, they are easily incorporated into the finite element solution.
2. They do not suffer from numerical difficulties sometimes associated with traditional slip elements.
3. They not only provide for slippage around the pier, but also provide a means of representing a thin layer of soil disturbed by drilling.

Soil Constitutive Relations

Three simple constitutive models are implemented in the program to model the stress-strain behavior of the soil: linear elastic, Duncan-Chang hyperbolic model with variable modulus of elasticity and constant Poisson's ratio (*25*), and the extended Duncan-Chang model with both variable modulus and Poisson's ratio. The linear elastic model is provided because of its simplicity and economy in making preliminary predictions. The Duncan-Chang nonlinear models, although simple, have been shown to work well under conditions of monotonic loading (*26*); the model parameters can be obtained from triaxial testing, and a wide data base currently exists in the literature. The nonlinear soil models are implemented in the computer program by an initial modulus incremental procedure (*27*). This procedure avoids problems of nonconvergence because the modulus is determined by a closed-form solution from the stresses existing in the elements and does not depend on iteration.

The initial states of stress of all the elements are required to calculate moduli when a nonlinear soil model is used. Furthermore, for stability calculations it is also necessary to evaluate the final states of stress rather than just stress differences. Although it would be preferable to model the entire formation process of a slope to determine the initial stresses, it does require significant effort and data (often not available) to do so. Although the computer program allows for the input of initial stresses directly (determined from an independent source) or for sequential computations to model a desired slope formation process, the most common procedure is to determine

an approximate initial stress field that is generic to all slopes. Approximate initial stresses can be created in this program by building a weightless slope and then instantly "turning on gravity."

Soil/Solution Interaction

The SPILES program is composed of two major finite-element modules. The first module solves for the incremental displacements in the soil on the assumption that the piers are rigid. The second module solves for the pile displacements using the forces obtained at the soil nodes. Both modules are used in each increment of loading. The solution process of each module follows the displacement-based finite-element technique using constrained and unconstrained degrees of freedom. The constrained degrees of freedom representing the pier-soil interface can be temporarily fixed during the solution of the first module, which maintains a specified displacement while the soil stiffness matrix is computed. The two-part solution process of the soil displacements (first module) is as follows:

$$r_u = sk_{uu}\, d_u + sk_{uc}\, d_c \tag{1a}$$

and, for the forces on the pier to be used in the second module,

$$r_c = sk_{cu}\, d_u + sk_{cc}\, d_c \tag{1b}$$

where

r_u = forces at unconstrained degrees of freedom (i.e., forces on the soil mass),
r_c = forces at constrained degrees of freedom (i.e., forces on the piers),
d_u = displacements at unconstrained degrees of freedom (i.e., soil movements),
d_c = displacements at constrained degrees of freedom (i.e., pier movements),
sk_{uu} = totally unconstrained stiffness matrix (i.e., equations relating soil degrees of freedom),
$sk_{uc} = sk_{cu}^{-1}$ = partially constrained stiffness matrix (i.e., equations relating soil to pier degrees of freedom), and
sk_{cc} = totally constrained stiffness matrix (i.e., equations relating pier degrees of freedom).

Because the initial pier displacements (the constrained displacements) are known at the beginning of each increment, the first set of equations (1a) can be solved for the unconstrained displacements. The unconstrained displacements are the displacements throughout the soil mass in the particular increment. Once the unconstrained displacements are known, the forces against the pier (the constrained forces) can be calculated from the second set of equations (1b). The constrained (pier) forces are then utilized to compute the new pier displacements in the second module described below.

The forces against the piers determined in the first module are resisted in two ways. First, forces are transferred to the bedrock through cantilever resistance of the piers, and, second, the soil in front (downslope) of the piers resists as they bend. Both these types of resistance are a function of the pier displacements, and both increase as the piers bend. The equation to be solved in the second module is

$$r_c = (a + sk_{cc})d_c \tag{2}$$

where r, d, sk have been defined above, and a is the pier stiffness matrix. The pier displacements, once computed at constrained degrees of freedom, can be incorporated in the calculation of the new soil element stresses and soil displacements during the next increment.

TYPICAL ANALYSIS

As noted earlier, a simplified version of the SPILES program was used previously to examine the problem of drilled piers used to stabilize a slope subjected to surcharge loading (*17*). The effects of pier position, size, spacing, and stiffness were related to slope movement. That study concluded that with proper positioning, the drilled piers could have a positive effect on slope movement. In order to evaluate further the capability of drilled piers to provide a permanent method of increasing stability and controlling displacement, the example of an excavation is studied first in this paper; it represents the condition of a highway embankment. Although (as will be discussed) this application does not use the piers' capabilities at their best or provide the optimal means of support, it is the best example to clearly illustrate the support mechanism provided by the piers and the characteristics of pier-soil interaction.

Problem Description

The problem considered is similar to the one addressed by Duncan and Dunlop (*28*): a 12.2-m (40-ft) excavation in 18.2 m (60 ft) of soft clay using 1:1.5 side slopes. Movements, stresses, and stability are analyzed without piers first and then with drilled piers installed at the crest of the excavated zone. The bedrock is assumed to be very stiff with respect to the soil and acts as a rigid boundary in which the piers can be socketed. It is located 6.1 m (20 ft) below the final excavation depth, one-half of the slope height.

The finite element mesh used to simulate this problem is shown in Figure 4. The wedge of soil shown slightly elevated in Figure 4 represents the portion of the mesh to be excavated. Excavation is to be conducted in eight increments, each consisting of a horizontal row of elements. To simulate excavation, the average stress in each element excavated is extrapolated to the excavation boundary. The forces on this boundary are computed and applied as upward forces on the new surface boundary. A nonlinear hyperbolic model is used to determine the modulus of elasticity in each soil element during each increment. The parameters of the soil model are given in Table 1. They are representative of a normally consolidated clay with strain hardening stress-strain curve and an undrained shear strength of 38.3 kPa (800 psf). The soil strength is such that the unreinforced slope has an unacceptable factor of safety after completion of the final increment of excavation—the two-dimensional factor of safety (Bishop's method) is 0.95 at the end of the excavation. One row of 1.22-m (4-ft) diameter piers with 2.44-m (8-ft) center-to-center spacings is to be used to reinforce the excavation.

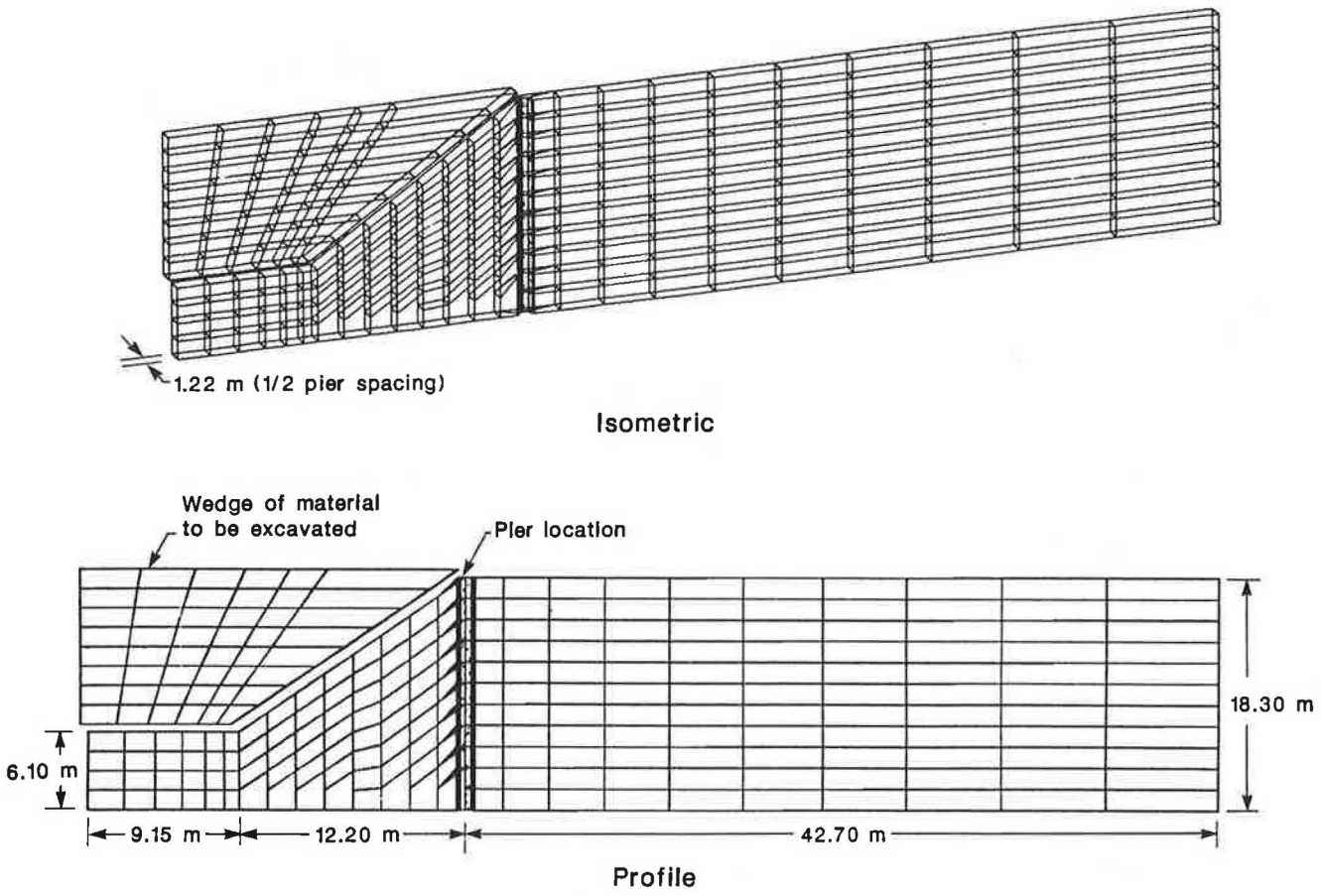

FIGURE 4 Finite element mesh for excavation problem.

TABLE 1 SOIL PARAMETERS FOR EXCAVATION PROBLEM

Type	Parameter	Value
Duncan-Chang for variable modulus of elasticity	Contant, K	47.2
	Constant, n	0.5
	Constant, R_f	1.0
Soil properties	Unit weight, γm	2.1 g/cm^3 (130 pcf)
	Cohesion, C	3900 kg/m^2 (800 psf)
	Friction angle, ϕ	0

Results of Finite-Element Study

Displacements

The nodal displacements for each stage of the excavation were the primary results of this analysis. Although the displacements are not directly applicable to stability analysis, they can give a relative assessment of the stability, and they are useful if the displacement or deformation of nearby existing structures is critical. Plots of the displacement fields can also give insight into the failure mechanism.

The effectiveness of the piers was illustrated by comparing the displacement fields of the two cases studied (i.e., without and with piers) at selected excavation stages and particularly after the last stage (Figure 5). The displacement plots clearly show how the piers act as a barrier, almost eliminating the horizontal component of displacements behind the row of piers. This barrier also significantly reduces basal heave represented by vertical (upward) displacement vectors in front of the piers. In fact, in the case of the reinforced slope, the vertical (upward) displacement represents essentially the rebounding of the unloaded soil rather than horizontal translation or sloughing, as occurs in the unreinforced slopes.

In addition to analyzing the final configurations of displacement, it is also useful to monitor the progression of displacements during the excavation. For example, in the case of the unreinforced slope, the point of maximum displacement on the slope surface moves downward as the excavation progresses and is approximately level with the bottom of the excavation for each stage. The magnitude of these maximum displacements does not grow proportionally with the excavation, but rather increases very rapidly during the last increments. The deepening of the zone of influence of the movement is also apparent as the displacement vectors at each point above the crest continually bend downward with each increment.

The most dramatic change in the displacement pattern for the unreinforced case occurred during the sixth increment, in which the surface displacement vector at the level of the excavation bottom (vector A in Figure 5) almost doubled in length,

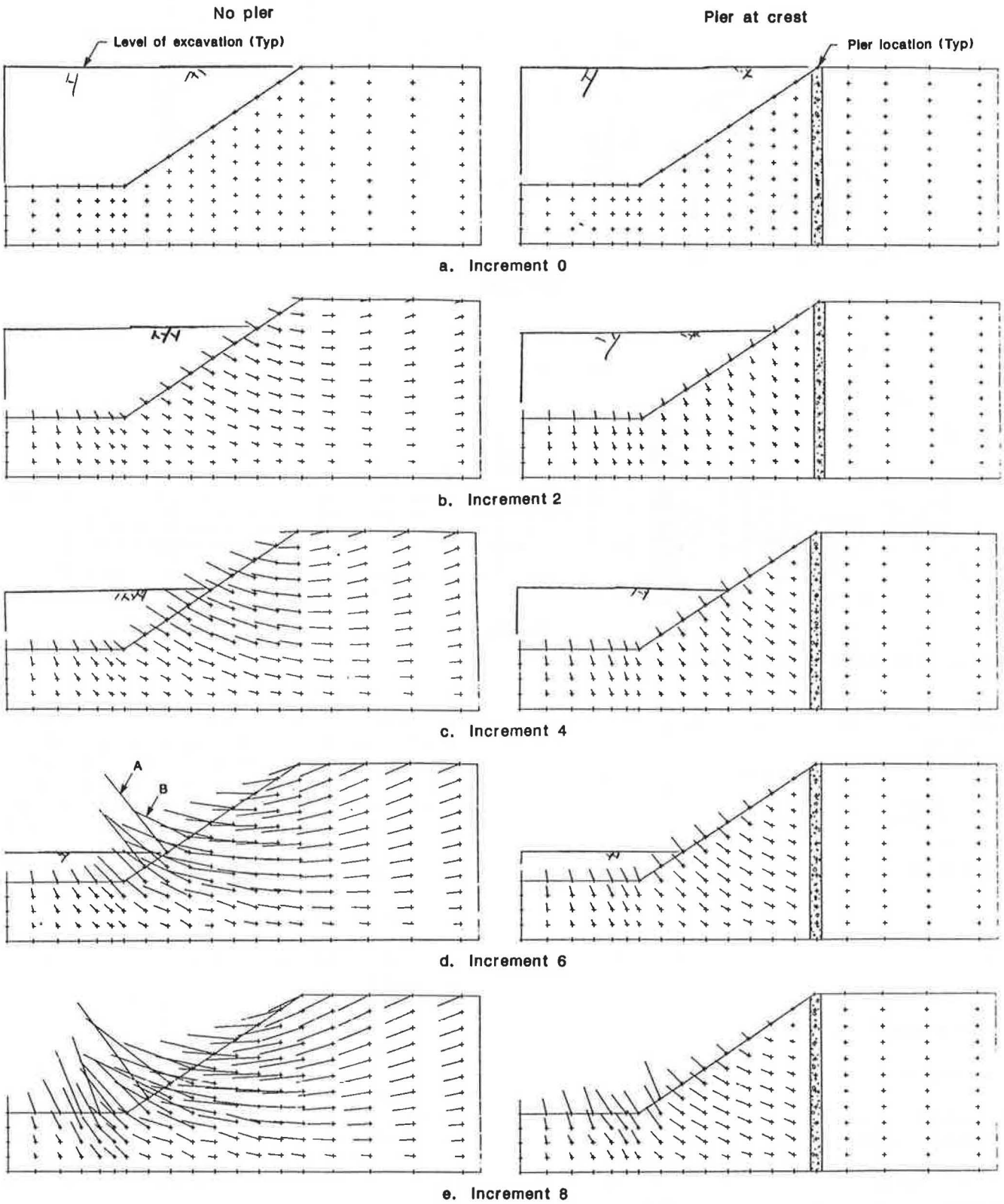

FIGURE 5 Soil displacements for selected stages of excavation.

primarily in an upward direction, whereas the surface nodal displacement vector just above the bottom (vector *B* in Figure 5) turned sharply downward. In contrast, the progression of the magnitude of the displacement for the case with pier reinforcement did not change significantly during excavation (i.e., the magnitudes increased almost proportionally with the number of excavation increments). No significant alteration in the displacement pattern could be readily identified and thus a state of sloughing did not occur.

Stresses

Element stresses were calculated from the nodal displacements on an elemental basis at each of the eight Gauss points and then averaged over the element. The Gauss point values or the average values, or both, can be included in the output.

Unlike the situation of surcharge loading (*19*), where increases in the vertical stress state (i.e., the direct cause of instability) could easily be absorbed by skin friction in the piers, this excavation example did not take full advantage of the vertical support that the piers could provide. For this reason, the vertical stress fields (not shown) were not significantly reduced by pier reinforcement. Similarly, the piers did not have a large effect on the horizontal stresses. The shearing stresses at the completion of excavation, however, were significantly higher for the case of the unreinforced slope, as shown in Figure 6.

The development of the shearing stresses was an important factor in the evaluation of the slope stability. The initial shearing stresses on horizontal planes (null for the half-space) were largely preserved (i.e., remained zero) behind the pier row in the reinforced case (Figure 6b). Under the slope itself (below the pier row), within the region where a shallow failure surface was likely to develop, the shearing stresses were also reduced when compared with the unreinforced case, especially in the vicinity of the toe where failure was likely to initiate. In addition, there was a reduction in the shearing stresses along the interface of the soil and foundation material.

Nodal Loads on the Piers

Through the equations of equilibrium, the elemental nodal loads could be calculated from the elemental stresses. A summation of all of the elemental nodal loads yielded the global nodal load field, and thus a summation of the nodal loads on elements with constrained degrees of freedom gives the forces against the piers. The nodal loads against the piers at the end of excavation are shown in Figure 7. These loads can be used in the structural analysis of the pier.

LIMITING EQUILIBRIUM ANALYSIS

In addition to providing data on slope movement and stresses, an assessment of the overall stability (i.e., factor of safety) of the slope was made using a two-dimensional limiting equilibrium analysis. The stress output from the finite-element analysis was used to make limiting equilibrium calculations (*21*) with a factor of safety defined as the sum of the resisting stresses (strength) over the sum of the shearing stresses along a discretized circular or log spiral failure surface. A grid-pattern-searching technique (two-dimensional mesh) was used to locate the most likely failure surface.

The most likely circular failure surfaces for each increment of the excavation problem are shown in Figures 8a and 8b for

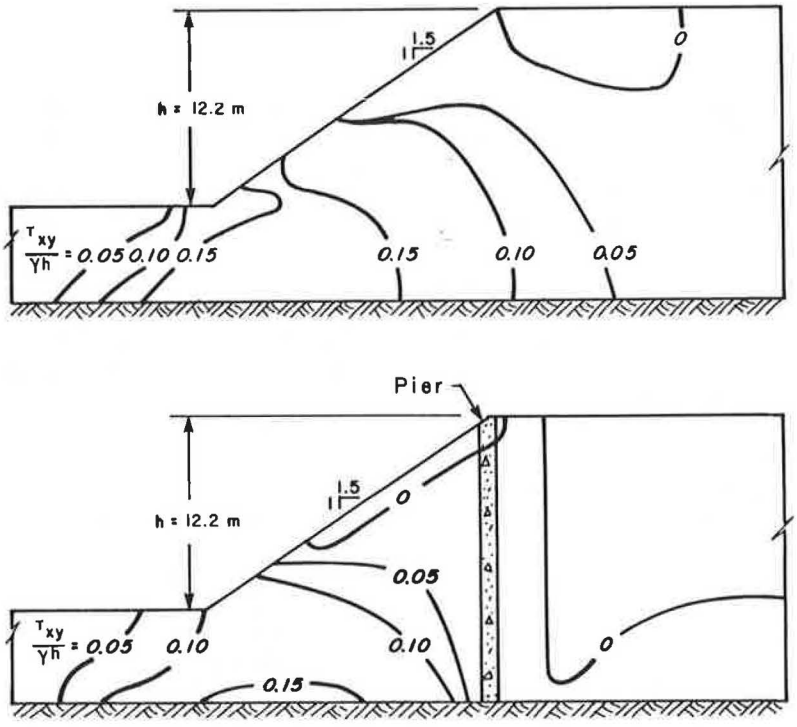

FIGURE 6 Normalized shearing stresses: (*top*) without pier reinforcement; (*bottom*) pier reinforcement at crest.

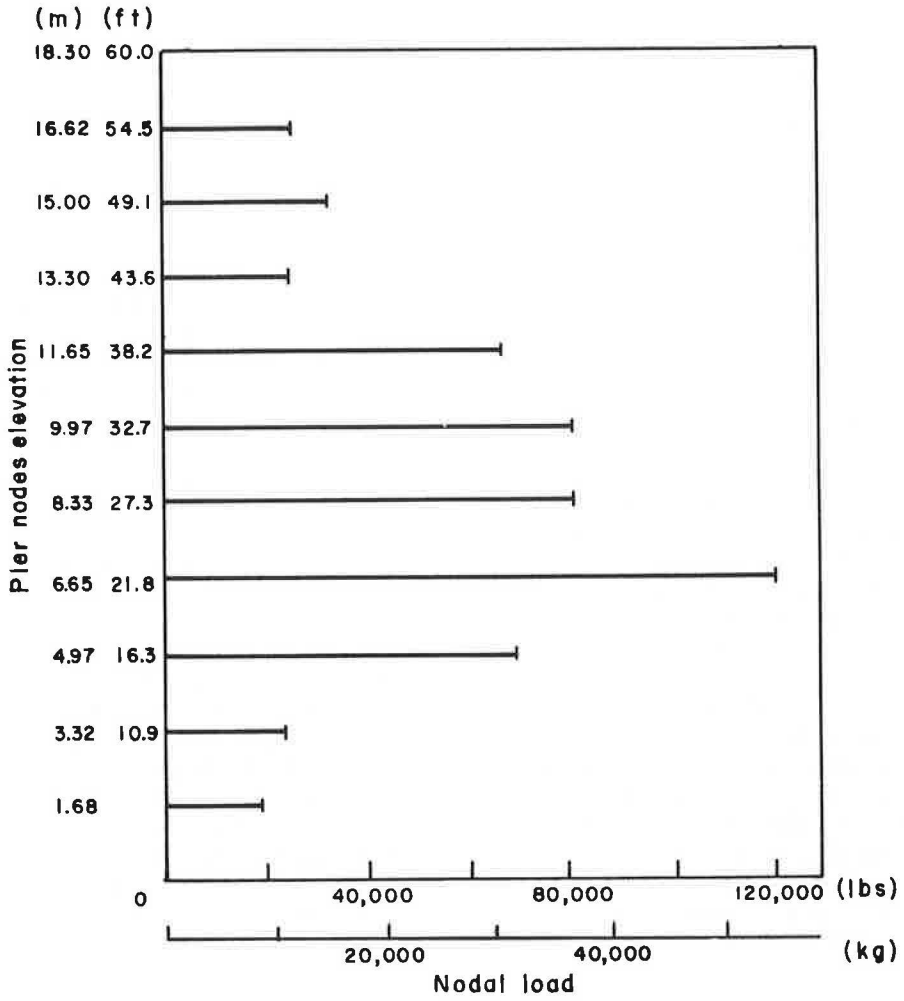

FIGURE 7 Nodal loads against pier.

the cases without and with a pier, respectively. The piers tended to reduce the volume of material involved in a potential slide. This reduction increased with excavation depth, as indicated by the location of the centers of the failure surfaces. In the case of a slope without a pier, these centers moved up, whereas they moved down for the case of a slope reinforced by piers, thus shortening the arc radius. A plot of the factor of safety with respect to the elevation of the bottom of the excavation is given in Figure 9. Note that the factor of safety for the case with a pier was less (although very high) after the first increment than that without a pier. This was due to the disturbed layer modeled around each pier, which provided a weak seam along the failure surface.

The pier reinforcement improved the stability from a factor of safety of 1.0 without reinforcement to approximately 1.7 at the end of excavation. Although this increase was significant, it was not as dramatic as had been seen in other examples (*21*). A review of the soil movements and stresses showed this case not to have used the piers to their fullest capacity. The direction of soil movement at the level of the pier was primarily horizontal, and thus the piers did not provide significant vertical support of the soil, which would have utilized the axial capacity of the piers. Under conditions of downward forces acting on the slope, such as for surcharge loading, this component was of great benefit. In conclusion, although the piers significantly increased the factor of safety of a slope during excavation, their greatest benefit under this loading condition was to control displacements and prevent bottom heave. Better reinforcement of the slope might have been achieved by positioning the piers lower on the slope. At lower positions, the piers could have absorbed additional stresses from the larger movements. However, the loads in the piers would become primarily horizontal and the structural demand on the piers would significantly increase unless tiebacks were used (*21*).

CUT SLOPE STABILITY

This example represents a practical application of the pier system that can be used to explore further the mechanics of drilled-pier reinforcement. The problem considered is a 1:2 slope with a height of 9.1 m (30 ft) and a depth to bedrock under the toe of 3.7 m (12 ft). Instability would initiate, as the slope is to be cut to a 1:1 slope for widening purposes. Reinforcement, consisting of 1.2-m (4-ft) diameter piers with

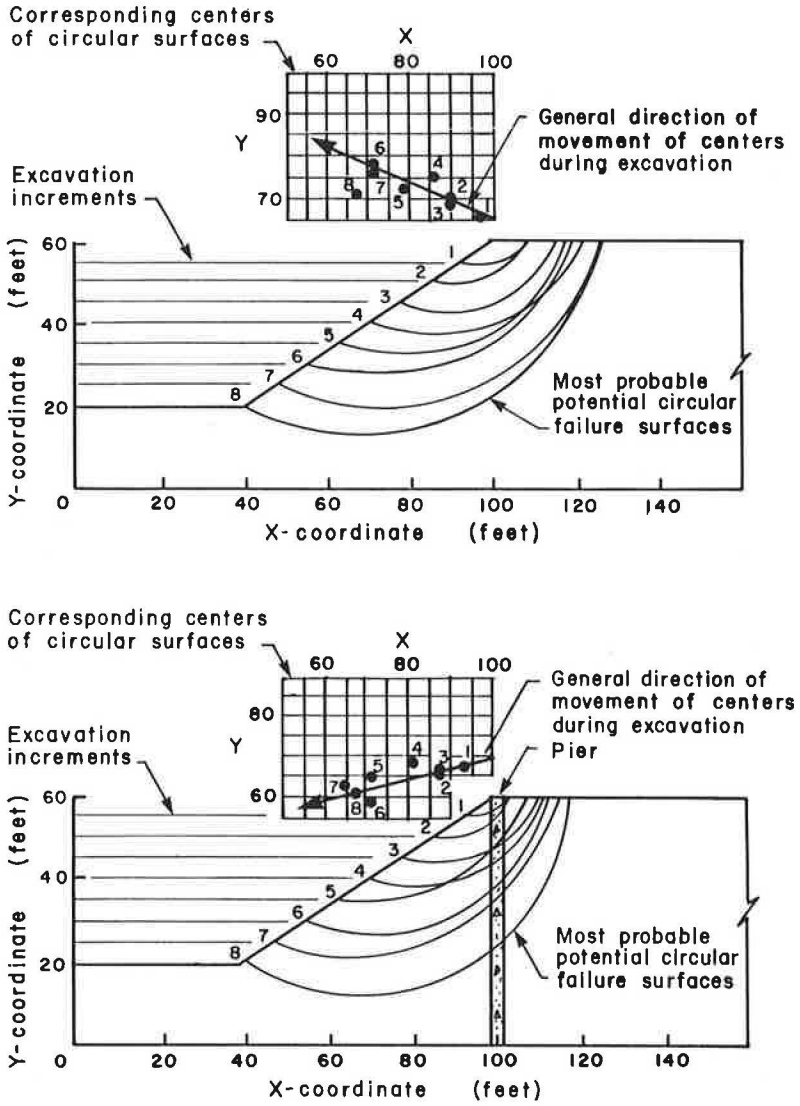

FIGURE 8 Most likely failure surfaces: (*top*) without pier reinforcement; (*bottom*) pier reinforcement at crest.

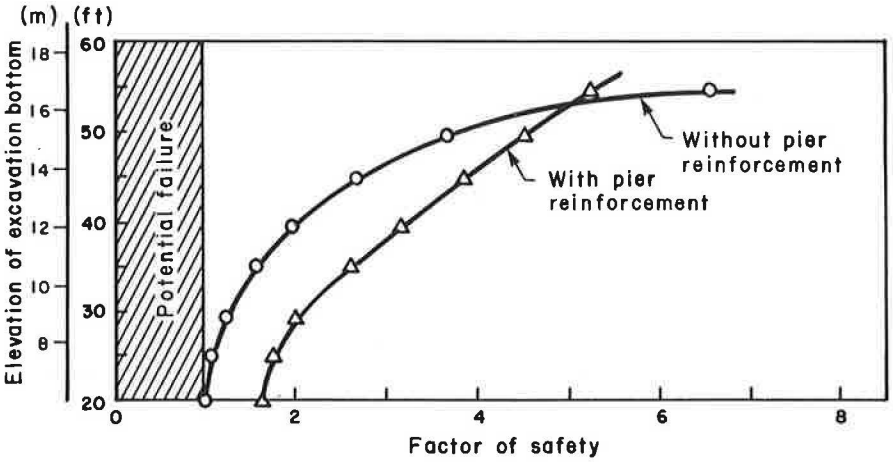

FIGURE 9 Factors of safety during excavation.

2.4-m (8-ft) center-to-center spacing, is implemented to control movements and provide stability. The piers are installed below the existing ground surface, 3.7 m (12 ft) from the toe. The shafts are drilled as usual; however, the piers are constructed only up to the future ground surface. The remainder of the shafts are backfilled with soil. Excavation of the slope then proceeds unhindered to the level of the top of the pier.

A soil with a frictional component of strength and a variable Poisson's ratio (i.e., extended Duncan-Chang model) is used. For the basic example, the soil has a cohesion of 200 psf (980 kg/m^2) and a friction angle of 36 degrees. The other parameters are given in Table 2. The initial stresses are established for the original 1:2 slope through the gravity turn-on procedure. These stresses, once established, are transferred to corresponding elements in the final 1:1 geometry, to which stresses created by surface loads representing the excavation operation are added. The surface nodal loads that simulate the excavation process are determined from the average elemental initial stresses and are applied in increments.

For excavations made in soils with a frictional component of strength, in addition to the piers reducing the shear stresses imposed by the steeper geometry, improvements to stability are also dependent on retention of the confinement initially present in the slope. The degree to which retention of confinement influences the final stability is a function of the degree to which the stability without piers is dependent on the frictional capacity of the soil. This mechanism can be demonstrated in this example by monitoring the elements with reduced modulus (i.e., failed elements in accordance with the Mohr-Coulomb criteria) for a variety of cohesion and friction values.

TABLE 2 SOIL PARAMETERS FOR CUT SLOPE PROBLEM

Type	Parameter	Value
Duncan-Chang for variable modulus of elasticity	Constant, K	47.2
	Constant, n	0.5
	Constant, R_f	0.8
Duncan-Chang for variable Poisson's ratio	Constant, G	0.33
	Constant, F	0.06
	Constant, d	4.0
Soil properties	Unit weight, γm	2.1 g/cm^2 (130 pcf)
	Cohesion, C	980 kg/m^2 (200 psf)
	Friction angle, ϕ	36°

For the original soil model (strength parameters given in Table 2), no element failed under the final, excavated, loading condition. If, however, the same excavation was made in a significantly weaker soil (values of friction angle reduced to 18 and 9 degrees), a bulb of failed elements did form as shown in Figure 10 for both the unreinforced slope and the slope with a row of piers at 3.7 m (12 ft) from the toe. As the friction angle was decreased to 18 degrees, failure initiated from the toe and at the foundation level below the toe. (These were the locations where the principal stress differences were highest.) As the friction angle of the soil was further reduced to 9 degrees and the stability became more dependent on the cohesive strength, additional failure spread from the foundation level, near the toe, where the deviator stresses were high before excavation, into areas where confinement prevented failure in soils with higher frictional capacity.

In this example, a significant amount of shear stress was present in the slope before excavation. Much of the additional shear stress was due to unloading and resulting increases in principal stress differences, which was not effectively absorbed by the piers. For this reason, as confinement became less important to stability (i.e., lower frictional strength with regard to cohesive strength), the failure bulbs for both the unreinforced slope and pier-supported slope became similar. Hence, in this example, the beneficial effects of the piers were fewer because the soil strength became dominated by its cohesive component.

Conversely, as the stability of the slope became more dependent on the frictional strength (i.e., the cohesion was reduced), the failure bulb grew along the slope surface and crest, where the confining pressures were small. The deeper soils at the foundation level, which failed with decreasing frictional capacity, did not fail under decreasing cohesion because the remaining overburden provided enough confinement not to require a substantial mobilization of cohesion. The effect of a decreasing cohesion with a constant friction angle is shown in Figure 11. As described above, the piers were ineffective in absorbing the shear stresses created in this

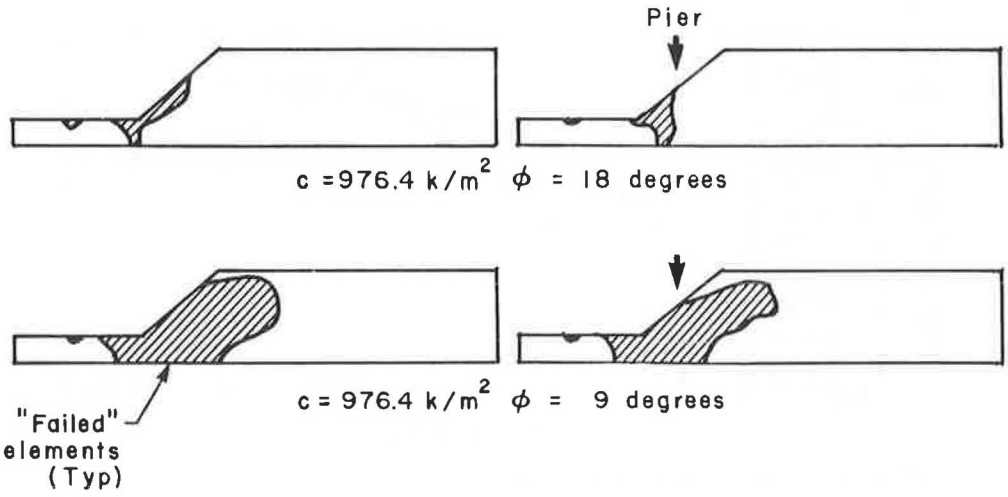

FIGURE 10 Failed elements: sensitivity to friction angle.

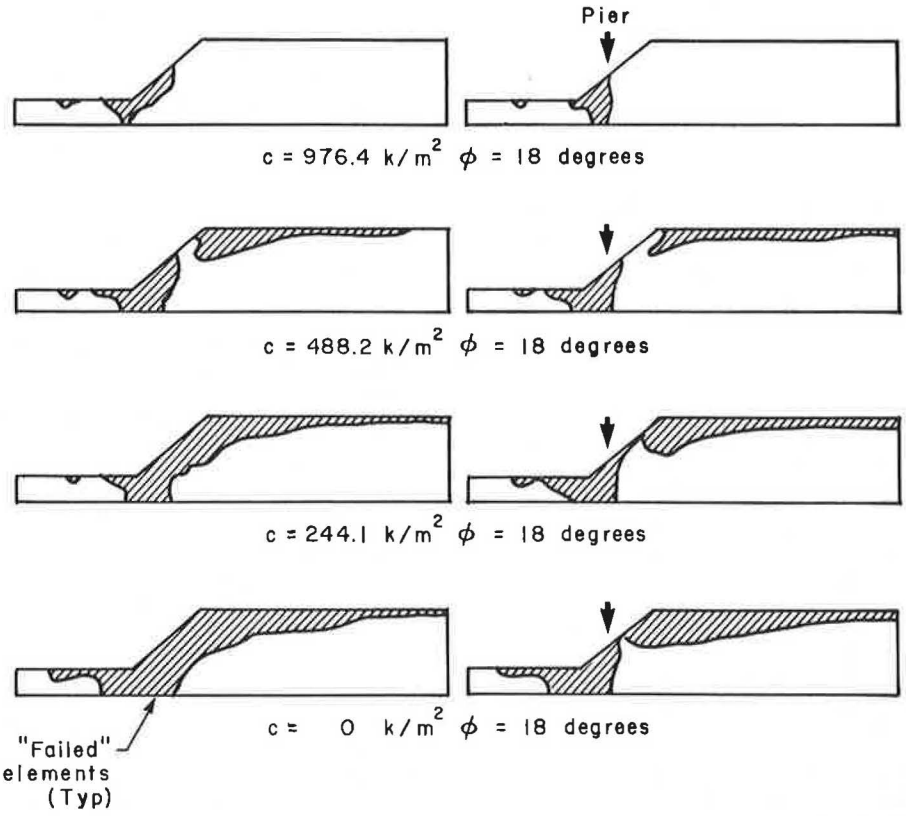

FIGURE 11 Failed elements: sensitivity to cohesion.

unloading situation. However, the piers did retard the loss of confinement through their skin friction. Thus, as reliance on the frictional component of the soil became more important with decreasing cohesion, the difference in the size of the failure bulb between the cases of the unreinforced slope and slope with piers became greater.

CONCLUSIONS

Three applications of the use of drilled piers for slope stabilization were investigated: surcharge loading (*19*), excavation from a horizontal ground surface, and cut slope stabilization. Several conclusions regarding slope-pier interaction can be drawn.

Of prime importance is that the piers must be positioned at a point where relatively large displacements are expected to occur; the magnitude of these displacements determines how much stress will be mobilized against the pier (i.e., how much stress the pier will absorb).

The direction of the displacement, and thus the direction of the stresses on the pier, should also be considered. Maximum benefit of the piers can be gained in axial compression, thus taking advantage of their greatest structural strength in that direction. For this reason, the case of surcharge loading lends itself well to this type of reinforcement.

The movements are primarily lateral for the case of excavation from a horizontal ground surface. The piers can still effectively absorb the stresses and transmit them to the foundation layers; however, the lateral load on the piers must be limited (unless tiebacks are used). The piers in our example were placed at the crest to take full advantage of the maximum vertical load. However, the limited mobilization of horizontal load due to limited movement of the soil at this point limited their ability to improve the stability. Better stability can be achieved by placing the piers lower in the slope, where horizontal movements are greater; however, analysis of these cases (*21*) showed that this results in high shearing stresses in the piers.

The relative mobilization of cohesive and frictional strengths is important to the performance of the stabilizing piers. Where upward movement is an important component, the support offered by the piers becomes indirect, increasing the confining pressure on the potential failure surface. The effectiveness of the piers in a soil with a frictional component and vertical downward component of movement is more complicated. Reducing the vertical stresses in the slope may have a negative effect because confining stresses are also being relieved. Thus, a major component of the piers' supporting action is of no benefit. The stability of the piers can be improved by retaining the vertical component of stress in areas of uplift, as shown in the example of cut slope stabilization. In general, however, unless the lateral reinforcement properties of the piers can be used, drilled piers may not always be an optimal solution to stability problems in frictionless soils.

In summary, when evaluating drilled piers for slope stabilization, the entire soil-structure interaction that occurs between the piers and soil mass must be considered, not simply the added shearing resistance provided by the piers. On the basis of analyses performed to date, the best applications of the piers seem to be in purely cohesive materials under loading conditions that can use the vertical resistance of the

piers. When used to their best advantage, drilled piers have been shown to be a versatile slope-stabilization alternative.

ACKNOWLEDGMENTS

Support for this research was provided by the Indiana Department of Highways and the Federal Highway Administration, U.S. Department of Transportation. The research was administered through the Joint Highway Research Project, Purdue University, West Lafayette, Indiana.

REFERENCES

1. T. Taniguchi. Landslides in Reservoirs. *Proc. of the Third Asian Regional Conference on Soil Mechanics and Foundation Engineering*, Bangkok, Thailand, Vol. 1, Southeast Asian Society of Soil Engineering, 1967, pp. 258–261.
2. B. B. Broms and I. M. Wong. Embankment Piles. *Third International Geotechnical Seminar, Soil Improvement Methods*, Singapore, 1985, pp. 167–178.
3. U. Dash and P. L. Jovino. Root Piles and Monnesen Pen. In *Transportation Research Record 749*, TRB, National Research Council, Washington, D.C., 1980, pp. 13–21.
4. R. D. Goughnour and J. A. DiMaggio. Soil Reinforcement Methods on Highway Projects. *Proc., Symposium on Earth Reinforcement*, American Society of Civil Engineers Annual Convention, Pittsburgh, Pa., April 1978, pp. 371–399.
5. R. D. Barksdale and R. C. Bachus. *Design and Construction of Stone Columns*. Report No. FHWA-RD-83-026. FHWA, U.S. Department of Transportation, 1985.
6. R. Merriam. Portuguese Bend Landslide, Palos Verdes Hills, California. *Journal of Geology*, Vol. 68, No. 2, March 1960, pp. 140–153.
7. G. H. Andrews and J. A. Klasell. Cylinder Pile Retaining Wall. In *Highway Research Record 56*, HRB, National Research Council, Washington, D.C., 1964, pp. 83–97.
8. J. D. Gould. Lateral Pressures on Rigid Permanent Structures. *Proc., Conference on Lateral Stresses in the Ground and Design of Earth Retaining Structures*, Cornell University Press, Ithaca, N.Y., 1970, pp. 219–269.
9. H. Mathis. Temporary Landslide Corrective Techniques Avert Catastrophe. *Proc., 32nd Annual Highway Geology Symposium*, Gatlinburg, Tenn., 1981, pp. 59–78.
10. J. H. Offenberger. Hillside Stabilization with Concrete Cylinder Pile Retaining Wall. *Public Works*, Sept. 1981, pp. 82–86.
11. R. de Paepe and M. Wallays. Stabilization of the Oudenberg Hill in Geraardsbergen. *Proc., International Conference on Case Histories in Geotechnical Engineering*, St. Louis, Mo., 1984, pp. 1345–1350.
12. G. Gudehus and W. Schwarz. Stabilization of Creeping Slopes by Dowels. *Proc., 11th International Conference on Soil Mechanics and Foundation Engineering*, Vol. 3, San Francisco, Calif., 1985, pp. 1697–1700.
13. H. G. Poulos. Analysis of Piles in Soil Undergoing Lateral Movement. *Journal of the Soil Mechanics and Foundation Division*, ASCE, Vol. 99, No. SM5, May 1973, pp. 391–406.
14. T. Ito and T. Matsui. Discussion: Methods to Estimate Lateral Force Acting on Stabilizing Piles. *Soils and Foundations*, Japanese Society of Soil Mechanics and Foundation Engineering, Vol. 19, No. 4, April 1975, pp. 43–57.
15. C. Viggiani. Ultimate Lateral Load on Piles Used to Stabilize Landslides. *Proc., 10th International Conference on Soil Mechanics and Foundation Engineering*, Stockholm, Vol. 3, 1981, pp. 555 560.
16. H. Winter, W. Schwarz, and G. Gudehus. Stabilization of Clay Slopes by Piles. *Proc., 8th European Conference on Soil Mechanics and Foundation Engineering*, Helsinki, Vol. 2, May 1983, pp. 545–551.
17. S. Hassiotis. *Stabilization of Slopes Using Piles*. Joint Highway Research Project JHRP-84-8. Purdue University, West Lafayette, Ind., 1984, 181 pp.
18. W. P. Hong. Design Method of Piles to Stabilize Landslides. In *Proceedings of the International Symposium on Environmental Geology*, Envo Publishing Company, Bethlehem, Pa., 1986, pp. 441–453.
19. M. W. Oakland and J. L. Chameau. Finite-Element Analysis of Drilled Piers Used for Slope Stabilization. *Laterally Loaded Deep Foundations: Analysis and Performance*. ASTM Special Technical Publication No. 835, Kansas City, Mo., 1984, pp. 182–193.
20. R. K. Rowe and H. G. Poulos. A Method for Predicting the Effect of Piles on Slope Behavior. *Proc., 3rd International Conference on Numerical Methods in Geomechanics*, Aachen, Vol. 3, April 1979, pp. 1073–1085.
21. M. W. Oakland and J. L. Chameau. *Drilled Piers Used for Slope Stabilization*. Joint Highway Research Project No. FHWA/IN/JHRP-86/7, Purdue University, West Lafayette, Ind., 1986.
22. R. D. Cook. *Concepts and Applications of Finite Elements Analysis*. 2nd ed., John Wiley and Sons, Inc., New York, 1981.
23. R. C. Bachus and R. D. Barksdale. Vertical and Lateral Behavior of Model Stone Columns. *Proc., In Situ Soil and Rock Reinforcement*, Paris, 1984, pp. 99–104.
24. C. S. Desai and S. Sargard. A Hybrid Finite Element Procedure for Soil-Structure Interaction. *Journal of the Geotechnical Engineering Division*, ASCE, Vol. 110, No. 4, April 1984, pp. 473–486.
25. J. M. Duncan and C. Y. Chang. Nonlinear Analysis of Stress and Strain in Soils. *Journal of the Soil Mechanics and Foundation Division*, ASCE, Vol. 96, No. SM5, 1970, pp. 1629–1653.
26. L. W. D. Finn. Evaluation of Critical State and Hyperbolic Stress-Strain Models: Working Group Three. *Proc., Workshop on Constitutive Modeling of Soils*, McGill University, Montreal, Canada, May 1980, pp. 132–150.
27. D. J. Naylor, G. N. Pande, B. Simpson, and B. Tabb. *Finite Elements in Geotechnical Engineering*, Pineridge Press, Swansea, United Kingdom, 1981.
28. J. M. Duncan and P. Dunlop. Slopes in Stiff-Fissured Clays and Shales. *Journal of the Soil Mechanics and Foundation Division*, ASCE, Vol. 95, No. SM2, March 1969, pp. 467–492.

Publication of this paper sponsored by Committee on Transportation Earthworks.

Analytical Study of Laterally Loaded Cast-in-Drilled-Hole Piles

SANGCHUL BANG AND C. K. SHEN

This paper summarizes the results of an analytical study of laterally loaded cast-in-drilled-hole (CIDH) piles, which are typically used as the foundations for signposts and sound barrier walls along urban freeways. The CIDH pile derives its bearing capacity from passive earth resistance and is typically considered to be rigid in design and analysis. The analytical formulation, which calculates the ultimate lateral resistance and the point of rotation, considers (a) the nonplane strain soil wedge and (b) the concept of developed friction angle and cohesion to describe the transition of passive lateral earth pressure development from the initial to the ultimate lateral loading condition. Finally, the developed formulation was used to compare the results with those obtained from field and laboratory model testing. Included are comparisons of the ultimate lateral load, the point of rotation, and the distribution of the passive lateral earth pressure.

Cast-in-drilled-hole (CIDH) piles are typically designed as the foundations of posts for large road and commercial signs and for sound barrier walls used to control noise along urban freeways. The CIDH pile derives its bearing capacity from passive earth resistance against translational or rotational lateral movements. It is typically less than 12 ft long with a length-to-diameter ratio ranging from 2 to 1 (for short piles) to about 10 (for longer piles). CIDH piles are considered rigid in their design and analysis because of their low slenderness ratio and high rigidity with respect to the surrounding soil.

This research includes both experimental and analytical investigations with the final objective of establishing an improved design methodology for CIDH piles. The laboratory model testing is intended to (a) provide a thorough understanding of the load transfer mechanism between the soil and the pile, (b) investigate the pertinent parameters that significantly influence the lateral loading capacity and the movement characteristics of the pile, and (c) provide clues for developing an analytical solution method.

A detailed description regarding the laboratory model testing and its results has been already presented (*1*). In this paper the development of the associated analytical solution method is described and the results are compared with the model-testing measurements.

LITERATURE REVIEW

Broms (*2,3*) first attempted to calculate the ultimate lateral resistance of a short rigid pile in cohesive and cohesionless soils. Piles in cohesive soils were assumed to develop a rectangular distribution of lateral soil resistance, starting from a depth of 1.5 times the pile diameter to the tip of the pile with a magnitude of 9 times the undrained shear strength of the soil. Piles in cohesionless soils were assumed to develop a linear lateral soil resistance, which varies from zero at the top to a maximum value at the tip of the pile with a magnitude equal to three times Rankine's passive lateral earth pressure.

Reese et al. (*4*) formulated the ultimate soil resistance of a short rigid pile based on the equilibrium of a tetrahedron-shaped soil failure wedge under lateral load. The total ultimate lateral resistance is calculated from the total passive force minus the active force. The passive force is computed from the geometry of the failure wedge with boundary forces calculated from the Mohr-Coulomb failure criterion, whereas the active force is calculated directly from Rankine's theory. Modifications were later suggested by Matlock (*5*) on the basis of experimental observations.

Ivey (*6*) suggested the inclusion of both the normal and shear stresses developed on all faces of the pile. The distributions of these stresses were assumed to vary along the circumference by cosine and sine functions for normal and shear stresses, respectively. These stresses were summed, and the equilibrium equations of forces and moments were then considered to calculate the ultimate lateral load and the resulting point of pile rotation. The proposed formulation, however, was later modified to satisfy the observed model test results.

Other formulations estimating the ultimate lateral resistance of rigid piles have been proposed by Hays et al. (*7*), Ivey and Dunlap (*8*), Ivey and Hawkins (*9*), Davidson et al. (*10*), Lytton (*11*), Ivey et al. (*12*), Seiler (*13*), Hansen (*14*), as well as others. Generally, the Ivey and Dunlap method and the Ivey and Hawkins method predict conservative values (*15*), whereas the Hansen and Lytton methods yield consistently unconservative values for larger piles (*16*). The Broms method tends to be conservative for stiff clays but unconservative for soft clays (*16*).

Many experimental measurements (*15,17–20*) indicate that (a) the developed passive lateral earth pressure distributions are nonlinear and close to parabolic in shape and (b) the point of rotation is located approximately at 0.7 times the embedded pile length as measured from the ground surface. In most cases, the point of rotation shifts downward from some point below the middle of the embedded pile for lighter loads to a point approximately three-fourths of the embedment depth for maximum lateral load.

Because CIDH piles involve a nonplane strain geometry and a rotational mode of movement, the classical Rankine lateral earth pressure expression may not be directly applicable. In addition, the ultimate lateral load of the CIDH pile

S. Bang, Department of Civil Engineering, South Dakota School of Mines and Technology, Rapid City, S. Dak. 57701. C. K. Shen, Department of Civil Engineering, University of California at Davis, Davis, Calif. 95616.

may not necessarily be obtained at the limiting state (i.e., when the soil develops its full passive resistance along the entire length of the pile).

LABORATORY MODEL TESTING

The testing facility included a large test bin, an instrumented pile, a loading system, and a data-acquisition system. The dimensions of the test bin were 12 ft by 4 ft by 4 ft. The model pile was made of an aluminum tube pipe 0.25 in. thick, 40 in. long, and with an outside diameter of 3.5 in.

The model pile-testing program included the construction of either level or sloping ground embankments made of pit-run air-dried sand or silty clay. Seventeen tests were conducted on sand and 27 tests were on silty clay. Parameters covered in the study were the embedment length of the pile, the type of loading, the direction of loading, the sloping nature of the ground, and the distance of the pile from the slope edge. For each test, parameters such as the load versus displacement response and the lateral earth pressure distributions were measured. A detailed description of the laboratory model testing and its results has been made by Shen et al. (*1*).

THEORETICAL FORMULATION

On the basis of the results obtained from model testing and literature review, it was decided that a reasonable model to analyze the rigid pile-soil interaction behavior should follow the soil failure wedge proposed by Reese et al. (*4*). Furthermore, Dubrova's concept of movement-dependent lateral earth pressure distribution (*21*) was also incorporated and modified to calculate the interface stresses under all intermediate states of lateral loading before failure.

The passive lateral earth pressure developed along the rigid pile can be expressed, in general, as

$$p = p_1 + p_2 + p_3 \tag{1}$$

where

p_1 = lateral earth pressure due to unit weight and soil friction,
p_2 = lateral earth pressure due to cohesion, and
p_3 = lateral earth pressure due to surcharge.

The formulation of passive pressure due to unit weight and soil friction, p_1, can be calculated from the consideration of the soil wedge as shown in Figure 1. One can apply the force equilibrium along vertical and horizontal directions to obtain the developed passive thrust,

$$P = \frac{d}{1 - \tan\delta' \tan\beta}\left(\frac{1}{2}\gamma Z^2 \tan^2\beta + \frac{1}{3}\gamma\frac{Z^3}{d}\tan^3\beta\tan\frac{\phi}{2} - \frac{1}{3}K_0\gamma\frac{Z^3}{d}\tan\beta\tan\frac{\phi}{2} + \frac{2}{3}K_0\gamma\frac{Z^3}{d}\tan\phi\tan\beta\sin\beta\right) \tag{2}$$

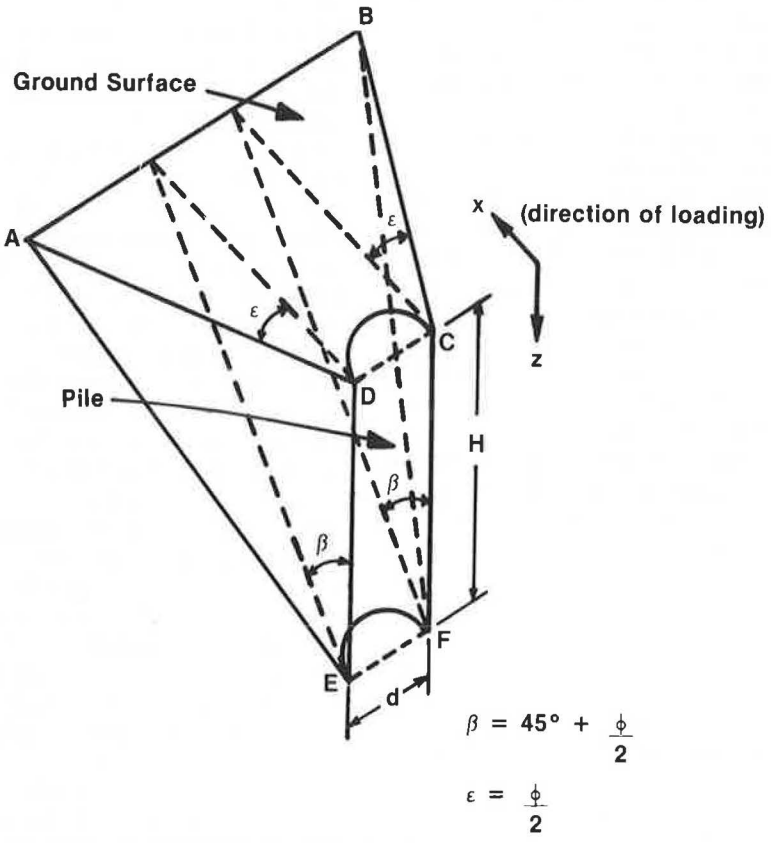

FIGURE 1 Soil wedge under lateral load.

where

δ' = developed friction angle between the pile and the soil,
β = failure wedge inclination angle at the pile tip ($45° + \phi/2$),
d = pile diameter, and
Z = depth from the ground surface to the point of interest.

Note that this expression is obtained at the time of failure (i.e., an inclination angle, $45° + \phi/2$ at the tip of the pile, and an orientation angle, $\phi/2$ at the ground surface, are used). If the inclination and orientation angles have values as described above everywhere along the length of the pile, the ultimate passive lateral earth pressure can be obtained by directly differentiating P with respect to depth Z. However, as discussed in the literature review, it is highly unlikely, particularly in the rotational mode of movement, that the angles reach full values everywhere as described by soil internal friction angle, ϕ. For this reason, it is assumed that the friction angle, ϕ, is replaced by the developed friction angle, $-\psi$, where $\psi = -\phi$ within the depth from the ground surface to where a sufficient lateral movement has taken place to achieve the passive state (i.e., within the failure zone). $\psi = 0$ at the point of no lateral movement (i.e., the point of rotation). Between these two points, a hyperbolic variation is assumed to describe the smooth transition of the values of ψ (Figure 2). For instance, the passive pressure distribution above the rotation point will have the developed friction angle

$$\psi = -1.01\phi + \frac{\phi\,(Z - \xi H)}{2\,\alpha H} + \left\{(0.02\phi)^2 + \left[\frac{\phi\,(Z - \xi H)}{2\,\alpha H}\right]^2\right\}^{1/2} \tag{3}$$

where ξH is the depth from the ground surface to the bottom of the failure zone and αH is the depth to the point of rotation.

In addition, the developed friction angle between the pile and the soil is assumed to be

$$\tan\delta' = -\tan\delta\,\frac{\tan\psi}{\tan\phi} \tag{4}$$

where δ is the maximum wall friction angle available.

Substituting all these parameters and differentiating the thrust, P, with respect to depth, Z, yields the following expression of developed passive lateral earth pressure due to the weight and the friction of the soil.

$$p_1 = -\frac{mA'}{(1 + mA)^2}\left[\frac{1}{2}\gamma Z^2 B - \frac{\gamma Z^3}{3d}(C - K_0 D + 2K_0 E)\right] + \frac{1}{1 + mA}\left[\frac{1}{2}\gamma(2ZB + Z^2 B') - \frac{\gamma}{d}Z^2(C - K_0 D + 2K_0 E) - \frac{1}{3}\frac{\gamma}{d}Z^3(C' - K_0 D' + 2K_0 E')\right] \tag{5}$$

where

$$m = \frac{\tan\delta}{\tan\phi}$$

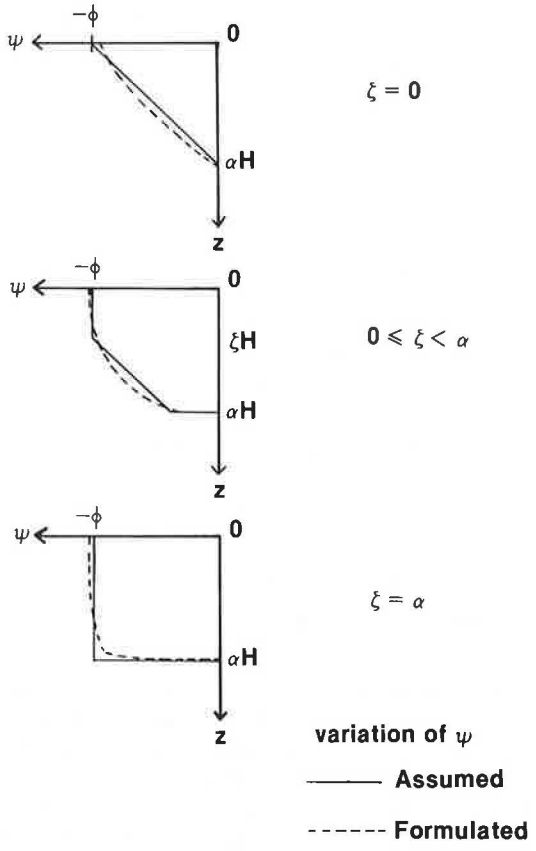

FIGURE 2 Variation of developed friction angle ψ.

$$A = \tan\psi + \tan\left(45° - \frac{\psi}{2}\right)$$

$$B = \tan^2\left(45° - \frac{\psi}{2}\right)$$

$$C = BD$$

$$D = \tan\left(45° - \frac{\psi}{2}\right)\tan\frac{\psi}{2}$$

$$E = A\sin\left(45° - \frac{\psi}{2}\right)$$

$$A' = \frac{\tan\left(45° - \frac{\psi}{2}\right)}{1 + \sin\psi}\frac{d\psi}{dZ}$$

$$B' = \frac{-\tan\left(45° - \frac{\psi}{2}\right)}{\cos^2\left(45° - \frac{\psi}{2}\right)}\frac{d\psi}{dZ}$$

$$C' = B'D + BD'$$

$$D' = \frac{\cos\psi - \sin\psi}{2\cos^2\frac{\psi}{2}(1 + \sin\psi)}\frac{d\psi}{dz}$$

$$E' = A'\sin\left(45° - \frac{\psi}{2}\right) - \frac{1}{2}A\cos\left(45° - \frac{\psi}{2}\right)\frac{d\psi}{dZ}$$

The passive lateral earth pressure distribution due to soil cohesion can be obtained similarly from the wedge considered previously (Figure 1). The resulting expression of the ultimate passive lateral earth pressure becomes

$$p_{2,u} = 3 \tan\left(45° - \frac{\psi}{2}\right) + \frac{\sqrt{2}}{2}\frac{CZ}{d}\tan^2\left(45° - \frac{\psi}{2}\right) \times \left[\cos\left(45° - \frac{\psi}{2}\right) - \tan\frac{\psi}{2}\right] + \frac{\sqrt{2}}{4}\frac{CZ^2}{d}\frac{d\psi}{dZ}\frac{\tan(45° - \psi/2)}{\cos(45° - \psi/2)} \times \left[\frac{\tan\psi/2}{\cos(45° - \psi/2)} - \frac{\sin(45° - \psi/2)}{2\cos^2\psi/2} - \frac{1}{2} - \frac{1}{2}\cos^2(45° - \psi/2)\right] - \frac{3CZ}{2} \times \left[\frac{1}{\cos(45° - \psi/2)}\right]^2\frac{d\psi}{dZ} \quad (6)$$

Note that fully available cohesion is included in this expression. The study should be modified to include the movement-dependent lateral earth pressure development. According to Matlock (*5*), the ratio of the developed versus ultimate pressure of the soft clay depends on the magnitude of movement as shown in Figure 3. Scott (*22*) later approximated this variation using a continuous exponential curve,

$$\frac{p}{p_u} = \left[1 - \exp\left(-\frac{1}{2}\frac{y}{y_c}\right)\right] \quad (7)$$

where y_c equals limiting elastic deformation of the clay.

Consideration of the thickness of the failure zone and the depth to the point of rotation yields an expression of the lateral earth pressure due to cohesion,

$$p_2 = P_{2,u}\left[1 - \exp\left(-4\frac{\alpha - Z/H}{\alpha - \xi}\right)\right] \quad (8)$$

For cases other than those considered (i.e., when stiff clay is considered) and when the point of rotation is located within the upper half of the pile, exactly the same or a virtually identical expression is derived. The detailed derivation is not elaborated, but has been discussed by Shen and Bang (*23*).

The passive pressure development due to ground surcharge, q, can be calculated in a similar manner,

$$p_3 = -\frac{qmA'}{(1 + mA)^2}\left[ZB - \frac{Z^2}{d}(C - K_0D + 2K_0E)\right] + \frac{q}{1 + mA}\left[B + ZB' - 2\frac{Z}{d}(C - K_0D + 2K_0E) - \frac{Z^2}{d}(C' - K_0D' + 2K_0E')\right] \quad (9)$$

where the coefficients were as previously defined for Equation 5.

The combined expression, $p = p_1 + p_2 + p_3$, can now completely describe the transition of the passive lateral earth pressure distribution from an initial failure state (i.e., when the limiting pressure is reached within a single soil element with the largest amount of deformation) to an ultimate failure state. The developed lateral active pressures can be calculated similarly but are neglected because (a) the magnitude of active pressure is virtually insignificant and (b) there may be a separation between the pile and the soil in the active zone, particularly for cohesive soils.

A similar formulation can be developed for the CIDH pile located on or near the sloping ground. Because of the complexity and the number of equations involved, it will not be shown here.

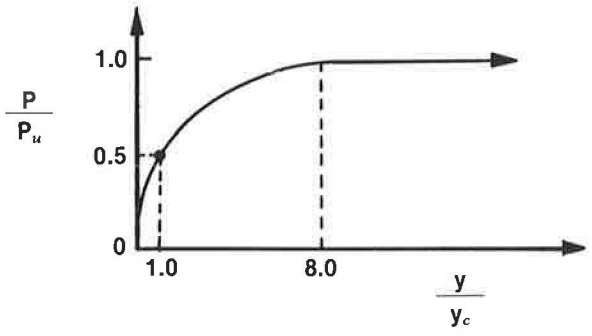

FIGURE 3 Stress-deformation relationship of clay.

ULTIMATE LATERAL LOAD

The distributions of the developed lateral earth pressures need to be modified to incorporate the circumferential variations. Because the normal stress is maximum at $\theta = 0°$ and minimum at $\theta = 90°$, where the angle, θ, is measured from the direction of the loading, one can introduce a cosine function to describe the variation of the normal stress acting on the pile along the circumference as

$$\sigma_r = p' + (p - p')\cos\theta \quad (10)$$

where p is maximum normal stress at $\theta = 0°$ from Equation 1 and p' is minimum normal stress at $\theta = 90°$.

The shear stresses are expressed as

$$\tau^2 = \tau_{r\theta}^2 + \tau_{rz}^2 \quad (11)$$

where $\tau = c + \sigma_r \tan\delta$ and c equals soil cohesion. Note that $\tau_{r\theta} = 0$ at $\theta = 0°$, $\tau_{r\theta}$ = maximum at $\theta = 90°$, τ_{rz} = maximum at $\theta = 0°$, and $\tau_{rz} = 0$ at $\theta = 90°$ (Figure 4). Sine and cosine variations for $\tau_{r\theta}$ and τ_{rz} are therefore assumed.

$$\tau_{r\theta} = (\sigma_r \tan\delta + c)\sin\theta$$

$$\tau_{rz} = (\sigma_r \tan\delta + c)\cos\theta \quad (12)$$

Once the distributions of σ_r, $\tau_{r\theta}$, and τ_{rz} are determined at given depth Z, the corresponding allowable lateral load of a CIDH pile and the corresponding point of rotation can be solved from the equilibrium condition. Figure 4 shows the free-body diagram of a CIDH pile including all the forces acting on it. The developed forces can be obtained from the

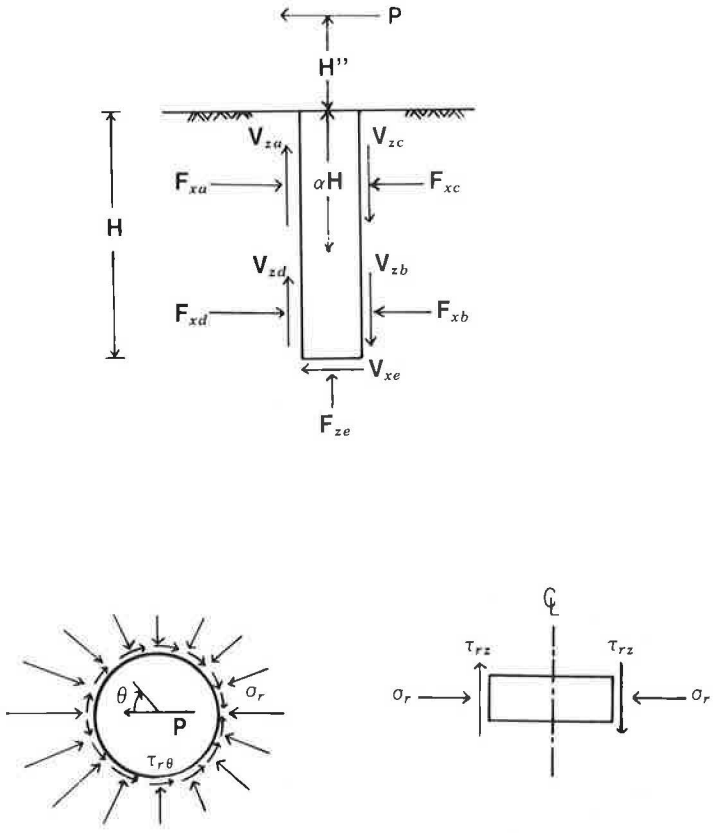

FIGURE 4 Free-body diagram.

integration of stresses acting on the pile. For instance, normal and shear forces acting on the passive side above the rotation point are calculated from

$$F_{xa} = \int_0^{\alpha H} \left[2 \int_0^{\pi/2} \sigma_r \cos\theta \, dA + 2 \int_0^{\pi/2} \tau_{r\theta} \sin\theta \, dA \right] dZ$$

$$V_{za} = \int_0^{\alpha H} \left[2 \int_0^{\pi/2} \tau_{xz} \, dA \right] dZ \qquad (13)$$

Other force components may be obtained in a similar manner.

The detailed analysis of CIDH piles involves an incremental procedure with iterations performed in each increment. Incremental procedure deals with the thickness of the failure zone, ξH, which progresses downward from the ground surface until the ultimate maximum lateral load is obtained. Within each increment, the number of pile segments increases iteratively until convergence is obtained in the solution between two successive values of the number of pile segments.

COMPARISONS

Compared below are the theoretical predictions and the field and laboratory model test results for ultimate lateral resistance and developed lateral earth pressure.

Ultimate Lateral Resistance

Results of 32 model and field tests were compared with the predictions; 20 were from available literature and 12 from the present study. Of the 32 tests, 18 were small-scale models—embedment length of 1 ft or less—and 14 were medium- to large-scale models. The test results covered a variety of soil conditions: 4 in clayey soils, 14 in silty clay soils, and 14 in sandy soils. The present study included 10 tests of CIDH piles in sloping ground.

Table 1 is the summary comparison of the 32 tests. The ultimate lateral resistance (P) and the corresponding point of rotation (α) were computed and compared with the test results. As can be seen, the ratio $P_{\text{measured}}/P_{\text{calculated}}$ (P_m/P_c) varies from 0.63 to 1.78 and the ratio $\alpha_{\text{measured}}/\alpha_{\text{calculated}}$ (α_m/α_c) ranges from 0.78 to 1.28. Note that these comparisons cover a wide variety in geometry of the pile, soil conditions, and ground surface conditions. The comparisons indicate that the proposed method of analysis can predict the ultimate lateral resistance of the CIDH piles reasonably well.

Table 2 shows a comparison of the ultimate lateral resistance values between the test results and those predicted by the several selected methods. On the basis of the information contained in Table 2, the following observations can be made.

1. Hansen's method and Ivey's method give good agreement with the small-scale test results.
2. Davidson's method, on the contrary, agrees reasonably well with the large-scale test results.

TABLE 1 COMPARISON BETWEEN MEASUREMENT AND PREDICTION

Test No.	measured		calculated		Remark
	α	P(lbs)	α	P(lbs)	
Texas C-1	0.56	246	0.57	389	Clay
(12) C-2	0.68	357	0.56	465	
C-3	0.66	290	0.57	348	
L-1	0.73	120	0.57	105	Silt
L-2	0.59	164	0.57	155	
L-3	0.63	238	0.57	217	
Adams (24)	--	25,200	0.64	33,911	
Coyle (16)	--	169,000	0.67	194,010	Pile failure
Texas E-1	0.46	498	0.57	337	Silt
(12) E-2	0.53	410	0.55	255	
E-3	0.54	500	0.56	407	
E-4	0.64	615	0.60	663	
E-5	0.63	352	0.57	309	
Davis Sand	0.67	1,000	0.74	1,092	
Texas S-1	0.65	27	0.73	20	Sand
(12) S-5	0.63	20	0.74	12	
S-12	0.60	34	0.74	20	
S-13	0.67	22	0.72	17	
S-14	0.58	48	0.74	27	
S-16	0.63	52	0.74	31	
S-17	0.69	115	0.78	73	
Davis 7	--	2,650	0.63	3,346	
10	0.72	1,900	0.70	2,196	Downslope loading
13	--	1,480	0.70	2,125	Downslope loading
Davis 19	0.74	1,050	0.70	1,666	Downslope loading
22	0.72	1,822	0.69	2,598	Downslope loading
Davis S-7	0.79	450	0.69	581	Downslope loading
S-9	0.84	520	0.69	586	Downslope loading
S-11	--	540	0.69	582	Downslope loading
S-12	0.73	880	0.73	980	Upslope loading
S-13	0.80	900	0.73	986	Upslope loading
S-14	0.86	875	0.73	981	Upslope loading

TABLE 2 COMPARISON OF ULTIMATE LATERAL LOADS BY VARIOUS METHODS

Test	Ultimate Lateral Load (lbs)				
	measured	Ivey method	Davidson method	Hansen method	Current study
Texas S-1	27	32.5	15.8		20
(12) S-5	20	23.9	11		12
S-12	34	38.2	17.2		20
S-13	22	23.3	11.9		17
S-14	48	50.8	18.6		27
S-16	52	52.5	24.7		31
S-17	115	134	57.3		73
E-1	498	459	241.8	459	337
E-2	410	337	179	388	255
E-3	500	535	249.7	582	407
E-4	615	871	414.4	975	663
E-5	352	384	204.9	481	309
C-1	246	300	271.1		389
C-2	357	344	333		465
C-3	290	241	274.5		348
L-1	120	92			105
L-2	164	154			155
L-3	238	324			217
Davis 7	2,650	8,446	1,871	9,665	3,346
Adams (24)	25,200	52,165	29,558	51,780	33,911
Coyle (16)	169,000	103,301	195,133	242,332	194,010

3. The proposed method of analysis seems to produce the closest predictions of ultimate lateral resistance.

Lateral Earth Pressure

The following are the comparisons of the predicted and measured lateral earth pressure along the length of CIDH piles in both level and sloping embankments. Note that all the lateral earth pressure values are those acting along the direction of the lateral load application ($\theta = 0°$).

Level Sandy Embankment

Five tests with the same soil properties and pile geometry were performed. Figures 5 and 6 show the lateral earth pressure comparisons on the passive sides at horizontal loads of approximately 200 and 1,000 lb, respectively. The measured pressures are expressed by two lines (i.e., upper and lower bounds of five measurements). These comparisons indicate that the proposed method of analysis can predict not only the magnitude of lateral earth pressure but also the approximate distribution. In general, the predicted values lie within the range of measured values.

Sloping Sandy Embankment

The test results of a model CIDH pile installed in a sloping sandy embankment with the lateral load applied away from the slope were compared. Comparison is made at the lateral load of approximately 250 lb as shown in Figure 7. As indicated, the prediction by the proposed method of analysis yields fairly good agreement with the model measurements, both in magnitude and in distribution.

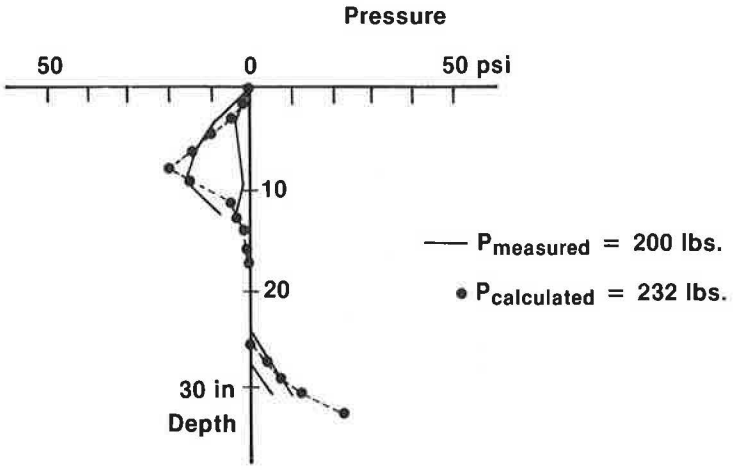

FIGURE 5 Lateral earth pressure comparison—level sand 1 (Test no. Davis sand).

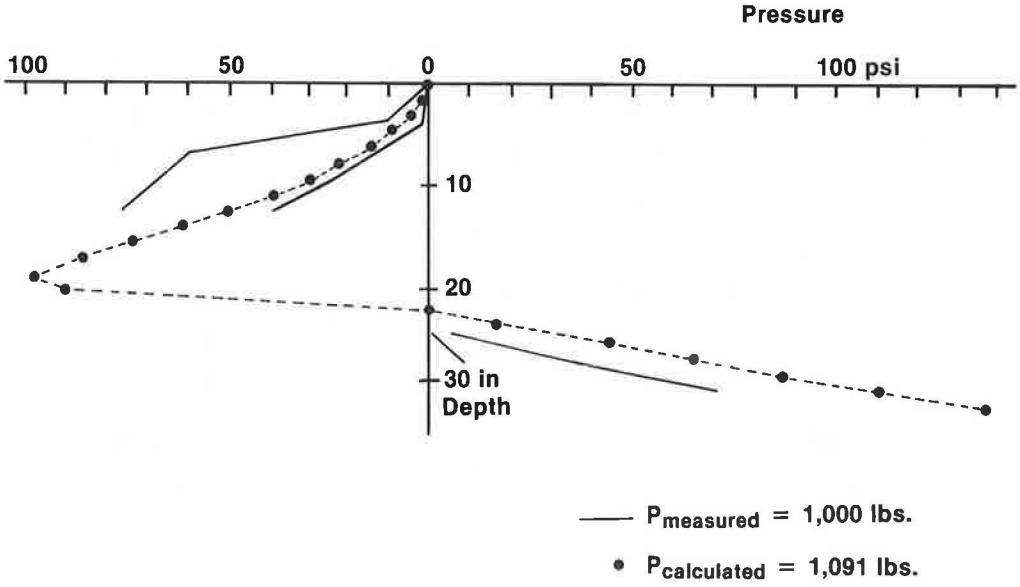

FIGURE 6 Lateral earth pressure comparison—level sand 2 (Test no. Davis sand).

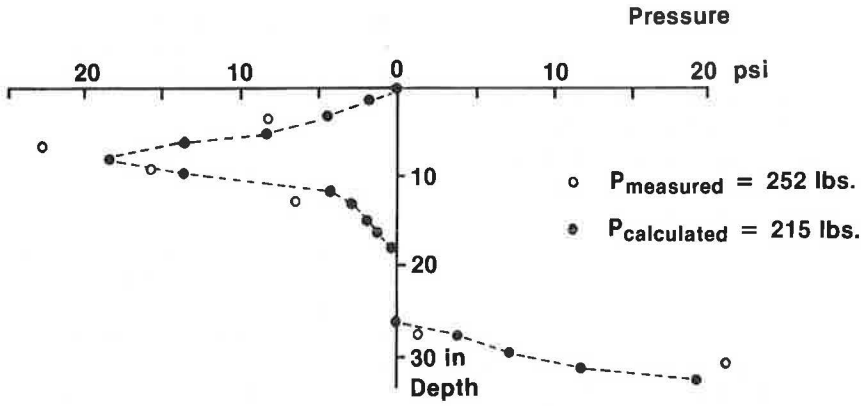

FIGURE 7 Lateral earth pressure comparison—sloping sand and upslope loading (Test no. Davis S-12).

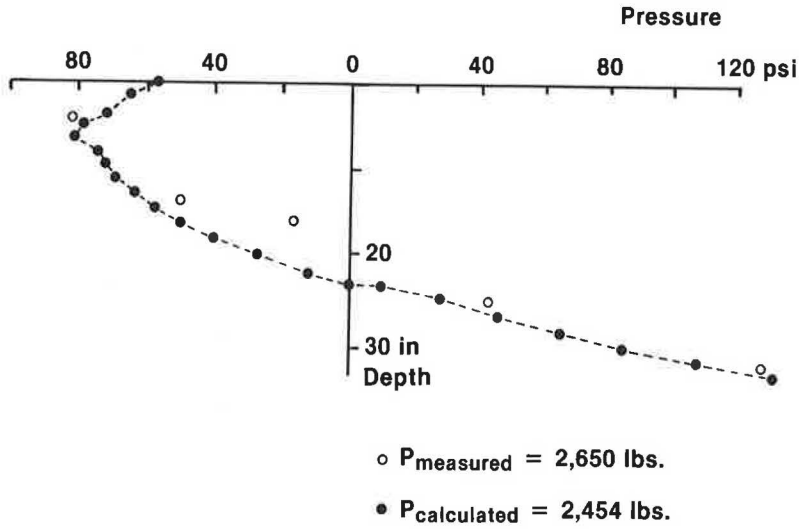

FIGURE 8 Lateral earth pressure comparison—level clay (Test no. Davis 7).

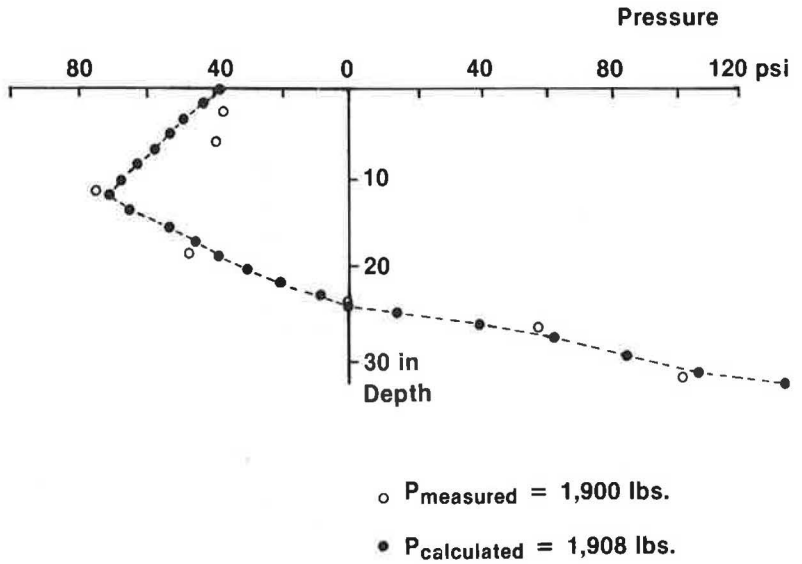

FIGURE 9 Lateral earth pressure comparison—sloping clay and downslope loading (Test no. Davis 10).

Level and Sloping Clayey Embankment

Two tests were studied and compared in this group: one on level ground (Test 7), the other on the sloping ground with the lateral load applied toward the slope (Test 10). The pressure distributions at lateral loads near or at failure were examined. Figures 8 and 9 indicate the individual comparisons. In general, fairly good agreement exists.

CONCLUSION

The research includes two major parts: a laboratory model study and an analytical formulation for detailed investigation of the laterally loaded CIDH piles. The model pile study was carried out in a test bin where both level and sloping embankments were constructed with either pit-run river sand or silty clay. An instrumented aluminum pipe pile was built to measure the load-versus-displacement relationship of the laterally loaded piles and the interface pressure distributions on the pile. The results were interpreted both quantitatively and qualitatively to describe the soil-structure interaction and the failure mechanism, and to compare with the analytical solutions.

The analytical solution was formulated on the basis of the failure wedge observed during the laboratory model pile tests and suggested by Reese et al. (*4*). Furthermore, Dubrova's movement-dependent lateral earth pressure distribution concept (*21*) was adopted and modified to calculate the interactive pressure distributions under all stages of lateral loading. A comprehensive set of design equations was developed applicable to both level and sloping ground.

Comparisons with model and field test results indicate that the proposed method of analysis is capable of predicting rea-

sonably well the magnitude and distribution of lateral earth pressure under various lateral loads for a wide range in pile geometry, soil conditions, and ground surface conditions. In particular, the nonlinear lateral earth pressure distributions at small lateral loads can be identified.

Though a relatively extensive comparison was made between the model test results (from this study and elsewhere) and the analytical predictions, additional field data are needed to further validate the usefulness of the developed formulation.

ACKNOWLEDGMENT

The authors are grateful for the financial and technical support provided by the California Department of Transportation.

REFERENCES

1. C. K. Shen, S. Bang, M. DeSalvatore, and C. J. Poran. Laterally Loaded Cast-In-Drilled-Hole Piles. In *Transportation Research Record 1191*, TRB, National Research Council, Washington, D.C., 1988, pp. 155–165.
2. B. B. Broms. Lateral Resistance of Piles in Cohesionless Soils. *Journal of the Soil Mechanics and Foundation Division*, ASCE, Vol. 90, No. SM2, 1964.
3. B. B. Broms. Lateral Resistance of Piles in Cohesive Soils. *Journal of the Soil Mechanics and Foundation Division*, ASCE, Vol. 90, No. SM3, 1964.
4. L. C. Reese, W. R. Cox, and F. D. Koop. Analysis of Laterally Loaded Piles in Sand. Presented at the Offshore Technology Conference, Paper No. 2080, Houston, Tex., May 1974.
5. H. Matlock. Correlations for Design of Laterally Loaded Piles in Soft Clay. Presented at the Offshore Technology Conference, Paper No. 1204, Houston, Tex., April 1970.
6. D. L. Ivey. *Theory, Resistance of a Drilled Shaft Footing to Overturning Loads*. Research Report 105-1. Texas Transportation Institute, Texas A&M University, College Station, Tex., Feb. 1968.
7. C. O. Hays, J. L. Davidson, E. M. Hagan, and R. R. Risitano. *Drilled Shaft Foundation for Highway Sign Structures*. Research Report D647F. Engineering and Industrial Experiment Station, University of Florida, Gainesville, Dec. 1974.
8. D. L. Ivey and W. A. Dunlap. *Design Procedure Compared to Full-Scale Tests of Drilled Shaft Footings*. Research Report 105-3. Texas Transportation Institute, Texas A&M University, Feb. 1970.
9. D. L. Ivey and L. Hawkins. Signboard Footings to Resist Wind Loads. *Civil Engineering*, Vol. 36, No. 12, Dec. 1966.
10. J. L. Davidson, C. O. Hays, and E. M. Hagan. Design of Drilled Shafts Supporting Highway Signs. In *Transportation Research Record 616*, TRB, National Research Council, Washington, D.C., 1976.
11. R. L. Lytton. *Design Charts for Minor Service Structure Foundations*. Research Report 506-1F. Texas Transportation Institute, Texas A&M University, Sept. 1971.
12. D. L. Ivey, K. J. Koch, and C. F. Raba. *Resistance of a Drilled Shaft Footing to Overturning Loads, Model Tests, and Correlation with Theory*. Research Report 105-2. Texas Transportation Institute, Texas A&M University, College Station, July 1968.
13. J. R. Seiler. Effect of Depth of Embedment on Pole Stability. *Wood Preserving News*. Vol. 10, No. 11, Nov. 1932.
14. J. B. Hansen. The Ultimate Resistance of Rigid Piles Against Transversal Forces. *Danish Geotechnical Institute Bulletin*, No. 12, Copenhagen, 1961.
15. V. R. Kasch, H. M. Coyle, R. E. Bartoskewitz, and W. G. Sarver. *Lateral Load Test of a Drilled Shaft in Clay*. Research Report 211-1. Texas Transportation Institute, Texas A&M University, College Station, 1977.
16. M. E. Bierschwale, H. M. Coyle, and R. E. Bartoskewitz. *Field Tests and New Design Procedure for Laterally Loaded Drilled Shafts in Clay*. Research Report 211-3F. Texas Transportation Institute, Texas A&M University, Jan. 1981.
17. G. L. Holloway, H. M. Coyle, R. E. Bartoskewitz, and W. G. Sarver. *Field Test and Preliminary Design Method for Lateral Loaded Drilled Shafts in Clay*. Research Report 211-2. Texas Transportation Institute, Texas A&M University, Sept. 1978.
18. N. F. Ismael and T. W. Klym. Behavior of Rigid Piers in Layered Cohesive Soil. *Journal of the Geotechnical Engineering Division*, ASCE, Vol. 104, No. GT8, Aug. 1978.
19. L. C. Reese. Design and Construction of Drilled Shafts. *Journal of the Geotechnical Engineering Division*, ASCE, Vol. 104, No. GT1, Jan. 1978.
20. W. V. Wright, H. M. Coyle, R. E. Bartoskewitz, and L. J. Milberger. *New Retaining Wall Design Criteria Based on Lateral Earth Pressure Measurements*. Research Report 169-4F. Texas Transportation Institute, Texas A&M University, Aug. 1975.
21. M. E. Harr. *Foundations of Theoretical Soil Mechanics*. McGraw-Hill, New York, 1966.
22. R. F. Scott. *Foundation Analysis*. Prentice-Hall, Englewood Cliffs, N.J., 1981.
23. C. K. Shen and S. Bang. *Lateral Resistance of Cast-In-Drilled-Hole Piles*. California Department of Transportation, Sacramento, 1989.
24. J. I. Adams and H. S. Radhakrishna. The Lateral Capacity of Deep Augered Footings. *Proc. of the 8th International Conference on Soil Mechanics and Foundation Engineering*, Vol. 2.1, Moscow, USSR, 1973.

Publication of this paper sponsored by Committee on Subsurface Soil-Structure Interaction.

Bolted Connections of Rib-Plate Structures

GLENN A. HAZEN, SHAD M. SARGAND, JIA-XIANG ZHAO, AND JOHN O. HURD

A field study of an aluminum box culvert subjected to backfill and live load is correlated with a laboratory load testing of a rib-reinforced plate. Stress concentration and distribution of stress are examined in the region where bolts connect reinforcing ribs to the corrugated plate. Moments and thrusts on ribs and plates are computed to examine composite behavior. Stresses in the region of bolts that attach ribs to the corrugated plate are only in approximate agreement with results obtained from the finite-element computer program CANDE. Experimental data suggest that plate distortion near the assembly bolts results in local bending stresses. Field measurements show that rib and plate forces act as noncomposite members during backfilling, but respond compositely with the application of live load. A flat, corrugated plate with no-rib, one-rib, and two-rib combinations was tested in the laboratory under a concentrated load acting at the center and a constant bending moment. Stresses were found to have significant variations perpendicular to the corrugations that may be corrected with a shift in the neutral axis. Stresses are in agreement with the constant ratio of composite response for the rib and corrugated plate when stresses are measured between bolts. Stress concentrations and local distortions at rib ends were duplicated in the laboratory.

A number of investigators have tested culverts with reinforced ribs. The normal procedure has been to assume composite action and to neglect thrust forces. This paper extends previous work on these assumptions and also examines shear transfer at the bolted connection. One mode of failure anticipated on these culverts is failure of the bolt connections (Figure 1); understanding connections is the key to increasing the efficiency of these structures.

Box culverts are assembled by bolting together curved, corrugated metal plates. Rib stiffeners are often used to increase the flexural stiffness and moment capacity of the plate. These stiffeners, curved to conform to the shape of the culvert, are bolted to the corrugated plate at intervals spaced along the length of the culvert. The ribs are spaced to support maximum applied moments and so do not extend to the foundation. The reinforced design permits the use of culverts at locations of shallow covers. Despite the use of reinforcing ribs, the stiffened structures are quite flexible, so the backfill must be good quality soil and properly compacted.

During the backfill process lateral soil pressure moves the sides of the culvert inward and the crown upward, a phenomenon known as *peaking*. Once the backfill has been placed to crown level, subsequent backfill placements reverse this trend by pressing the crown downward and the sides outward. Similarly, when the live load is applied, the structure deflects downward at the top and outward at the sides.

A number of studies have compared field measurements with finite-element solutions or design standards. The results from several of these studies are useful in examining composite action and local stress variations. Duncan (*1*) made an in-depth study of the interaction between flexible metal culverts and the surrounding backfill for both shallow and deep-cover conditions using field data and finite-element analyses. In a more recent study, Duncan (*2*) investigated the behavior of an aluminum box-type culvert with electric strain gauges attached to the haunch and the crown. Comparisons of the experimental data with the finite-element analysis indicate that moments in the crown are likely to be the same, but moments in the haunch are likely to be appreciably smaller than design moments.

In a research project, Beal (*3*) instrumented an aluminum box culvert at the crown and haunches with strain gauges and curvature-measuring devices. The data analysis used to convert measured strains to bending moments was modified to account for the degree of composite action between the plate and the rib, thus allowing the calculation of bending moment independent of the thrust. Beal reasoned that the magnitude of thrust in a low-cover culvert is small and can be neglected. In another research project, Beal (*4*) instrumented an aluminum structural plate culvert at 16 locations spaced around the structure. Beal made several observations that are useful when instrumenting ribbed aluminum culverts:

1. Gauges mounted on the plate located directly under the ribs did not give reliable estimates of average plate strain,
2. The backfill placement sequence resulted in distortion of the culvert shape, and
3. Live load stresses were small compared with backfill load stresses.

INSTRUMENTATION

This study consisted of a field investigation coordinated with a laboratory study. The field study was conducted on an aluminum box culvert installed under State Route 269 in Noble County, Ohio. The rib-plate structure had a 14-ft, 10-in. span, 4-ft, 10-in. rise, and was 42 ft long with concrete headwalls.

G. A. Hazen, S. M. Sargand, and J-X. Zhao, Civil Engineering Department, Ohio University, Athens, Ohio 45701. J. O. Hurd, Ohio Department of Transportation, 25 South Front Street, Columbus, Ohio 43216-0899.

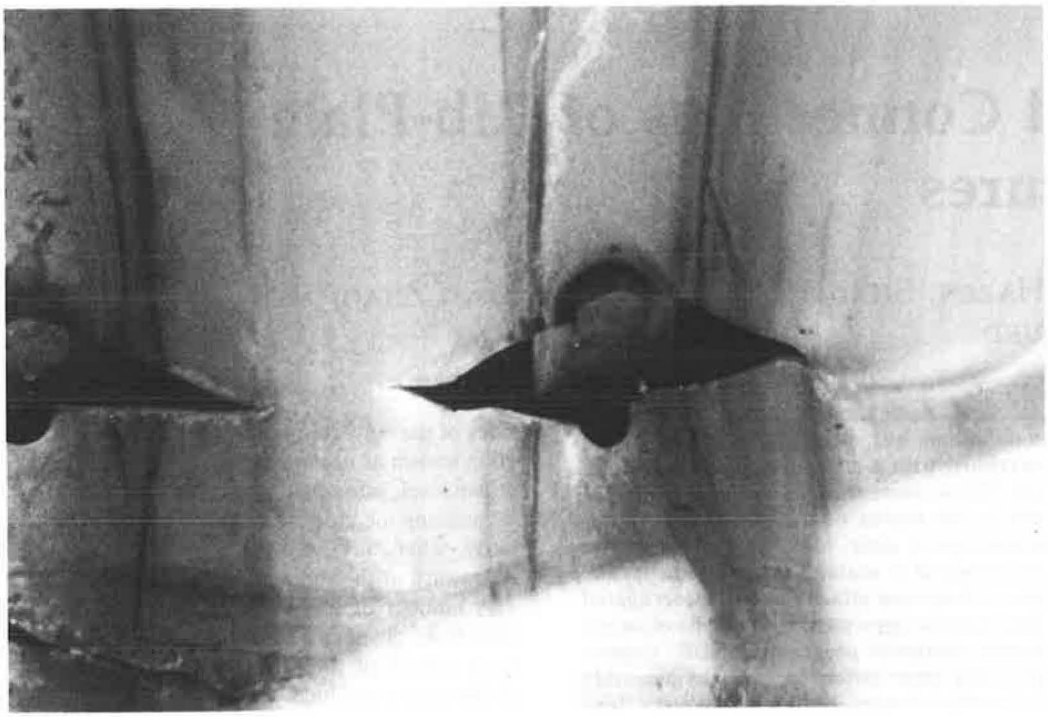

FIGURE 1 Failed box culvert. (Cross section located at the end of side rib.)

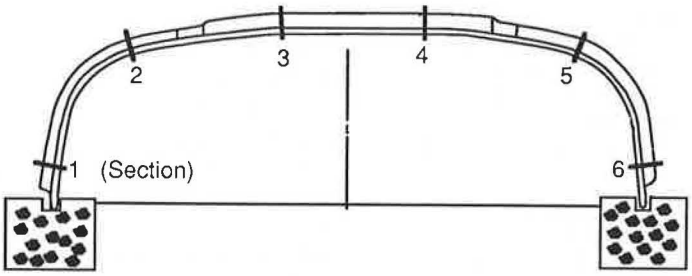

FIGURE 2 Location of instrumented sections.

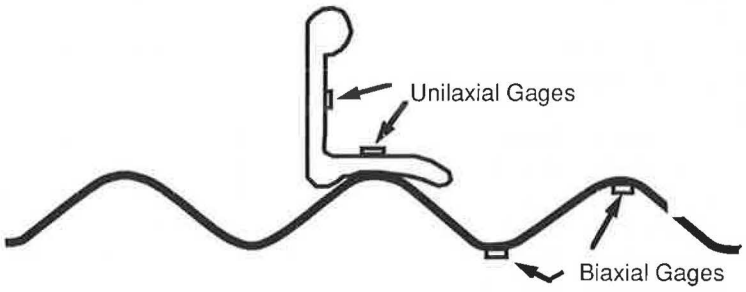

FIGURE 3 Typical location of strain gauges.

The ends of the corrugated plate were embedded in 3- by 3-ft concrete strip footings. The cross section of the structure is shown in Figure 2. Ribs were bolted to the structure as shown in Figures 2 through 5. The top ribs were spaced on 18-inch centers, whereas the side ribs were spaced every 27 inches. Sections 1 through 6 were instrumented with strain gauges to determine the bending moments and thrusts on these sections, as shown in Figures 2 and 3. At each section, two uniaxial electric strain gauges were attached to the outside rib and two biaxial strain gauges were attached to the inside corrugated plate. Biaxial gauges mounted on the plate were located one corrugation from the rib in order to move away

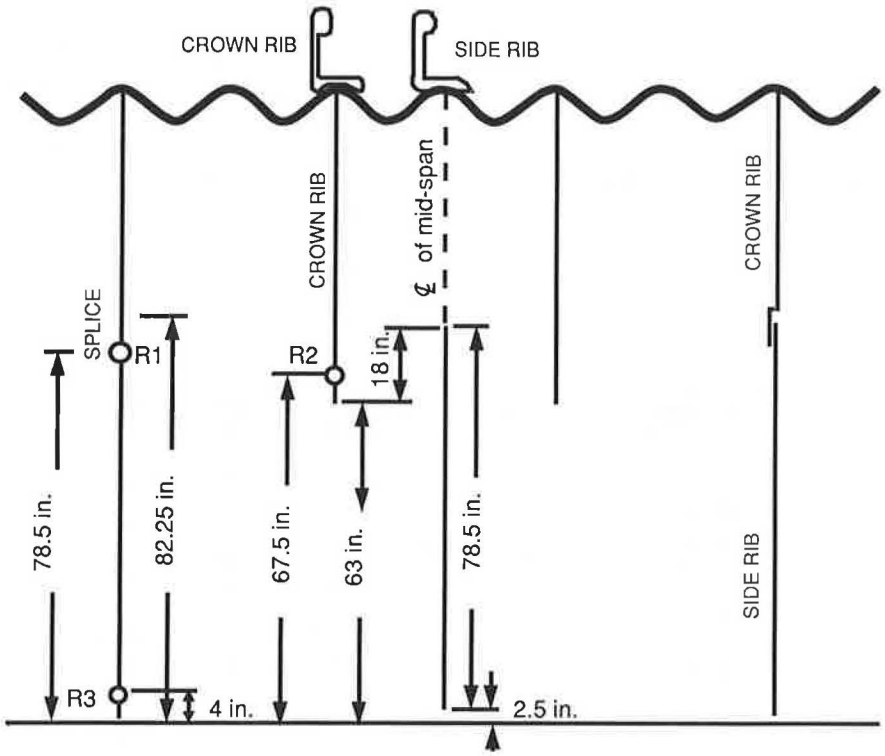

FIGURE 4 Location of rosette groups.

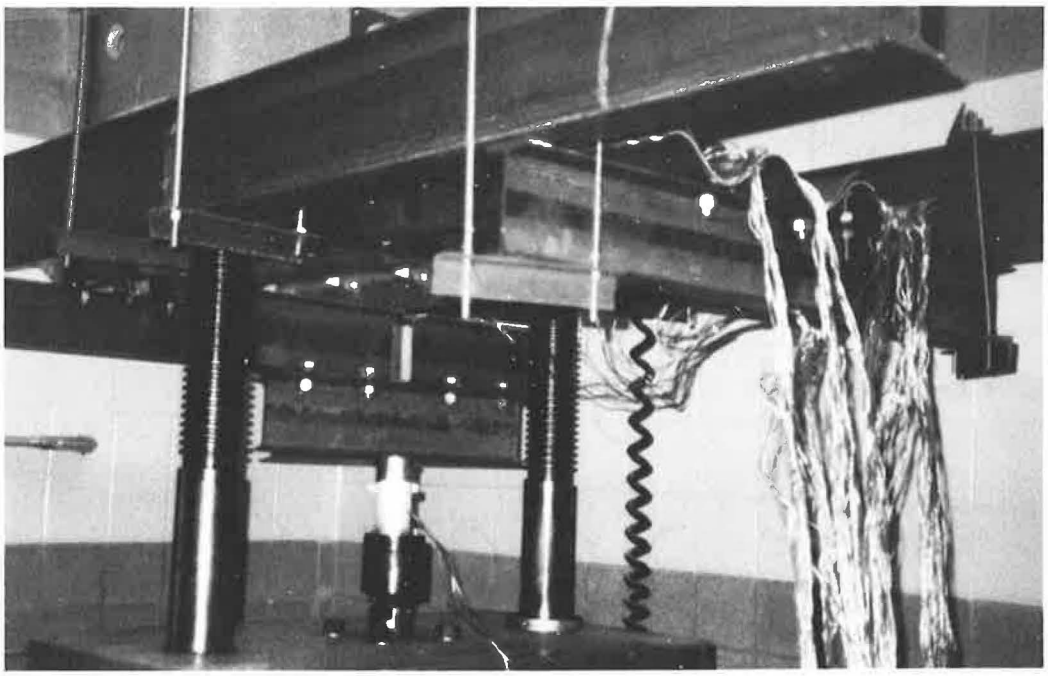

FIGURE 5 Laboratory loading apparatus.

from possible strain disruption. Electric strain gauge rosettes were placed in patterns at locations R_1, R_2, and R_3 as shown in Figure 5. Strain gauge rosettes were cemented along planes rotated 0°, 45°, and 90° to the longitudinal plane of the culvert. These patterns were located at the ends of reinforcing ribs because the local bending effect was expected to be large.

Before field testing, electric strain gauges were mounted on bending specimens. These gauges were tested for stability of readings under a variety of load levels and environments. Several recommended gauge protection systems were tested. All electric strain gauges installed were 350 ohms to minimize wire resistance. A powered bridge, three-wire reading system was used to read strain values. Data were recorded automatically in a computer, printed, and inspected visually as readings were taken.

A laboratory study was designed to examine field results in an environment that could be more closely monitored. Identical plate and crown ribs were obtained from the manufacturer and used in the laboratory study. Four sections across the rib-plate were instrumented for moment and thrust, and a bolt located at the rib end was instrumented to examine local stress concentration. The aluminum corrugated plate tested in the laboratory had a 6-ft, 10-in. span and a 2-ft, 3-in. width and was loaded with two sides free and the other two sides bolted to I-beams. Bags of granular fill were placed between a short I-beam and the plate crown. Corrugations provided side support to the bags of backfill so they would not split.

The test setup is shown in Figures 5 and 6. A constant moment and a concentrated center loading were applied to a

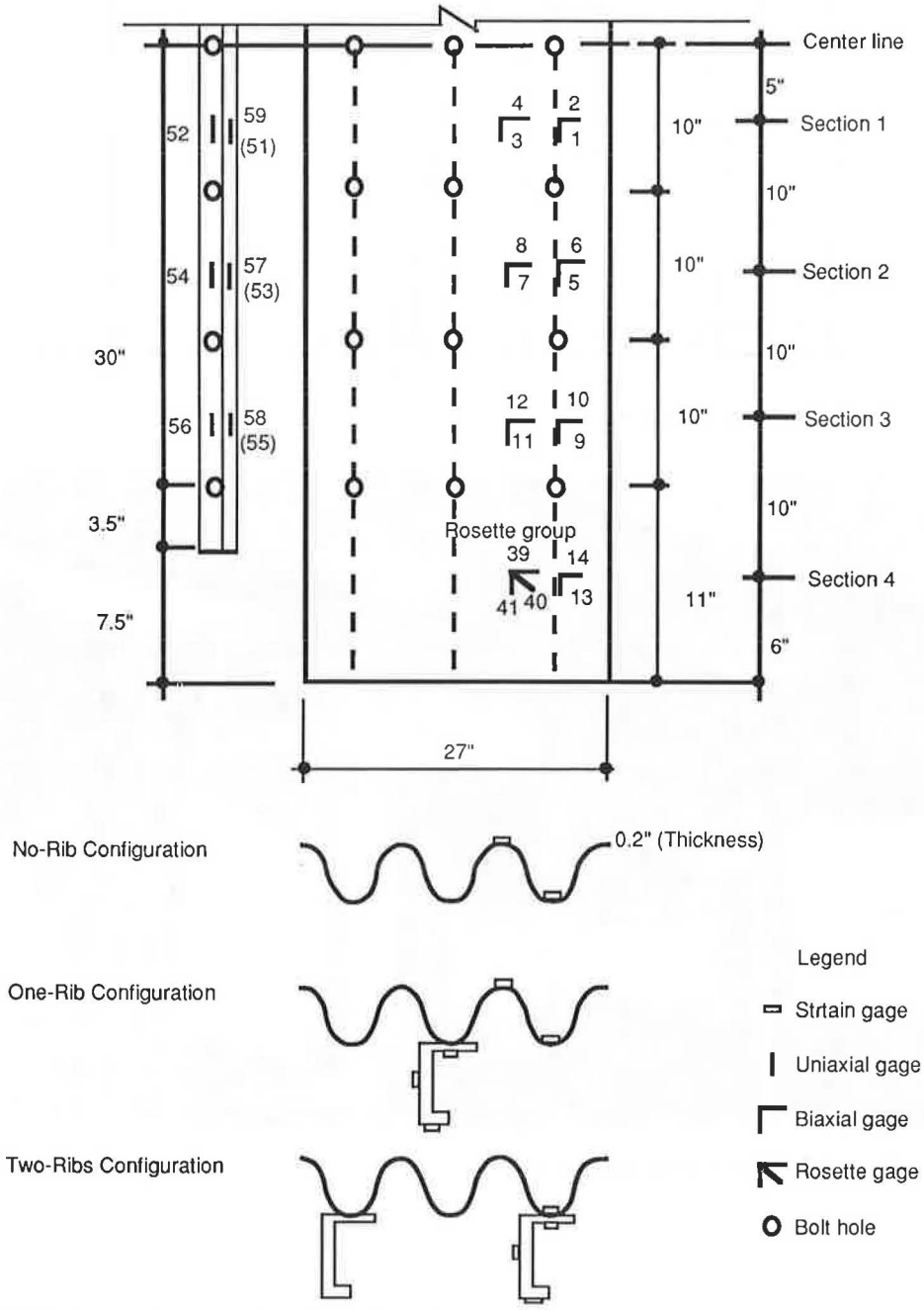

FIGURE 6 Laboratory plate-rib configurations.

no-rib, one-rib, and two-rib configuration. To duplicate field conditions, the ends of the plate were attached to an I-beam for all loading situations, as shown in Figure 5. The plate was mounted upside down to accommodate the loading frame. A concentrated center load was applied by the load piston to the plate center line. When a constant bending moment was applied, the load was applied symmetrically. All bolts were torqued to field specifications.

FIELD RESULTS FOR MOMENT AND THRUST UNDER LIVE LOAD

Bending moment and thrust forces in instrumented sections of the box culvert are shown in Figures 7 and 8. Noncomposite moments and thrusts were calculated from the four strain gauges shown in Figure 3. A linear response was assumed across the rib and across the plate. Thus, the moment was calculated as the sum of moment in the rib, moment in the plate, and moment resulting from the couple created by the rib thrust and the plate thrust. Composite moments and thrusts were calculated from only the two outside gauges. A linear response was assumed across the combined section. Thus, the moment was calculated directly. For initial backfilling, the agreement was not good between composite and noncomposite action. However, the assumption of composite action showed improvement with an increase in load and appeared to be good for 130 percent of H20 traffic load (42 kips).

Moment compared favorably with theoretical calculations, with maximum moments at the center and haunches of the

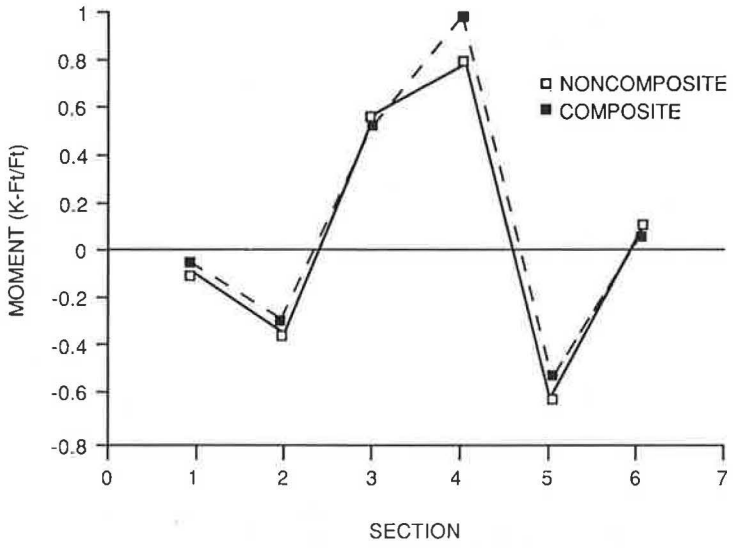

FIGURE 7 Moment comparisons with 42-kip live load at center position.

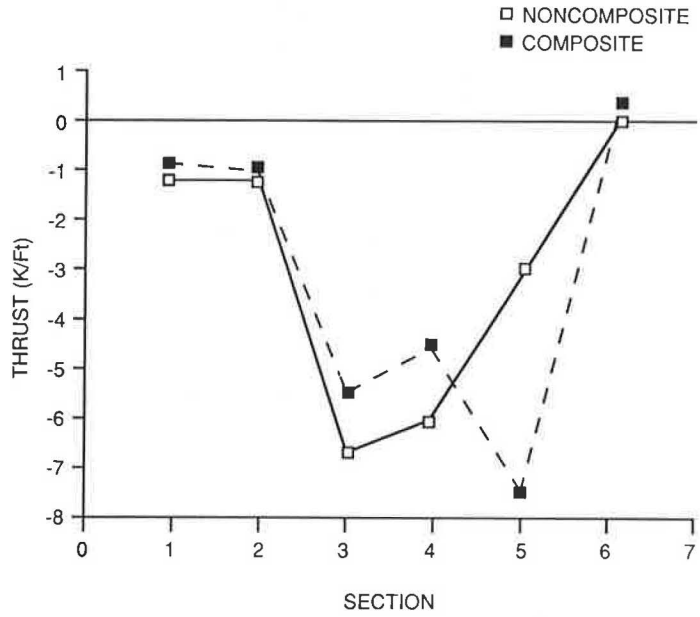

FIGURE 8 Thrust comparisons with 42-kip live load at center position.

culvert. Coupons were tested from both the plate and the rib. The moduli tested confirmed published moduli (5) of 10.2 × 10^3 ksi for plate 5052 and 10.0 × 10^3 ksi for plate 6061-T6. The proportional limit recorded was 27.5 ksi in the plate coupon. The experimental moment for all sections did not approach the plastic moment capacity of 13.72 k-ft/ft on the crown or 7.94 k-ft/ft on the side. Hence, plastic action was not a consideration. Thrust (Figure 8) accounts for an important share of the load-carrying capacity of the culvert, and thus cannot be neglected. Again, the thrusts compared well with composite response for live loading.

LABORATORY RESULTS FOR MOMENT

In the laboratory, composite moments (which were calculated with the procedure used for field data) compared poorly with theoretical values as shown in Figure 9. Moments calculated

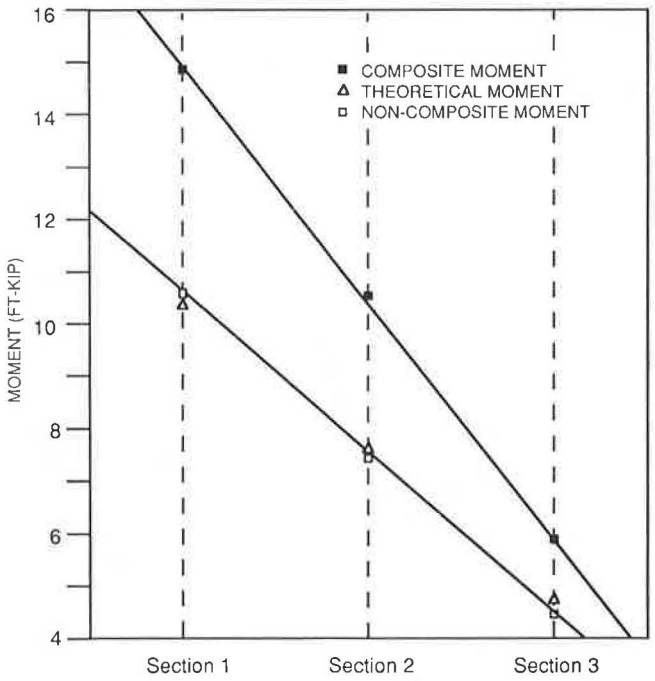

FIGURE 9 Laboratory moment comparison with concentrated center load of 7.43-kip, one-rib configuration.

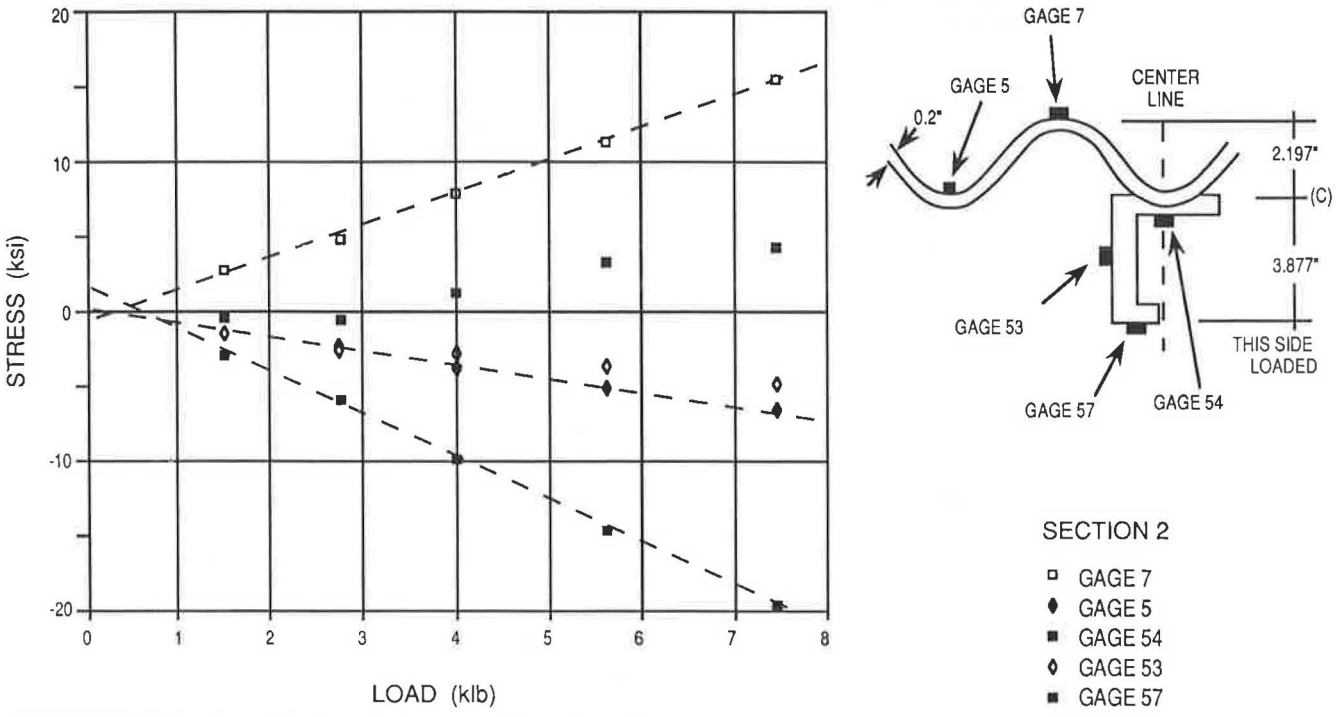

FIGURE 10 Laboratory test of center load, one-rib configuration.

TABLE 1 RATIO OF CROWN STRESS AND VALLEY STRESS IN CORRUGATION DIRECTION

Load	no rib center load			Load	no rib constant moment		
P	section 1	section 2	section 3	P	section 1	section 2	section 3
(kip)	$\lvert\sigma_3/\sigma_1\rvert$	$\lvert\sigma_7/\sigma_5\rvert$	$\lvert\sigma_{11}/\sigma_9\rvert$	(kip)	$\lvert\sigma_3/\sigma_1\rvert$	$\lvert\sigma_7/\sigma_5\rvert$	$\lvert\sigma_{11}/\sigma_9\rvert$
-0.53	1.62	1.63	1.59	-1.48	1.63	1.74	2.0
-0.90	1.64	1.64	1.56	-2.4	1.66	1.77	2.0
-1.52	1.62	1.62	1.54	-4.8	1.65	1.78	2.2
-2.12	1.62	1.63	1.54	-5.8	1.63	1.79	2.2
-2.86	1.62	1.63	1.57				
-3.01	1.62	1.63	1.58				

Note: σ_3, σ_7, σ_{11} are stresses at crown of corrugation.
σ_1, σ_5, σ_9 are stresses at valley of corrugation.

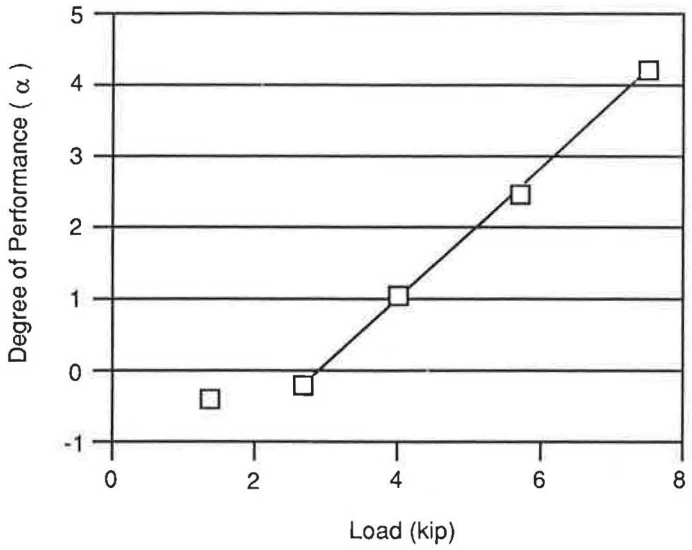

FIGURE 11 Degree of performance versus load with one-rib center load.

from composite strains, top of rib and valley of corrugation, resulted in much higher values than applied moments. Noncomposite calculations duplicated the theoretical values calculated from the applied load. Figure 10 shows that bending in the rib was not composite, because Gauge 54 (rib) records a higher strain than Gauge 5 (plate). If bending were composite, Gauge 5 would read slightly more positively. The results were similar to those for other loading configurations. To better understand the rib-plate response to load, the rib was removed and the ratio of plate stresses was recorded (Table 1). It should be noted that the ratio of stresses was constant, except where affected by supports. Because stresses can be calculated across the rib-plate interface, a composite thrust was added.

$$T = T_p + T_r + T_c$$

where

T_p = thrust in the plate,
T_r = thrust in the rib, and
T_c = the composite thrust calculated at 4 kips.

A plot of α (Figure 11) clearly shows that α becomes constant after the load reaches 3 kips.

Other configurations were also tested. When a two-rib plate was tested, a biaxial gauge was located beneath the rib. Measurements taken in this situation were composite for a concentrated center load (Figure 12) as well as a constant bending moment. In contrast to results by Beal (*3*), readings taken beneath the rib were more consistent with composite calculations. However, in Beal's study, the ribs were spaced 27 in. apart.

It is also interesting to note that in a laboratory situation, where fit is not a problem and torques can be exactly applied, the initial loading response was linear.

FIELD STRESS DISTRIBUTION AT BOLT CONNECTIONS

To investigate the stress distribution around bolts, three bolts were instrumented with patterns of electric strain rosettes. A live load 130 percent of the H20 loading applied to the center

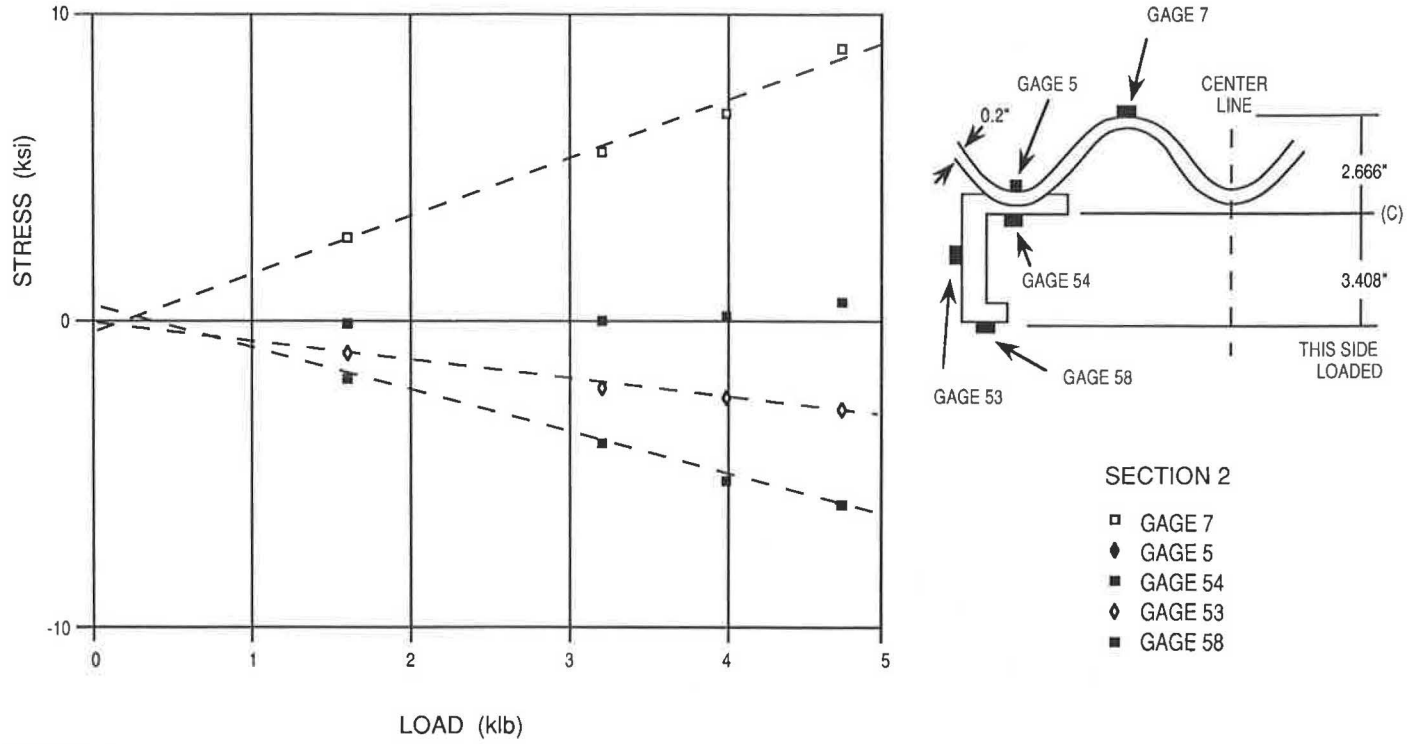

FIGURE 12 Laboratory test of center load, two-rib configuration.

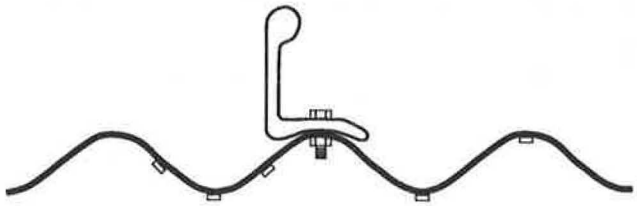

i. Circumferential Stresses

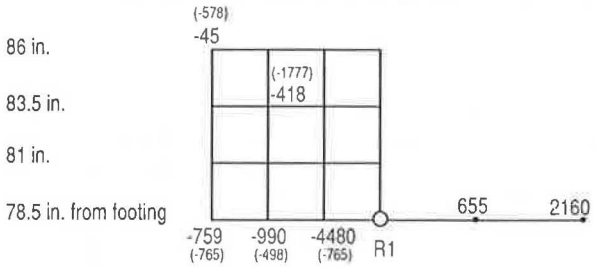

ii. Longitudinal Stresses

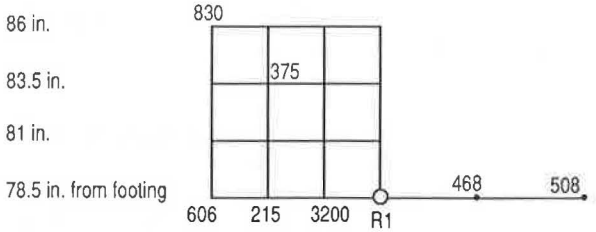

FIGURE 13 Circumferential and longitudinal stresses in rosette Group One, with 42-kip live load at center position (CANDE).

of the culvert resulted in circumferential and longitudinal stresses at the haunch as shown in Figure 13. The location of the instrumented bolt (R_1) is shown in Figure 4. To provide a comparison with values that may be determined theoretically, the culvert was modeled with the finite-element program CANDE. (The results of the computer program are given in parentheses in Figure 13.) For comparison, the culvert was assumed to act as a composite structure. When principal stresses were calculated, the stress concentration was more obvious, as shown in Figure 14. The reinforcing effect of the rib was clearly seen as the principal directions were rotated around the bolt. However, in general the comparison between CANDE and field measurements is good at the haunch.

At the end of the rib, located close to the footer (R_3 in Figure 4), there was no agreement between theory and field data. When compared with the finite-element solution from CANDE in Figure 15, the bolt clearly disrupted the stress distribution since the circumferential stresses decreased in magnitude away from the bolt. Large stresses close to the bolt represented stress concentrations and large local distortion. This occurred in circumferential as well as in the longitudinal directions. The plate, as it contacted the footer, also recorded stress disruptions. The crown corrugation on both sides of the bolt showed compressive stress yet did not agree in magnitude. A difference in magnitude suggests local distortion and a side force on the rib. Compressive stress, as calculated by CANDE, rather than the tensile stresses that were measured in the field, would be expected below the last bolt. The plot of principal stresses at the footer (Figure 16) again emphasizes the random stress field and high stress concentrations. On the basis of these measurements, it is suggested that the rib be extended into the footer.

Examining the effect of the bolted connection in the laboratory, a comparison was drawn between the plate only (no rib) and the plate with a central rib. Figure 17 shows that the stresses were linear with respect to distance along the corrugation, reaching almost zero at the hole (Position 4). The stresses continued to increase locally but returned to zero. The same rosettes with a rib bolted to the plate showed a compressive stress that increased as it passed the bolt location (Figure 18). In both cases, the stresses increased in proportion to load. The local effect of the connection, which was very apparent in the field measurements, could be clearly duplicated in the laboratory as shown in Figure 19. The values of stress within the parentheses were theoretical values calculated for a composite section. Compressive stresses appeared as a local stress effect created by the bolt.

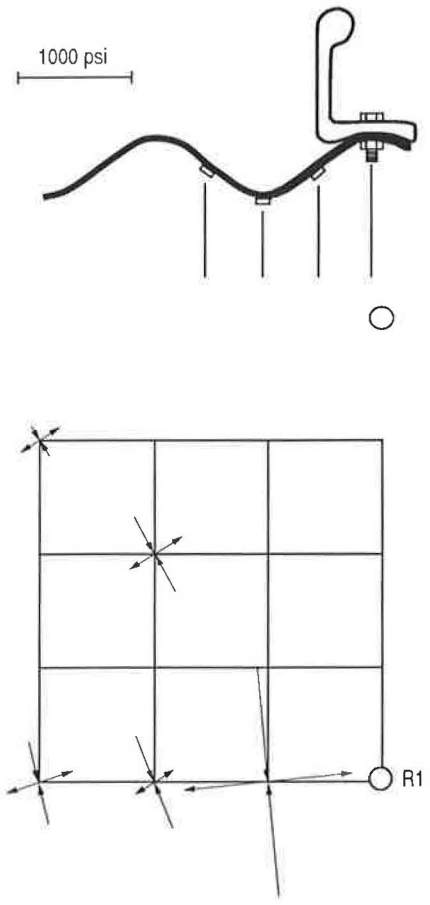

FIGURE 14 Principal stresses in rosette Group One, with 42-kip live load at center position.

CONCLUSIONS

The results for this field and laboratory investigation may be summarized as follows:

1. Many variables are involved in determining whether full composite action occurs in the rib-plate structure. The degree of composite action increases as backfill height increases and the culvert deformation returns from early peaking. Then composite response is recorded under live load. Slip may occur betweeen the plate and the stiffening ribs because the fit is not tight enough in the assembled culvert.
2. In the bolted connection, a linear response was recorded, yet the response does not represent the load response of the culvert. Local bending and stress concentration play a more decisive role in determination of the stress distribution around the bolt hole.
3. Because the end of the rib and the connection to the footer create a region of high local stresses, box-culvert design would be improved by extending the rib into the footer.
4. Because strains perpendicular to the corrugations are frequently larger than the circumferential strains, accurate stress determination depends on recording strains in both directions.
5. Field measurements are consistent with analysis by the finite-element computer program CANDE. However, CANDE cannot calculate local stress concentration around bolted connections.

ACKNOWLEDGMENTS

The authors appreciate the cooperation and financial support of the Federal Highway Administration, U.S. Department of Transportation, and the Ohio Department of Transportation.

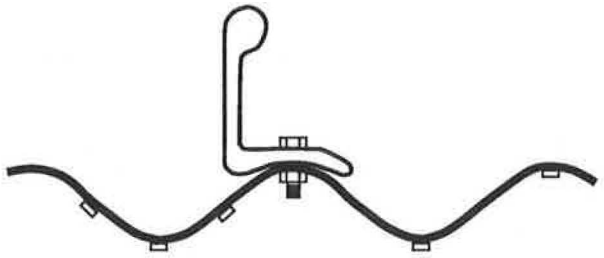

i.Circumferential Stresses

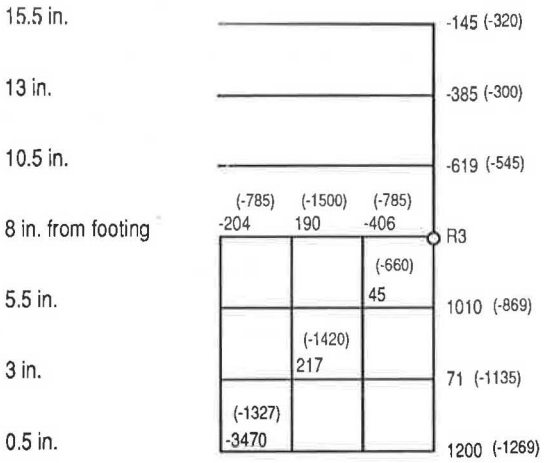

ii. Longitudinal Stresses

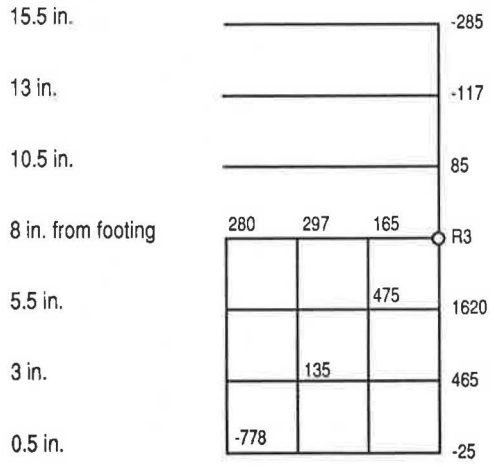

FIGURE 15 Circumferential and longitudinal stresses in rosette Group Three, with 42-kip live load at center position (CANDE).

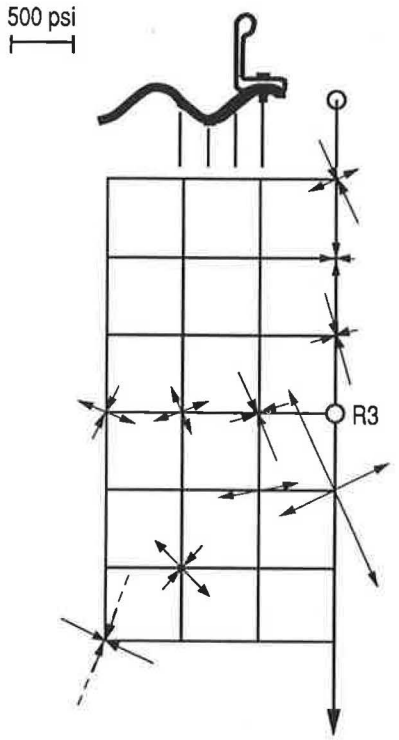

FIGURE 16 Principal stresses in rosette Group Three, with 42-kip live load at center position.

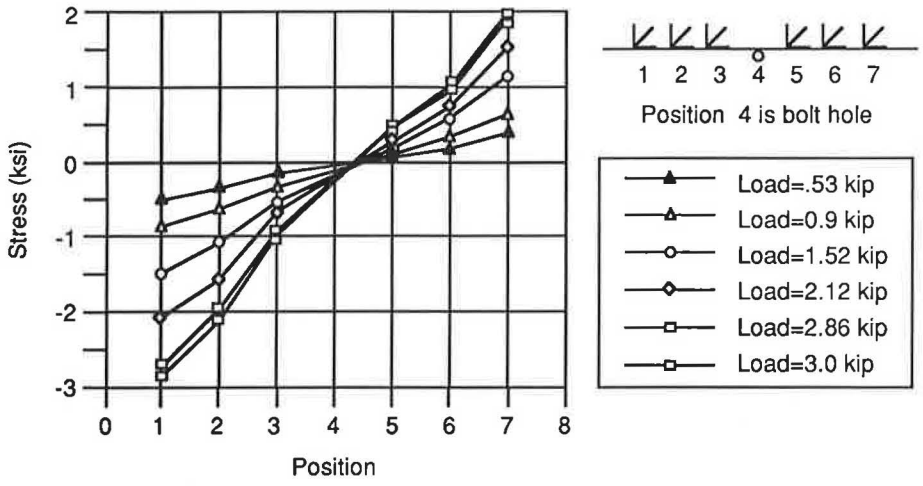

FIGURE 17 Rosette stresses lined up with bolt hole along corrugation direction for no-rib center load.

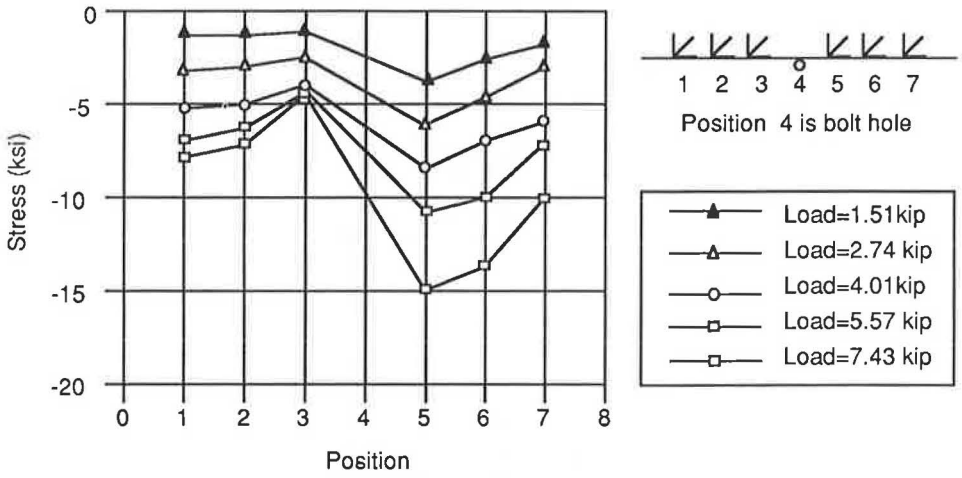

FIGURE 18 Rosette stresses lined up with bolt hole along corrugation direction for one-rib center load.

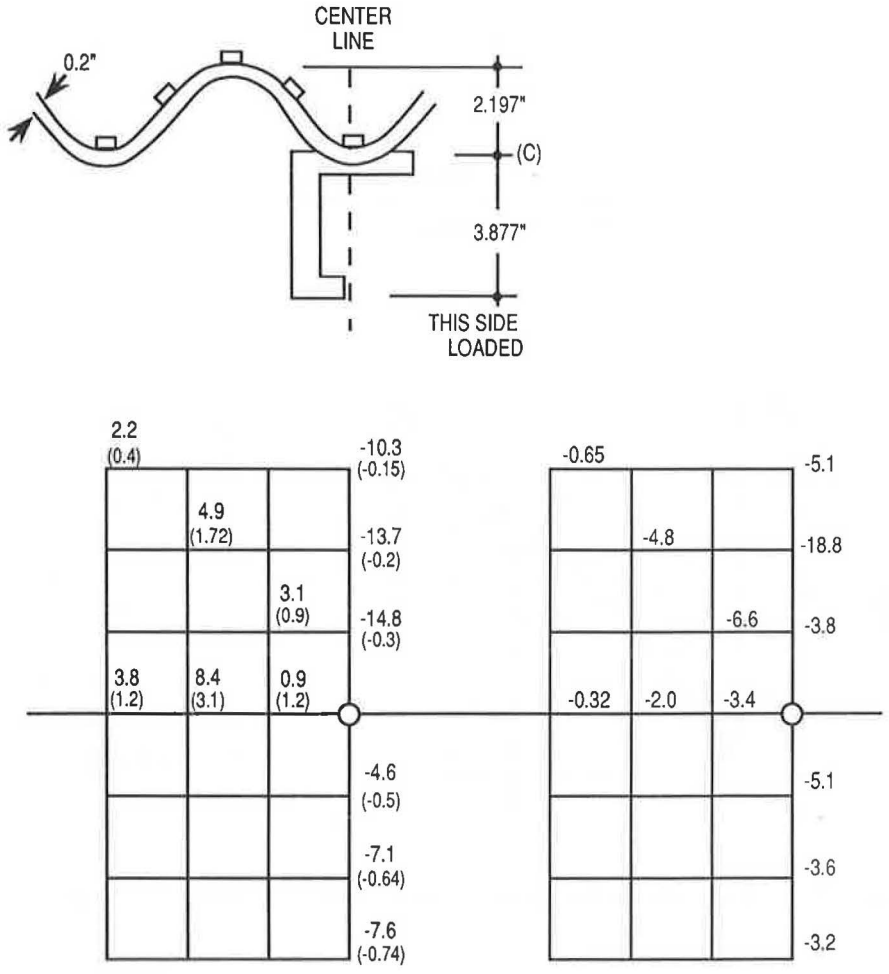

FIGURE 19 Circumferential and perpendicular stresses in rosette group located between Sections 3 and 4 with concentrated load, one rib, and at 7.43 kips.

REFERENCES

1. J. M. Duncan. Behavior and Design of Long-Span Metal Culverts. *Journal of the Geotechnical Engineering Section*, ASCE, Vol. 105, No. GTS, March 1979, pp. 399–418.
2. J. M. Duncan. *Field Instrumentation Study of an Aluminum Box Culvert Structure*. Report UCB/GT/82-09, Department of Civil Engineering, University of California, Berkeley, March 1982.
3. D. B. Beal. *Behavior of a Corrugated Metal Box Culvert*. Final Report on Research Project No. 183-1. Engineering Research and Development Bureau, New York State Department of Transportation, Albany, Nov. 1986.
4. D. B. Beal. *Behavior of an Aluminum Structural Plate Culvert*. Research Report 90. Engineering Research and Development Bureau, New York State Department of Transportation, Albany, June 1981.
5. The Aluminum Association, *Aluminum Standards and Data, 1982*. Washington, D.C., 1982.

Publication of this paper sponsored by Committee on Subsurface Soil-Structure Interaction.

Validation of Correlations Between a Number of Penetration Tests and In Situ California Bearing Ratio Tests

MOSHE LIVNEH

Previous papers have presented correlations among the dynamic cone penetrometer, the dynamic probing Type A, the standard penetration test, and the in situ California bearing ratio (CBR) test. As is known, these penetration tests are intended to determine, among other things, the bearing capacity of subgrades or of existing pavements without requiring the digging of test pits. This paper presents validation for these correlations as recently tested in four bearing capacity evaluations of subgrades and pavements on existing Israeli roads and airport runways. The analysis was made possible by simultaneously carrying out the above penetration tests in combination with the in situ CBR test after test pits had been dug. Results indicate that the existing correlations are valid for translating the values of the above penetration tests into in situ CBR values. In addition, the above investigations indicated the following: (a) the layer thicknesses obtained by means of the penetration tests plausibly correspond to the thickness obtained in the test pits, and (b) the friction that develops during penetration, or the effect due to the overburden pressure, does not significantly influence the final results. Finally, it should be noted that the experience that has accumulated until now regarding an evaluation method based entirely on the above penetration tests proves the feasibility of the method for regular use in other evaluation projects.

Previous papers (*1–5*) have presented correlations among the dynamic cone penetrometer (DCP), the dynamic probing Type A (DPA), the standard penetration test (SPT), and the in situ California bearing ratio (CBR) test.

These penetration tests are intended to determine, among other things, the bearing capacity of subgrades or of existing pavements without requiring the digging of test pits. Their ability to do away with test pits is their greatest advantage, reducing costs and minimizing traffic disturbances. Practically, these tests can be termed semi-nondestructive (semi-NDT) tests. Moreover, the direct in situ CBR test occasionally leads to considerable scatter of results, sometimes as high as a coefficient of variation of 60 percent (*4*, *10*), leading to diminished predictive power. Therefore, in such cases, the above penetration tests are preferable, because their coefficient of variation is usually lower (*4*, *10*).

Naturally, the correlative equations used to calculate the CBR value from the above test results are empirical ones, the validity of which must occasionally be tested. This paper presents validation of these correlations as recently tested in four investigations of subgrade and pavement bearing capacity on existing Israeli roads and airport runways. The analysis for this validation was made possible by simultaneously carrying out the above penetration tests and the direct in situ CBR tests after test pits had been dug. It was also possible to determine the subgrade DCP values by means of two methods: (1) the conventional method (i.e., penetration through the structural layers after drilling the asphalt core) and (2) inside the test pit, with penetration of the subgrade only. It thus became possible to determine the influence of friction development, or, alternatively, of the layer overburden pressure on the results.

In addition to examining the above correlations for use in calculating CBR values, it is also possible to compare the structural thickness values obtained by means of the penetration tests with those obtained through digging test pits.

Finally, the validation described in this paper is aimed at contributing to the issue of the applicability of the above penetration tests to subgrade and pavement evaluation—work whose practical value has been recently shown in Israel in a number of important site investigations, both in airfields and on urban roads.

DCP TEST

The DCP test is described in a number of works [e.g., a report by Kleyn (*6*)] and is therefore not included here. At the same time, the Israeli transformation equation from DCP to CBR values is slightly different from those presented in the technical literature (*3*, *4*), and its expression for a 30° angle is

$$\log \text{CBR} = 2.20 - 0.71 (\log \text{DCP})^{1.5} \quad (1)$$

where DCP is the ratio between the depth of penetration in millimeters and the number of blows required to achieve such penetration, and CBR is the material's CBR in percent, corresponding to the depth of DCP penetration.

The above expression and other expressions have been compared in the technical literature (*3*, *4*). This comparison indicates the plausible validity of Equation 1. Recently, however, an additional correlation obtained from field and laboratory studies has been published (*7*, *8*), and an additional comparison with it is warranted. This correlation for a 60° cone angle is

$$\log \text{CBR} = 2.81 - 1.32 (\log \text{DCP}) \quad (2)$$

Table 1 presents the required comparisons for a number of

Transportation Research Institute, Technion-Israel Institute of Technology, Haifa, Israel.

typical DCP values. Table 1 also indicates that Equation 1 leads to CBR values that are approximately 15 percent higher than those obtained by means of Equation 2, for DCP values of approximately 15 mm/blow and upward. This increase stems from the fact, mentioned before, that the cone head angle is 30° in the test that leads to Equation 1 and 60° in the test that leads to Equation 2. The difference between the above two penetrometers, as obtained in a special investigation designed to assess it (*6*), was indeed of a similar order of magnitude. In addition, it is important to note that the advantage of Equation 1 is in the lower range of DCP values, where the CBR values calculated by means of this equation are more plausible than those calculated by means of Equation 2.

TABLE 1 COMPARISON OF CALCULATED CBR VALUES

DCP (mm/blow)	CBR (%)	
	Equation 1	Equation 2
100	1.6	1.5
50	4.2	3.7
25	10.6	9.2
15	19.7	18.1
10	30.9	30.9
5	61.0	77.2
1	158.5	645.7

SPT TEST

The SPT test is commonly used in site investigations for building foundations. The easy availability of this test makes it useful in determining pavement bearing capacity as well, especially in those cases where penetration by means of the DCP is difficult, or in cases where pavement thickness exceeds 800 mm (the maximum thickness at which the DCP test can be applied).

The equation for transforming SPT values into CBR values was presented by Livneh and Ishai in 1987 (*2*) and was then improved in 1988 (*5*). Now, after additional field data have been gathered, it is possible to determine the following recommended expression:

$$\log \text{CBR} = -5.13 + 6.55 (\log \text{SPT})^{-0.26}$$

$$N = 19$$

$$R^2 = 0.955 \qquad (3)$$

where SPT is the relationship between the depth of penetration in millimeters (300 mm) and the number of blows required for such penetration.

A description of the above equation and the results of the field tests are presented in Figure 1. The data in Figure 1 were used to formulate Equation 3. Finally, it is important to mention here that the applicability of this test is in the SPT

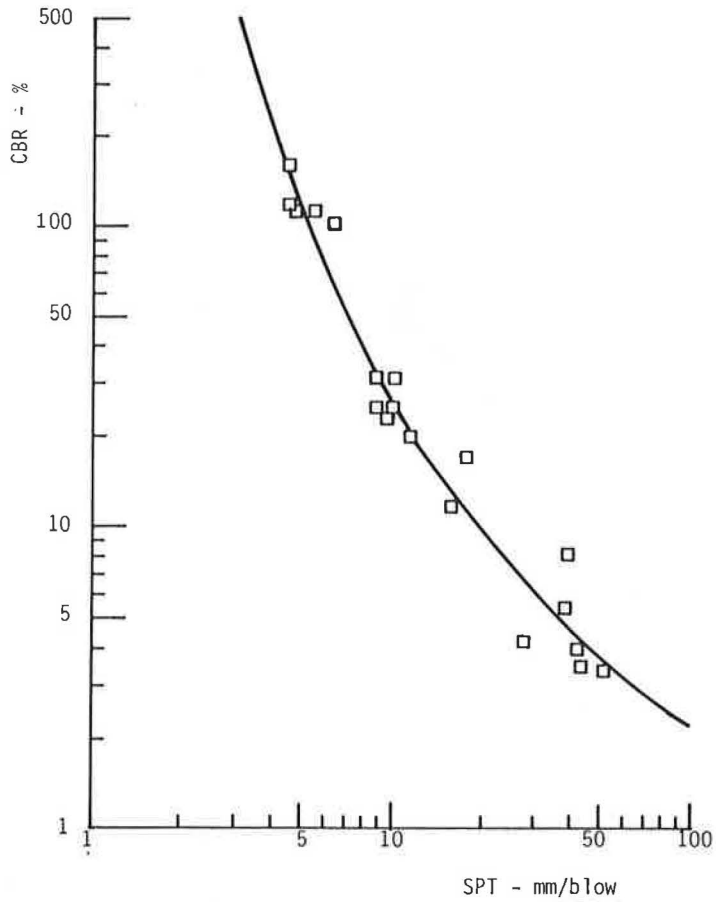

FIGURE 1 Relationship between calculated CBR from SPT-test and direct in situ CBR test.

range, corresponding to CBR ranges from approximately 15 percent to very high values.

DPA TEST

The DPA test is also used in site investigations for building foundations. A description of this test is presented by Bergdahl (*9*), and the recommended (*5*) transformation equation is

$$\log \text{CBR} = 2.20 - 0.45\,[\log (3.47 \times \text{DPA})]^{1.5} \quad (4)$$

where DPA is the relationship between the depth of penetration in millimeters (200 mm) and the number of blows required for such penetration.

It is important to note that the applicability of this test is in the DPA range corresponding to the CBR range from very low values up to approximately 20 percent (*5*). Its obvious advantage lies in the fact that it also allows determination of subgrade strength in existing pavements of great thickness (for example, in airfield pavement structures).

TESTING FOR CORRELATION VALIDATION

Mahanaim Airfield

In an investigation of a runway for light aircraft, which was conducted at the Northern Israeli Mahanaim Airfield, all of the above penetration tests were carried out in combination with the direct in situ CBR test after test pits had been dug in the existing pavement. The subgrade of this runway consists of clay mixed with fine gravel, and some measure of scatter is therefore expected in its characteristics. Its AASHTO classification is A-7-6 with a liquid limit of up to 70 percent.

The CBR results obtained in the direct test, with a surcharge of 409 N (90 lb), are compared with the CBR results computed from the various penetration test values using Equations 1, 3, and 4. This comparison is presented in Figure 2. It should be mentioned in this context that the CBR values appearing in Figure 2 were calculated from the DCP values and include both the DCP test conducted on the pavement surface after drilling asphalt cores and the DCP test conducted inside the test pits. Figure 2 indicates that the results of all

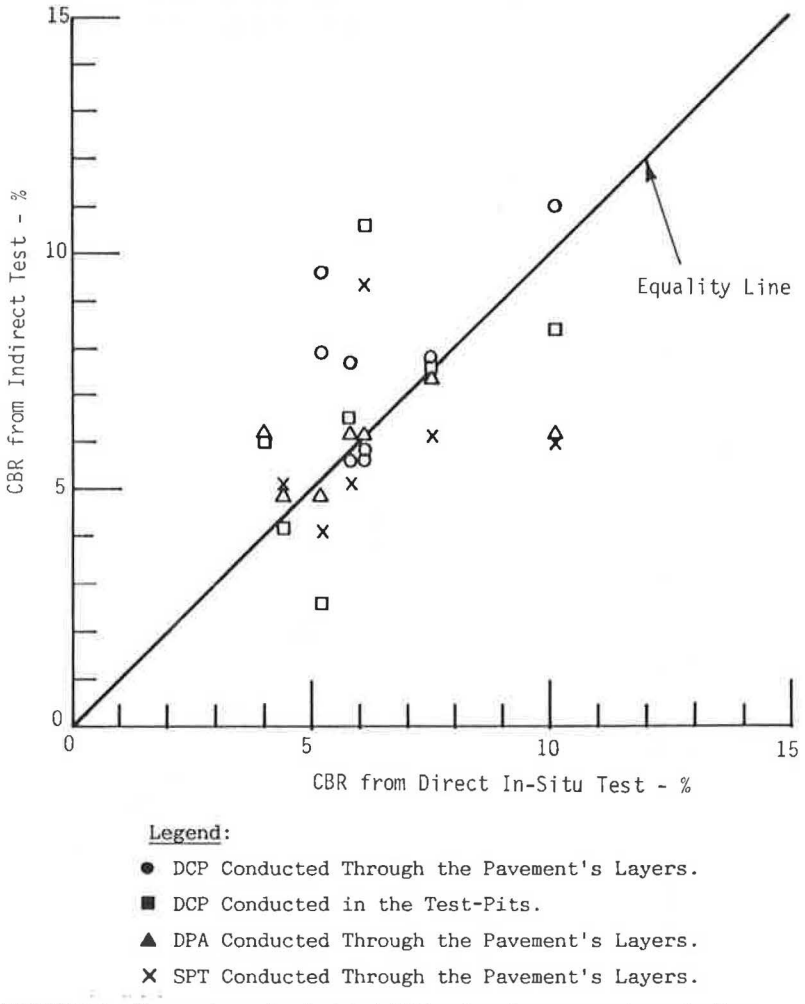

FIGURE 2 Comparison of calculated CBR values from several penetration tests and direct in situ CBR values: Mahanaim Airfield.

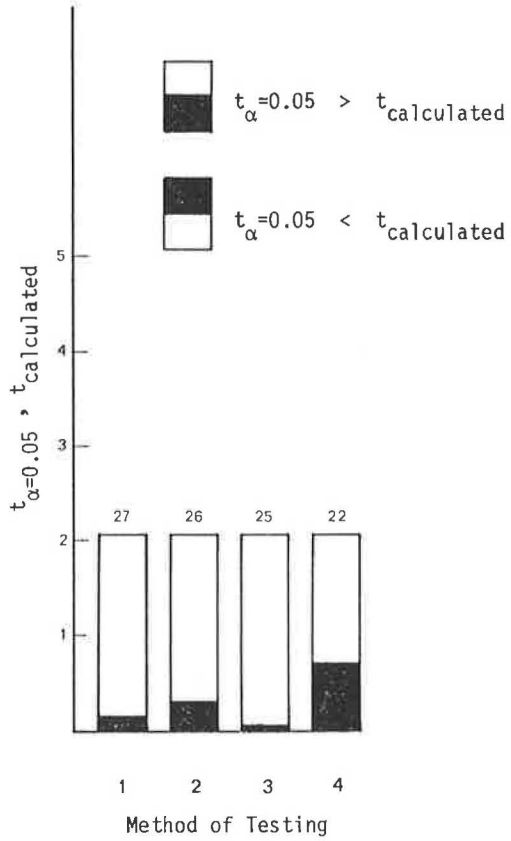

Legend:

1. DPA Conducted Through the Pavement's Layers.
2. DCP Conducted in the Test-Pits.
3. DCP Conducted Through the Pavement's Layers.
4. SPT Conducted Through the Pavement's Layers.

FIGURE 3 Statistical *t*-test for various penetration test results: Mahanaim Airfield. (Numbers denote degrees of freedom.)

the tests range above and below the equality line in a certain scatter, which probably stems from the natural scatter of the subgrade's characteristics. To examine this scatter, a statistical *t*-test was conducted to determine the identity or nonidentity of the various test populations. The results of this test (presented in Figure 3) indicate that it is actually possible to state, at a level of reliability of $\alpha = 0.05$, that the results population of the direct in situ CBR test is identical to the results populations of the Livneh DCP, SPT, or DPA tests.

Thus, this work has proven the validity of the above correlative equations. It should be noted in this context that the coefficient of variation obtained for the direct in situ CBR test in the test pits ranged between 5 percent and 47 percent—the upper value being a high significant value as stated in the beginning of this paper.

In addition to the above comparison, Figure 4 compares the DCP tests conducted inside the test pits and the DCP tests conducted through the structural layers of the existing pavement. Here too, the results have been found to scatter above and below the line of equality, indicating that (a) the friction developing during penetration or alternatively the effects of the overburden pressure do not constitute the only cause and (b) the natural scatter of the subgrade's characteristics also contributes its part to the difference in results. Ultimately, Figure 3, again, indicates that the results populations of the above two DCP tests do not differ statistically from the results population of the direct in situ CBR test.

Finally, it is interesting to compare the thickness of the pavement obtained in the test pits with that obtained through the analysis of the DCP test results. The thickness of the pavement obtained in the test pits was approximately 300 mm, and the DCP tests showed this thickness to range between 260 and 340 mm, with an average of 310 mm and a coefficient of variation of 12.5 percent. These results indicate the capacity of the DCP test to determine the thickness of the structural layers at an acceptable level of reliability.

Ben-Gurion Airport

In recent works of subgrade investigation, which had been carried out for purposes of designing a runway pavement for heavy aircraft at the Ben-Gurion Airport, all of the tests discussed in the preceding section were used, except for the SPT test. The in-situ CBR tests of the subgrade, which is a heavy clay subgrade (A-7-6) with a liquid limit of up to 75 percent, were carried out in test pits every half meter of depth, up to a total depth of 1.5 meters. These test pits made it possible to determine the in-situ CBR at a given depth from two DCP test measurements. One DCP measurement was taken at a level approximating the required depth (first reading) and the second measurement was taken 0.5 meter deeper than the first (second reading). Figure 5 demonstrates the variation of the results with the depth and illustrates the significance of the first and second readings.

Table 2 compares the various test results. The significance of the difference between the average values is examined by means of the statistical *t*-test. The results of the *t*-test are presented in Figures 6 and 7. According to this test, the result populations of the DPA and DCP tests are identical at any depth, apart from those DCP results that are correlated with first and second readings (all readings) or with second readings only, both for the 0.5 meter depth. In other words, at the depth of 0.5 meter, only the DCP population of the first readings is identical to the CBR population. The reason for this unique deviation in DCP results at a depth of 0.5 meter, as compared to other depths, is unclear. Yet, this deviation as compared to the other good results is insufficient in itself to alter the correlation between DCP and CBR values. Here too, the direct in situ CBR values were found to scatter greatly, starting from a coefficient of variation of 2 percent in one pit and up to 54 percent in another pit, values that might constitute the reason for the above phenomenon. Additionally, the *t*-test analysis (Figure 8), also indicates that the population of first DCP readings is identical to the population of second DCP readings. (See the scatter below and above the equality line in Figure 9.) Thus, here too, it can be shown that the friction that is developed during penetration, or alternatively, the effect of the overburden pressure, is not a significant factor.

In addition to evaluating the above subgrade, a bearing-

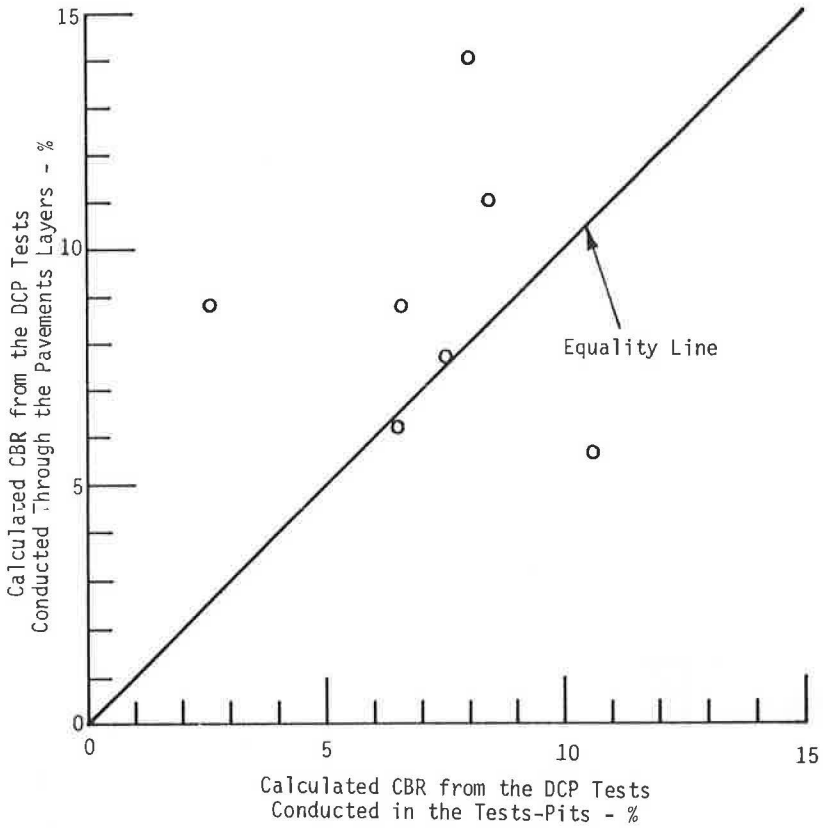

FIGURE 4 Comparison between DCP test conducted through pavement layers and DCP test conducted in test pits: Mahanaim Airfield. (CBR values are for subgrade.)

capacity evaluation of the structure of an existing pavement was also recently carried out at the Ben-Gurion Airport. Because field operating conditions made it impossible to dig test pits, only penetration tests were carried out in the pavement structure and its subgrade; vane shear tests were carried out also, in the subgrade only, of course. Translation of the vane shear strength values, S, calculated from the vane shear test results into CBR values, was carried out by means of the following expression:

$$\text{CBR} = 4.79 \times S^{0.63} \quad (5)$$

where S is the vane shear strength, expressed in kg/cm^2, and CBR is the corresponding CBR value, expressed in percentages.

The above expression is the product of a correlation study that was conducted simultaneously during previous projects at the Ben-Gurion Airport. Figure 10 presents an example of results obtained from that work. Here too, it was shown, by means of the statistical t-test, that the result populations of the DPA and the SPT tests do not differ, despite the scatter that can be seen in Figure 11. Moreover, the calculated CBR values that were obtained from these tests correspond with those obtained in the direct in-situ CBR tests that had been carried out in two test pits about two years before the present investigation. It should be noted that this latter comparison is the only one that refers to testing not done at the same time.

Finally, it is important to note that an appropriate correlation has also been found between the thicknesses of the structure as obtained through analysis of the DPA test and the thicknesses obtained through drilling for the SPT tests. These thicknesses also correspond to those obtained from the two test pits that had been dug two years earlier.

Road No. 34

A study was recently carried out to assess the pavement bearing capacity of an urban road, Road No. 34. The pavement of this road is mainly based on silty soil with medium to very high strength. Its thickness was found to average approximately 60 cm. Direct in situ CBR and DCP tests were carried out in five test pits on this pavement. In addition, near the test pits, five DCP tests were conducted on the base-course surface following drilling of asphalt cores. Comparative CBR results are presented in Figure 12. As can be seen in Figure 12, a scatter exists between the direct in situ CBR values and the calculated CBR values. However, in light of the experience gained in the preceding work described in this paper, this scatter is still within the boundaries of identity between the two results populations. In contrast to Figure 12, Figure 13 compares the CBR values calculated from the DCP tests for two cases: the test conducted inside the test pit and the test conducted beside the test pit. Here too, results are

TABLE 2 COMPARISON OF CBR RESULTS DERIVED FROM VARIOUS TESTS

Depth in meters	Value	CBR in % Calculated From the Following Tests				
		CBR	DPA	DCP	DCP 1st Readings	DCP 2nd Readings
0	$\bar{x}$	6.14	8.86	6.80	6.80	-
	σ	4.05	4.17	3.45	3.45	-
	n	14	5	11	11	-
	c.v.	0.66	0.47	0.51	0.51	-
0.5	$\bar{x}$	12.10	10.50	16.50	14.90	17.37
	σ	4.82	2.76	5.46	4.29	6.02
	n	14	5	17	6	11
	c.v.	0.40	0.26	0.33	0.29	0.35
1.0	$\bar{x}$	11.02	10.32	13.01	12.96	13.05
	σ	2.11	2.61	3.06	3.75	2.73
	n	11	5	11	5	6
	c.v.	0.21	0.25	0.24	0.29	0.21
1.5	$\bar{x}$	8.39	10.92	11.06	7.88	14.24
	σ	3.62	3.96	7.90	3.23	10.23
	n	10	5	10	5	5
	c.v.	0.42	0.36	0.71	0.41	0.72

Legend:

$\bar{x}$ - Average value. n - Number of readings.

σ - Standard deviation. c.v. - Coefficient of variation.

scattered considerably, yet the main feature of the scatter is the considerable heterogeneity of the subgrade.

Finally, Figure 14 compares the pavement thicknesses obtained from both test pits and DCP tests. Here too, the scatter is considerable, but essentially stems from the heterogeneity of the structural thickness. It is worthwhile noting that this thickness, according to the test pits, ranges between approximately 30 cm and 70 cm; and the above scatter is, therefore, only natural. Obviously, this fact also influences the decoding of the NDT tests.

SUMMARY AND CONCLUSIONS

This paper has attempted to validate empirical correlations among direct in situ CBR tests and three penetration tests (DCP, SPT, and DPA) with respect to determining the bearing capacity of subgrades and existing pavements in roadways and airport runways. After analyses of four studies recently carried out in Israel, the following three primary conclusions were reached:

1. The correlative transformation from DCP, SPT, or DPA values to direct CBR values can be used with plausible reliability. The equations of these transformations (Equations 1, 3, and 4) are presented in this paper, and it is not necessary to modify them.
2. The effect of friction or alternatively the effect of overburden pressure on the results of DCP tests is negligible. This is expressed in the reasonable correspondence that exists between the DCP results of the first readings (a test conducted on the base-course surface of the pavement following the

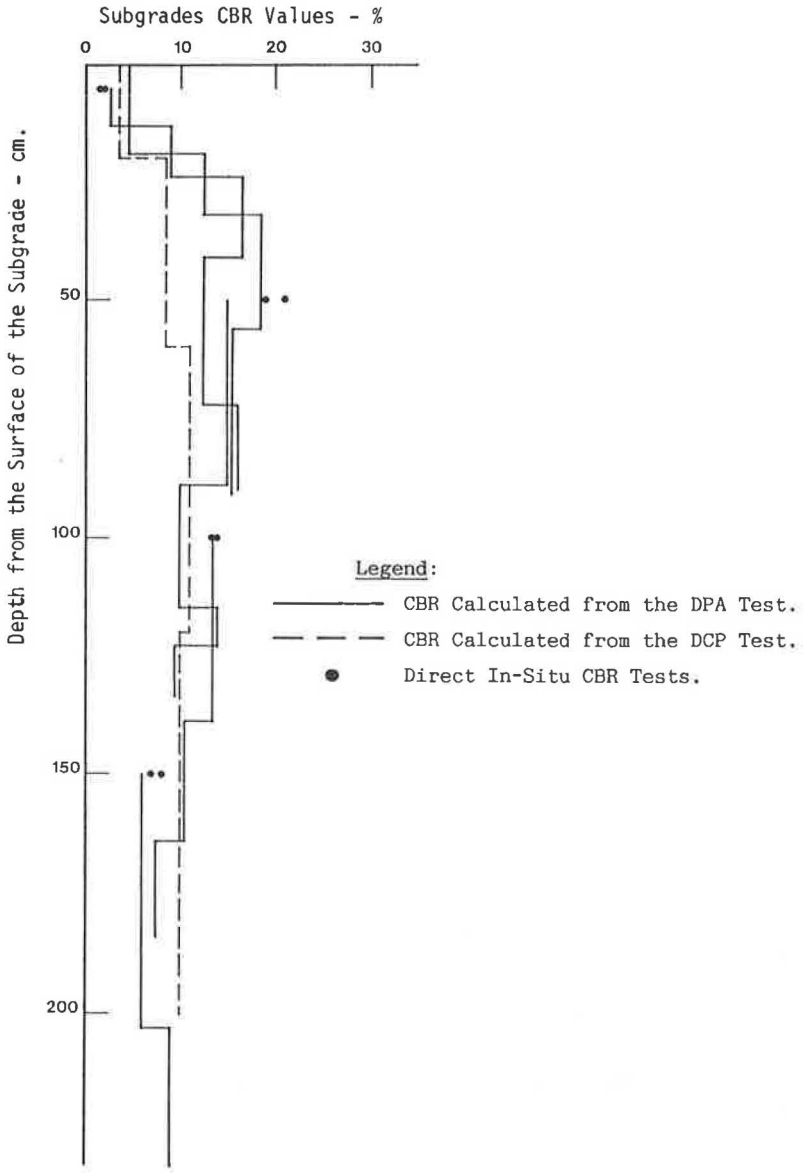

FIGURE 5 CBR distribution with depth as derived through various tests: Taxiway Y, Ben-Gurion Airport.

drilling of an asphalt core) and the DCP results of the second readings (a test conducted on the surface of the subgrade in the test pit). Similar findings have been obtained for tests carried out in pits dug in the subgrade only.

3. There is a plausible correlation between the thickness of the pavement as obtained through test pit measurements and the thickness of the pavement obtained through decoding the results of the various penetration tests.

Finally, it is important to emphasize that the DCP test permits determining the in situ CBR value of materials with any range of strength but to a limited depth of 80 cm. In contrast, the DPA test permits determining the in situ CBR of materials with a medium to low range of strength but to a greater depth. Owing to the strength limitation, this test cannot always be carried out from the existing pavement's base course; and it is therefore necessary to drill vertically through the structural layers until the DPA cone achieves the depth at which the strength values of the structural layers are appropriate to the test's ability. Similarly, the SPT test is not limited in depth but always necessitates vertical drilling. It is applicable to materials with a strength range of medium to high.

In summary, it can be stated that the in situ practical work with the above penetration tests and without digging test pits in order to determine the direct in situ CBR values has proved itself to be more efficient and faster. It is therefore recommended that this method of assessing bearing capacity of subgrades and pavements, as recently expressed in the assessment of a taxiway at the Ben-Gurion Airport, also be adopted for other evaluations.

Finally, it should be emphasized that differences in geographic areas throughout the world may lead to changes in the empirical equations presented in the paper, although the method shown here is most likely to be applicable everywhere.

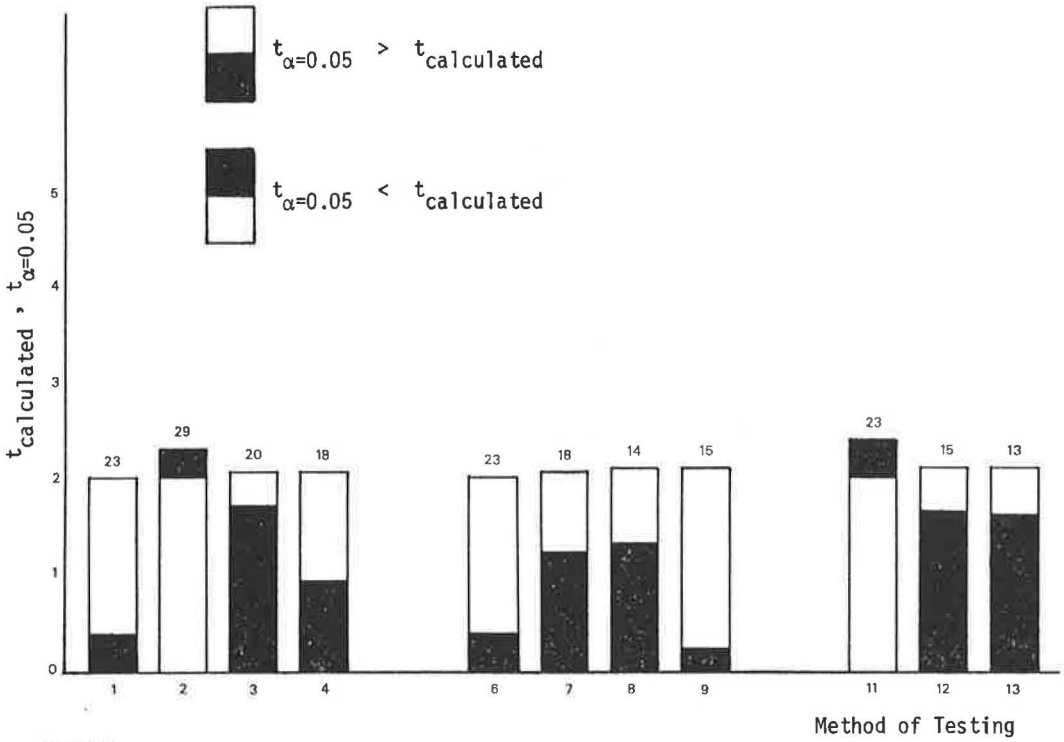

Legend:

CBR From the DCP Test (All Readings)	CBR From the DCP Test (First Readings Only)	CBR From the DCP Test (Second Readings Only)
1. Depth of 0.0 meters	6. Depth of 0.0 meters	11. Depth of 0.5 meters
2. Depth of 0.5 meters	7. Depth of 0.5 meters	12. Depth of 1.0 meters
3. Depth of 1.0 meters	8. Depth of 1.0 meters	13. Depth of 1.5 meters
4. Depth of 1.5 meters	9. Depth of 1.5 meters	

FIGURE 6 Statistical *t*-test for direct in situ CBR versus DCP test: Taxiway Y, Ben-Gurion Airport. (Numbers denote degrees of freedom.)

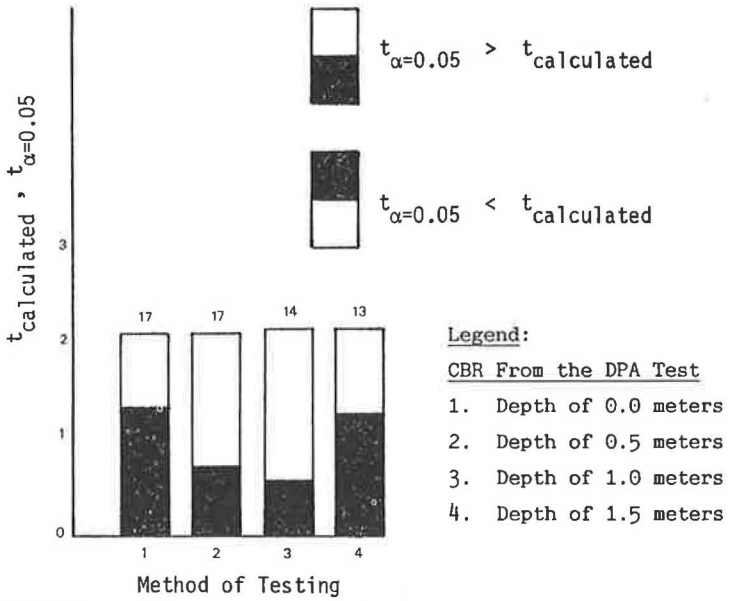

Legend:

CBR From the DPA Test

1. Depth of 0.0 meters
2. Depth of 0.5 meters
3. Depth of 1.0 meters
4. Depth of 1.5 meters

FIGURE 7 Statistical *t*-test for direct in situ CBR test versus DPA test: Taxiway Y, Ben-Gurion Airport. (Numbers denote degrees of freedom.)

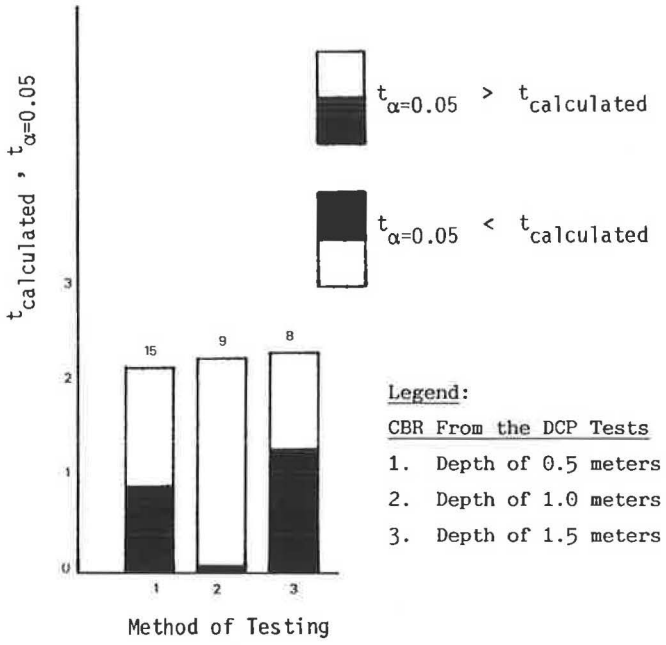

FIGURE 8 Statistical *t*-test for DCP test, first readings versus second readings: Taxiway Y, Ben-Gurion Airport. (Numbers denote degrees of freedom.)

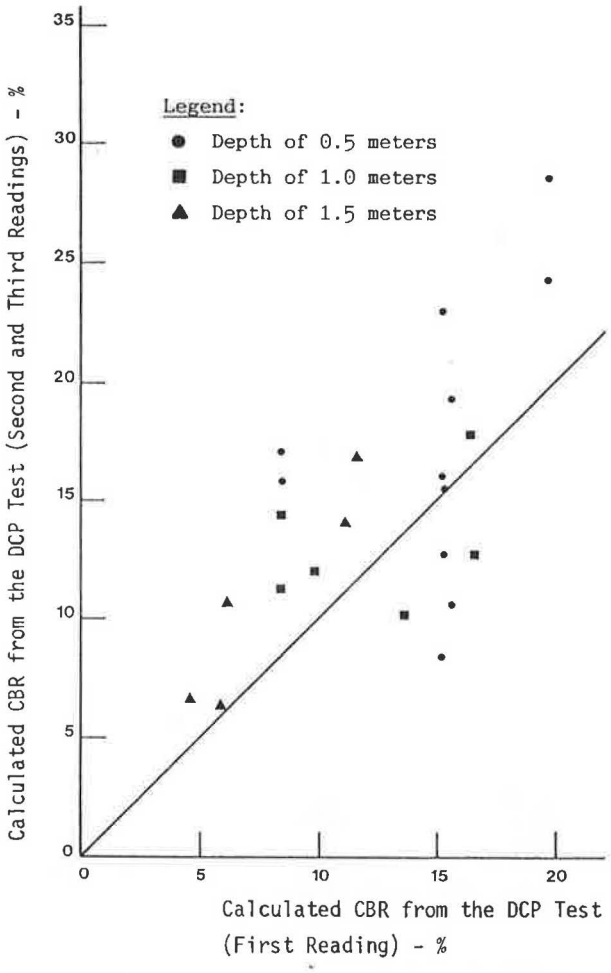

FIGURE 9 Comparison of calculated CBR for DCP tests, first readings versus second and third readings: Taxiway Y, Ben-Gurion Airport.

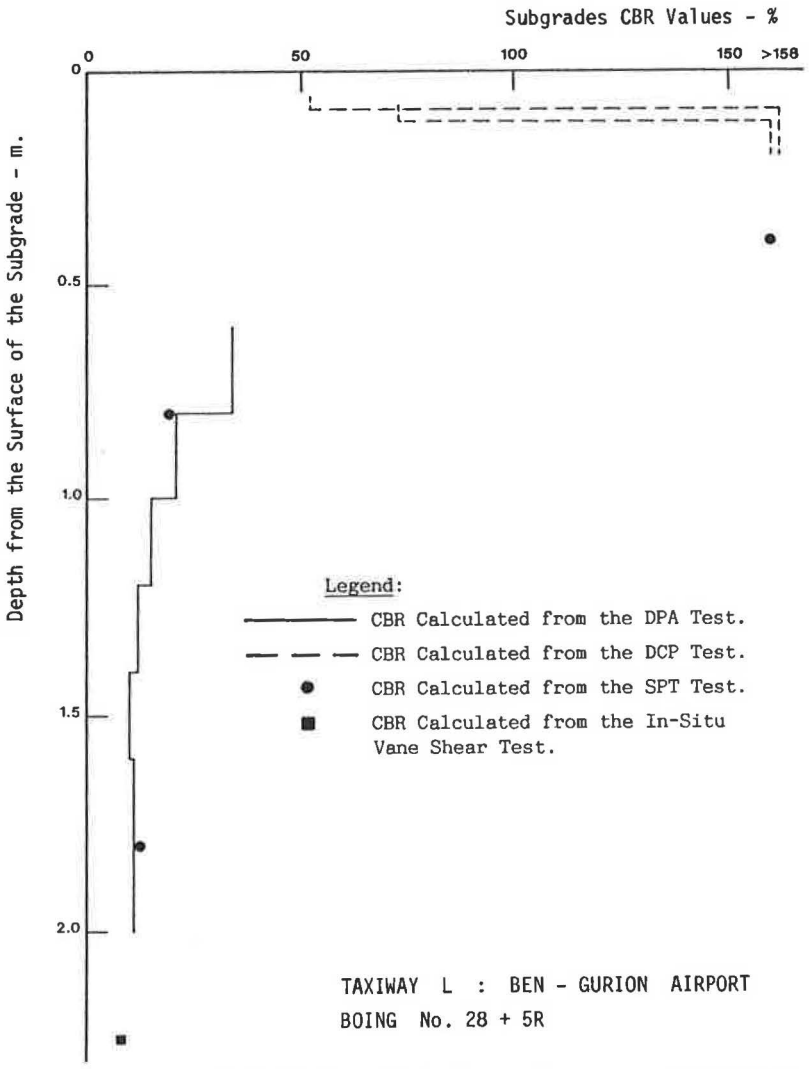

FIGURE 10 Strength distribution with depth according to various penetration and vane shear tests: Taxiway L, Ben-Gurion Airport.

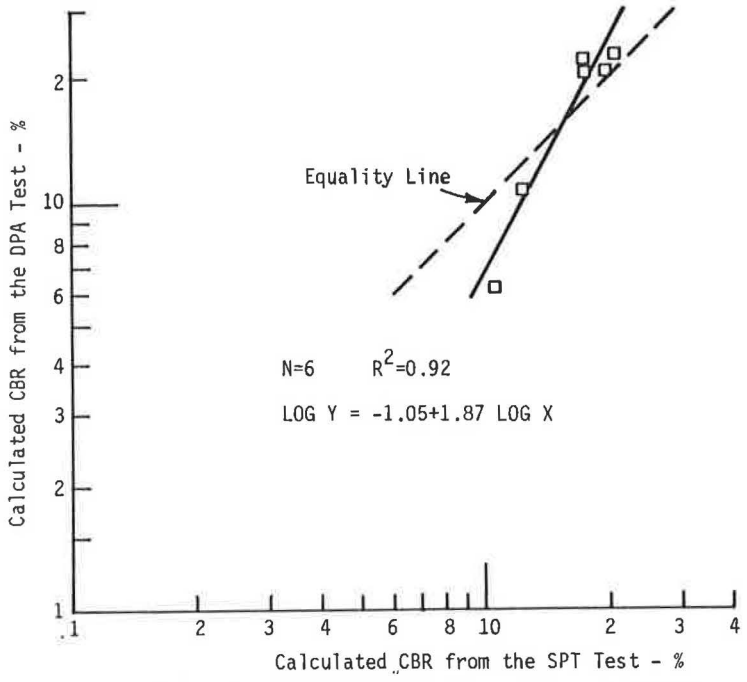

FIGURE 11 Comparison of CBR calculated from DPA and SPT tests.

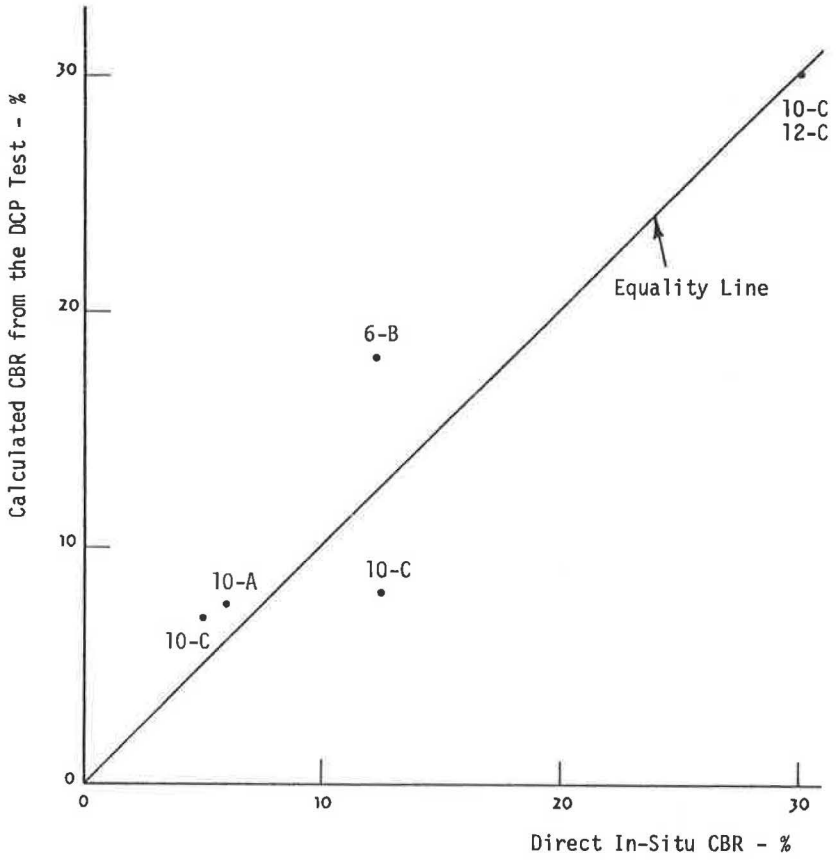

FIGURE 12 Comparison of CBR results derived from direct in situ tests and DCP tests: Road No. 34.

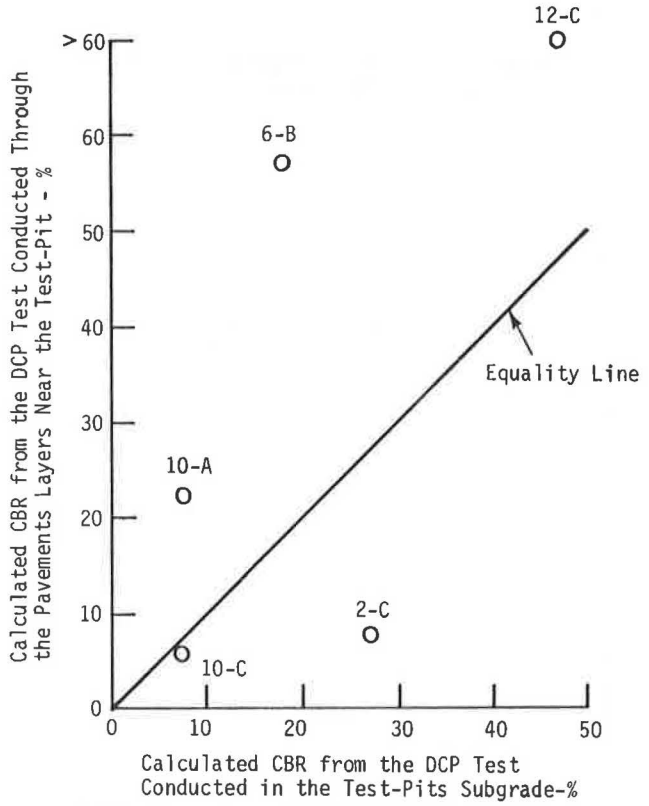

FIGURE 13 Comparison of CBR calculated from DCP tests conducted near test pits and inside test pits: Road No. 34.

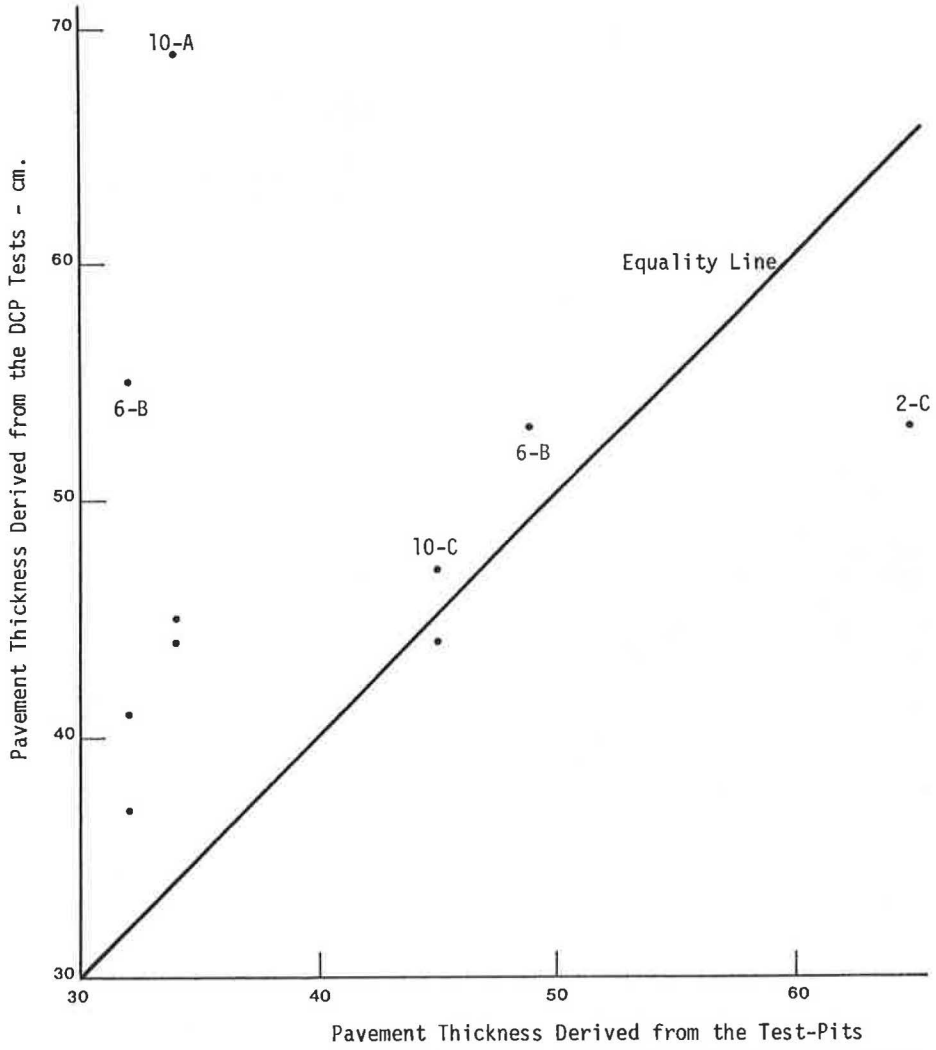

FIGURE 14 Comparison of pavement thickness derived from DCP test and test pits: Road No. 34.

ACKNOWLEDGMENTS

Most of the results of the penetration tests and the direct in situ CBR tests presented in this paper were obtained from work recently carried out for the Israeli Airports Authority, to which thanks are therefore due. Thanks are also due the Israeli Public Works Department for use of the test results obtained for Road No. 34.

REFERENCES

1. M. Livneh and I. Ishai. Pavement and Material Evaluation by a Dynamic Cone Penetrometer. *Proc., 6th International Conference on the Structural Design of Asphalt Pavements*, Ann-Arbor, 1987.
2. M. Livneh and I. Ishai. The Relationship between SPT and In-Situ CBR Values for Subgrades and Pavements in Arid Zones. *Proc., 8th Asian Conference on Soil Mechanics and Foundation Engineering*, Kyoto, 1987.
3. M. Livneh. The Use of Dynamic Cone Penetrometer in Determining the Strength of Existing Pavements and Subgrades. *Proc., 9th Southeast Asian Geotechnical Conference*, Bankok, 1987.
4. M. Livneh. *The Correlation between Dynamic Cone Penetrometer Values (DCP) and CBR Values*, Transportation Research Institute Publication 87-303. Technion-Israel Institute of Technology, Haifa, 1987.
5. M. Livneh and I. Ishai. The Relationship between In-Situ CBR Test and Various Penetration Tests. *Proc., 1st International Symposium on Penetration Testing*, ISOPT-1, Orlando, 1988.
6. E. G. Kleyn. *The Use of the Dynamic Cone Penetrometer (DCP)*. Transvaal Roads Department Report No. L2/74. 1975.
7. J. A. Harison. Correlation between California Bearing Ratio and Dynamic Cone Penetrometer Strength Measurement of Soils. *Proc., Institution of Civil Engineers*, Part 2, Vol. 83, Technical Note No. 463, 1987.
8. J. McElvaney, A. Jayaputra, and J. Harison. Correlation of CBR and Dynamic Cone Strength Measurements of Soils. *Proc., 3rd Indonesian Conference on Geotechnics*, Vol. 1, Jakarta, 1985.
9. V. Bergdahl. *Development of the Dynamic Probing Test Method, Design Parameters in Geotechnical Engineering*. VII ECSMFE, Brighton, 1979.
10. R. B. Smith and D. N. Pratt. A Field Study of In-Situ California Bearing Ratio and Dynamic Penetrometer Testing for Road Subgrade Investigation. *Australian Road Research*, Vol. 13, No. 4, 1983.

Publication of this paper sponsored by Committee on Soil and Rock Properties.

Class C Fly Ash as a Full or Partial Replacement for Portland Cement or Lime

KENNETH L. MCMANIS AND ARA ARMAN

A study was undertaken to evaluate the stabilization or modification of sands and clays using ASTM Class C fly ash as a full or partial replacement for hydraulic cement or hydrated lime. Strength and durability tests demonstrated that the Class C fly ashes of the study could be substituted for cement in some sands. Improvement of the sands was provided by the matrix formed with fly ash acting as a filler and as a cementing agent. The test results indicate the importance of the gradation characteristics of the materials and the effects on matrix quality due to the presence of fines in the natural sands. Also, improvements in the plastic properties and gains in soil support with the addition of fly ash and/or lime were evaluated for two clays. However, test results and analyses demonstrated that the Class C fly ash does not effectively compete as a substitute for lime in the treatment of clays.

Electrical power plants in Louisiana use western coals and are producing ASTM Class C fly ash. In addition to being pozzolanic, many Class C fly ashes have been shown to exhibit cementitious properties similar to portland cement. In recent years, an increasing number of stabilization projects has been performed using Class C fly ash alone (*1*). Class C fly ash with calcium oxide contents of 20 percent or more has reportedly adequately stabilized fine-grained plastic soils, as well as coarse-grained soils, without the use of lime (*1–4*). The objectives of this research were (a) to evaluate ASTM Class C fly ash as a lone or partial replacement for portland cement in sands and lime in clays and (b) to identify the manner in which improvements to the soils occur and the important characteristics of the materials.

TEST METHODOLOGY

The testing program included two sands commonly used in base construction and two clays: a nonplastic A-3-0 sand, a slightly plastic A-2-4 silty sand (liquid limit = 21, plastic index = 7), an A-6(9) silty clay, and an A-7-6(20) clay. Table 1 gives the engineering properties of the natural soils.

Three fly ashes produced in Louisiana's Big Cajun, Nelson, and Rodemacher power plants were included in the testing program. The physical and chemical properties were analyzed according to ASTM C 311 (Table 2). All the fly ashes were ASTM Class C. The calcium oxide content ranged from 21.5 percent to 27.2 percent. A hydrated, high-calcium lime (ASTM Designation C 207, Type N) and a Type I portland cement (AASHTO Designation M85) were used in the study.

A base or subbase material is usually evaluated with respect to its strength and durability. Louisiana Department of Transportation and Development (DOTD) criteria (TR 432-82) were used to evaluate the performance of the sand specimens (i.e., sand plus fly ash alone, sand plus fly ash and lime, sand plus fly ash and cement, and sand plus cement alone). This specification required the minimum cement content to correspond to a strength of 250 psi with a 7-day curing period at a temperature of 73° ± 3° F. The strength and durability of the specimens were tested using ASTM C 593 procedures, except that the curing temperature was modified to agree with DOTD TR 432-82.

Class C fly ash used as a clay modifier was also studied. Both clays were evaluated with respect to changes in their plastic properties, strength index, and curing time. Atterberg limit tests were conducted on the clays to evaluate the effects of the additives on the soil plasticity. *R*-value tests were performed to measure resistance to deformation and change in soil support values.

The standard Proctor (ASTM D 698) procedure was used in molding the mixtures into sets of three specimens. In compacting the specimens, moisture contents were not allowed to vary beyond ±1 percent of optimum; and dry densities were maintained to within ±3 lb of the theoretical dry weight density. Those specimens not meeting these criteria were remolded.

The molded specimens were extruded and cured for 7, 28, and 56 days at a temperature of 73° ± 3° F and at a relative humidity of 90 percent or greater. At the end of each curing period, the mixtures were tested for compressive strength and durability. The average compressive strength of the three specimen groups was used for comparison purposes. The coefficient of variance of the individual group test values was computed and compared as a measure of the relative test dispersion. The coefficient of variance ranged from 5 to 14 percent with an overall value of 9 percent.

DOTD TR 433-81 criteria for lime treatment of soils used in Louisiana highways were used to determine the minimum amount of lime required. This requires that the liquid limit (LL) and plastic index (PI) after lime treatment cannot exceed 40 and 10, respectively, for soils used as a base course and 40 and 15, respectively, when soils are used as a subbase. These criteria were also applied when fly ash was evaluated as a replacement for lime with the clays. Both the A-3 sand and the A-2-4 silty sand met this requirement without treatment.

K. L. McManis, Civil Engineering Department, University of New Orleans, New Orleans, La. 70148. A. Arman, Louisiana Transportation Research Center, Louisiana State University, 4101 Gourrier, Baton Rouge, La. 70804-9245.

TABLE 1 SOIL PROPERTIES

Variable	Soil			
	A-3	A-2-4	A-7-6(20)	A-6(9)
Coarse sand (Ret #40) (%)	40	3	0	1
Fine sand (Ret #200) (%)	52	62	14	3
Clay and colloids (%)	3	17	55	34
Liquid limit (%)	NP	21	60	31
Plastic index (%)	NP	7	40	13
Max. dry wt. den. (pcf)	109.7	119.7	98.8	104.9
Optimum moisture (%)	13.0	12.1	23.1	19.0
R-value			<5	30

NOTE: NP = nonplastic.

TABLE 2 CHEMICAL AND PHYSICAL ANALYSES OF FLY ASHES

Variable	Fly Ash Source		
	Cajun	Rodemacher	Nelson
Retained #325 (%)	9.2–7.6	12.0–11.0	13.9–18.3
Loss on ignition (%)	1.3–0.5	0.5–1.9	0.7–1.0
Total oxides[a] (%)	65.8–66.5	62.3–64.7	51.5–62.9
Calcium oxide (%)	21.5–24.5	27.20–24.0	25.2–25.8
Magnesium oxide (%)	4.4–4.7	4.9–4.5	4.9–2.9
Sulfur trioxide (%)	2.8–2.8	2.7–2.9	3.1–3.3
Alkalies (%)	1.34–0.66	1.49–1.06	1.45–1.74

NOTE: Materials were tested according to ASTM Designation C 311.
[a] $SiO_2 + Al_2O_3 + Fe_2O_3$.

As a measure of performance of the two treated clays in an embankment or subbase, the *R*-value test (resistance value—ASTM D 2844) was used. A few specimen sets were subjected to an *R*-value retest with an additional 7 days to observe any increase that may have occurred.

EVALUATION OF TEST RESULTS WITH SANDS

To satisfy the stated acceptance criteria (250 psi compressive strength with a 7-day cure), the following minimum proportions of stabilizing agents were required with the sands:

Stabilizing Agent	*A-3 Sand (%)*	*A-2-4 Silty Sand*
Fly ash	20–25	None meeting criteria
Lime + fly ash	4–6 lime + 15 fly ash	None meeting criteria
Cement + fly ash	All proportions acceptable except 4 cement + 5 fly ash	All acceptable
Cement	8	All acceptable

The test results were evaluated in an attempt to identify or explain the behavior of the fly ash mixtures.

Moisture Density

The density of the mixture has a major effect on the strength and durability of cement- and lime-fly ash stabilized materials (*5,6*). The curves for maximum dry density and optimum moisture content versus the percent fly ash additive for both sands are shown in Figure 1. All three fly ashes gave similar results. The addition of fly ash to the A-3 sand significantly increased the maximum dry density and decreased the optimum moisture content throughout the range of fly ash percentages tested. The reduction in optimum moisture content is attributed to the spherical shape of the fly ash particles in the sand voids, which lubricates the mix and aids in the densification efforts.

The addition of the fly ash to the A-2-4 silty sand produced a small increase in dry density between 3.3 and 6.9 pcf with the different fly ashes. The maximum density occurred at fly ash percentages of 15 to 20 percent for all three fly ashes. Additional fly ash beyond 20 percent produced a decrease in density. The fly ash percentage corresponding to the maximum density of the A-2-4 silty sand also seemed to coincide with the minimum value of the optimum moisture content.

Other mix combinations of cement plus fly ash and lime plus fly ash with the A-3 sand also produced gains in density. Both lime and cement increased the density at different percentage levels. The resulting increase or decrease varied among the different fly ashes. This was not the case for the A-2-4 silty sand. A decrease in density, below that of the raw soil, occurred with the addition of lime and was attributed to the effects of the fines present.

The aggregate gradation had a significant effect on the density, strength, and durability of the mix (*2,6*). Using Talbot's relationship for computing the ideal gradation necessary for maximum density, a grain size analysis was made for each sand.

$$P = (d/D)^{0.5} \quad (1)$$

where

P = percent finer by weight for grain size,
d = grain size being considered, and
D = maximum grain size.

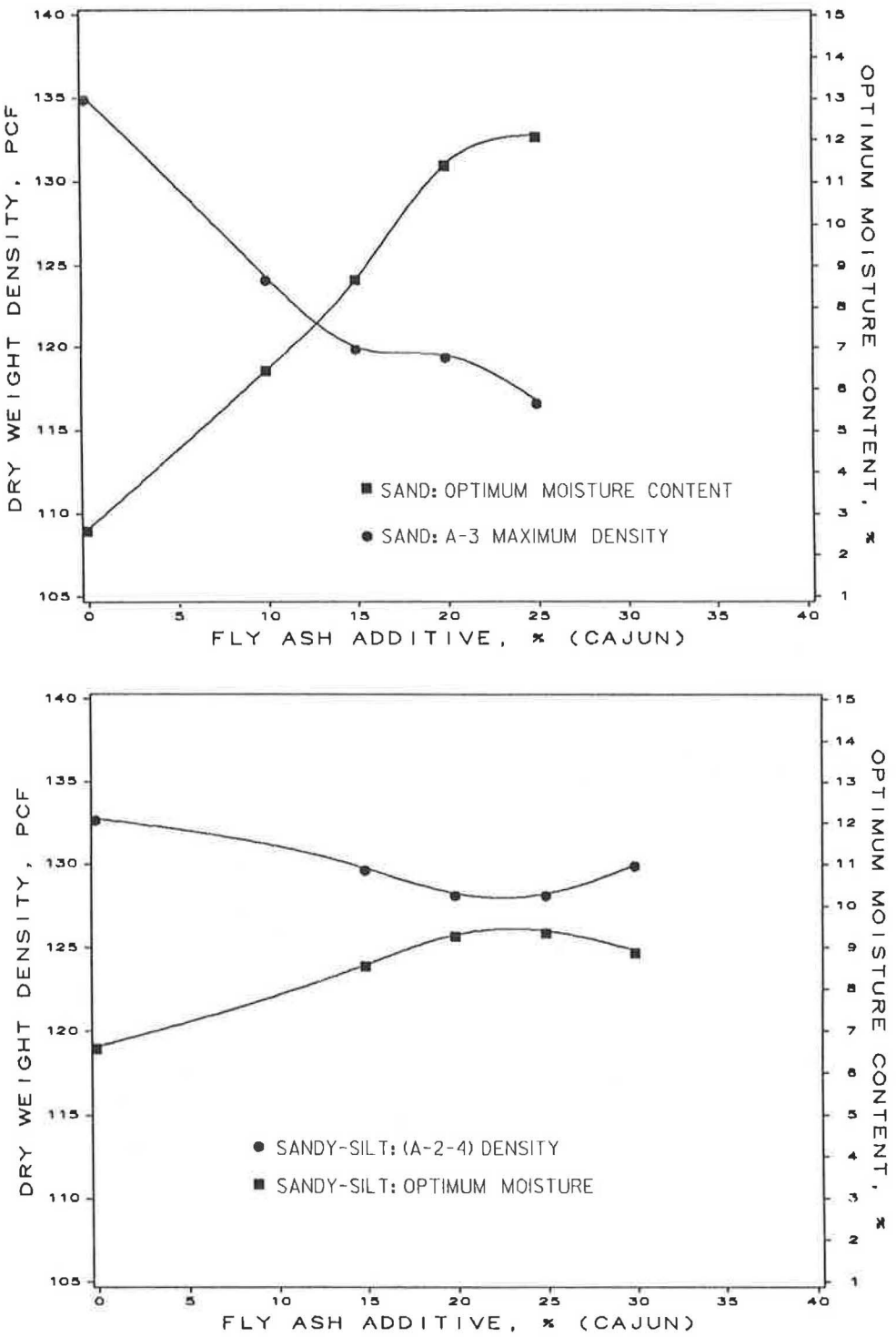

FIGURE 1 Dry density/optimum moisture content versus fly ash additive.

Figure 2 shows the original gradation curves for Rodemacher fly ash, the two sands, and the resulting gradation curves for the soils blended with different percentages of Rodemacher fly ash. Note that the additional fly ash brings the resulting gradation curves closer to the ideal curve for maximum density of the A-3 sand (i.e., maximum density is achieved at 25 percent fly ash). With the absence of fines in the A-3 sand, the addition of the silt-size fly ash fills the voids, providing a matrix for the sand particles. The maximum dry density was increased from 109.1 to 132.8 pcf with 25 percent fly ash.

Figure 2 indicates that the addition of approximately 15 percent fly ash would maximize the dry density of the A-2-4 silty sand compacted with the Rodemacher fly ash. Test results demonstrated that 20 percent fly ash actually provided the maximum dry density. The increase in maximum dry density

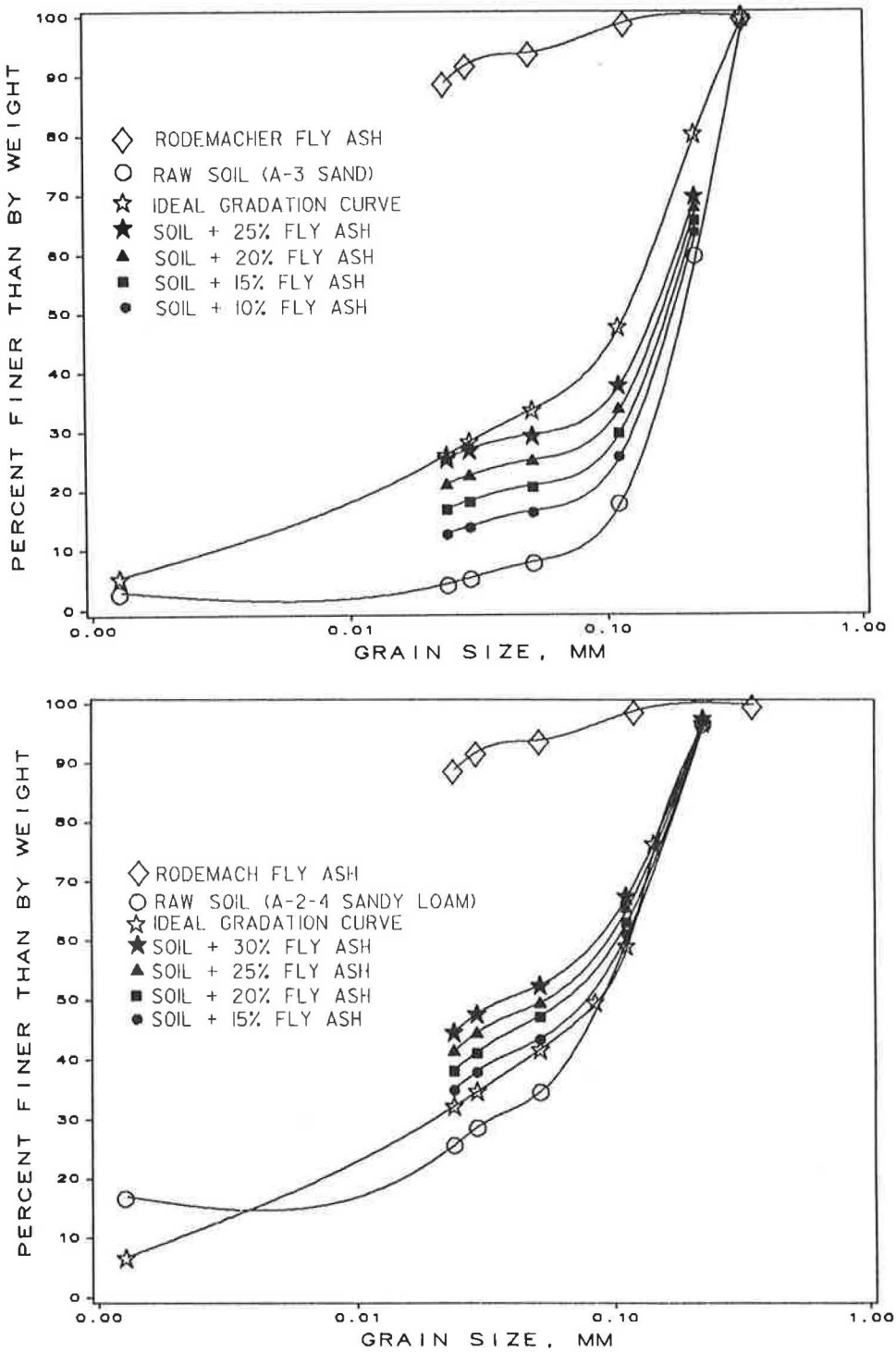

FIGURE 2 Comparison of the gradation curves for the A-3 and A-2-4 sands with and without Rodemacher fly ash.

with the addition of fly ash was modest—increasing from 119.1 pcf to values ranging from 120.5 pcf to 124.8 pcf for the different fly ashes. The A-2-4 silty sand contained 35 percent fines (18 percent silt size and 17 percent clay size) for the natural soil. The addition of 20 percent fly ash to the natural silt and clay constituents of the A-2-4 soil gives 48 percent fines. It would appear that the small gain in density occurs with a suspension of the sand particles in a matrix consisting of a secondary structure of silt and fly ash with clay particles between.

Unconfined Compressive Strength

Strength variation with increasing fly ash reflects the changes observed in density for both of the sands (Figure 3). Large

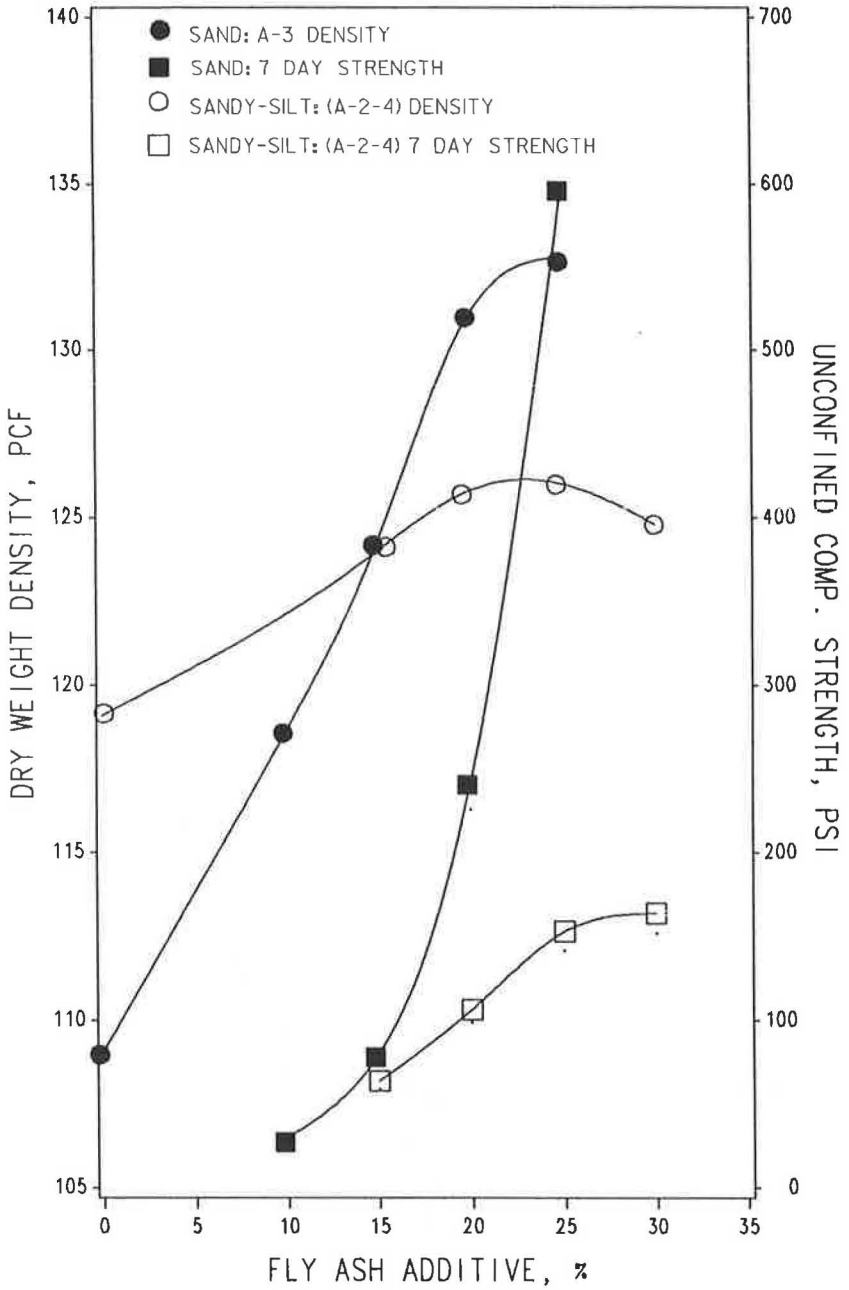

FIGURE 3 Strength/dry density versus percent Cajun fly ash additive.

gains in strengths were developed in the A-3 sand with each increment of increased fly ash. The strength variation of the A-2-4 silty sand with fly ash also paralleled that of its variation in dry density. The fly ashes contained approximately 25 percent calcium oxide (Table 2). Several investigators (*7–10*) have shown that much of the CaO in some Class C fly ash is combined with silicates and aluminates similar to that found in portland cement. In comparing the performance of the A-3 sand and the A-2-4 silty sand with the addition of 20 percent fly ash, the maximum cementing CaO constituents possibly available would be 5 percent of the total mixture (25 percent CaO content × 20 percent fly ash). This would be true for both sands. However, the A-3 sand would have a 25 percent CaO concentration in its fly ash matrix as opposed to 10.4 percent for the A-2-4 silty sand matrix of fly ash, silt, and clay (25 percent CaO content × 20 percent fly ash/48 percent fly ash, silt, and clay). The performance of the stabilized sands, as measured by their strength and durability tests, is closely related to the quality of the cementitious matrix of the mixture. In comparing the strength gain between mixtures of fly ash and the A-3 sand and A-2-4 silty sand, the difference can be seen.

There was an additional gain in strength corresponding to the addition of lime or portland cement with fly ash and the two sands. The strength gain with the addition of lime was not as significant in the A-2-4 silty sand as that occurring in the A-3 sand. Also, the A-2-4 soil seemed to produce more erratic test measurements than did the A-3 sand. The clay and silt-size fraction of the A-2-4 sand did not appear to have strong pozzolanic characteristics. The fines of the natural soil

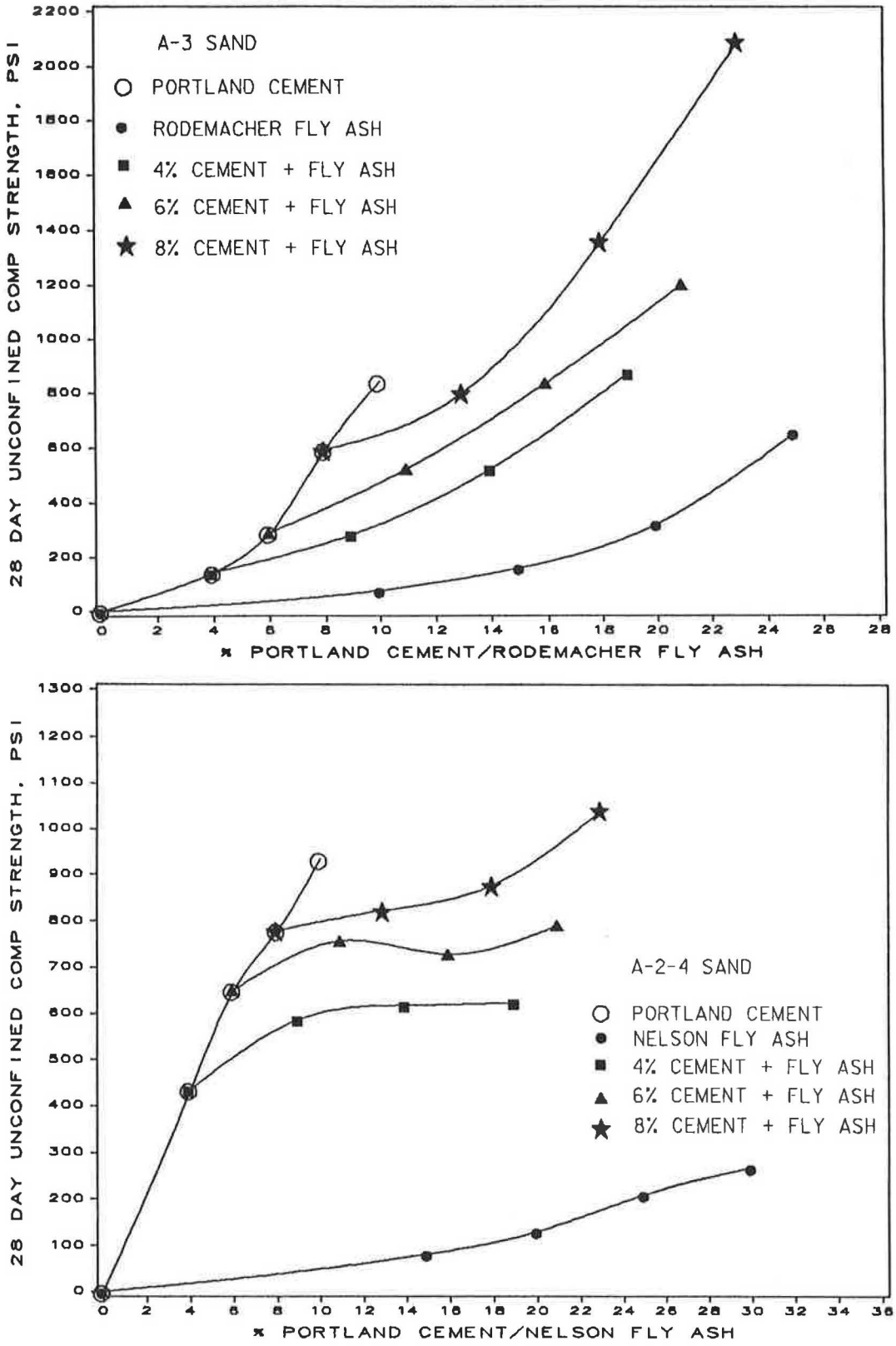

FIGURE 4 Unconfined compressive strength versus percent portland cement/fly ash.

may interfere with and produce discontinuities in the cement formed within the matrix by the fly ash and fly ash combinations of additives. In the A-3 sand, the density (i.e., increased percentages of fly ash) seemed to be more critical for strength gain than did the added lime.

A plot of the relationship between the 28-day strength and the additives for the cement–fly ash combinations appears to take the shape formed by shifting and combining the strength curves for cement and fly ash used alone (Figure 4). The cement–fly-ash strength of the A-3 sand demonstrates that combining portland cement and fly ash contributes significantly to the cementing properties of the matrix. Similar trends

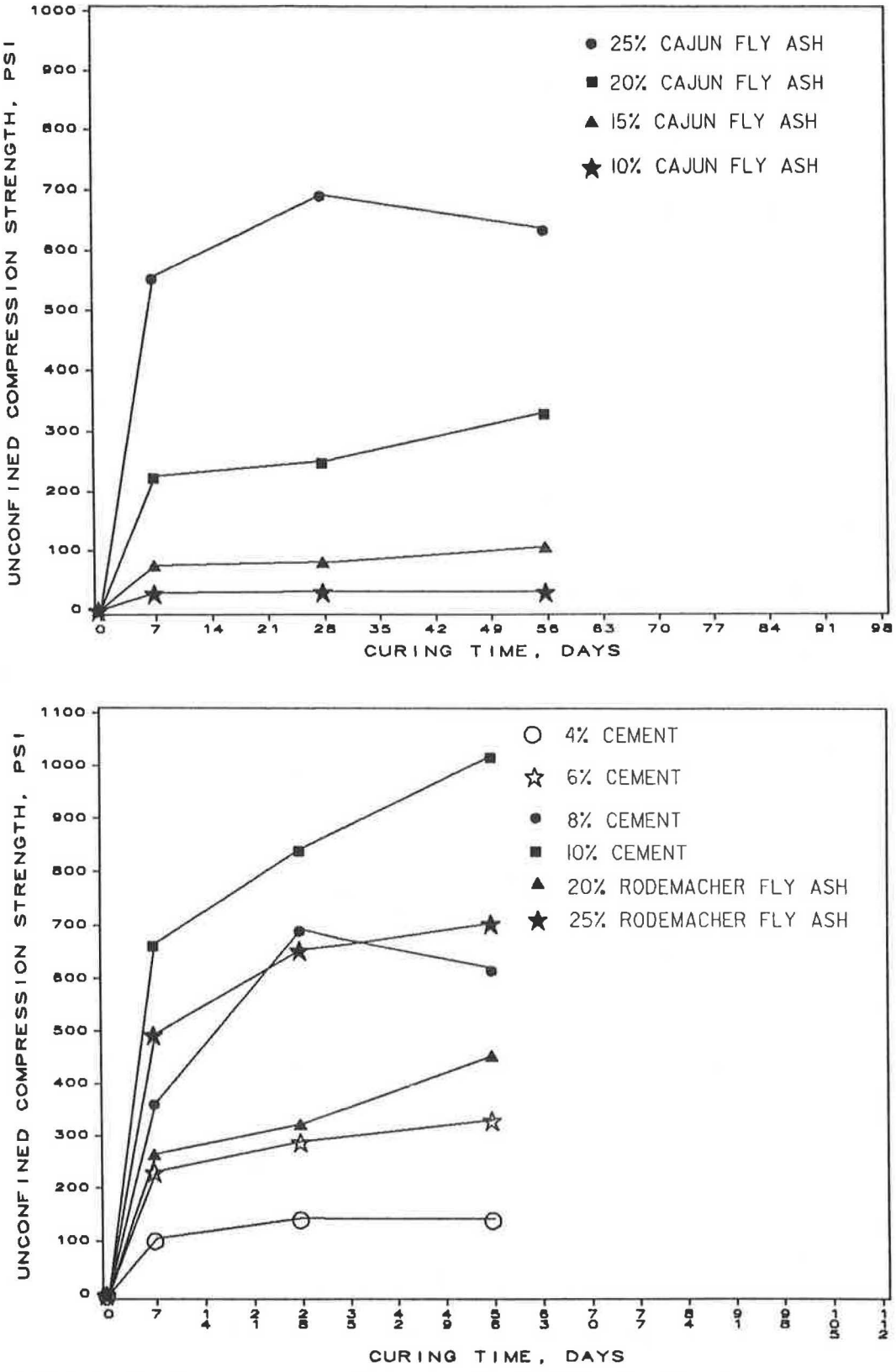

FIGURE 5 Strength gain versus curing time for the A-3 sand with fly ash and cement.

occurred in the cement–fly-ash mixtures of the A-2-4 silty sand. However, the magnitude of the strength gain with additional fly ash was much less, and the values were more erratic.

Curing Time

In Figure 5, the initial slope of the strength-time curve is indicative of the early self-hardening characteristics of the fly ashes. The initial set times of Class C fly ash have been reported to occur very rapidly in other studies (*8,11*). Laboratory tests conducted with slurries of sand mixed with Cajun, Nelson, and Rodemacher fly ashes measured short initial set times ranging from 21 min to 3 hr 20 min. Thus, to get the full advantage of Class C fly ash, the soil should be quickly mixed and compacted (*11*).

Comparisons of the A-3 sand with cement alone and with the Rodemacher fly ash alone are shown in Figure 5. The 25 percent fly ash mixture compared well with the 8 percent cement and provided a denser mixture that may be more durable. Using the current Louisiana DOTD strength/curing criteria and using the current local costs of cement and fly ash, the fly ash appeared to be competitive as a replacement for cement in a clean sand.

Durability

Specimens were conditioned in a vacuum saturation chamber and tested for compressive strength according to ASTM C 593 specifications, with the exception that they were cured in a humidity room at 73° ± 3° F rather than the 100° F specified in the ASTM procedure. A comparison of the differences in strength between specimens subjected to this procedure and those not subjected provided a relative measure or indication of the durability of all sand mixtures (Figure 6). There did not seem to be any consistent loss of strength with the A-3 sand beyond what might be expected as experimental variation. However, the A-2-4 silty sand demonstrated a consistent loss in strength in the vacuum saturation test.

EVALUATION OF TEST RESULTS WITH CLAYS

DOTD TR 433-81 was used as the criterion to evaluate attempts to modify the clay's plasticity (i.e., maximum LL of 40 and maximum PI of 10 and 15 for bases and subbases, respectively). The Atterberg limits of the untreated A-6(9) silty clay satisfied the subbase criteria. The results of modification efforts on the plasticity of both soils produced the following proportions:

Stabilizing Agent	*A-6(9) Clay (%)*	*A-7-6(20) Clay (%)*
Fly ash	20 (base requirements)	30 (base criteria, Rodemacher only) 25–30 (subbase criteria)
Lime	2	3 (base and subbase criteria)
Lime + fly ash	<2 lime + fly ash	Varies, approximately 2 lime with 10 fly ash

Some reports have indicated that a portion of the calcium oxide in some fly ashes exists as free lime, making it possible for flocculation and agglomeration of clay minerals to occur and reduce the soil's plasticity (*1,4*). However, other investigators (*7–10*) report that the CaO (lime) present in the Class C fly ash is not in a free (available) state and, as a soil stabilizing agent, will not modify the plastic behavior of fine-grained soils. The tests performed on the two clays in this study were reviewed and analyzed in an attempt to examine the role of the CaO in the fly ash.

Soil Plasticity

The Atterberg test results for the two clays, treated and untreated, are shown in Figure 7. Lime added to the A-7-6 clay reduced the liquid limit and greatly increased the plastic limit—resulting in a much-reduced plastic index. The lime fixation for this soil (i.e., the amount of lime required to produce a constant value of the plastic index) is 4 percent lime. This corresponds to a PI of 4 (raw soil PI = 40) and a liquid limit of 38 (raw soil LL = 60). The A-6 clay was somewhat lime-reactive, and modifications to the plastic properties of the soil occurred with the addition of lime. The PI was reduced from 13 to 7 with 2 percent lime and to 4 with 5 percent lime.

Adding fly ash to the clays also produced changes in the plasticity. These changes were greater in the A-7-6 clay (Figure 8). However, these changes occurring in the plastic properties can be attributed to the effects of diluting the clay constituents with a nonplastic material (i.e., the fly ash). Theoretical relationships between the liquid and plastic limits and the clay content were developed by Seed et al. (*12*). It was shown that the variation of the liquid limit with the clay content can be expressed as

$$w_{LL} = (C/100)\, w_{CLL} \tag{2}$$

where

w_{LL} = liquid limit of the soil mixture,
w_{CLL} = liquid limit of clay fraction, and
C = percent of clay particles.

A similar relationship for the plastic limit (*14*) is

$$w_{PL} = (C/100)\, w_{CPL} \tag{3}$$

where w_{PL} is the plastic limit of soil mixture, and w_{CPL} is plastic limit of clay fraction; or $w_{PL} = 0.5C$ (for $C > 40$).

Assuming that the fly ash consists of particle sizes in the fine sand-to-silt range (*2*) (Table 2) and that the only source of clay-size particles is from the A-7-6 clay alone, then

$$C = [1 - (FA/100)]\ (\%\ \text{clay in raw soil}) \tag{4}$$

where FA equals percent fly ash.

Table 3 compares the liquid and plastic limits measured in laboratory tests using the three fly ashes with those limits predicted on the basis of variations in the clay content as shown above. Average values of the percent clay in the raw soil were assumed to vary between 55 and 60 percent, and the mean values tested for the liquid and plastic limits of the raw soil were used. The outcome of the laboratory Atterberg tests did not vary greatly from what would be expected by blending a fine-grained, nonplastic soil with the A-7-6 clay.

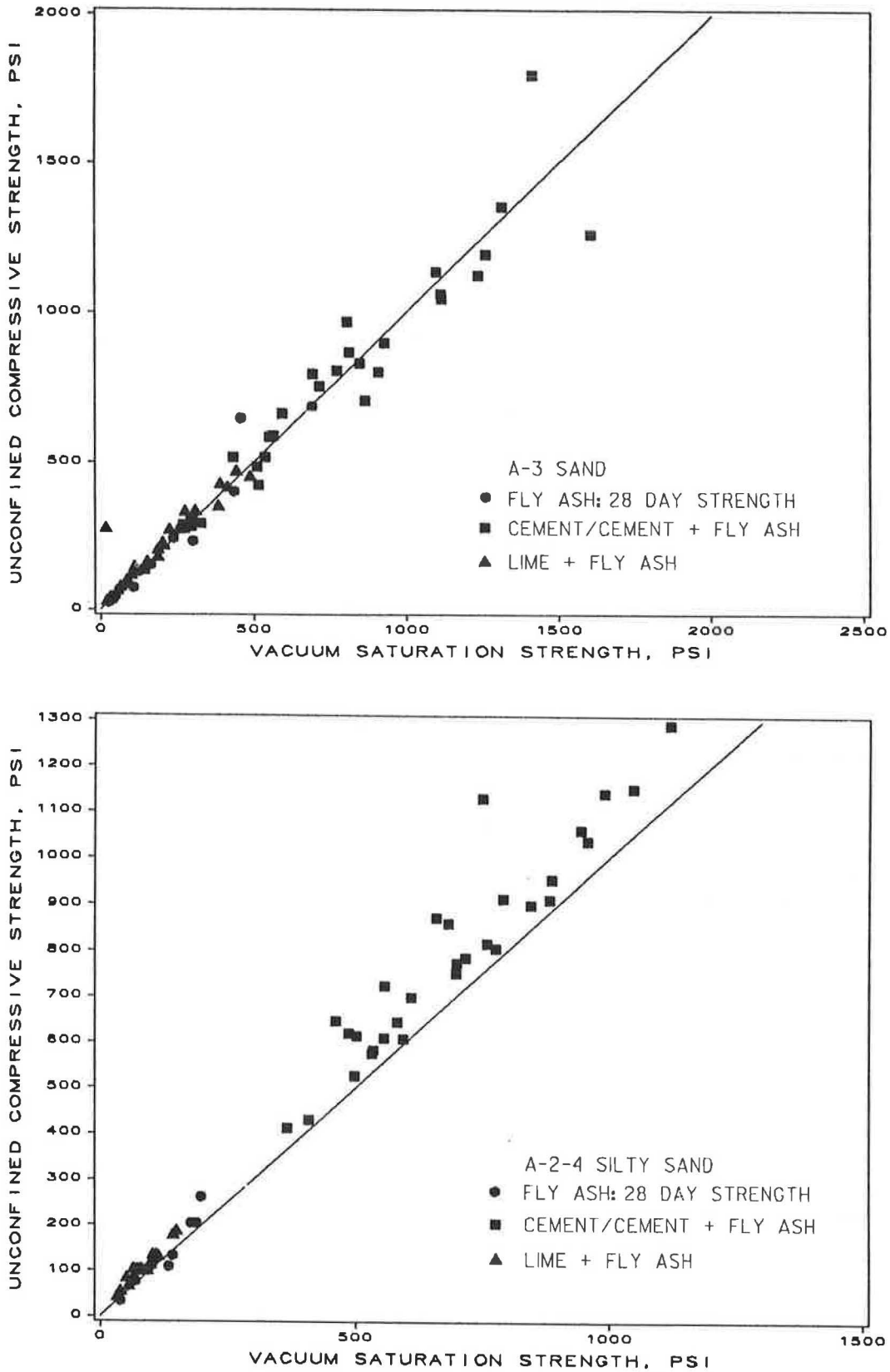

FIGURE 6 Unconfined versus vacuum-saturated strength for the A-3 and A-2-4 sands.

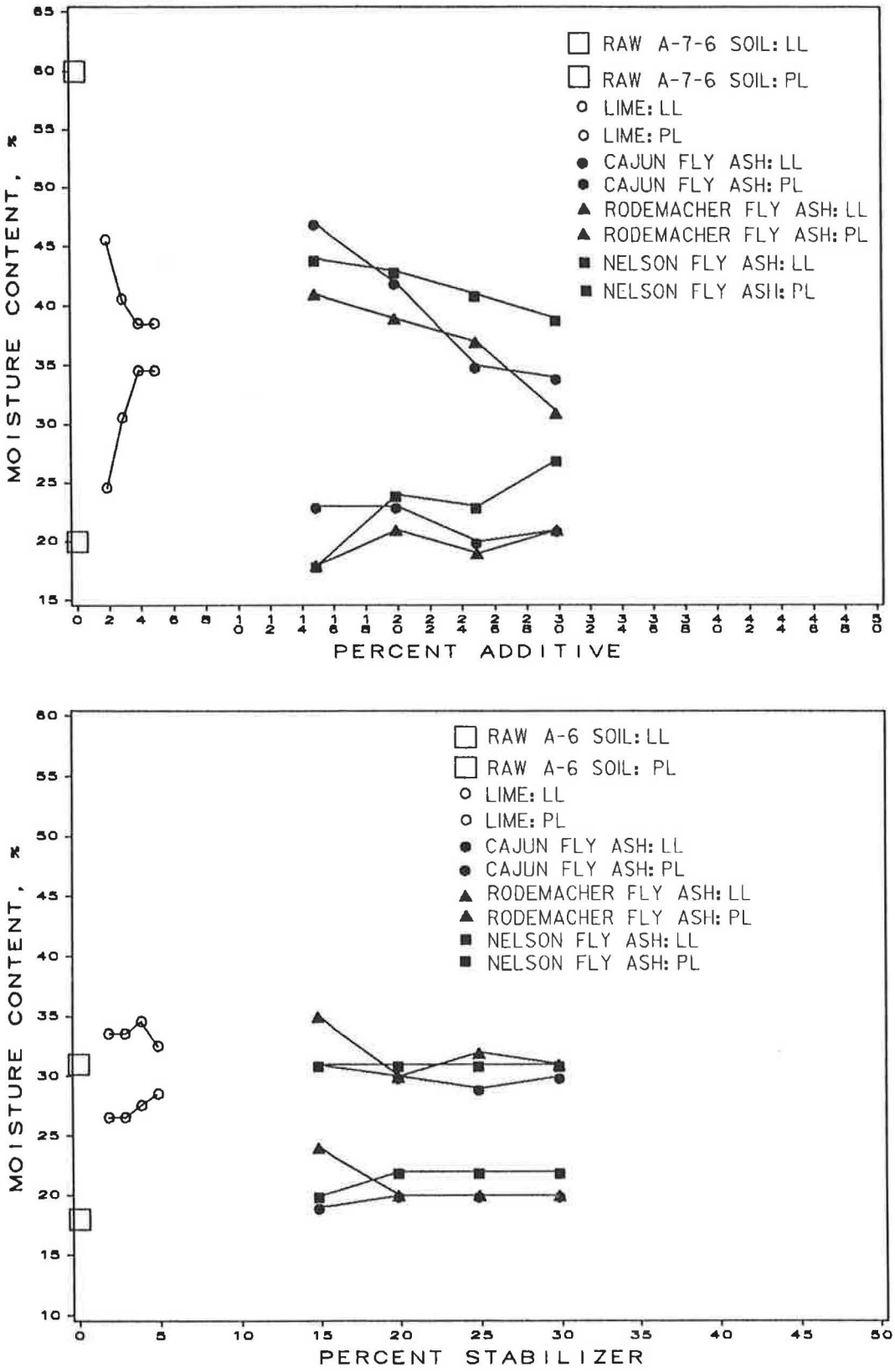

FIGURE 7 Atterberg tests versus percent additive for the A-7-6 and A-6 clays.

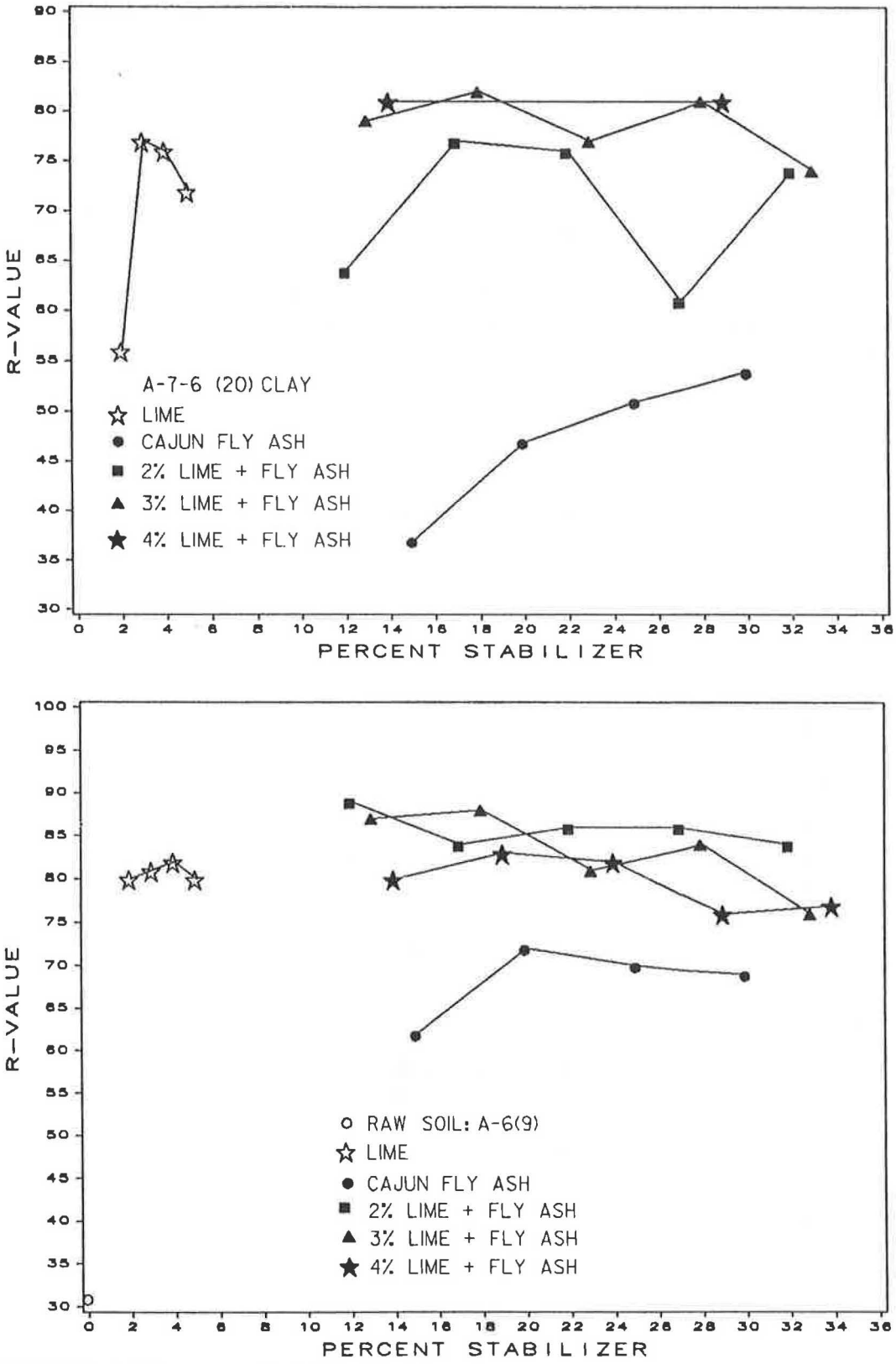

FIGURE 8 Stabilometer tests for A-7-6 and A-6 clays.

TABLE 3 ATTERBERG LIMITS: PREDICTED AND OBSERVED

Percent		A-7-6	Fly Ash			
FA	C	Raw Soil	Cajun	Nelson	Rodemacher	Predicted
			Liquid Limit			
0	55	60				
15	47		47	44	41	47-51
20	44		42	43	39	44-47
25	41		35	41	37	41-44
30	39		34	39	31	39-43
			Plastic Limit			
0	55	20				
15	47		23	18	18	16-24
20	44		23	24	21	15-22
25	41		20	23	19	14-21
30	39		21	27	21	13-20

FA - fly ash percentage

C - clay fraction percentage

Thus, it appeared that the changes in plastic properties of the fly ash-soil mixtures for these Class C fly ashes could be credited more to a decrease in the clay fraction than to chemical alteration of the clays. This is not to say that there was not some effect or change due to whatever percentage of free lime was available. However, there did not appear to be enough free lime to provide substantial changes.

Dry Density

As expected, the addition of lime to the compacted clays produced a density less than that for the raw soil. Although the fly ash-soil density values varied, they seemed to produce densities that were approximately equal to those obtained with the untreated soil. However, combining the lime and fly ash with the A-6 soil further reduced the density of the mix. The pronounced effect that the addition of lime had on the density of both clays, with and without fly ash, and the lack of change (reduction) in density with the soil plus fly ash are further indications of the absence of free lime in the fly ash.

Soil Support Resistance Value

The resistance or *R*-values of the A-7-6 and A-6 silty clays were greatly improved with additions of lime, fly ash, and lime-fly ash combination (Figure 8). However, the addition of lime or lime in combination with fly ash produced the greatest gain in the measured *R*-values for both soils.

The testing procedure should be considered in evaluating the results. In this procedure, the test specimens were compacted after being mixed with the stabilizing agents and slaked with water for a 72-hr period. Within the ensuing 24 hr, they were tested for exudation pressure followed by determination of expansion pressures. The *R*-values were measured approximately 24 hr after compaction or 4 days after being initially mixed with the stabilizing agents and slaking water. This is not enough time to assess the pozzolanic gain in strength. There are also the effects of the slaking period on the Class C fly ashes. Mixing the fly ash, soil, and water with the 72-hr slake period in the *R*-value test procedure is probably counterproductive with respect to the fast initial set of the Class C fly ashes.

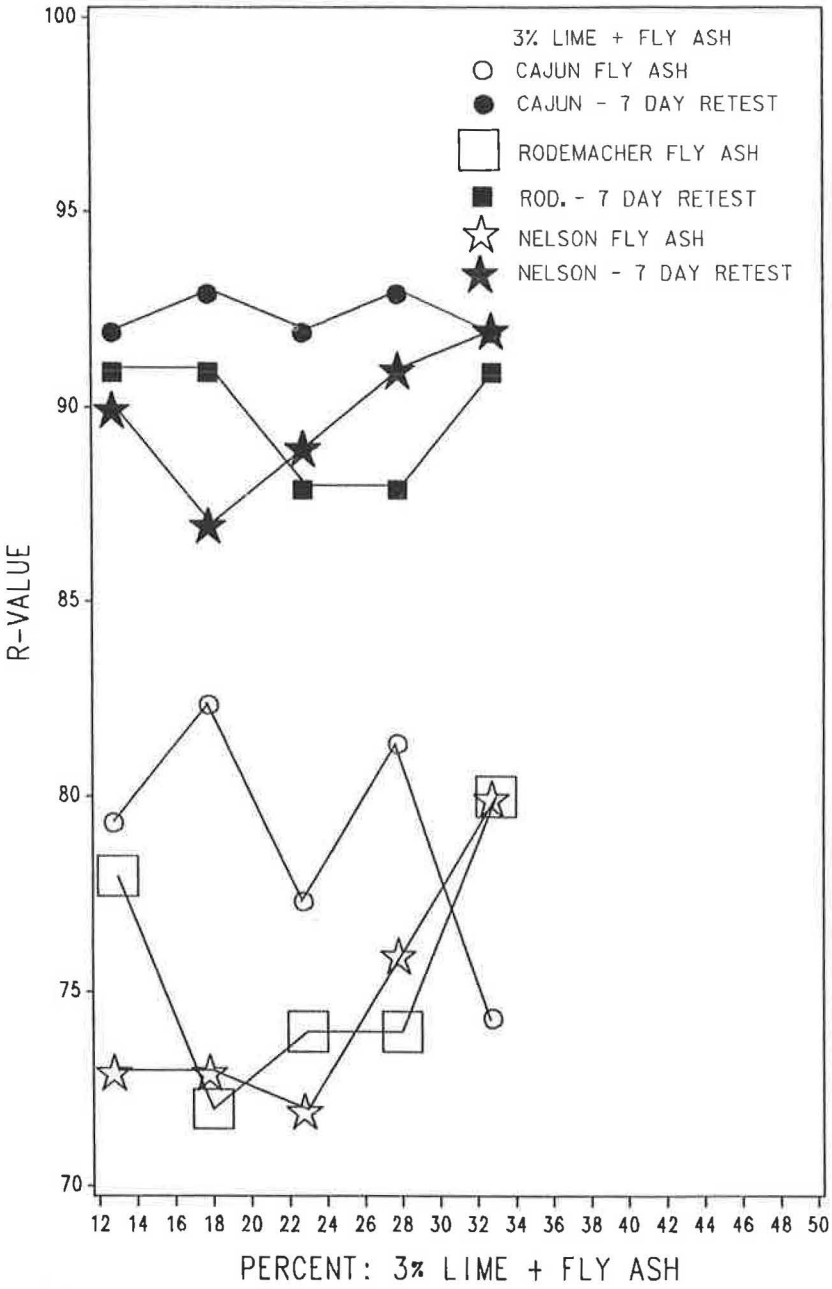

FIGURE 9 ***R*-value gain with 7-day retests of A-7-6 clay with lime plus fly ash.**

The uncured lime-soil and fly ash-soil mixtures immediately improved the strength and deformation properties of both soils, with the most dramatic gain occurring in the A-7-6 clay (Figure 8). Treating the A-7-6 soil with the lime or with the lime-fly ash produced final *R*-values almost as high as those of the treated A-6 silty clay (*R*-values of 77 versus 85)—the A-7-6 being the most lime-reactive of the two soils. Lime was the most effective stabilizing agent, although some small gains in the *R*-values were achieved in some cases by combining the lime and fly ash. Large quantities (30 percent) of fly ash added to the lime showed no improvement over the smaller proportions (10 percent).

Some of the A-7-6 specimens were retested for their *R*-values after an additional 7-day curing period. Figure 9 shows the test results of one set. The results varied but consistently showed a significant gain in a relatively short time. Because these test specimens were previously subjected to loading in the stabilometer in the initial *R*-value test, the second *R*-value determined at the end of an additional 7-day curing included some autogeneous healing in addition to further development of their pozzolanic strength.

CONCLUSIONS

The test results of this study demonstrate that ASTM Class C fly ash could be used as a lone or partial replacement of portland cement in sands, depending on their gradation char-

acteristics. The improvement of the sands with the Class C fly ash tested is credited to its dual role as a matrix filler and cementing agent. The engineering and physical properties of the sand–fly-ash mixtures varied with changes in the fly ash source. However, the general behavior was consistent for all.

Proportioning the A-3 sand and fly ash for maximum density produced a correspondingly large gain in strength. However, large quantities of fly ash (20 to 25 percent) were required to maximize the density. Fly ash alone and the A-2-4 silty sand did not fare well. Success in stabilizing a silty sand or sandy silt with Class C fly ash will depend on the quantity and reactive properties of the fine-grained material (< #200 sieve), that is, the matrix quality. The importance of the matrix materials with respect to durability was also reflected in a greater loss of strength for the A-2-4 silty sand in the vacuum saturation tests.

Alterations of the plastic properties of the clays with the Class C fly ashes used alone are attributed to an overall reduction in the percentage of clay content corresponding to the high percentages of fly ash used. The amount of free lime available in the fly ashes for cation exchange and flocculation-agglomeration reactions is insufficient to compete effectively as a lime substitute.

The soil support resistance of both clays as measured by the stabilometer test was greatly improved with the addition of lime or fly ash, or both. The greatest improvements occurred in the poorest soil [the A-7-6(20) clay]. As a lone additive, lime provided the greatest improvement in soil support. A small gain in the *R*-values resulted when fly ash was added to the lime. However, lime alone performed almost as well without the fly ash. Unless proven economical to do so, there does not appear to be any advantage to using a Class C fly ash over lime in the treatment of clays.

ACKNOWLEDGMENTS

This study was sponsored by and conducted in cooperation with the Louisiana Department of Transportation and Development and the Federal Highway Administration, U.S. Department of Transportation. The testing program was performed by the Louisiana Transportation Research Center.

REFERENCES

1. A. M. Digiola, R. J. McLaren, D. L. Burns, and D. E. Miller. *Fly Ash Design Manual for Road and Site Applications, Volume 1: Dry or Conditioned Placement*. Electric Power Research Institute, Palo Alto, Calif., Feb. 1986.
2. R. Pachowski et al. *Brown Coal Fly Ash in Soil Stabilization*. Interim Report FHWA/RD-84/072. U.S. Department of Transportation, Federal Highway Administration, Oct. 1984.
3. M. Mateos. Stabilization of Soils with Fly Ash Alone. *Highway Research Record 52*, HRB, National Research Council, Washington, D.C., 1964.
4. R. C. Joshi, D. M. Duncan, and H. McMaster. New and Conventional Engineering Uses of Fly Ash. *Transportation Engineering Journal*, ASCE, Vol. 101, No. TE4, Nov. 1975.
5. B. J. Dempsey and M. R. Thompson. Vacuum Saturation Method for Predicting Freeze-Thaw Durability of Stabilized Materials. *Highway Research Record 442*, HRB, National Research Council, Washington, D.C., 1973.
6. R. Andres, R. Giballa, and E. J. Barenberg. Some Factors Affecting the Durability of Lime-Fly Ash-Aggregate Mixtures. In *Transportation Research Record 560*, TRB, National Research Council, Washington, D.C., 1976.
7. W. C. McKerall, W. B. Ledbetter, and D. J. Teague. *Analysis of Fly Ashes Produced in Texas*. Research Report 240-1. Texas Transportation Research Institute, Texas A&M University, Jan. 1981.
8. W. B. Ledbetter. *Is Lime in Fly Ash Available for Soil Stabilization*? Civil Engineering Department, Texas A&M University, April 1981.
9. M. L. Mings, S. M. Schlorholtz, J. M. Pitt, and T. Demirel. Characterization of Fly Ash by X-Ray Analysis Methods. In *Transportation Research Record 941*, TRB, National Research Council, Washington, D.C., 1983, pp. 5–11.
10. J. M. Pitt, M. L. Mings, and T. Demirel. Characterization and Techniques for Rapid Evaluation of Iowa Fly Ashes. In *Transportation Research Record 941*, TRB, National Research Council, Washington, D.C., 1983, pp. 12–17.
11. S. I. Thornton and D. G. Parker. *Self-Hardening Fly Ash*. AHTD Report H-52. Arkansas Highway and Transportation Department, Little Rock, Oct. 1975.
12. H. B. Seed, R. J. Woodward, and R. Lundgren. Fundamental Aspects of the Atterberg Limits. *Journal of the Soil Mechanics and Foundation Division*, ASCE, Vol. 90, No. SM6, Nov. 1974.

Publication of this paper sponsored by Committee on Lime and Lime-Fly Ash Stabilization.

Accelerated Curing of Fly Ash–Lime Soil Mixtures

GOKHAN BAYKAL, ARA ARMAN, AND RAY FERRELL

The morphological, mineralogical, and stress-strain properties of compacted bentonite-fly ash-lime, bentonite-fly ash, and bentonite-lime cured at 23°C and 50°C were compared. The development of microstructure and cementitious crystals was observed by scanning electron microscopy, energy dispersive spectral analysis, and x-ray diffractometry. The elastic moduli and compressive strengths were obtained from unconsolidated, undrained triaxial and unconfined compression tests. Curing at 50°C increased the rate of strength development. Similar elastic moduli were obtained for specimens cured for one day at 50°C and 28 days at 23°C. However, strain at failure after one day of curing at 50°C was considerably higher than that obtained after 28 days of curing at 23°C. The samples cured at 50°C yielded higher compressive strengths relative to the samples cured at 23°C. Cementitious minerals formed at both curing temperatures were similar except that the cementitious minerals observed after 50°C curing had a higher degree of crystallinity. Short-term, high-temperature curing may be substituted for the prediction of long-term design parameters; however, the relationship between short-term, high-temperature curing versus long-term, low-temperature curing must be statistically established by further testing.

Laboratory tests for determining compressive strengths and elastic moduli use compacted and cured mixtures of soils and additives, such as fly ash or lime. Curing time, temperature, proportions of soil and additives, and compaction water content are important factors in this evaluation process. This study concentrates on the relationship between curing temperature and curing period. Higher curing temperatures generally increase the rate of strength development; thus elevated curing temperatures and shorter curing periods are sometimes used to predict engineering properties developed after longer curing periods at ambient temperatures.

The effects of elevated curing temperatures on the morphology, mineralogy, and stress-strain properties of test specimens must be studied to evaluate the viability of design parameters derived from tests performed on specimens cured at accelerated (one day at 50°C) temperatures. It is also essential to establish the relationship (or the similarity) of stress-strain properties, the mineralogy, and the morphology of mixtures that are subjected to accelerated curing before comparisons can be made of the properties of the two with any degree of confidence.

Thus the main objectives of this study were to compare the observed morphological, mineralogical, and stress-strain properties of fly ash-lime stabilized bentonite cured at 23°C and 50°C for 1, 28, 90, and 180 days and to use the results to evaluate the feasibility of an accelerated curing procedure.

A laboratory investigation was undertaken using bentonite-lime, bentonite-fly ash, and bentonite-fly ash-lime cured at 23°C and 50°C for periods of 1, 28, 90, and 180 days. As a follow-up study to provide results from even longer curing periods, bentonite-fly ash-lime mixtures were also cured for about 600 days. Unconsolidated, undrained triaxial tests were conducted to determine the stress-strain relationship. Mineralogical and morphological observations were accomplished by using x-ray diffractometry, scanning electron microscopy, and energy dispersive spectroscopy.

Bentonite, which is essentially a monomineralic montmorillonite, was chosen to eliminate variable mineralogical compositions associated with natural clays. For the accelerated curing test, 50°C for 24 hr was selected for its practicality. Other temperature and time combinations may produce similar results, but 50°C is probably the maximum temperature because other types of cementitious minerals may occur at higher temperatures.

The reactions between clay and lime cured at elevated temperatures have been studied by a number of researchers (*1–7*). The reaction products vary with the type of clay, reaction conditions (especially temperature), curing time, mixture proportions, and whether slurries, pastes, or compacted samples are used. Commonly the reaction products observed are composed of calcium silicate hydrates (C-S-H) and calcium aluminate hydrates. Poorly crystallized C-S-H (I) is the most frequently reported mineral (*1,2,8,7*). Tetracalcium aluminate thirteen hydrate is often observed at room temperature (*2,9,10*), whereas cubic tricalcium aluminate hexahydrate is more common in the mixtures that are cured at elevated temperatures (*3–5,11*).

The compressive strengths of clay-lime mixtures cured at elevated temperatures are higher than the compressive strengths of those cured at room temperatures for short and long time periods (*1,2*). In montmorillonite-lime mixture, the same cementitious minerals were observed at room and elevated temperatures. However, in the latter case, the compounds developed higher crystallinities and the mixtures had higher compressive strengths (*2*). Arabi and Wild (*1*) studied red marl–lime mixtures cured at temperatures up to 75°C. He reported higher unconfined compressive strengths for mixtures cured at elevated curing temperatures.

Anday (*12*) suggested that short-term curing at elevated temperatures simulated the long-term behavior of the lime-stabilized soils at normal temperatures. He recommended that two-day 50°C curing be used instead of long-term normal-temperature curing. However, no one has studied the response

Louisiana Transportation Research Center, Louisiana State University, 4101 Gourrier, Baton Rouge, La. 70804-9245.

of combined fly ash-lime stabilization at the elevated temperatures, and because the reactions are more complex, previous results cannot be extrapolated for these mixtures.

PROCEDURE

Materials Used

The bentonite used for this study was obtained from NL Industries of Houston, Texas. Type C fly ash was obtained from the Cajun Electric Power Plant at New Roads, Louisiana. This fly ash contained a considerable amount of glassy spherical material and some free lime. The calcitic hydrated lime was obtained from the Dravo Lime Company of Baton Rouge, Louisiana.

Specimen Preparation, Curing, and Testing

Mixture proportions were determined by a variety of procedures (*13*). To determine the appropriate lime content for this study, plastic limit and pH values of different proportions of bentonite-lime mixtures were determined, and the percentage of lime that corresponded to the point at which no increase in pH or plastic limit occurred was used as the lime content for this study. Following determination of the lime content, 8 to 30 percent fly ash by dry weight was added to the bentonite-lime mixture, and compressive strengths were determined after 1 and 7 days of curing at 23°C. Increased fly ash percentages continued to produce increased compressive strengths within the range of the experiment; therefore, 20 wt% fly ash was arbitrarily selected as the highest practical amount to be included in a stabilization project. Twenty percent fly ash, 5 percent lime, and 75 percent bentonite (by dry weight) were selected as the mixture proportions. The effects of only lime or fly ash additives on microstructure development and strength were assessed by removing one additive at a time from this principal mixture, while maintaining the same dry weight ratios for the remaining materials. The mixture percentages, compaction water contents, and dry densities are presented in Table 1.

Cylindrical specimens having a diameter of 3.334 cm (1.313 in.) and a height of 7.153 cm (2.816 in.) were compacted in a Harvard miniature compaction device (using an 89 N-20 lb spring) (*14*). After compaction, all specimens were weighed and placed in practically airtight plastic bags and kept in an oven at 50°C or in a moisture-controlled room for ambient temperature curing (23°C, relative humidity greater than 95 percent) for up to 180 days. The moisture contents of cured specimens were determined before and after testing.

Compressive strength tests, with and without confining pressures, were conducted by using triaxial testing equipment at a strain rate of 0.25 mm/min (0.01 in./min). Six samples of the bentonite-fly ash-lime mixture and three samples of the other mixtures were tested for each curing temperature and time. The elastic moduli of the samples were calculated by using stress-strain values corresponding to 70 percent of the maximum deviator stress, which approximately represented the linear portion of the stress-strain curve (*15*). After the samples were fractured, representative subsamples were frozen and vacuum dried for mineralogical and textural analyses. Gold coating was used for scanning electron microscopy. X-ray diffraction (XRD) samples were prepared by a side-loading technique to obtain random orientation (*16*).

RESULTS

Stress-Strain Relationships

The relationships between unconfined compressive strength and curing time for the mixtures containing bentonite and additives are presented in Figure 1. In general, the compressive strengths for specimens cured at 50°C were higher than for those cured at 23°C. The compressive strength of the bentonite-fly ash-lime mixture reached 3947 kPa at 50°C curing after 624 days, which was 1.5 times the compressive strength of the mixture cured at 23°C for the same amount of time.

A similar response to elevated curing temperature was observed for the bentonite-fly ash mixture cured at 50°C. It developed a compressive strength of 1915 kPa after 180 days of curing, which is 1.4 times the compressive strength obtained at 23°C. The compressive strengths of the fly ash-bentonite mixtures after one day of curing at 50°C were higher than those cured at 23°C for 28 days. For samples cured at 23°C, the major portion of the compressive strength developed after the first 28 days of curing.

The strains at failure ranged from 0.92 percent to 1.65 percent for the one-day cured samples (Figure 2). After 28 days of curing, failure strains decreased to between 0.6 and 1.0 percent. No further decrease in strain was observed at normal and elevated curing temperatures. The failure strains of the samples cured at 50°C were consistently larger than those cured at 23°C. This difference, however, became negligible after 180 days of curing for most of the samples. The bentonite-fly ash-lime mixture cured at 50°C failed at an average strain of 0.98 percent, which is 1.3 times that of the 23°C cured sample after 624 days of curing. The elevated curing temperature generally produced higher failure strains for the samples containing fly ash after long curing periods, which in turn affected the elastic moduli.

TABLE 1 MIXTURE PROPORTIONS, COMPACTION WATER CONTENTS, AND DRY DENSITIES

Mixture	Proportion (%)				Dry Density (mg/m^3)
	Bentonite	Fly Ash	Lime	Water	
Bentonite + fly ash + lime	75	20	5	34	1.25
Bentonite + fly ash	79	21	0	24	1.40
Bentonite + lime	94	0	6	40	1.15
Fly ash + lime	0	80	20	20	1.65
Fly ash	0	100	0	11	1.90

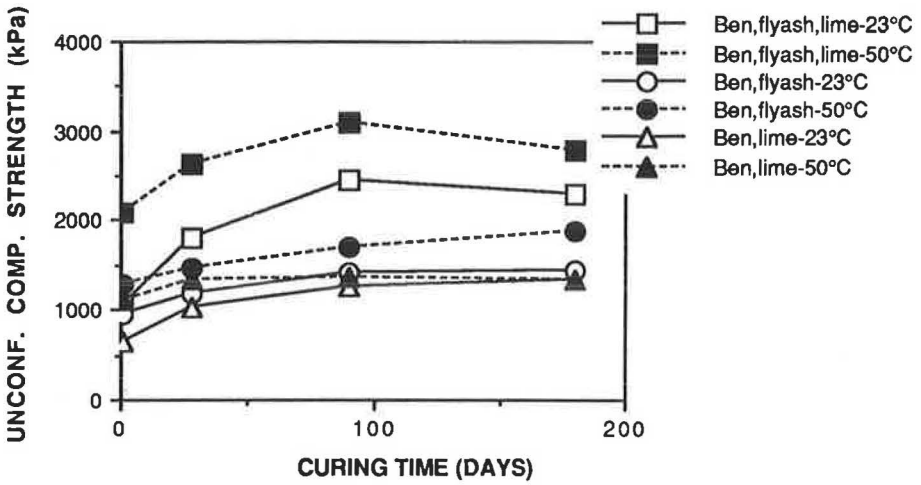

FIGURE 1 Average unconfined compressive strength (UCS) of bentonite-fly ash-lime, bentonite-fly ash, and bentonite-lime mixtures versus curing time. UCS for bentonite-fly ash-lime at 23°C and 50°C was 2600 and 3900 kPa, respectively.

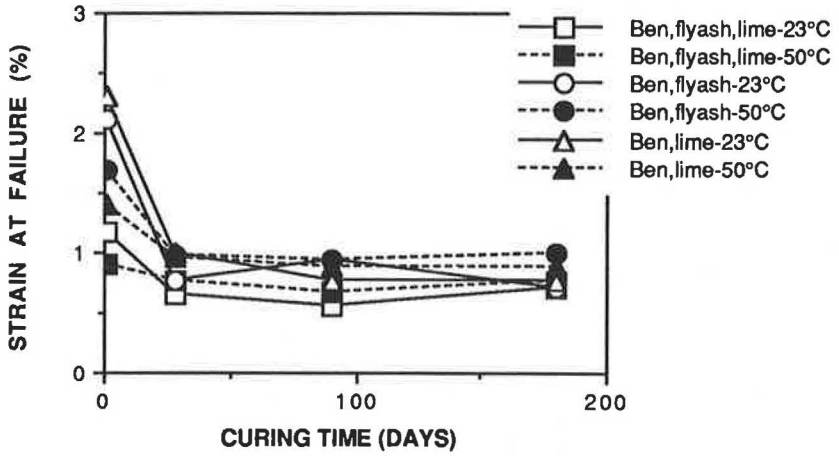

FIGURE 2 Average strain at failure for bentonite-fly ash-lime, bentonite-fly ash, and bentonite-lime mixtures versus curing time. Average strain for bentonite-fly ash-lime at 23°C and 50°C was 0.7 and 1.0 percent, respectively.

The changes in elastic moduli with time are presented in Figure 3. For the bentonite-fly ash-lime mixture, the average elastic modulus for the one-day curing period at 50°C was 349,250 kPa, which was 90 percent of the elastic modulus of the mixture cured for 28 days at 23°C; after 90 days, no significant difference was present. A sharp increase in elastic moduli was observed at 90 days of curing for both curing temperatures, which was then followed by a decrease. After 180 days of curing, the elastic moduli of the bentonite-fly ash-lime mixture were approximately twice that of bentonite-lime and bentonite-fly ash mixtures. After 90 days, the samples cured at 50°C produced comparable elastic moduli to the samples cured at 23°C.

Morphology of Cementitious Products

The morphological studies assisted in the interpretation of changes in the stress-strain relationships. In Figure 4, the fractured surface of the one-day cured (23°C) bentonite–fly ash–lime mixture contains mostly clay particles. The boundaries of the clay particles are not distinct—a feature typical of plastic materials such as montmorillonite-rich clays. After 28 days of curing at 23°C, a network of acicular crystals dominates the microstructure of the fracture surface as seen in Figure 5. These crystals are identified as C-S-H and ettringite.

The formation and the increase in the abundance of the acicular crystals are accompanied by a compressive strength increase from 1061 kPa to 1800 kPa and a decrease in strain at failure from 1.13 percent to 0.66 percent. The more rigid behavior is attributed to the formation of the three-dimensional network of rods and needles that supports the montmorillonite aggregates and the fly ash spheres, thus restricting the gliding of clay plates past one another and their relative displacement.

Figure 6 shows a representative fracture surface of the one-day cured bentonite-fly ash-lime mixture cured at 50°C. Well-developed acicular and lath-like crystals span the pores and

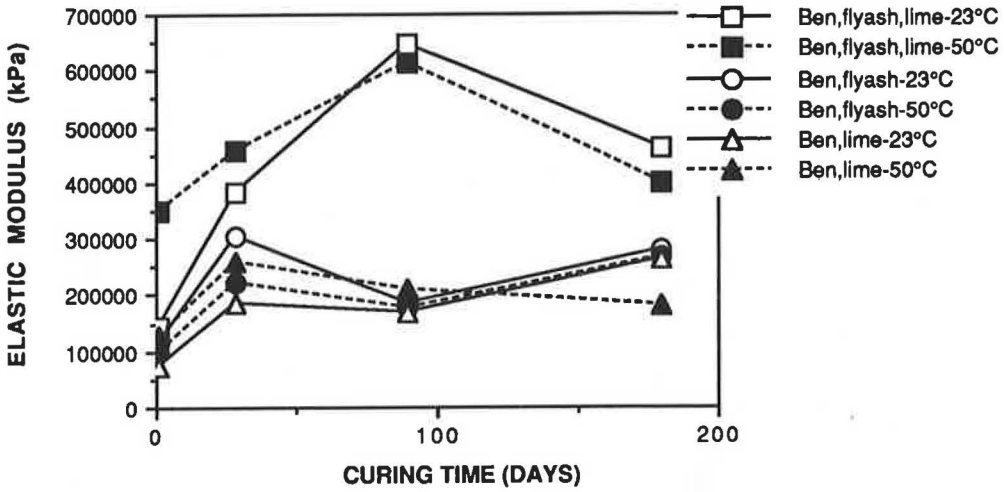

FIGURE 3 Average elastic modulus for bentonite-fly ash-lime, bentonite-fly ash, and bentonite-lime mixtures versus curing time. Elastic modulus for bentonite-fly ash-lime at 23°C and 50°C was 480 000 and 510 000 kPa, respectively.

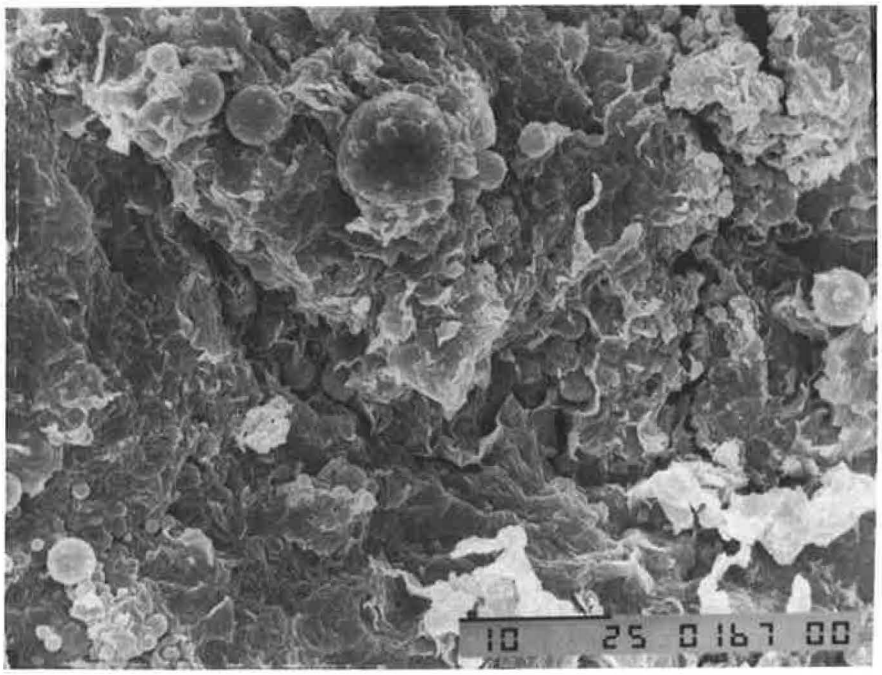

FIGURE 4 Representative fracture surface of the one-day 23°C cured bentonite-fly ash-lime sample. The fracture surface contains mostly clay particles.

support the fly ash spheres and the montmorillonite aggregates. As mentioned previously, the time of observation of the acicular crystals corresponded to a major increase in compressive strength and a decrease in failure strain. Although a quantitative measure was not possible, fewer acicular crystals were observed at 50°C curing, which may be the cause of the consistently larger failure strains at 50°C. A comparison of the morphologies of the 624-day cured samples at 23°C and 50°C supports this observation.

Figure 7 presents a representative fracture surface of the 624-day 23°C cured bentonite-fly ash-lime mixture. The fly ash spheres are embedded in a 50-μm-diameter montmorillonite aggregate and are interwoven with randomly oriented, tiny acicular crystals. At the center of the micrograph, a typical reacted shell of a fly ash grain can be seen. The mixture cured at 50°C had fewer acicular crystals; however, the degree of crystallinity of these acicular crystals was higher (Figure 8). The acicular crystals are thicker and longer and their outlines are sharper than those observed at 23°C.

The higher compressive strengths of the 50°C cured samples containing fly ash after long curing periods are attributed to the increased degree of reaction of the fly ash grains and glassy spheres found in fly ash, which provide calcium, silicon, and aluminum for the formation of more cementitious minerals.

The same morphological changes were also observed with the bentonite-fly ash mixture. In this mixture, the elevated

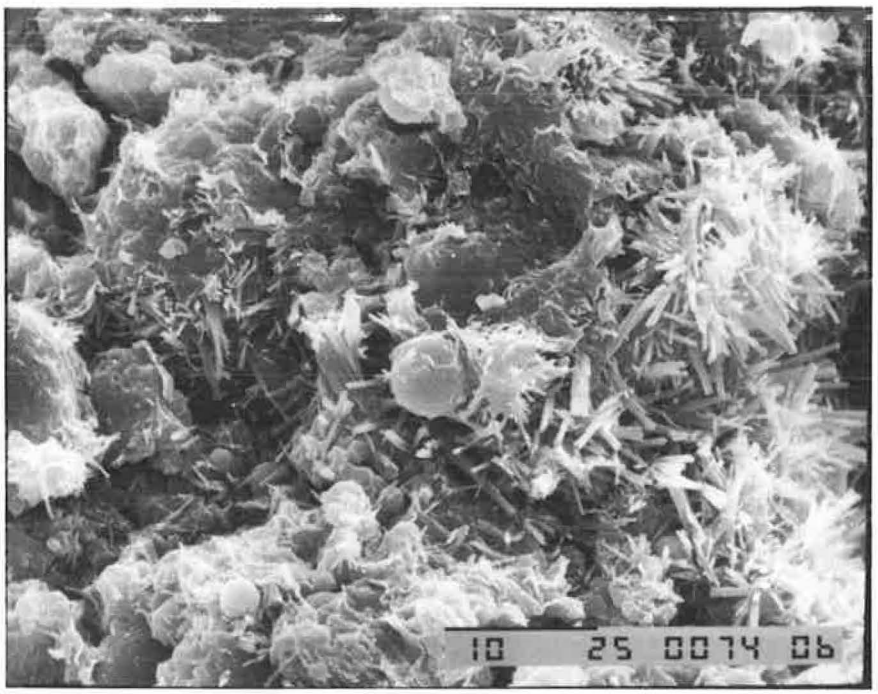

FIGURE 5 Representative fracture surface of the 28-day 23°C cured bentonite-fly ash-lime sample. Acicular crystals dominate the fracture surface.

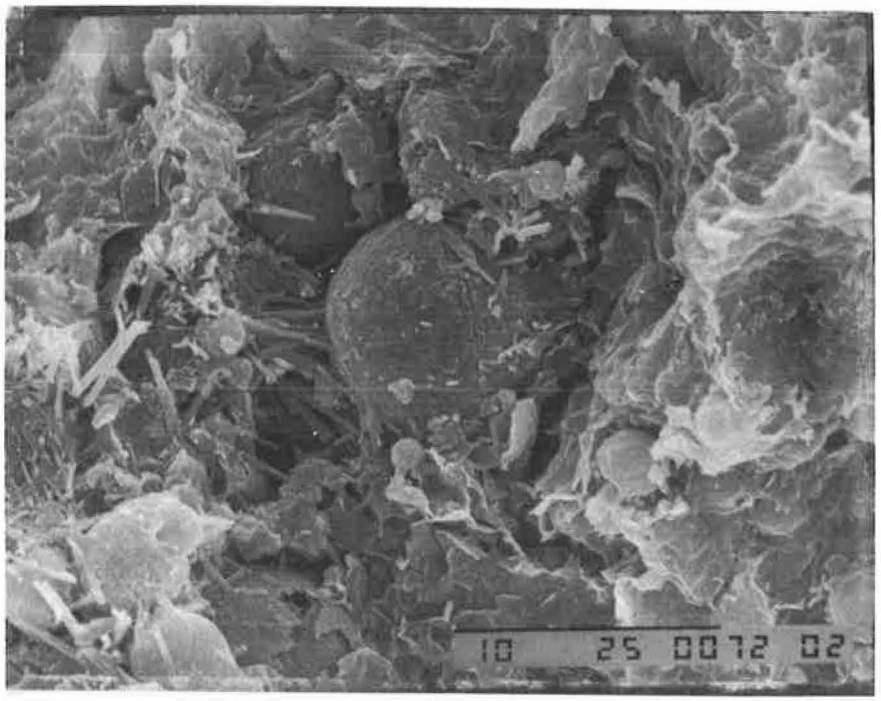

FIGURE 6 Representative fracture surface of the one-day 50°C cured bentonite-fly ash-lime sample. Acicular crystals span the pores and support the fly ash spheres and the montmorillonite aggregates.

temperature increased the rate of the reaction, and well-defined clay aggregate boundaries were observed after one day of curing at 50°C instead of 28 days of curing at 23°C. In bentonite–fly ash specimens, a larger number of reacted fly ash spheres was observed after curing at 50°C. A typical fracture surface of the bentonite-fly ash mixture cured for 180 days at 50°C is presented in Figure 9. The fly ash grain in the center has undergone more reaction relative to the fly ash grains observed at 23°C.

Mineralogy

The mineralogical observations support the observations made with the scanning electron microscope. The identifications of

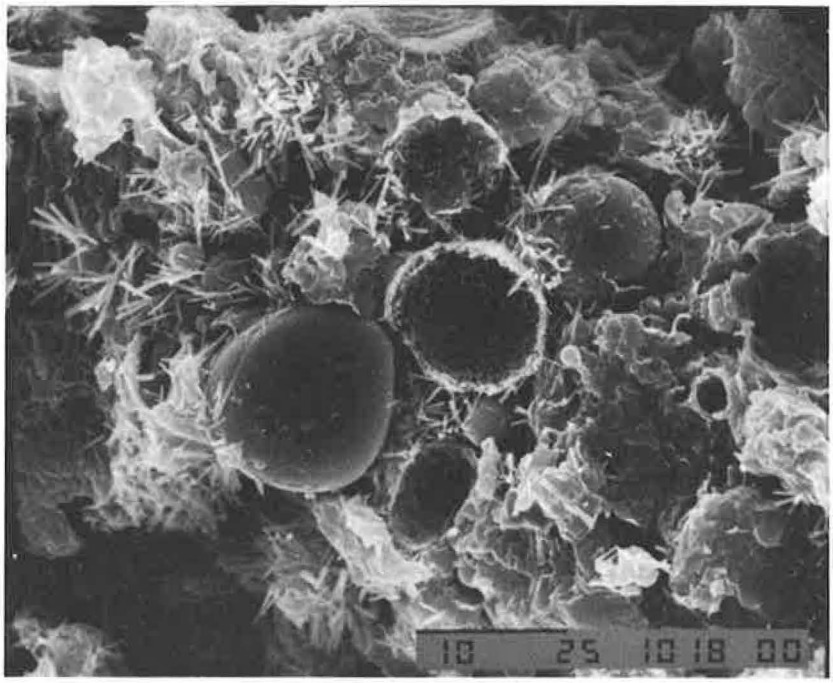

FIGURE 7 Representative fracture surface of bentonite-fly ash-lime cured for 624 days at 23°C.

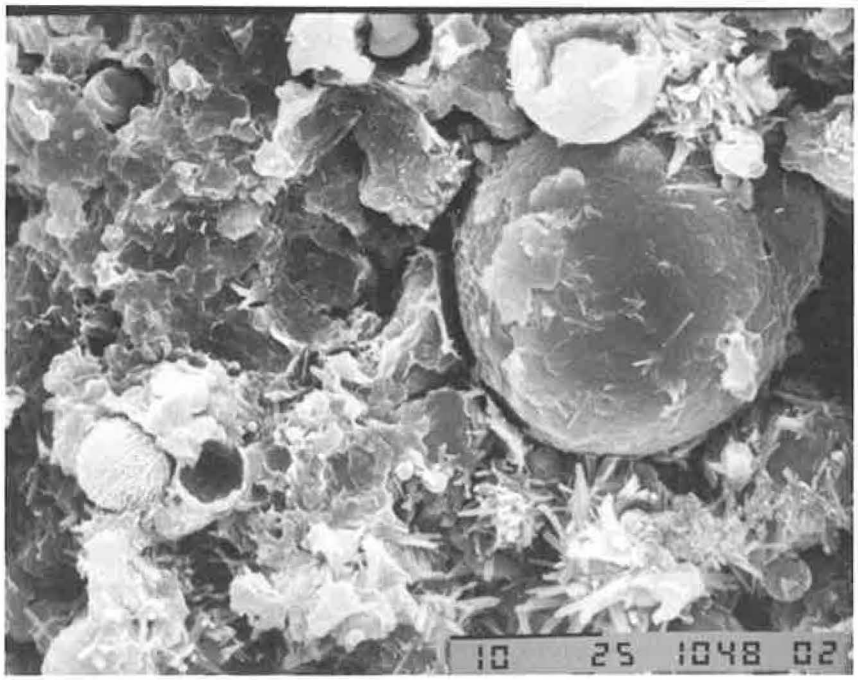

FIGURE 8 Representative fracture surface of bentonite-fly ash-lime cured for 624 days at 50°C.

the cementitious minerals are based on a limited number of d-spacings due to the overlapping of many peaks. Scanning electron microscope (SEM) observations and measured element ratios were used to aid in interpreting the x-ray diffraction patterns. The minerals recognized in the x-ray powder patterns are presented in Table 2. Ettringite is present after one day of curing in all mixtures. In the bentonite-fly ash-lime mixture, C-S-H and afwillite were observed after 28 days of curing at 23°C. In the bentonite-lime and bentonite-fly ash mixtures, afwillite was observed after one day of curing, while C-S-H was observed after 28 days in the bentonite-lime mixture and after 90 days in the bentonite-fly ash mixture at 23°C. At 50°C, the major cementitious minerals (afwillite, C-S-H, and ettringite) were observed after only one day of curing. In both cases, the formation of these minerals corresponded to major increases in strength as presented in Table 3. Addi-

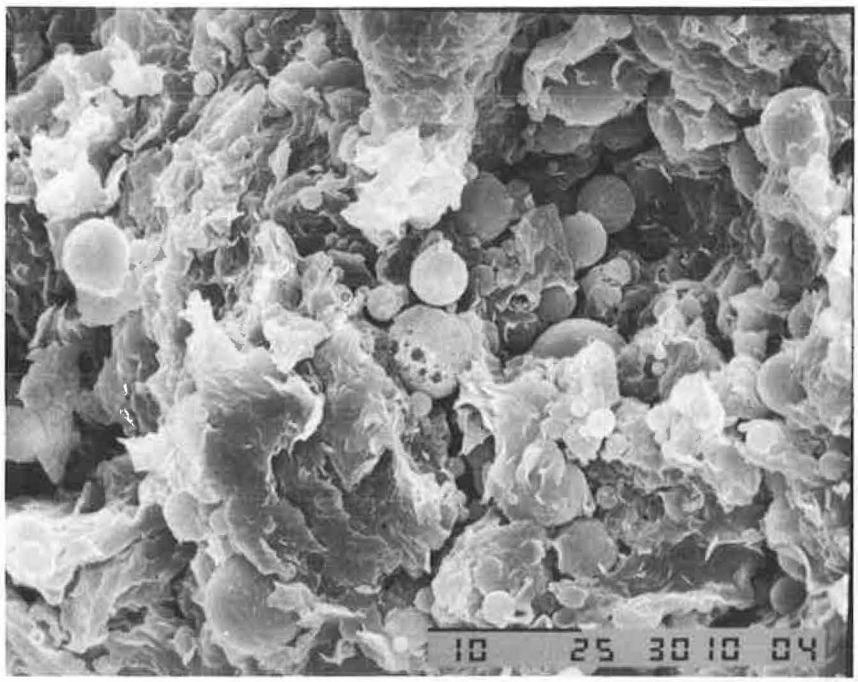

FIGURE 9 Representative fracture surface of bentonite-fly ash mixture cured for 180 days at 50°C.

tional similarities of the cured samples are revealed in the XRD patterns of Figure 10. The one-day 50°C sample and the 28-day 23°C sample are almost identical.

DISCUSSION OF RESULTS

In general, the specimens cured for one day at 50°C produced compressive strengths within ±15 percent of those cured for 28 days at 23°C (Table 3). The bentonite-fly ash-lime mixture had an unconfined compressive strength of 1800 kPa after 28 days of curing at 23°C. When the same mixture was cured for one day at 50°C, it developed a compressive strength that was 17 percent higher than the mixture cured at 23°C (2099 kPa). After 28 days of curing, the bentonite fly ash mixture failed at 1414 kPa, 15 percent higher than the compressive strength of the one-day 50°C cured sample. The bentonite-lime mixture yielded a compressive strength of 996 kPa after 28 days of curing at 23°C, which was 8 percent lower than that of the one day compressive strength of the same mixture at 50°C curing.

Although the compressive strengths were comparable for one-day 50°C and 28-day 23°C cured mixtures, the strains at failure were higher in the former case. The strain at failure after one day of curing at 50°C was 0.92 percent or 1.4 times the failure strain obtained at 23°C after 28 days. The same situation was also observed for bentonite-fly ash and bentonite-lime mixtures. The average strain at failure of the bentonite-fly ash samples cured for one day at 50°C was 1.36 percent, which was 1.9 times greater than the average failure strain of the sample cured for 28 days at 23°C (0.72 percent). The failure strain of the one-day 50°C cured bentonite-lime mixture was 1.49 percent, which was approximately two times the failure strain of the mixture cured for 28 days at 23°C (0.77 percent). In general, the calculated elastic moduli were lower after short-term high-temperature curing.

For most of the specimens, one-day 50°C curing produced compressive strengths similar to long-term compressive strengths of the mixtures cured at 23°C. One-day 50°C curing produced compressive strengths that were between 80 percent and 90 percent of the compressive strengths of bentonite-fly ash-lime, bentonite-fly ash, and bentonite-lime cured at 23°C for 28 days.

The morphological and mineralogical data support the interpretation that the physical behavior of the 23°C cured samples and the 50°C cured samples is roughly similar. The major cementitious minerals are the same in both groups of samples. The cementitious products form the same textural arrangements in the high- and low-temperature specimens. The cements form earlier and have better crystallinities at the higher temperature, suggesting that the rate of reaction is accelerated. Thus, it appears that laboratory curing of one day at 50°C could be substituted for 28-day tests at 23°C. More combined physical and mineralogical morphologies are required before these observations can be fully applied to similar mixtures.

CONCLUSIONS

1. The same cementitious minerals form at 23°C and 50°C curing temperatures, although their crystallinity may be of a higher degree at higher temperatures.
2. At 50°C curing, the rate of the strength-forming chemical reactions increased.
3. Curing at 50°C for one day developed elastic moduli comparable to those of samples cured for 28 days at 23°C.

TABLE 2 MINERALS IDENTIFIED BY X-RAY DIFFRACTION

	BENTONITE-FLY ASH	BENTONITE-LIME	BEN-LIME-FLY ASH
	(23°C) CURING TEMPERATURE		
1 DAY	Montmo.	Montmo.	Montmo.
	Quartz	Quartz	Quartz
	Calcite	Calcite	Calcite
	TCA	Hematite	TCA
	Periclase	Afwil.*	Periclase
	Hematite	Ettrin.*	Hematite
	Ettrin.*		Ettrin.*
	Afwil.*		
28 DAYS	Same	Same+	Same+
		CSH I*	CSH I*
			Afwil.*
90 DAYS	Same+	Same	Same
		CSH I*	
180 DAYS	Same	Same	Same
		50°C CURING TEMPERATURE	
1 DAY	Montmo.	Montmo.	Montmo.
	Quartz	Quartz	Quartz
	Calcite	Calcite	Calcite
	TCA	Hematite	Hematite
	Periclase	Afwil.*	CSH I*
	Hematite	CSH I*	Ettrin.*
	CHS I*	Ettrin.*	Afwil.*
	NO CHANGE IN MINERALS WITH LONGER CURING TIMES		

Note: (*) indicates the newly forming cementitious minerals. Montmo. = montmorillonite, Afwil. = afwillite, Ettrin. = ettringite, Portlan. = portlandite. FA = Fly ash, FL = Fly ash-lime, F = Bentonite-fly ash, L = Bentonite-lime, S = Bentonite-fly ash-lime, TCA = tricalcium aluminate.

TABLE 3 COMPARISON OF COMPRESSIVE STRENGTH TEST RESULTS OF SAMPLES CURED AT 23°C FOR 28 DAYS AND AT 50°C FOR ONE DAY

		CURED AT 23°C 28 DAYS	CURED AT 50°C 1 DAY
	Unconfined:		
BENTONITE FLY ASH LIME	UCS[1] (kPa):	1800 (3.05)[2]	2099 (3.56)
	FAILURE STRAIN,% :	0.66	0.92
	ELASTIC MODULUS (kPa):	386882	349250
	With 100 kPa Confinement:		
	CS[3] (kPa):	1957 (3.32)	2220 (3.76)
	FAILURE STRAIN,% :	0.89	1.31
	ELASTIC MODULUS (kPa):	402751	358066
	Unconfined:		
BENTONITE LIME	UCS (kPa):	996 (1.69)	1084 (1.84)
	FAILURE STRAIN,% :	0.77	1.49
	ELASTIC MODULUS (kPa):	217945	85861
	With 100 kPa Confinement:		
	CS (kPa):	1108 (1.88)	1144 (1.94)
	FAILURE STRAIN,% :	1.47	1.1
	ELASTIC MODULUS (kPa):	140063	207692
	Unconfined:		
BENTONITE FLY ASH	UCS (kPa):	1414 (2.40)	1234 (2.09)
	FAILURE STRAIN,% :	0.72	1.36
	ELASTIC MODULUS (kPa):	278289	140950
	With 100 kPa Confinement:		
	CS (kPa):	1277 (2.16)	1343 (2.28)
	FAILURE STRAIN,% :	1.11	2.03
	ELASTIC MODULUS (kPa):	237267	56697

[1]Unconfined Compressive Strength.

[2]Compressive Strength of Treated/Untreated Bentonite.

[3]Compressive Strength.

Samples cured at 50°C for one day failed at higher strains than those cured at 23°C for 28 days.

4. Major strength development and decrease in failure strain were observed after 28 days of curing at ambient temperatures. Comparable strength development was observed after only one day at 50°C.

5. Accelerated curing procedures may be used to determine the potential strength development of lime, fly ash, and montmorillonite mixtures. However, specimens cured for short terms at elevated temperatures yield higher failure strains relative to those cured at lower temperatures.

6. It is recommended that those involved in testing soil, lime, and fly ash or any combination perform comparative (curing time versus temperature) studies and develop statistically acceptable data. It may be possible to completely replace the 28-day, 23°C curing with the 24-hr, 50°C curing procedure.

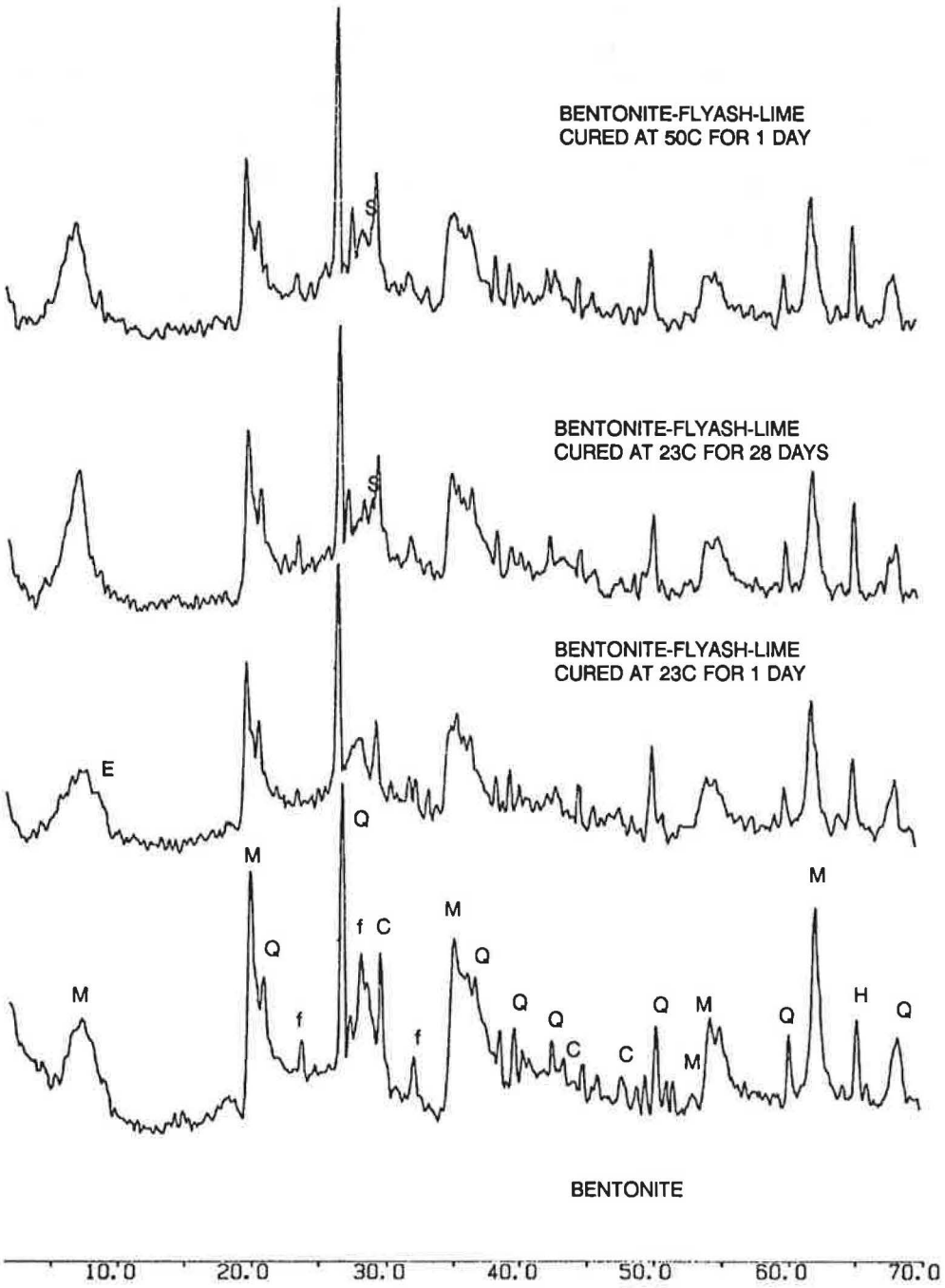

FIGURE 10 X-ray powder diffractograms of bentonite and bentonite-fly ash-lime cured for 1 and 28 days at 23°C and 1 day at 50°C, showing distinct differences from the starting bentonite and 1-day 23°C sample. (*M*, montmorillonite; *Q*, quartz; *f*, feldspars; *C*, calcite; *H*, hematite; *E*, ettringite; *S*, calcium-silicate-hydrate.)

REFERENCES

1. M. Arabi and S. Wild. Microstructural Development in Cured Soil-Lime Composites. *Journal of Materials Science*, Vol. 21, 1986, pp. 497–503.
2. J. B. Croft. The Processes Involved in the Lime Stabilization of Clay Soils. *Proc., Australian Road Research Board*, Vol. 2, 1964, pp. 1169–1203.
3. S. Diamond and E. B. Kinter. Mechanism of Soil-Lime Stabilization: An Interpretive Review. In *HRB Record No. 92*, 1965, pp. 83–101.
4. S. Diamond, J. L. White, and W. L. Dolch. Transformation of Clay Minerals by Calcium Hydraoxide Attack. *Proc., 12th National Conference on Clays and Clay Minerals*, New York, 1964, pp. 359–379.
5. J. L. Eades and R. E. Grim. Reaction of Hydrated Lime with Pure Clay Minerals in Soil Stabilization. In *HRB Bulletin 262*, 1960, pp. 51–63.
6. W. Kronert and K. Wetzel. Reactions of Alkaline Earth Hydroxides with Clay Minerals. *Ziegelindustrie*, Vol. 25, 1972, pp. 562–567.
7. M. M. Sabry. *Mineralogy and Engineering Properties of Com-*

pacted Soil-Lime Mixes. Ph.D. thesis. Oklahoma State University, 1977.
8. S. Diamond. Cement Paste Microstructure—An Overview at Several Levels. Presented at Conference on Portland Cement Paste, University of Sheffield, England, 8–9 April 1976.
9. G. R. Glenn and R. L. Handy. Lime-Clay Mineral Reaction Products. *HRB Record No. 29*, 1963, pp. 70–82.
10. G. H. Hilt and D. T. Davidson. Isolation and Investigation of a Lime-Montmorillonite Crystalline Product. *HRB Bulletin 304*, 1961, pp. 51–64.
11. A. Ariizumi, T. Maki, and M. Oba. *On Stabilization of Kanto Loam by Means of Lime Gypsum Admixtures*. Annual Report of Roads, Japan Road Association, Tokyo, 1962, pp. 22–31.
12. M. C. Anday. Accelerated Curing for Lime Stabilized Soil. In *HRB Bulletin No. 304*, 1961, pp. 1–13.
13. G. I. Baykal. *The Effect of Micromorphological Development on the Elastic Moduli of Fly Ash-Lime Stabilized Bentonite*. Ph.D. dissertation. Louisiana State University, Baton Rouge, 1987.
14. S. D. Wilson. Suggested Method of Test for Moisture Density Relations of Soils Using Harvard Compaction Apparatus. STP 479. ASTM, Philadelphia, Pa., 1970, pp. 101–103.
15. M. R. Thompson. Shear Strength and Elastic Properties of Lime Soil Mixtures. *HRB Record 139*, 1966, pp. 1–15.
16. G. Brown, ed. *The X-Ray Identification and Crystal Structure of Clay Minerals*. The Mineralogical Society of London, London, 1961.
17. M. Mateos. Heat Curing of Sand-Lime-Fly Ash Mixtures. *ASTM Materials Research and Standards 4*, No. 5, 1964, pp. 212–217.

Publication of this paper sponsored by Committee on Lime and Lime-Fly Ash Stabilization.

Frost Resistance of Lime-Stabilized Clay Soil

M. ARABI, S. WILD, AND G. O. ROWLANDS

A frost-susceptible soil (red marl) was treated with various amounts of lime (calcium hydroxide) and cured for up to 24 weeks at different temperatures. Frost resistance of the cylindrical specimens was determined by measuring the frost heave in a controlled freezing environment. Soil-lime specimens with 2 wt% lime were more susceptible to frost action than soil alone—regardless of curing time and curing temperature. However, cured specimens with relatively high lime contents (>2 wt%) showed significant improvement in frost resistance. From previous studies by the authors, it was found that cementitious gel forms and develops in these specimens during curing—increasing the degree of interparticle bonding and producing greater strength. It is suggested that this restricts ice segregation and prevents heave and that frost resistance is dependent on the extent of the formation and growth of the cementitious gel within the cured soil-lime composites.

Strength development and improvement in durability of clay soils by the addition of lime is widely recognized. The pH value of clay soil increases sharply when lime and water are mixed with the soil. Workability improves and plasticity decreases (*1*). These changes occur quite rapidly and are attributed to the adsorption of calcium ions onto the clay particle surfaces, thus causing modification of the electrical double layer and the characteristic flocculation of the fine clay particles to form a workable material.

The particles within each floc are thought to be weakly bonded together by the formation of small amounts of cementitious material at the contact points. Long-term reaction is complex and, according to Diamond and Kinter (*2*), is due to pozzolanic activity between the lime and clay minerals. Cementitious materials comprising calcium silicate hydrate gel and calcium aluminate hydrate are formed during the curing stage.

REVIEW OF PREVIOUS WORK

Wild et al. (*3*) analyzed the cementitious materials formed when a lime clay mixture was cured at different temperatures using techniques of X-ray diffraction, transmission and scanning electron microscopy (TEM and SEM), energy dispersive analysis by X-ray (EDAX), and thermogravimetry (TG). No evidence of the formation of calcium aluminate hydrate was detected in this investigation.

The reaction products were found to be poorly crystalline, even at high curing temperatures [75°C (167°F)] and longer curing periods (1 year). The amorphous products were found to comprise coarse platelets in the early stages of curing, but at later stages they formed fine foils and filaments of an aluminum-containing calcium silicate hydrate gel. This gel was found to bind the soil particles together, resulting in an increase in compressive strength. The increase in compressive strength was found [see work by Arabi and Wild (*4*)] to be directly related to the amount of gel formed.

The formation and growth of the cementitious products were also found to affect the porosity and pore size distribution, which in turn affected the permeability of the reacted soil. These changes in strength, porosity, and permeability, due to the gel formation, are also likely to affect the frost susceptibility of the soil significantly.

Wild et al. (*5*) observed that gel formation leads to an increase in the proportion of pores in the size range of 4 to 40 nm. In a relatively open-textured material, this is likely to lead to a reduction in pore sizes greater than 40 nm as the gel forms. However, the development of the gel does not seem to influence the overall porosity significantly. In fact, the porosity of compacted material was found to increase slightly as the material cured.

The permeability of the soil-lime mixture also changed as curing proceeded. The addition of a small quantity of lime (2 wt%) resulted in a sharp increase in permeability compared with that of compacted lime-free material. This was found to be independent of the amount of gel formed and was probably due to the coarsening of the pore structure and the opening of capillary channels as a consequence of flocculation or soil modification.

At low curing temperatures only a limited amount of gel formation was observed and both porosity and permeability were found to increase with increase in curing time, implying a gradual coarsening of the pore structure with age. At elevated curing temperatures and particularly with higher lime contents and longer curing periods, substantial gel formation was observed. This was associated with a decrease in permeability, but the porosity continued to increase slightly as the gel developed. The population of pores also moved toward the 4- to 40-nm size range. The effect of the growth and development of the microporous gel was, therefore, to shift the pore size distribution toward the finer pore sizes and to block some pores and channels.

It is apparent from this discussion that lime stabilization is likely to affect the frost susceptibility of clay soils by modifying the pore structure and, hence, the permeability and tensile strength of the soil. The mechanism of frost heave is complex, but it is widely recognized that the governing factors are the particle size distribution, the permeability of the soil, the

Department of Civil Engineering and Building, Polytechnic of Wales, Pontypridd, Mid Glamorgan CF 37 1DL, United Kingdom.

availability of water, and the duration of the freezing period. In weakly cemented soils, the tensile strength is also likely to be an influencing factor. Croney and Coleman (*6*) indicated that the addition of a small quantity of portland cement to frost-susceptible granular materials can render them less prone to frost damage without materially affecting their permeability in the unfrozen state.

These materials develop frost resistance because the small level of tensile strength developed is adequate to restrict ice segregation (i.e., it is sufficient to resist the suction forces on the ice phase alone as it tries to expand). Townsend and Klym (*7*) have shown that the frost resistance of cured soil-lime specimens is directly related to their tensile strength, but they contend that the compressive strength may also be used to give an indirect indication. Thompson (*8*) suggested a minimum compressive strength value of 1.4 N/mm^2 (200 lb/in^2) for a saturated soil-lime specimen in order to restrict heave to 2 percent.

In relation to lime content, Brandl (*9*) found that the frost heave in a highly plastic clay (PI = 32.2 percent) and a silty clay (PI = 15.5 percent) increased with the addition of 1 percent lime but decreased with the addition of 5 percent lime and with the curing period. He also noted that the compressive strength of cured specimens decreased after freezing and thawing.

Other researchers [e.g., Allen et al. (*10*), Rosen and Marks (*11*), and Dempsey et al. (*12*)] have shown that the strength of cured specimens decreases with increasing number of freeze-thaw cycles. No doubt, this is due to the rupturing of the bonds between particles as a consequence of ice formation in the freezing zone. It is now also recognized that actual measurement of heave yields a more realistic criterion of assessing frost susceptibility than compressive strength.

Although Dempsey and Thompson (*13*) have shown a linear relationship between heave of test specimens and the number of freeze-thaw cycles (for up to 12 cycles), a simple continuous freezing test is preferred, because this is likely to yield results more quickly. This is the basis on which Croney and Jacobs (*14*) developed the Transport and Road Research Laboratory (TRRL) freezing test to assess the frost susceptibility of road materials. In this test, a limiting heave of 12.5 mm (½ in.) is accepted for compacted cylindrical specimens [100 mm (4 in.) in diameter by 150 mm (6 in.) high] subjected to continuous freezing at −17°C (1.4°F) for 10 days. Through the work of Roe and Webster (*15*), this time has now been reduced to 4 days.

The current work is intended to accomplish the following:

1. To determine the effect that different additions of lime and different curing conditions have on the frost heave of a particular clay soil (Devonian red marl), and
2. To relate the changes in frost behavior of the cured lime-treated soil to changes [previously reported by the authors (*3–5*)] in its porosity, permeability, and strength.

MATERIALS AND TESTING

A local silty clay of the Devonian series (a red marl) was chosen as a test material. Its engineering properties were as follows:

Property	*Amount*
Liquid limit	32–33 percent
Plasticity index	11–12 percent
pH value	6.4
Specific gravity	2.73
Optimum moisture content	12.5 percent
Maximum dry density	1.89 g·cm^{-3} (118.4 lb·ft^{-3})

Its mineralogical components were quartz, feldspar, and illite with traces of chlorite and hematite. The particle size distribution of the soil was determined using a combination of sieve analysis for the coarse fraction (>63 μm) and a hydrometer method for the fine fraction in compliance with British Standard (BS) 1377 (1975). The clay fraction (particles <2 μm) was found to be 12 percent by weight. The lime used was commercially available, high-calcium hydrated lime conforming to BS 890 (1972).

Standard 50-mm (2-in.) diameter by 100-mm (4-in.) long cylinders were prepared with moisture contents of 12 wt% (expressed as a percentage of the total dry weight) and with lime contents of 2, 6, and 10 wt% (expressed as a percentage of the dry weight of the soil), in accordance with BS 1924 (1975). All cylinders were compacted to a constant dry density of 1.89 g·cm^{-3} (118.4 lb·ft^{-3}). Samples were sealed in polyethylene containers, cured at temperatures of 25, 50, and 75°C (77, 122, and 167°F) for periods of 1, 6, 12, and 24 weeks, and then subjected to the freezing test.

The TRRL freezing test equipment was modified to accommodate six standard stabilized soil specimens 50 mm (2 in.) in diameter by 100 mm (4 in.) long as shown in Figure 1. The specimens were first saturated with water in the following manner. The assembled specimens, supported in a polystyrene block, were placed on a metal tray in a vacuum chamber, and their lower ends were immersed to a depth of 15 mm (0.6 in.) in distilled water. They were left in this condition until they showed no further gain in weight. The period of time required for saturation was found to be up to a maximum of 48 hr. Fully saturated specimens were placed in the freezing cabinet with the lower 10 mm (0.4 in.) immersed in water maintained at a constant temperature of 4°C (39.2°F). The cabinet was then placed in a freezing chamber and maintained at a temperature of −10°C (14°F).

Figure 2 gives a detailed illustration of the immediate specimen environment. The temperature directly above the specimen was −10°C (14°F). Vertical movement of the specimens was monitored at regular intervals for seven days, and the heave at this time was taken as an indication of the frost susceptibility of the specimen. Measurements were made relative to a fixed reference point, using a traveling microscope.

Only one frost heave determination was made for each composition and for each curing condition. In addition, two specimens were prepared for each strength test and one specimen for each permeability test. This relatively small number of specimens per test was chosen because of the practical problems associated with preparing, processing, and testing very large numbers of specimens. This was, however, compensated for by careful control of materials, mixing, pressing, curing, and testing. Details of the porosity, permeability, and strength tests performed on these specimens have been reported elsewhere (*3–5*).

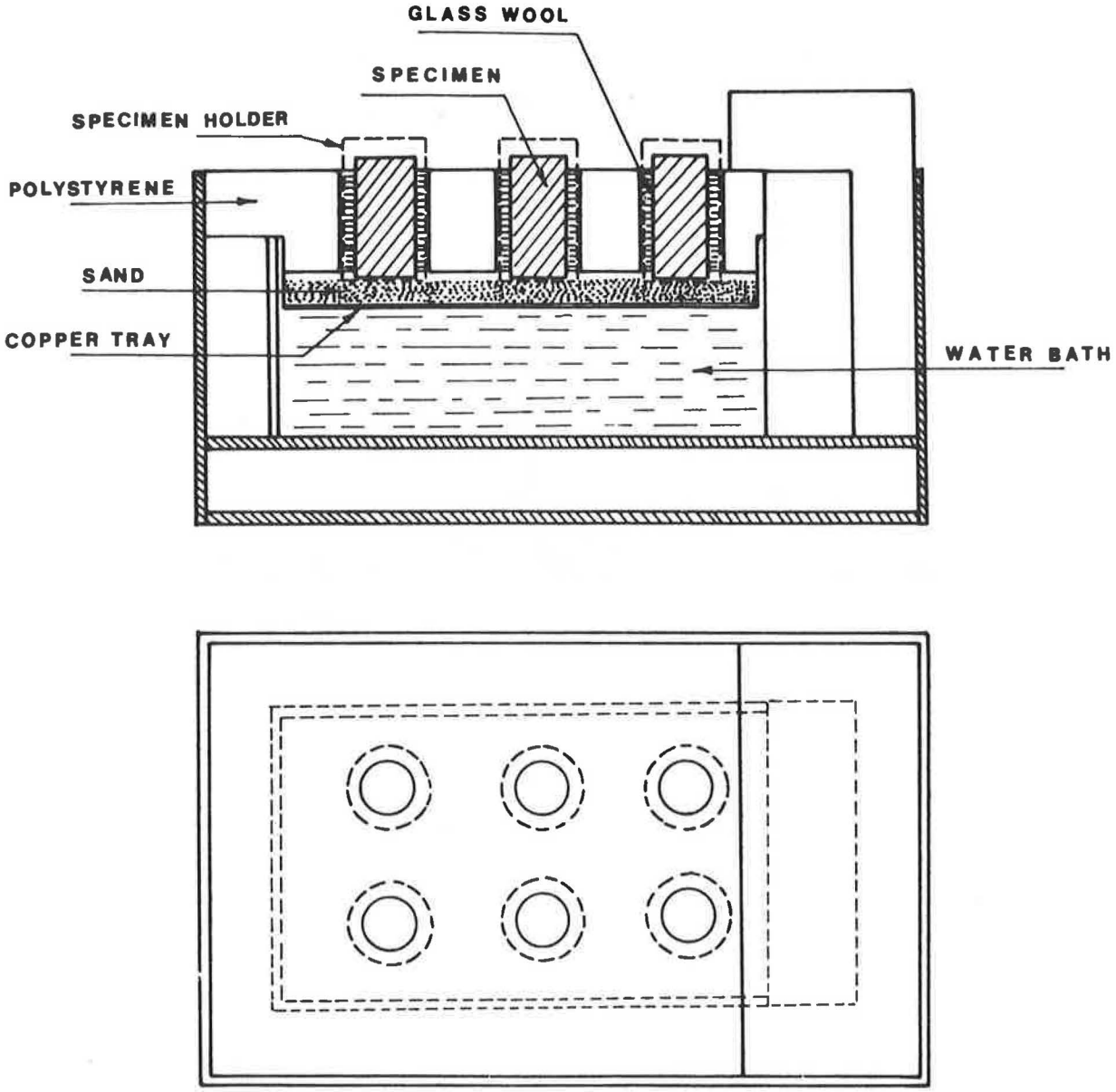

FIGURE 1 Apparatus used to measure frost heave.

DISCUSSION OF TEST RESULTS

Figure 3 shows the heave developed after seven days of continuous freezing versus curing time for samples cured at 25°C (77°F). The heave with 2 percent lime was almost twice the amount that developed for untreated soil and decreased slightly with longer curing times. With 6 percent lime, however, the heave increased slightly after 1 week of curing, but it decreased with longer curing times to a low value after 12 weeks and to zero after 24 weeks. With 10 percent lime, the heave after 1 week of curing was less than that of the untreated soil and decreased to an insignificant value after 12 weeks.

Figure 4 shows the development of heave versus curing time for specimens cured at 50°C (122°F) with the same lime contents as used previously. In this case, the heave developed with 2 percent lime was again about twice the amount developed for the untreated soil after 1 week of curing, but it decreased to less than 80 mm (3.15 in.) after 12 weeks, and to about 70 mm (2.76 in.) after 24 weeks. The material with 6 and 10 percent lime, however, showed a heave of about 20 mm (0.8 in.) after 1 week of curing, and thereafter the heave decreased to zero after 12 weeks.

The results for the material cured at 75°C (167°F) are shown in Figure 5. Here again, the heave that developed with 2 percent lime after 1 week of curing was more than twice the amount that developed with untreated soil, but it decreased thereafter to approximately 40 mm (1.57 in.) after 24 weeks. With 6 percent lime content, however, only a slight heave was observed in specimens cured for 1 week, and heave decreased to an insignificant value in specimens cured for 6 weeks. No heave was observed even after 1 week with 10 percent lime content.

As outlined above, previous studies by Wild et al. (*5*) on the porosity and permeability of these specimens showed a

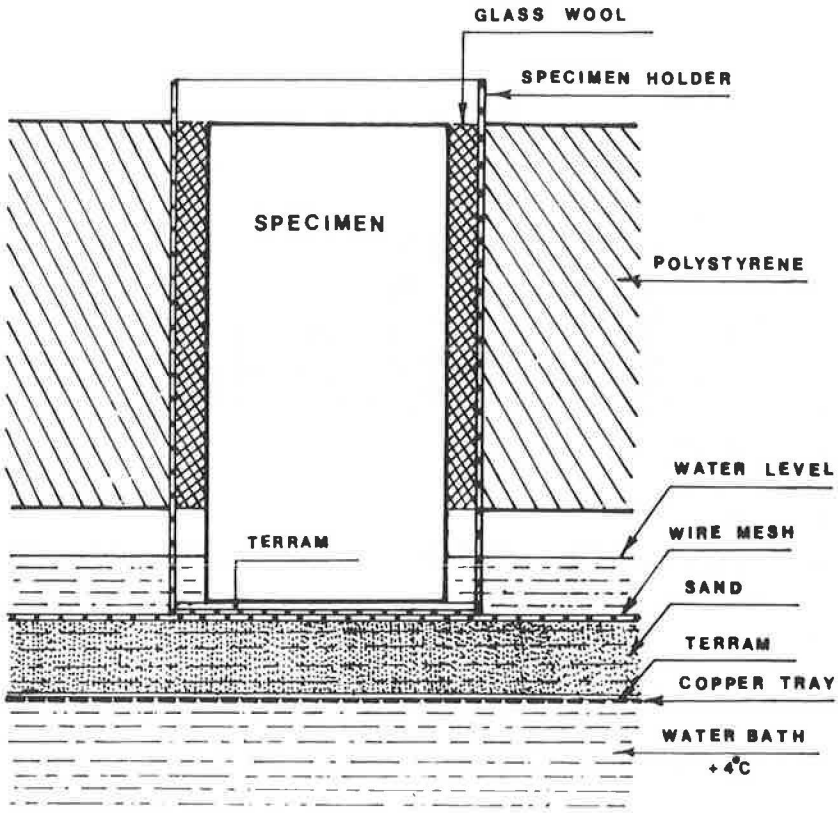

FIGURE 2 Immediate specimen environment during frost heave testing.

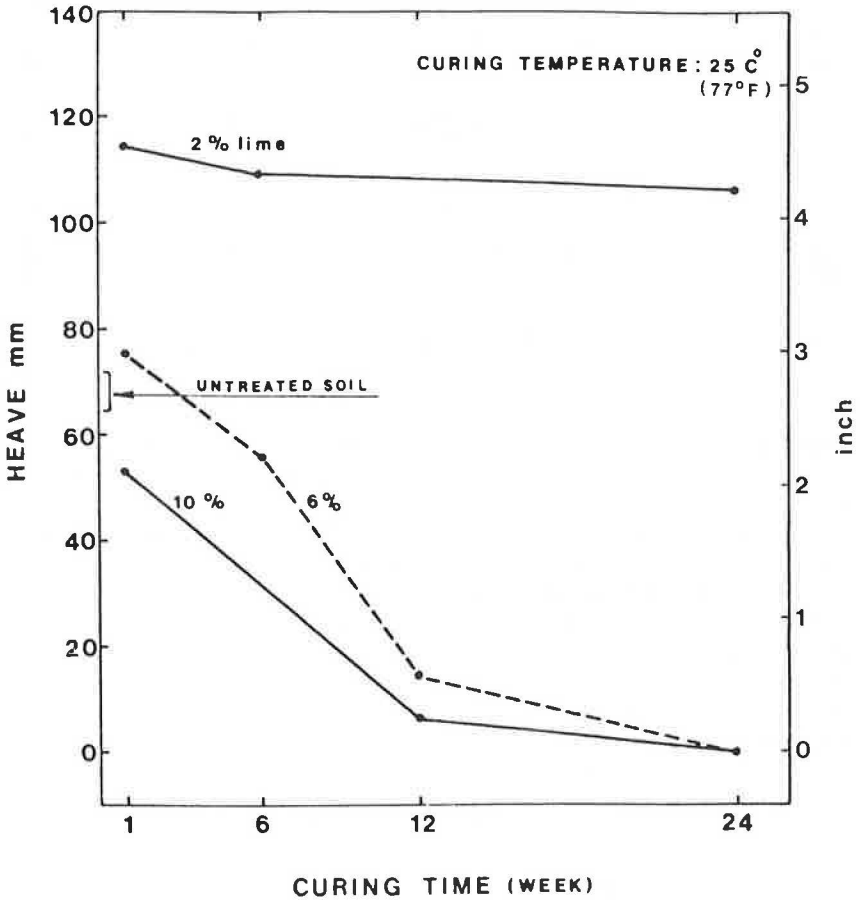

FIGURE 3 Frost heave after 7 days of freezing versus curing time for specimens cured at 25°C (77°F).

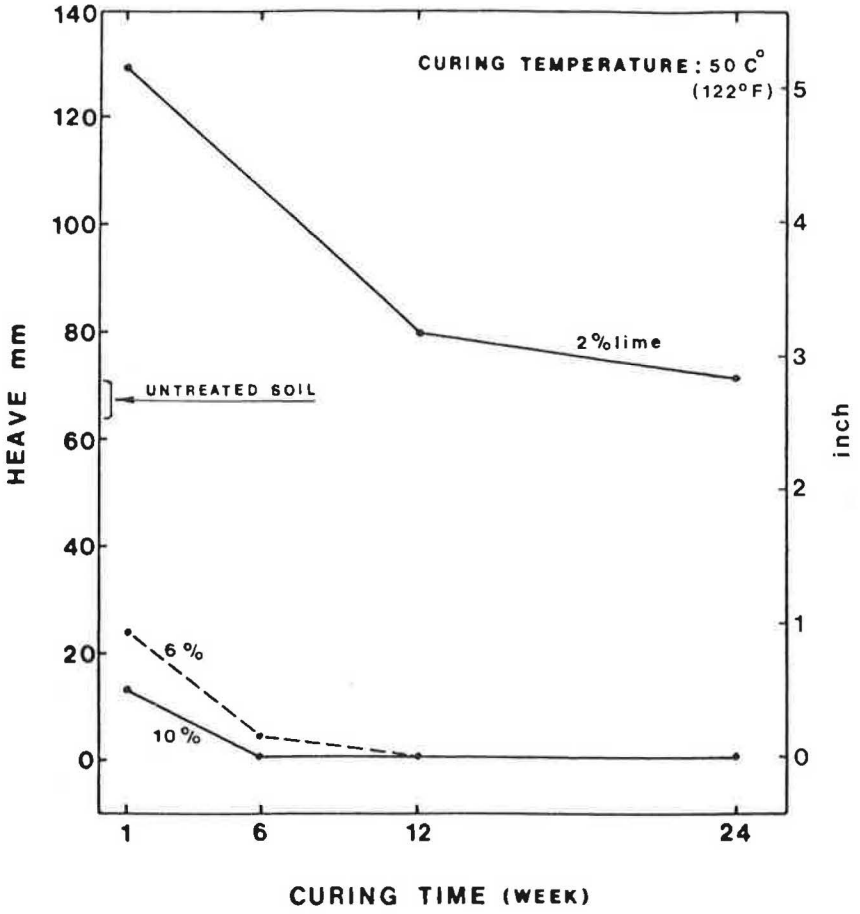

FIGURE 4 Frost heave after 7 days of freezing versus curing time for specimens cured at 50°C (122°F).

general decrease both in porosity and permeability with increasing lime content for lime contents greater than 2 percent by weight. These changes therefore appear to correlate with the observed changes in frost heave behavior.

However, the change in frost heave behavior with curing time did not, in the same way, reflect the changes in porosity and permeability. For example, at 25°C (77°F) curing, permeability actually increased with increased curing time (Figure 6). For higher curing temperatures, permeability was found to decrease only slightly with curing time at 50°C (122°F) (Figure 7), although at 75°C (167°F) curing (Figure 8), the decrease in permeability with curing time was more substantial. Porosity was found to increase with curing time at all curing temperatures.

Evidently, the improvement in frost resistance with curing time for the specimens tested in this study is not principally a function of changes in porosity and permeability. However, continuous development of interparticle bonding occurs with increase in curing time for these specimens, particularly at high lime contents and high curing temperatures. This is apparent from observations of microstructural changes (*3,4*) and compressive strength increases (*3*) previously reported by the authors.

Figures 9–11 show the changes in compressive strength with curing time for specimens with different lime contents cured at different temperatures. The strength developed at low lime content (2 wt%) is very small even at high curing temperatures [75°C (167°F)], whereas strength increases significantly with curing time at the higher lime contents, particularly as curing temperature is increased.

Typical photographs of heaved specimens are shown in Figure 12. The nature of the surface cracking shows a characteristic variation in relation to the degree of interparticle bonding that has developed. For short curing times and low lime contents, only limited interparticle bonding occurs even at 75°C (167°F). The surface (Figure 12a) shows particle agglomerates that are coarse and widely separated close to the unfrozen zone (lower part) and much finer and less widely separated toward the frozen zone (upper part). The spaces between the particle agglomerates are created by the development and growth of ice lenses.

At longer curing times and higher lime contents, even at 25°C (77°F), some interparticle bonding occurs, and the surface (Figure 12b) shows a network of large cracks separating areas that are still essentially coherent. At even higher lime contents (10 wt%) and increased curing temperature [50°C (122°F)], specimens exhibit very limited cracking and retain their original shape and dimensions (Figure 12c).

CONCLUSIONS

From the work reported in this paper, it appears that the addition of a small amount of lime (up to 2 wt%) is likely to

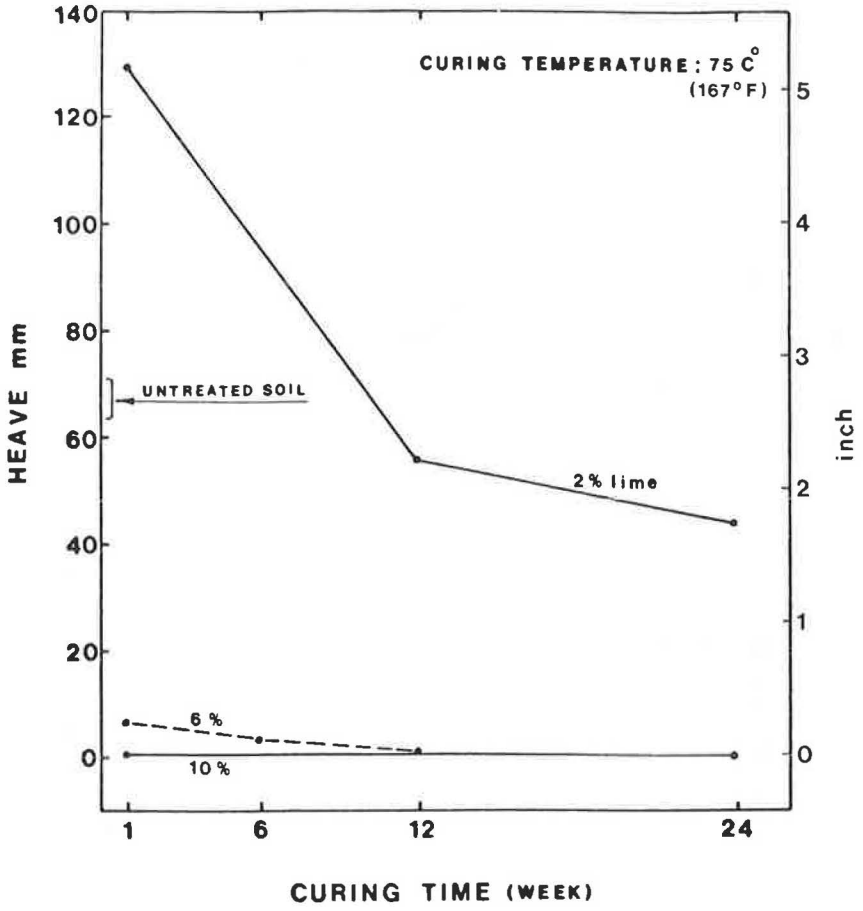

FIGURE 5 Frost heave after 7 days of freezing versus curing time for specimens cured at 75°C (167°F).

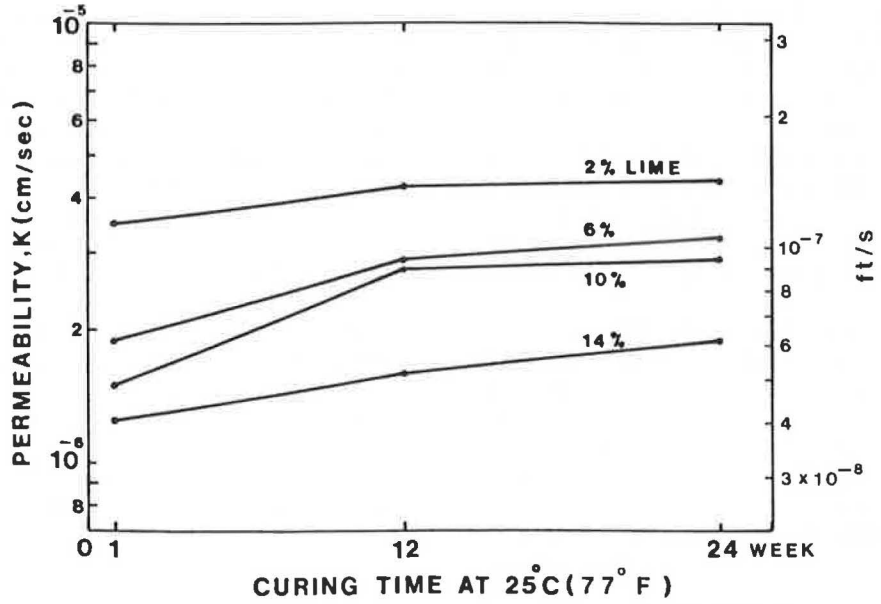

FIGURE 6 Permeability versus curing time for specimens cured at 25°C (77°F).

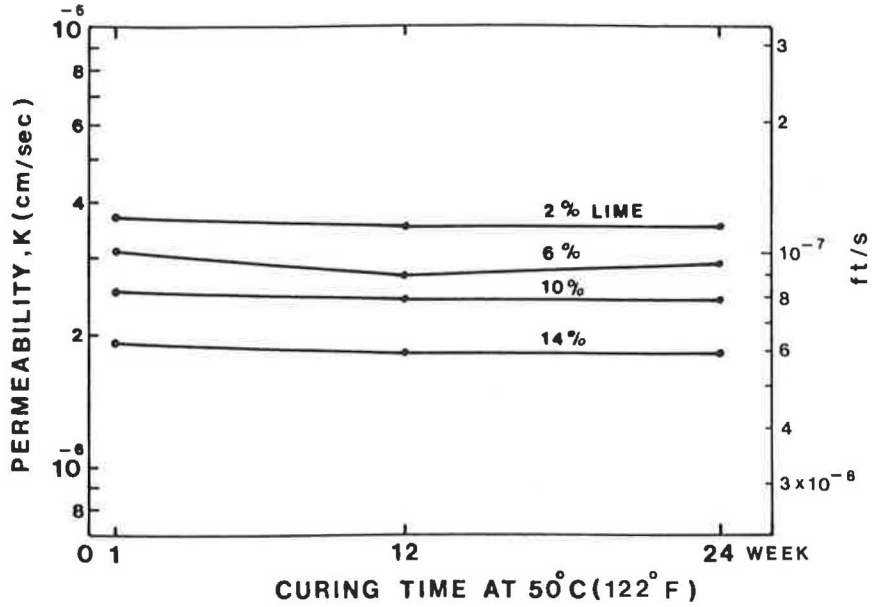

FIGURE 7 Permeability versus curing time for specimens cured at 50°C (122°F).

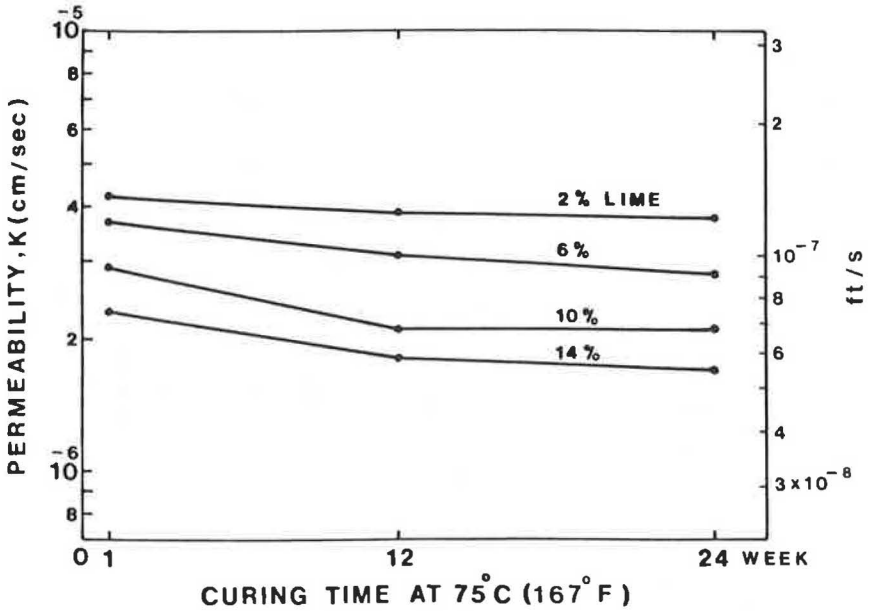

FIGURE 8 Permeability versus curing time for specimens cured at 75°C (167°F).

increase the frost susceptibility of the soil, even after long curing periods and high curing temperatures. It is suggested that this initial sharp increase in the observed frost heave (relative to the heave observed for the untreated soil compacted to the same initial dry density) is a result of the substantial increase in permeability on addition of lime to the soil. The permeabilities of 1-week cured soil cylinders containing 2 wt% lime (see Figures 6–8) are between 4 and 5 times that for untreated soil [0.83×10^{-6} cm·s^{-1} (2.72×10^{-8} ft·s^{-1})]. This increase in permeability following the addition of lime is attributed to the effect of flocculation of the clay particles, which produces a more open and permeable soil structure. Brandl (*9*) observed a similar effect.

The addition of 6 percent or more lime reduces the frost susceptibility of the soil significantly, even at short curing times (1 week) and low curing temperatures [25°C (77°F)] (see Figure 3). Under these conditions, there is negligible cementitious gel formation and only limited interparticle bonding. The reduction in frost heave with increased lime content for specimens cured for these very short periods at low curing temperatures is attributed mainly to the reduction in the permeability of the compacted soil as the lime content is increased above the 2 wt% level (see Figure 6).

It is suggested that the observed improvement in frost resistance with curing time is due predominantly to the development of interparticle bonding, even at the low curing tem-

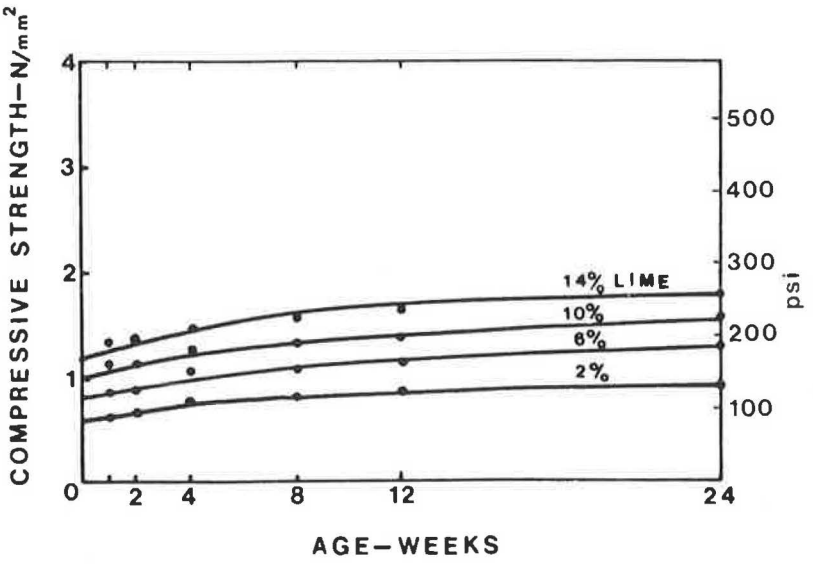

FIGURE 9 Compressive strength versus curing time for specimens cured at 25°C (77°F).

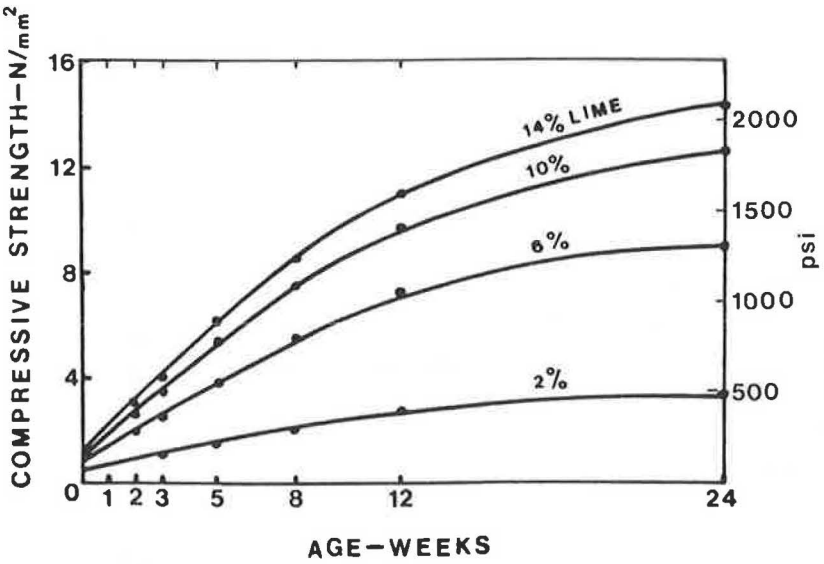

FIGURE 10 Compressive strength versus curing time for specimens cured at 50°C (122°F).

perature of 25°C (77°F), where formation of cementitious material is limited and strength gains are small (see Figure 12). At high curing temperatures (Figure 5) the amount of heave falls off rapidly with curing time. A 75°C (167°F) cured 10 wt% lime-soil cylinder is fully frost resistant within one week, and a 2 wt% lime-soil cylinder experiences less heave than the untreated soil after 12 weeks at 75°C (167°F), even though it is more permeable than the soil alone. This reflects the rapid rate of strength development and interparticle bonding at high curing temperatures (see Figures 10 and 11).

Both permeability and interparticle bonding play a role in determining the frost resistance of soil-lime composites. The development of interparticle bonding during curing improves the mechanical properties, including tensile strength, which restricts ice segregation and reduces heave. The small changes in permeability that occur during curing have a negligible effect on frost heave behavior. This is in contrast to unbonded materials (e.g., soil-lime composites cured for short times at low temperatures), in which frost resistance is dictated mainly by the permeability of the materials.

It would appear from this investigation that, under conditions of high ambient temperatures often met in the summer in arid regions, only relatively short periods of curing are required to protect clay soils from the problems of heave often experienced in winter—as long as the lime added to the soil is above an optimum level (6 wt% in the present work). Hence, whenever an improvement in the frost resistance of

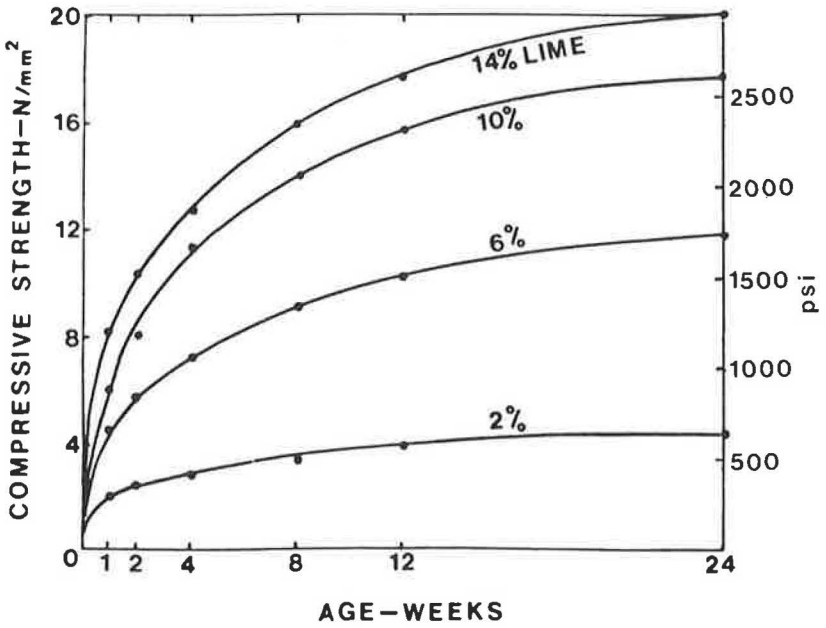

FIGURE 11 Compressive strength versus curing time for specimens cured at 75°C (167°F).

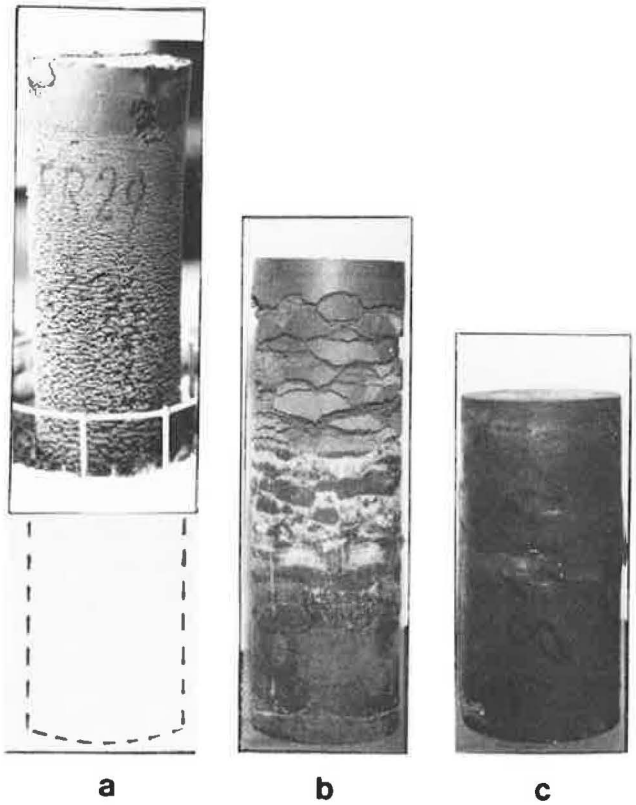

FIGURE 12 Frost heave and cracking of soil-lime cylinders: (a) 2% lime cured for one week at 75°C, (b) 6% lime cured for 6 weeks at 25°C, and (c) 10% lime cured for 6 weeks at 50°C.

road materials such as the subgrade is required, lime stabilization should be considered as an appropriate solution, particularly if the work can be carried out in warm weather.

REFERENCES

1. G. O. Rowlands, M. Arabi, and R. Delpak. Lime and the Plasticity of Clays. *Journal of the Institution of Highways and Transportation*, Vol. 34, No. 5, 1987, pp. 21–24.
2. S. Diamond and E. B. Kinter. Mechanisms of Soil-Lime Stabilization. In *Highway Research Record 92*, HRB, National Research Council, Washington, D.C., 1965, pp. 83–102.
3. S. Wild, M. Arabi, and G. Leng-Ward. Soil-Lime Reaction and Microstructural Development at Elevated Temperatures. *Clay Minerals*, Vol. 21, 1986, pp. 279–292.
4. M. Arabi and S. Wild. Microstructural Development in Cured Soil-Lime Composites. *Journal of Materials Science*, Vol. 21, 1986, pp. 497–503.
5. S. Wild, M. Arabi, and G. O. Rowlands. Relation between Pore Size Distribution, Permeability and Cementitious Gel Formation in Cured Clay-Lime Systems. *Materials Science and Technology*, Vol. 3, Dec. 1987, pp. 1005–1011.
6. D. Croney and J. D. Coleman. Pore Pressure and Suction in Soil. *Proc., Conference on Pore Pressure and Suction in Soils*, London, 1960, pp. 31–37.
7. D. L. Townsend and T. W. Klym. Durability of Lime-Stabilized Soils. In *Highway Research Record 139*, HRB, National Research Council, Washington, D.C., 1966, pp. 25–41.
8. M. R. Thompson. Lime Stabilization of Frost-Susceptible Soils. *Frost I Jord*, 1973, pp. 45–52.
9. H. Brandl. Alteration of Soil Parameters by Stabilization with Lime. *Proc., 10th International Conference on Soil Mechanics and Foundation Engineering*, Stockholm, Vol. 3, 1981, pp. 587–594.
10. J. J. Allen, D. D. Currin, and D. N. Little. Mix Design, Durability, and Strength Requirements for Lime-Stabilized Layers in

Airfield Pavements. In *Transportation Research Record 641*, TRB, National Research Council, Washington, D.C., 1977, pp. 34–41.
11. W. J. Rosen and B. D. Marks. Cold Weather Lime Stabilization. In *Transportation Research Record 501*, TRB, National Research Council, Washington, D.C., 1974, pp. 35–41.
12. B. J. Dempsey and M. R. Thompson. Vacuum Saturation Method for Predicting Freeze-Thaw Durability of Stabilized Materials. In *Highway Research Record 442*, HRB, National Research Council, Washington, D.C., 1973, pp. 44–57.
13. B. J. Dempsey and M. R. Thompson. Durability Properties of Lime-Soil Mixtures. In *Highway Research Record 235*, HRB, National Research Council, Washington, D.C., 1968, pp. 61–75.
14. D. Croney and J. C. Jacobs. *The Frost Susceptibility of Soils and Road Materials*. Report No. 90. U.K. Transport and Road Research Laboratory, Crowthorne, Berkshire, England, 1967, pp. 1–68.
15. P. G. Roe and D. C. Webster. *Specification for the TRRL Frost-Heave Test*. Supplementary Report 829. U.K. Transport and Road Research Laboratory, Crowthorne, Berkshire, England, 1984, pp. 1–17.

Publication of this paper sponsored by Committee on Lime and Lime-Fly Ash Stabilization.

Stabilization of Expansive Clay Soils

THOMAS M. PETRY AND J. CLYDE ARMSTRONG

Natural hazards cause billions of dollars of damage to transportation facilities each year—only flooding causes more damage than expansive soils. Nearly all types of transportation facilities have been affected by expansive soil behavior and, as a result, many have failed or are no longer serviceable. It is imperative that the damage caused by expansive soils be controlled, and proper application of soil stabilization methods can significantly reduce the damage that results from these problem soils. The purpose of this presentation is to discuss the phenomena associated with stabilizing these soils, their behavioral patterns that affect stabilization, and the initial and remedial stabilization methods that can be applied to them. The factors considered include conditions requiring and allowing stabilization, changes of properties with time, the effects of stress history and desiccation, the influence of climate, and the effects of physicochemical environments. Effects that can be improved by stabilization are pinpointed. Stabilization methods are described that improve selected properties of expansive soils by mechanical and chemical means. Well-established methods are discussed along with those that are very promising. Examples of remedial treatments are discussed. It is concluded that there is a need for analyses of all alternatives and for stabilization during construction rather than costly remedial projects. Research needs are outlined that can improve our understanding of the stabilization requirements of these problem soils.

It has been estimated that the damage to the infrastructure caused by natural hazards may account for direct costs of at least 1 percent of the gross national product. The damage caused by expansive soils is surpassed only by that resulting from flooding. Expansive soils are found in every state and cover approximately one-fifth of the land area; however, if soil stabilization is widely adopted, the billions of dollars of damage that occur each year can be significantly reduced. These efforts may reduce the new construction losses by 75 percent and overall losses by approximately one-third by the year 2000 (*1*).

Few transportation facilities are immune to problems associated with expansive soils. Roadways and runways have suffered from destructive differential movements caused by these soils. The nature of these soils has led to many slope failures, and retaining walls and bridge abutments have experienced extreme distortion and have been overturned by swell pressures associated with these soils. Track systems have been moved out of alignment, both vertically and horizontally, by the effects of expansive soils, and port facilities have been affected by both the power and the amount of volume change. Even pipelines have had their share of damage, as exhibited in changes in alignment and crushing. It is imperative, therefore, that the detrimental effects of these problem soils be controlled or limited.

The object of this paper is to look at the phenomena associated with stabilizing expansive soils, the problem behavioral patterns of these soils, the possible and most efficient stabilization methods, and remedial stabilization methods. It is important to realize that problem soils can be successfully and economically stabilized, especially when the costs of probable damage and remedial corrections are taken into account. Traditionally, only stabilization methods well-proven or accepted have been used. This has meant that, in some cases, more effective and economical methods were not considered because they were less well-known. One of the purposes of this presentation will be to discuss those methods now commonly used and to propose others, less well known but also effective, that may be used. It is not the intention of the authors to provide new and innovative methods, but to promote the consideration and use of all alternative methods.

PHENOMENA AFFECTING STABILIZATION

The phenomena associated with expansive clay soils that affect stabilization include (a) the specific clay mineralogies present, (b) the stress histories of the respective soil masses, (c) the desiccation histories of the subgrades, (d) the climates where these soils are found, (e) the property changes that occur in these soils with time, and (f) the physicochemical environments existing in the soil masses and around the clay particles. For some of these phenomena, soil stabilization can be used to improve the properties of the soil masses.

The effects of particular clay minerals are, for the most part, well-known and documented (*2*). The clay minerals present are not normally determined during the investigation procedures used, but certain clay minerals, including those from the smectite, illite, and (sometimes) chlorite families, are known to exhibit expansive characteristics. Of these, the members of the smectite family have proven to be the most active. It is not likely that stabilization can totally change the clay minerals present, but their effects can often be lessened.

Those phenomena that relate to particular stress histories and desiccation cannot be changed by stabilization. One must take these effects into consideration during analyses of methods that may work for particular situations. Generally, these methods are known to increase the expansive nature of the soil masses because of the residual stress release that occurs with time, diagenetic bond releases that result in long-term heave, strength loss with time, and the general fractured nature of the soil mass as a result of desiccation stresses (*3*).

The effects of climate on the behavior of expansive clay

Department of Civil Engineering, University of Texas at Arlington, P.O. Box 19308, Arlington, Tex. 76019.

soils are known to be extremely important (*4*). In climates that provide natural moisture year round or a continuously dry environment, the associated long-term soil mass moisture changes are minimal. Semiarid climatic conditions lead to the most damaging behavior of expansive clays. This climate provides significant periods of both wetting and drying, which, in turn, will cause both swelling and shrinkage of active soils each year. Over a number of years or cycles, this causes the soil subgrade to become fissured, and many facilities tend to experience significant differential movements. The effects of all climatic situations on expansive soils must be considered during design analyses and may very well need to be overcome by stabilization methods in areas where seasonal moisture variations occur.

The phenomena associated with property changes that occur in expansive clay soils include (a) shear strength losses as the soils take on moisture and release negative pore pressures, (b) changes in volume change characteristics as in situ conditions change in subgrades between initial sampling and the construction phase, (c) alterations to soil properties as these materials are remolded during construction, (d) changes to soil mass macrostructures that occur during the cyclic processes caused by climatic conditions, and (e) changes that occur as the result of variations in stress during construction. Most of these property changes are well documented and can be considered during design analyses, and a number of these can be overcome or used as part of stabilization methods.

The physicochemical environment around and inside expansive clay particles has much to do with how these particles react to changes in load and moisture levels. Physical environmental factors include dry unit weight, soil mass particle microstructure, soil mass block or clod macrostructure, overburden pressures, load-induced pressures, soil mass porosity, soil mass block or clod porosity, moisture levels at the time of construction, and relative exposure of parts of the soil mass to drying or wetting. The environmental factors that are of a chemical nature have to do with the type and concentrations of cations both inside clay particles and in the water around these particles. Most of the effects of physical environmental factors are well known; however, the effects of chemical factors are still understood only in gross terms (*5*).

The combined effects of overburden, dry unit weight, and water content on the expected expansion of active clay soils are shown in Figures 1 and 2. Figure 1 shows the relationship of water content at the beginning of swell versus the relative amount of swell that occurs for differing overburden pressures. As the magnitude of overburden increases, the amount of swell for any water content decreases. In addition, it can be seen that there is some water content for each magnitude of overburden where the swell that occurs is minimal or nonexistent. Figure 2 is a three-dimensional plot of how the amount of swell is related to both dry unit weight and water content at construction. The general trends illustrated in Figure 2 form a surface, which explains behavioral patterns. The amount of swell occurring is directly related to the dry unit weight and inversely related to water content.

Soil particle orientation causes the most volume change to develop perpendicular to the flat surfaces of the particles. This would lead one to deduce that a parallel structure would cause the most volume change in the direction perpendicular to these particle surfaces and that much less would occur in the direction parallel to the particle edges. It is well documented that the vast majority of swell or volume change in these soils happens between the clay mineral layers, so that soil particle orientation has a significant effect on swelling (*2*).

The effects of soil structure are far more complex than described above, however. Actual soil subgrades are not only made up of discrete clay particles but also include packets of clay particles that lie together (like the pages of a book) and may be made less homogeneous by the presence of cracks, fissures, and slickensides. All these features make up the pattern of blocks, columns, and clods of soil particles called the macrostructure. The particular amount of volume change that occurs is therefore affected by the complex orientation of clay particles and the relative compressibility of the soil mass in each direction caused by macrostructure features. The relative porosity and permeability of the soil mass in each direction are also affected by its micro- and macrostructures, and the ease with which the clay will gain and lose moisture is directly related to these porosities and permeabilities.

Another physical factor that affects the behavior of expansive clay soil subgrades is their relative exposure to concentrated drying and wetting. These situations lead to the most damaging type of soil mass movements, because transportation facilities will endure significant differential shrink and swell. Those situations in which concentrated wetting occurs include improper drainage and cracks through the facilities that allow concentrated infiltration of moisture. Nonuniform exposure to rainfall and runoff will eventually cause nonuniform movements. Concentrated drying occurs where the soil mass is exposed differentially to climatic effects and to the roots of large bushes and trees. It has been established that tree roots have a drying effect that extends at least as far from the tree as it is tall and, in many cases, much farther (*6*).

Many of the physical environmental factors affecting the behavior of expansive clay soils can be modified and controlled by stabilization methods. These methods are usually of the mechanical type.

As important as the physical environment factors are to the behavior of expansive clay soils, the chemical environment around and inside clay particles affects their behavior much more profoundly. Differences in this environment can cause an expansive clay to have high volume change potential or to have none at all. Depending on the type and concentration of cations associated with the clay, these behavioral patterns exist. The capacity of a clay soil to associate with cations is determined by its cation exchange capacity (CEC), and the capacity of cations to have water associated with them is dependent on type.

The most active clays are those with sodium cations in their exchange complex, or cation exchange sites. The least active generally have bivalent cations, which have the least affinity for water. In addition, the types and concentrations of cations in the water around the clay particles will affect the ease with which water can move into and out of the clay. Cation concentrations in the exchange complex also affect the flocculation of clay particles, thereby affecting clay behavioral patterns. Finally, there are chemicals in the soil or that may be added to the soil that affect the way water is held by clay particles and in the pore water, thereby affecting the volume change behavior of the clay, which is directly dependent on

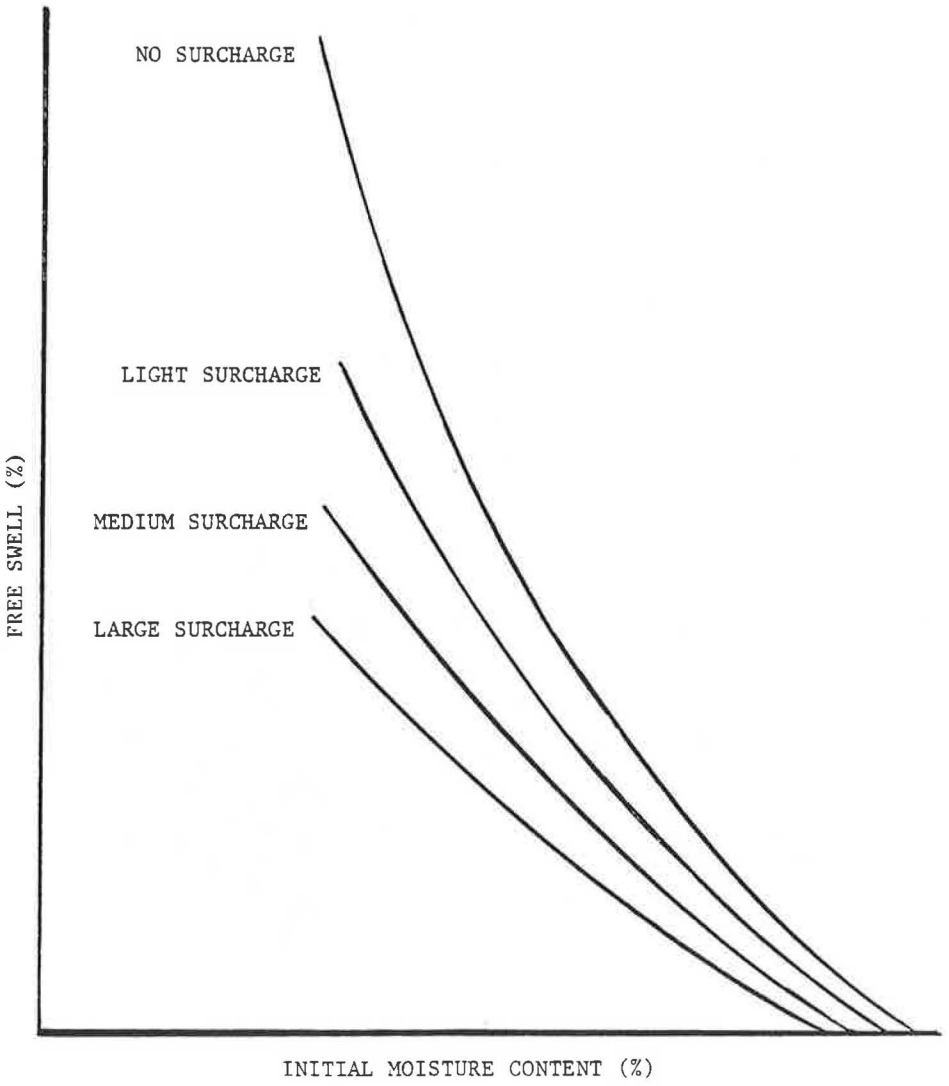

FIGURE 1 Free swell with overburden versus initial moisture content.

water content change. It can be seen that chemical stabilization, which changes the environment around and inside the clay complex, will have an important influence on the behavior of these soils (*5*).

One may conclude, considering the factors affecting expansive clay soil behavior, that several problems must be overcome by stabilization methods. These include the effects of heave, the cyclic and differential effects of shrink and swell, the changes of properties (such as shear strength) with time, and the prediction of behavior during design procedures. The rest of this presentation will deal with how all but the last of these may be dealt with by using stabilization methods.

MECHANICAL STABILIZATION METHODS

Mechanical stabilization includes all improvements to either soil or soil mass properties without the addition of stabilizing agents. The central idea of mechanical stabilization of expansive clay soils is production of a soil or soil mass that (a) will not or cannot change in volume, (b) has sufficient strength to safely sustain the loads applied to it, or (c) causes no damage to transportation facilities as its volume changes. The possible methods for each of these conditions will be discussed in turn.

A preferred or stable swelled condition will eventually develop naturally in nearly all expansive soil subgrades because water will migrate into the system. It makes sense then to provide this level of moisture during construction, and this may be done for natural or cut subgrades by prewetting them to the desired levels of moisture. This has been accomplished with some degree of success by ponding, but most successfully by injecting water that contains surfactants. Prewetting of expansive soil subgrades by transfer of ponded water to sufficient depths into the ground can take months to accomplish satisfactorily; however, injection of moisture into these subgrades may be successfully accomplished in only weeks. For the injections to work, the subgrade needs to be somewhat fractured. As many as four passes may be made during the injection process, and if these are spaced at, say, 4-day intervals, significant water content change will occur (*7*). Another advantage of the injection process is the depth to which the

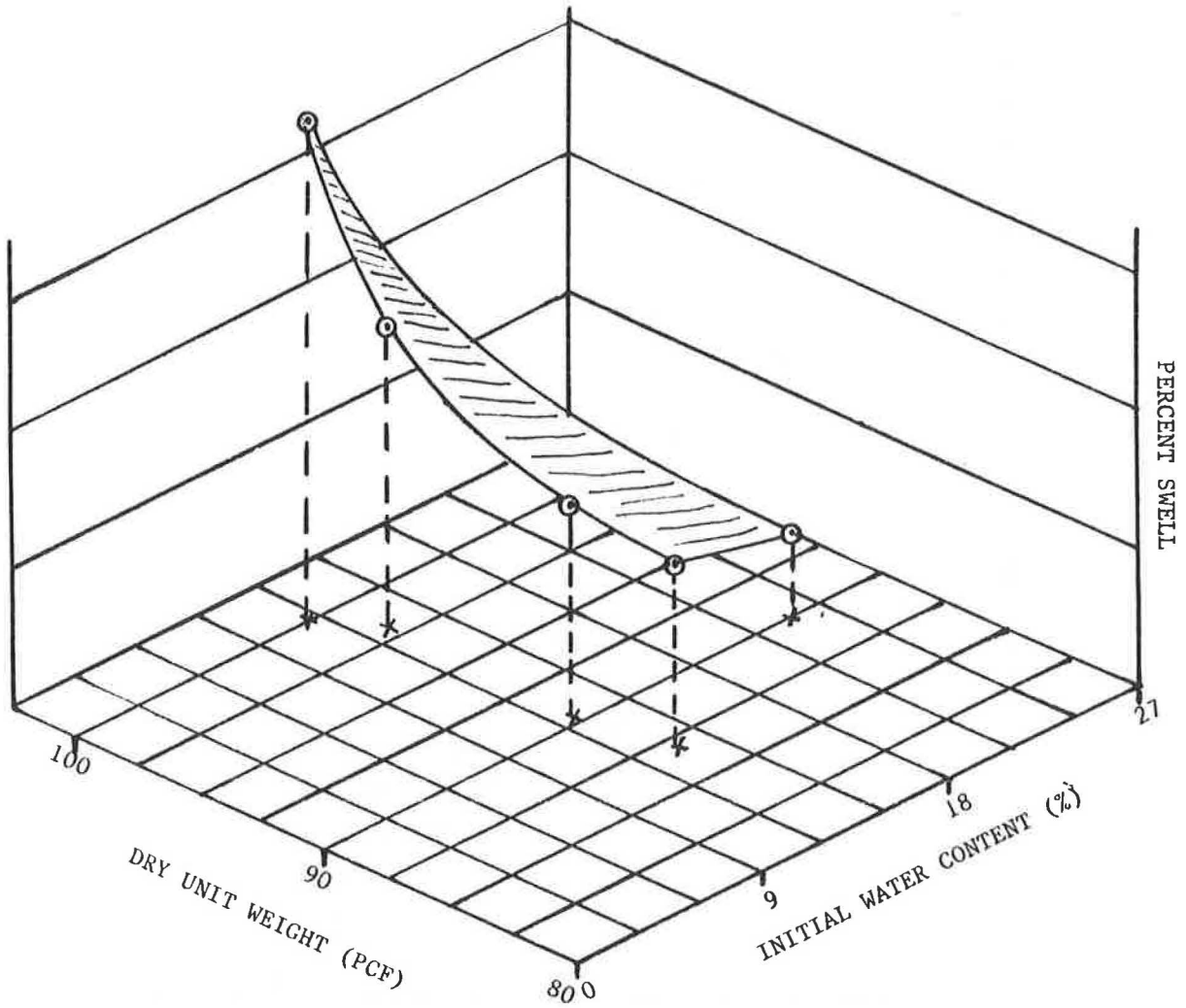

FIGURE 2 Percent swell versus dry unit weight and initial water content.

subgrade is preswelled, which may be from as little as 5 ft to as much as 10 ft, normally.

When one is constructing a fill of expansive soil, establishment of these preferred moisture levels is a matter of controlling compaction water content. Compaction moisture contents above the optimum will provide a subgrade that will have little swell potential in most cases, with the practical limit being 4 percent above optimum because of difficulties with compaction and equipment movement. One danger of high water contents during compaction is the buildup of excessive pore water pressure in high fills. Because of these factors, one may compact these high fills at lower water contents and provide time for them to achieve their preferred levels of moisture naturally before the facility is finished. Monitoring of soil suction and pore pressure levels would be advisable in these cases (*2*, *7*, *8*). Once a stable moisture level is achieved in subgrade soils, it is then necessary to ensure that it will not change significantly during the life of the facility.

Maintenance of nearly constant moisture levels in expansive soil masses includes deletion of those previously described conditions that result in concentrated wetting or drying. Special attention should be paid to proper drainage grading, placement of large bushes and trees, handling of facility water runoff, and draining of retaining wall backfill. One recently well-proven concept for retention of established stable levels of moisture is the vertical moisture movement barrier. These barriers are constructed using asphalt, recycled chips of rubber, well-densified lean concrete, lime slurry pressure injection (LSPI), and relatively thick sheets of polyvinyl chloride (PVC) or geomembranes. All of these, except the recycled rubber and LSPI barriers, have performed extremely well. The effects of LSPI will be discussed in the section on chemical stabilization. Figures 3 and 4 show this concept of moisture maintenance, which maintains moisture levels by encapsulating the soil mass and thus removing sources of change (*8–11*).

Other methods used to limit the movement of expansive soils have to do with imposed loads and the internal compressibility of the soil structure. Expansive clay soils are compacted at dry unit weights that are lower than normally acceptable for a particular application to lessen the effects of swelling. A common type of specification may call for at least 90 percent, but no more than 95 percent, of maximum dry unit weight established by the Standard Proctor test at water contents of at least optimum, but no more than about 4 percent above optimum. The reason for limiting the range of water

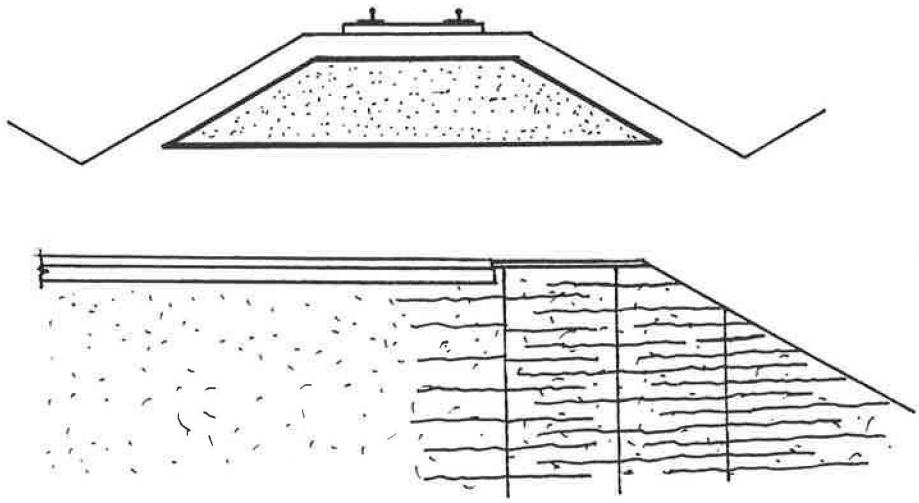

FIGURE 3 (*top*) **Encapsulation with asphalt membrane;** (*bottom*) **injected moisture movement barrier.**

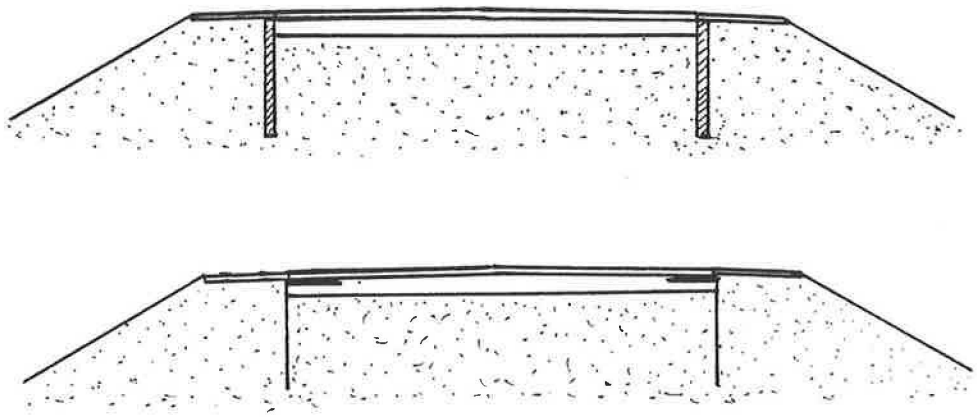

FIGURE 4 (*top*) **Lean concrete moisture movement barriers;** (*bottom*) **PVC moisture movement barriers.**

content is to provide adequate compacted dry unit weight, as shown in Figure 5.

In some applications, this percentage of maximum dry unit weight could be even lower than 90 percent, but few are willing to risk the possibility of low soil shear strength and increased compressibility. With appropriate testing, the impact on these properties of lowering percentages of compaction could be assessed. The reduction of compaction requirements, therefore, can reduce the effects of swelling. The other method of limiting swell is the use of soil mass contact pressures imposed by the facility that are as high as or higher than the soil's swelling pressure. In this way, theoretically, no swell can occur. It should be recognized that these measures do not prevent shrinkage from occurring, however. Both of these methods have been applied with good success in differing types of transportation facilities (*6*, *12*).

The first three types of stabilization for expansive clay subgrades and slopes might not be considered actual stabilization, but rather maintenance of stable conditions. It makes sense for soil subgrades to be stable in both water content and strength before facilities are placed on them. In this way, the changes in soil properties that may occur with increases of moisture level will be eliminated. Prevention of swelling will provide the shear strengths on which the original designs were made. The actual methods used to accomplish these conditions have been discussed above.

Strength for slopes and backslopes is often underdesigned in transportation facilities. The strength actually used is that determined as peak strength during direct shear and triaxial shear tests. In actuality, the shear strength at failure of the soils involved can be as low as the residual strength, and the residual strength is significantly lower than the peak strength. Several processes cause this phenomenon to occur: gradual stress release, loss of soil suction potential, and increase of moisture levels during cyclic shrinking and swelling caused by climate. Soil stabilization during these processes includes proper selection of testing conditions to establish the real strength to be expected for the field soil mass.

Another way of maintaining stable subgrades for transportation facilities is proper isolation of the subgrade from both construction and operating loadings. During construction, the use of self-propelled compaction equipment may lead to fracturing of subgrade soil layers, particularly when these layers are made of friable chemically stabilized soils. The fractures

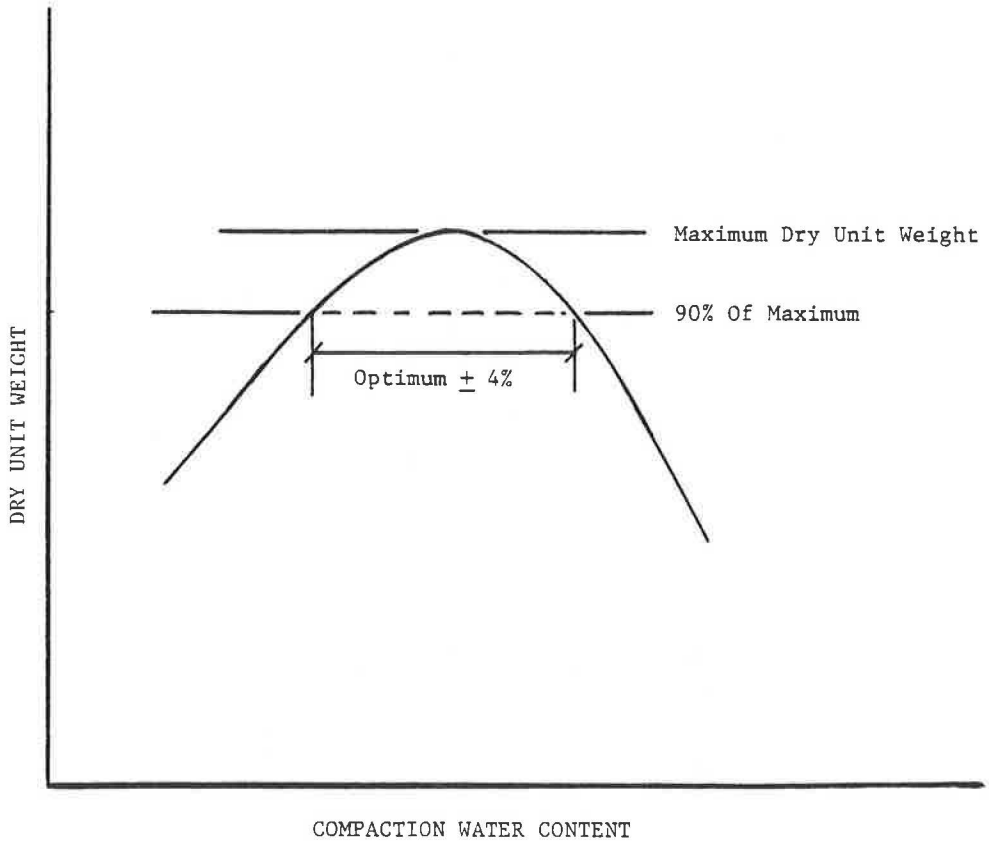

FIGURE 5 Example of compaction water content controls.

that result allow moisture to infiltrate both the stabilized layer and the nonstabilized soils below. This process eventually leads to swelling, which further fractures the stabilized subgrade, allowing large quantities of moisture to infiltrate, and so on (Figure 6).

The initial fracture can be prevented by proper operation of construction equipment to prevent continual direction reversals of self-propelled rollers at nearly the same place. Isolation of soil subgrades from excessive loadings caused by operational situations is well understood and should be based on adequate determination of real subgrade strengths and operational loads prior to design (*4*). When operational loadings exceed those used for design, fracturing of the subgrade and the facility will likely lead to swelling and softening, as described earlier.

These prevention measures are normal to the design process, because the damage that might result is most severe in expansive clay subgrades. The most obvious mechanical stabilization method to prevent damage in the design process is to bridge over the movements expected of the expansive soil mass. Such designs support the facility deep in the soil mass where volume change will not occur and separate the facility from the part of the soil mass that will change in volume. The design usually includes types of pier and beam structures, supported initially near the surface by degradable cartons and structurally designed to transmit the imposed loads to pier elements. Another method is used for the backfill behind retaining walls. The expansive soil mass surface behind the wall is cut back to at least 45 degrees from the horizontal, so that as it swells, it will not impose loads on the wall. The remaining backfill material is made of nonactive, free-draining material, and a system of weep holes and filter-protected drains is installed at the base of the wall in the backfill (Figure 7). The remaining method includes design of the facilities to take the expected movements without loss of service or significant damage. Of course, this method cannot be used when the alignment and grade of the facility are critical, but where movement can be figured and allowed, it is a workable concept. One example is retaining wall elements that will not suffer loss of function or cause failure under these circumstances.

CHEMICAL STABILIZATION METHODS

Chemical stabilization for expansive clay soil property improvement consists of changing the physicochemical environment around and inside clay particles, changing the nature of the water that moves into and out of the voids, and effecting behavioral changes in the soil mass as a whole. These methods include making the clay require less water to satisfy the charge imbalance, making it difficult for water to move into and out of the system, flocculating the clay to cause aggromulation, and, perhaps, cementing particles together to reduce volume change. If chemical stabilizing agents are mixed intimately with soil layers, it may be desirable to apply compaction aids to improve achievable dry unit weight after heavy flocculation of the clay. When such agents are injected into the soil, surfactants are added to the agent slurries to lower their surface tension characteristics. In addition, electroosmosis has been

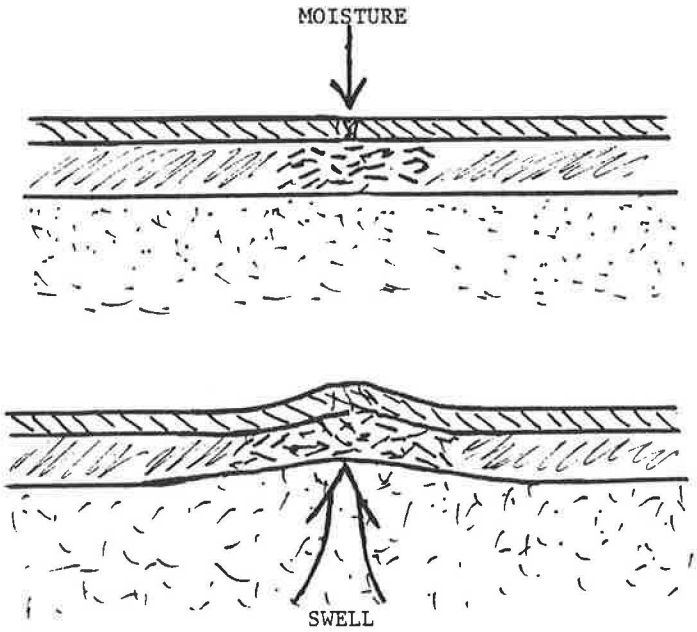

FIGURE 6 (*top*) **Construction fracturing;** (*bottom*) **subgrade swelling damage.**

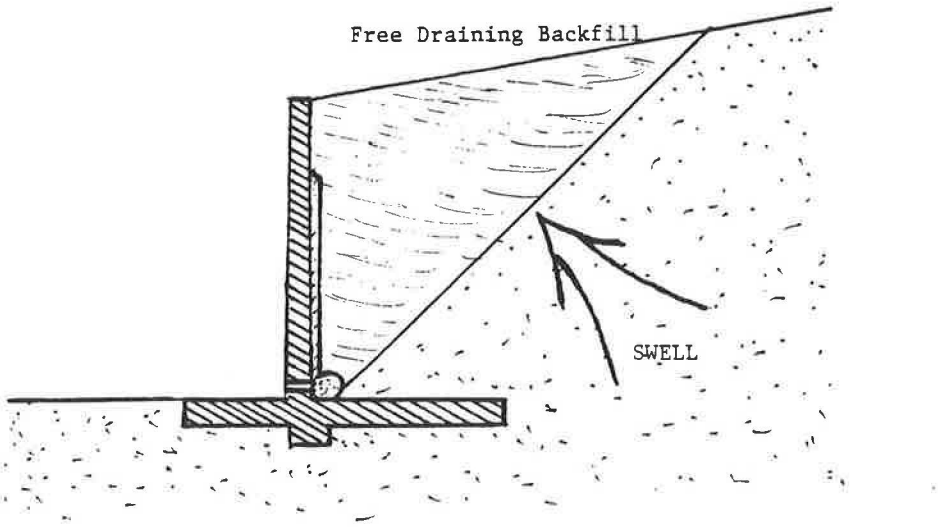

FIGURE 7 Retaining wall backfill treatment.

used to a limited extent with some success to supply cations to expansive clay soil subgrades. It would be most advantageous if the agents were effective as surface treatments, but few, if any, are (*4*).

Probably the most effective chemical stabilization of expansive clays occurs when the cations associated with the natural clay are exchanged for types that are bivalent or have low affinities for water. Many types of cations have been researched, but the most effective and readily available for use is calcium. Potassium has been proven somewhat useful at reducing the swell capacity of these clays and, in some cases, has been found to cause smectites to act and even look like illites in x-ray diffraction analyses. The exchange process is dependent on several factors, of which soil pH, cation concentrations, and temperature are most important. It is important to note that this process of cation exchange alone will not render these clays nonexpansive in behavior.

Another outcome of the cation exchange process is the accumulation of exchanged cations around the clay particles in the associated and free pore water. This ion crowding is believed to be a major contributing force to further reduce active clay behavior. The many cations in the water around the clay will significantly restrict the passage of water into and out of the clay particles. These two phenomena together cause the soil to behave, in some cases, nonexpansively.

The flocculation, or as some might call it, superflocculation, of the clay particles that occurs at the same time as cation exchange has a further stabilizing effect. The clay particles are somewhat more tightly held together by this phenomenon and therefore exhibit less active behavior. In addition, this

process tends to assist in the waterproofing of the clay. Agents that have cementing properties would work in these clays, also.

One of the problems associated with flocculation is a lowering of the compactibility of these clays, resulting in significant losses in the dry unit weights achievable. To help overcome these losses, compaction aids, which are usually made of sodium compounds, are added in small quantities to the compaction water. It is believed that these aids reduce the flocculation enough to improve the compactibility of the soil to that in its natural condition.

Many inorganic and organic agents have been tested as stabilizers for expansive clay soil. Because of their proprietary nature, the chemical makeup and the mechanism by which they stabilize are unknown for most. Manufacturers and distributors of these compounds make claims of how they work around and within the clay, but few compounds have withstood independent testing and evaluation. In addition to the amount of cation exchange that occurs with their use, these compounds usually change the nature of the water surrounding the clay particles so that some or all of the volume change behavior of the soil is negated. More than one will effectively reduce the swelling tendencies of the soil but have little effect on its shrinkage behavior. It is therefore important that before any stabilizer is used, it be thoroughly tested by an independent laboratory, using the same testing sequences for all agents compared, and the economics of its use must be studied. One little-discussed effect that must be determined for all chemical stabilizers is the effect they have on the environment. Environmental impact studies should be part of the considerations for using the various agents, especially for those agents that are less well known.

The success of injecting stabilizing agents into the soil subgrade is dependent on the nature of the macrostructure of the soil. In order to provide agent to as much of the subgrade as possible, it is necessary that the subgrade be highly fissured. To ensure that these fissures are open enough to allow adequate penetration of the agent slurries, the subgrade must be relatively dry or elevated injection pressures must be used, or both. On the other hand, injection pressures that are too high may cause excessive hydraulic fracturing of the subgrade or may overcome the overburden pressure present and cause damage to the subgrade. One relatively new concept is short-term, relatively high-pressure pulses during the injection process. Some skepticism still exists about the use of injection stabilization for expansive clay soil subgrades, primarily because of those contractors who choose not to follow accepted procedures and inspections. This method of placing stabilizing agent slurries into the subgrade can be done effectively, however, so long as one realizes its limitations and the possible stabilizing effects of its use (*7*).

The stabilizing effects of surfactants, compaction aids, and the general chemical agents were discussed earlier, but the stabilizing effects of the most common agents require some additional explanation. The following discussion will include a brief synopsis of these stabilizing effects.

The effects of lime and lime slurries are well known; they depend on how and in what form the lime is applied. Mixing hydrated lime and hydrated lime slurries intimately in those expansive clay soils that react favorably with lime will cause cation exchange, ion crowding, flocculation, and if enough lime is present, pozzolanic cementation. In many cases, this will render the stabilized material nonexpansive, nonactive, and waterproof. Quicklime and quicklime slurries result in much the same property improvements and less agent is required for the same amount of stabilization. It is believed that the use of high-temperature quicklime slurries will result in better and quicker stabilization. This belief is based on the facts that chemical reactions work better at higher temperatures and that these slurries have finer gradations of lime and more highly calcium-charged supernatants. The injection of proper lime slurries into well-fractured and desiccated subgrades results in somewhat differing stabilization results, which include filling of the fissures with lime, preswelling of the soil mass between the lime-filled seams, some modifying of the clay between the lime seams, reducing moisture change in the soil mass, and modifying the surface layer where the slurries are mixed intimately with the soil. It is believed that either injection of water after lime slurries or injection of high-temperature quicklime slurries, or both, will result in all of the foregoing effects plus further modification of the clay between the lime seams (*7*). Because of these factors, lime is the most popular agent used to stabilize expansive clay soils.

Other agents that may provide calcium cations for stabilizing expansive clay soil include calcium chloride, portland cement, and calcareous fly ash. The reasons why calcium chloride has not been widely used are not clear. It is believed that the main one is economics, but perhaps it is also because little definitive research has been done to define or support its use. Calcium chloride is known to be more easily made into a calcium-charged supernatant than is lime. Another possible reason for its restricted use is that the resulting pH of the soil will not adequately promote cation exchange.

Portland cement has been used successfully to modify clay, but the mechanisms involved are not the same as those for lime. The small amounts of lime in the cement provide some cation exchange, but the similarity to lime ends there. The water-cement paste is known to coat the clay particles, thereby waterproofing them, and the cement binds particles together, causing what appears to be flocculation and agglomulation. Looking at the stabilized material, one would believe that both lime and cement accomplish the same modification using nearly the same amount of agent.

Calcareous fly ash is known to have two effects when mixed intimately with expansive clay soils. The available quicklime in the fly ash will produce significantly the same amount of change that lime alone would provide and pozzolanic cementation will occur similar to that caused by portland cement. In some cases, the addition of relatively low percentages of fly ash alone will have the same effects as nearly the same quantities of lime, but most often the addition of some lime with the fly ash will be necessary. Fly ash, which is considerably less expensive than either lime or portland cement, seems a natural alternative, but its use has not been that extensive, mostly because of the lack of experience with this agent and the relatively poor quality control. Until there are much faster methods to evaluate the quality of fly ash as it is delivered in the field, the use of this valuable resource will likely be severely limited.

REMEDIAL TREATMENTS

Remedial treatments are actually after-the-fact stabilizers of expansive clay soils and the facilities on which they are built. The processes used may be as simple as drainage corrections

or as complex as rebuilding of the facility, and they are almost always more costly to institute than the stabilization that should have been done initially. It is interesting to note that the best methods of remedial stabilization are usually the simplest and most direct. One of the greatest detriments of remedial treatment is the interruption in use of the facility while the work is being performed.

Three procedures must be completed if the remedial treatment is to be a success. First, adequate information should be sought about the soil conditions, including sampling and testing. Second, a history of the project should be compiled to determine the processes that resulted in the need for remedial treatment. The information gathered during this phase will usually be very valuable when the methods of stabilization are determined. Third, the possible alternative ways to correct the problem should be determined. It is essential that the process chosen result in a final product that will require no further remedial treatment and will function adequately for the purpose for which it was designed (*6*).

An example that highlights how remedial treatments are accomplished is a slope that has been determined to be unstable or has failed. To lower the potential of failure, the angle of the slope may be decreased, and (if right-of-way is available) the slope can simply be flattened. The slope may also be terraced to lower the effective angle of the total slope. If the angle of the slope cannot be changed, the strength of the soil mass must be improved. This may be done by draining the slope in some cases, and by injecting agents that will improve the strength of the soil along potential failure planes. These methods are generally applicable to slopes that have not failed. Once the slope has failed, the material must be cleaned from the failure plane, and the slope must be rebuilt either at a flatter angle or with material that has an improved strength. The surface of all slopes must be protected from erosion, and this may require surface stabilization techniques.

Another frequent problem is the distortion and misalignment of pavement systems caused by differential movements of expansive clay soils. It is likely that this condition is the result of lack of stabilization of these materials and may be a problem that changes with the effects of the climate. The first step in the remedial process is to provide stability for the active foundation soils of the pavement. This may be done by (a) providing vertical moisture barriers to hold moisture in the soils and waiting for the moisture stability to return naturally, (b) applying moisture at the edge of the pavement and devising some means of maintaining the stable moisture levels achieved, or (c) injecting water or stabilizing agents (or both) into the soil. An integral part of the moisture stabilization process is sealing all cracks in the pavement system that would allow entrance or exit of moisture and correcting drainage conditions that may lead to concentrations of water at the subgrade level.

Once moisture stabilization is complete, realignment of the pavement can be accomplished. The most frequently used methods to realign pavements are grouting and mudjacking. If the differential movements are severe, replacement of the pavement may be necessary; and the process of stabilization begins with subgrade soil stabilization. Injection stabilization may well be used during this process, and as with all injection remedial processes, the spread of the injected slurry must be confined so that more damage outside the distressed area does not result.

The failure of retaining walls caused by the action of expansive clay soils can be remedied by using the same methods recommended for initial stabilization. Soils retained by walls may be repaired in similar ways to soils in slopes, and clay backfill should be cut back as indicated previously. Rebuilding or replacement of the wall, or both, may often be necessary when the damage is severe. With this in mind, it is easy to see why these remedial processes are much more expensive than constructing the facilities correctly in the first place.

CONCLUSIONS

It is almost always most advisable, from the standpoint of economics, to stabilize expansive clay soils during the construction of a transportation facility rather than leave the soils unstable, thereby risking the need for remedial treatment. Stabilization can be performed more economically and more completely initially than when repairs are needed to keep up with an unstable situation. Unstable expansive clay soils do not have to be accepted for use. Even at this time, much is known about stabilizing these problem soils, and the stabilization processes are economical alternatives to potential problems.

RESEARCH NEEDS

Further research is needed to provide answers to some of the questions raised in this paper and to continually investigate new agents and methods. This research is most useful when it includes full-scale applications and is best done by independent organizations that have no vested interest in the outcome. There is a definite need to investigate available waste products to determine their efficiency for stabilization. One such material, fly ash, is becoming more accepted for use, but there are still problems in determining the quality of the ash in the field. Research should be publicized so that decision makers can make maximum use of alternative methods of stabilization.

Two problems with the behavior of these problem soils need further attention: (a) the effects of cyclic shrink-swell on the behavior of the soil mass and (b) prediction of the vertical rise expected from the soil mass.

Last, with the potential for damage caused by expansive clay soils and the condition of the nation's infrastructure, more funds for research must be forthcoming in this area.

REFERENCES

1. D. H. Baer. *Building Losses from Natural Hazards: Yesterday, Today, and Tomorrow*. J. H. Wiggins Company, Redondo Beach, Calif., 1978.
2. R. G. McKeen. *Design of Airport Pavements for Expansive Soils*. New Mexico Engineering Research Institute, Albuquerque, 1981.
3. R. F. Reed. Foundation Failures in Expansive Soils. *Proc., Geotechnical Engineering Sessions,* ASCE, Corpus Christi, Tex., May 1983.
4. D. R. Snethen. *Technical Guidelines for Expansive Soils in Highway Subgrades*. Report FHWA-RD-79-51, Federal Highway Administration, U.S. Department of Transportation, Washington, D.C., June 1979.
5. D. R. Snethen, ed. *Proc., Fourth International Conference on Expansive Soils*, Vols. 1 and 2, American Society of Civil Engineers, New York, 1980.
6. Colorado State University Geotechnical Engineering Program.

Report of Workshop—Expansive Soils: Problems and Practices in Highway and Foundation Engineering. National Science Foundation, Washington, D.C., Dec. 1982.
7. T. M. Petry, J. C. Armstrong, and T. Chang. Short Term Active Soil Property Changes Caused by Injection of Lime and Fly Ash. In *Transportation Research Record 839*, TRB, National Research Council, Washington, D.C., 1982.
8. A. R. Poor. *Final Report of Experimental Residential Foundation Designs on Expansive Clay Soils*. U.S. Department of Housing and Urban Development, Washington, D.C., June 1978.
9. D. Forstie, H. Wash, and G. Way. Membrane Technique for Control of Expansive Clays. In *Transportation Research Record 705*, TRB, National Research Council, Washington, D.C., 1979.
10. M. Picornell, R. L. Lytton, and M. Steinberg. Matrix Suction Instrumentation of a Vertical Moisture Barrier. In *Transportation Research Record 945*, TRB, National Research Council, Washington, D.C., 1983.
11. M. L. Steinberg. Deep-Vertical-Fabric Moisture Barriers in Swelling Soils. In *Transportation Research Record 790*, TRB, National Research Council, Washington, D.C., 1981.
12. E. B. McDonald. Stabilization of Expansive Shale Clay by Moisture Density Control. In *Transportation Research Record 641*, TRB, National Research Council, Washington, D.C., 1977.

Publication of this paper sponsored by Committee on Lime and Lime-Fly Ash Stabilization.

Expansion of Cement-Stabilized Minestone due to the Oxidation of Pyrite

M. D. A. THOMAS, R. J. KETTLE, AND J. A. MORTON

Despite the successful use of cement-stabilized minestone (CSM) in road construction, some CSM pavements have suffered deformation attributed to the expansion of the CSM layer. Three sites where deformation has occurred are described, and evidence from field samples is presented. Chemical analyses of the retrieved samples showed that the materials had reduced iron sulfide and increased sulfate contents when compared with reported values for the raw minestones. Examination of thin sections suggested that much of the distress within the CSMs was associated with deteriorating pyritic minestone particles. In addition, sulfate minerals were frequently found in close association with both the pyritic minestone and the products of cement hydration. X-ray diffraction analysis and scanning electron microscopy produced further evidence of sulfate minerals in the cracks of the CSMs. It is concluded that the long-term expansion of CSM is due to the oxidation of pyrite, a component of the raw minestone, to form sulfate minerals. Not only does the ongoing sulfate production increase the potential for sulfate attack on the products of cement hydration, but the reduced mineral density of the sulfate products generates crystallization pressures within the CSM.

Minestone, or unburned colliery shale, is the by-product of the coal mining industry and is principally composed of the shales, mudstones, and seatearths closely associated with the coal seam. The mineralogy is dominated by quartz and a variety of clay minerals (*1*), commonly kaolinite, illite, chlorite, and a mixed-layer illite-montmorillonite.

In the United Kingdom, minestone is currently produced at the rate of 60 Mtonnes a year with existing stockpiles totaling 3000 Mtonnes (*2*). Approximately 5 Mtonnes are used each year through a variety of outlets (*3*), many of which are within the construction industry.

Early studies (*4*) of cement-stabilized minestone (CSM) indicated its potential as a structural pavement layer. Subsequent field trials (*5,6*) also met with some success and, following improvements in the availability of suitable mix-in-place and continuous-mixing plant, CSM has been used as the main structural layer in many applications within British Coal including hardstandings, coal stacking areas, and haul roads (*6–8*). CSM has also been used in the construction of public roads (*9*), particularly in southeast England where the supplies of traditional road-building aggregates are limited.

M. D. A. Thomas, Department of Materials, Imperial College of Science and Technology, c/o Building Research Station, Garston, Werts WD2 9JR, United Kingdom. R. J. Kettle, Department of Civil Engineering, and J. A. Morton, Department of Geological Sciences, University of Aston, Birmingham B4 7ET, United Kingdom.

The design of pavements incorporating CSM is usually carried out in accordance with Road Note 29 (*10*) and the construction is controlled by the requirements of the Department of Transport (*11*). CSM is required to achieve a 7-day crushing strength of 3.5 MPa for cubic specimens. Durability requirements include proven resistance to a British Standard immersion test (*12*) and the Transport and Road Research Laboratory frost heave test (*13*). In addition, the raw minestone must satisfy grading and plasticity criteria and must not have an acid-soluble sulfate content in excess of 1 percent (as SO_4).

Despite the rigorous testing employed before use of CSM, some CSM structures have suffered considerable disruption due to swelling (*14,15*). The most dramatic case occurred within a few days of compaction of the CSM layer (*14*) and was due to short-term swelling mechanisms inherent in mudrocks (*16,17*). In other cases, failure occurred following reasonable periods of satisfactory performance; the examination of three such pavements forms the subject of this study.

SITES EXAMINED

Three failed cement-stabilized pavements were made available for detailed examination, one in northeast England, the other two in Kent. All three pavement structures had performed adequately for the first year. Distress was first noticed during the summer between 1 and 2 years after construction.

Lorry Park

A lorry park was constructed in 1981 using minestone from the Wardley Colliery in northeast England both as a compacted unbound layer to achieve grade and as a 150-mm cement-stabilized base layer. The Wardley minestone had been extensively examined (*18*) and was considered suitable for use as a cement-stabilized material. The cement content of 8 percent produced a mean 7-day crushing strength of 5.75 MPa for the test cubes made at the site (*8*). This value is in excess of the minimum 3.5 MPa required by the Department of Transport (*11*).

Despite the apparent suitability of the material, the parking area showed some distress at a construction joint after 12 to 18 months of service. Excavation at the location of the distress showed that movement of one or both of the CSM layers had occurred adjacent to the construction joint. Although the distress may have been exacerbated by a poorly finished con-

struction joint, the movement was undoubtedly the result of CSM expansion. An intact slab from either side of the joint was removed for laboratory examination.

Car Park

A large industrial car park was constructed in two distinct phases using minestone from the Snowdown Colliery in southeast England. Although comprehensive construction details are not available, it is known that the minestone was blended with 30 percent waste sand before cement stabilization. A cement content of 8 to 10 percent was used throughout.

The suitability of Snowdown minestone has been well reported (*9*). However, after approximately 12 months, the second phase suffered visible disruption in the form of asphalt ridges, often 50 mm high, in the wearing course. When cores were cut through the ridges, a discontinuity was found extending from the ridge through the CSM layer at a slope of approximately 45° (Figure 1). Evidence of matching fractured particles on each side of a discontinuity suggested that the problem stemmed from shear failure of the CSM rather than a poorly formed construction joint. The shear stresses were produced by the horizontally constrained expansion of the CSM layer. Cores were also taken from the failure zone, and these appeared to be intact.

The first phase was still performing adequately with no visible signs of distress. Nevertheless, cores were taken from this phase to compare them with those from the second phase.

School Playground

The material used to surface a school playground was again obtained from the Snowdown Colliery and also contained 30 percent waste sand and a cement content of 8 percent. Eighteen months after construction, visible deterioration of the structure occurred in the form of asphalt override at the site of concrete drains that subdivided the playing areas into smaller bays. The drains were fractured in many places. The cause of distress was again attributed to the expansion of CSM (Figure 2). An intact slab of CSM was removed for laboratory investigation. It is noteworthy that as the slab dried following excavation, it developed a white crystalline efflorescence. A similar but less pronounced effect was noted for the samples taken from the other sites.

In a few isolated cases, disintegrating aggregate particles were detected in the samples removed from the Kent sites. The disintegration took the form of crumbling and splitting along laminae. On one occasion, yellow deposits were evident in the laminations of such particles.

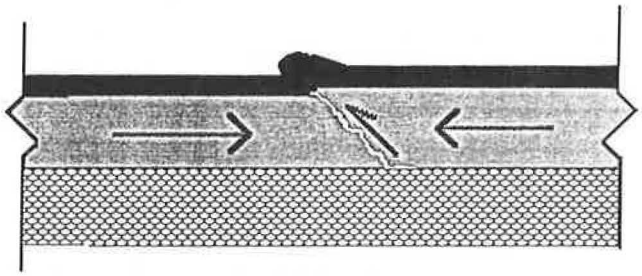

FIGURE 1 Mode of failure in Snowdown CSM: car park.

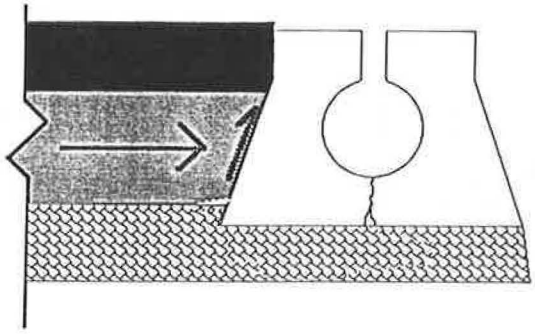

FIGURE 2 Mode of failure in Snowdown CSM: school playground.

TABLE 1 EQUIVALENT CUBE STRENGTHS AND SULFUR CONTENTS FOR COLLECTED CSM SAMPLES.

Site	Equivalent Cube Strength (MPa)	Forms of Sulfur (% SO_3)		
		Total	Pyritic	Sulfate
Lorry park	4.56	1.21	0.65	0.40
Car park, Phase 1	3.01	2.10	1.45	0.45
Car park, Phase 2	2.38	3.64	2.70	0.63
School playground	2.65	2.80	2.05	0.58

LABORATORY EXAMINATION OF CSM SAMPLES

In the laboratory the following tests were employed to assess the CSM samples:

1. Compressive strength;
2. Total, pyritic, and sulfate sulfur contents;
3. X-ray diffraction analysis of CSM and, where possible, crack infill material and efflorescence;
4. Preparation and examination of thin sections; and
5. Examination of crack surfaces by scanning electron microscopy.

Specimen preparation and test methods are described elsewhere (*17*). Table 1 shows the results of the strength tests and gives the sulfur values.

DISCUSSION OF RESULTS

Strength

The CSM sampled from the lorry park recorded compressive strength in excess of the specified 3.5 MPa. However, the equivalent cube strength of the CSM was considerably lower than the reported 7-day strength of 5.75 MPa for site-prepared cubes (*8*).

The compressive strengths of the cores taken from the three CSM sites using Snowdown minestone were all below the required 3.5 MPa. Although no strength data are available from site-prepared cubes, previous field trials have reported 7-day strengths in excess of 7 MPa for Snowdown CSM cubes compacted at the average field density (*19*). In addition, blending 30 percent waste sand can increase the compressive strength of Snowdown CSM by at least 20 percent (*20*).

At all three sites, the CSM remote from the area of disruption was intact. However, evidence based on compressive strength determinations would suggest a degree of strength loss in this CSM as well.

Chemistry

The sulfur chemistry of Wardley minestone was determined before its use at the lorry park (*18*):

Form of Sulfur	*Percent SO_3*
Total	1.4
Pyritic	0.96
Acid-soluble	<0.1
Water-soluble	<0.1

The main anomaly between these data for the raw minestone and the determinations made for the CSM (Table 1) is the distribution of the total sulfur between pyritic and sulfate sulfur. Allowing for a typical sulfate content of 2 percent for cement (*21*) and for a cement content of 8 percent as used at the lorry park (*8*), the sulfate contribution of the Wardley minestone in the CSM increased to 0.24 percent (or 0.27 percent by mass of raw shale). Conversely, the measured pyritic sulfur content decreased to 0.65 percent, which is equivalent to 0.70 percent by mass of raw shale.

Chemical analyses of the raw Snowdown minestones used in the Kent sites are not available. An examination of the chemical data for the Snowdown CSM shows disparities between the sulfur contents (total, pyritic, and sulfate) for the CSM used in the two phases of the car park—the Phase 1 material having less sulfide or sulfate-bearing minerals. All three Snowdown CSMs have higher levels of sulfide and sulfate than the Wardley CSM. This is in spite of the considerable dilution due to the sand addition in the Snowdown CSMs.

X-ray Diffraction Analysis

The x-ray diffractometer traces of the three CSM sites are similar, and the trace from the CSM used in the construction of the second phase of the car park is shown in Figure 3. The principal peaks can be assigned to the quartz and the various clay minerals normally associated with minestone (*1*) and also to calcite ($CaCO_3$). The majority of the calcite is undoubtedly the result of the carbonation of the portlandite [$Ca(OH)_2$] released during the hydration of cement. The absence of a portlandite trace would suggest that little portlandite remains after 12 to 18 months' exposure. The fairly broad peak at an angle of 32° may be due to a combination of siderite ($FeSO_4$) and cement clinker minerals.

The only discernible differences between the sample traces for the Snowdown and Wardley CSMs were enhanced quartz peaks and subsequently reduced clay peaks for the Kent materials (resulting from the addition of a waste sand to the minestone before stabilization). A comparison between the relative peak heights of quartz and clay minerals for the two phases from the car park suggests an increased quartz content for the first phase.

During the preparation of thin sections from the intact samples of Snowdown CSM, cracks were detected in the cut surfaces. In many cases, a white crystalline infill material was found. Where possible, this material was removed from the cut face opposite that used for the thin section and analyzed by x-ray diffraction. A typical diffractogram trace of material removed from a crack in the CSM from the car park is shown in Figure 4. Some of the peaks correspond to those shown in Figure 3, because it was impossible to avoid removing some of the main body of material. The most noticeable differences between the two traces are the additional peaks associated with gypsum ($CaSO_4 \cdot 2H_2O$) and ettringite ($3CaO \cdot Al_2O_3 \cdot 3CaSO_4 \cdot 31H_2O$) and the increased heights of

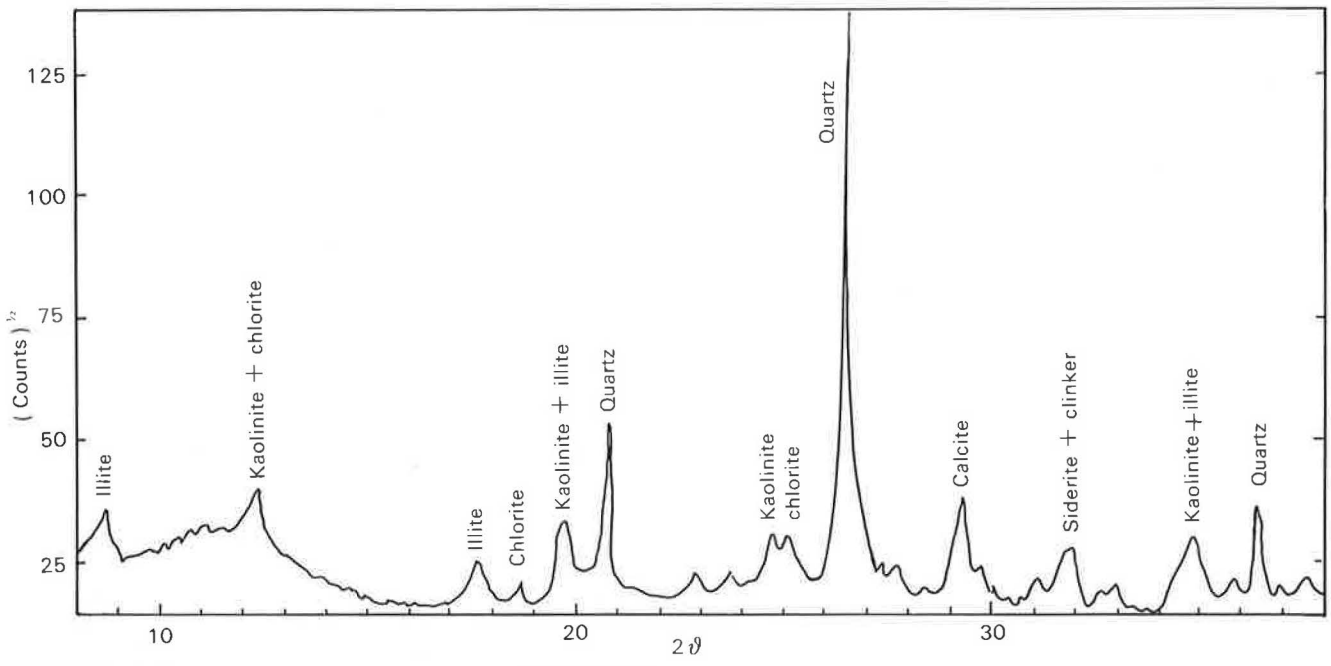

FIGURE 3 Diffractogram for CSM from car park, second phase.

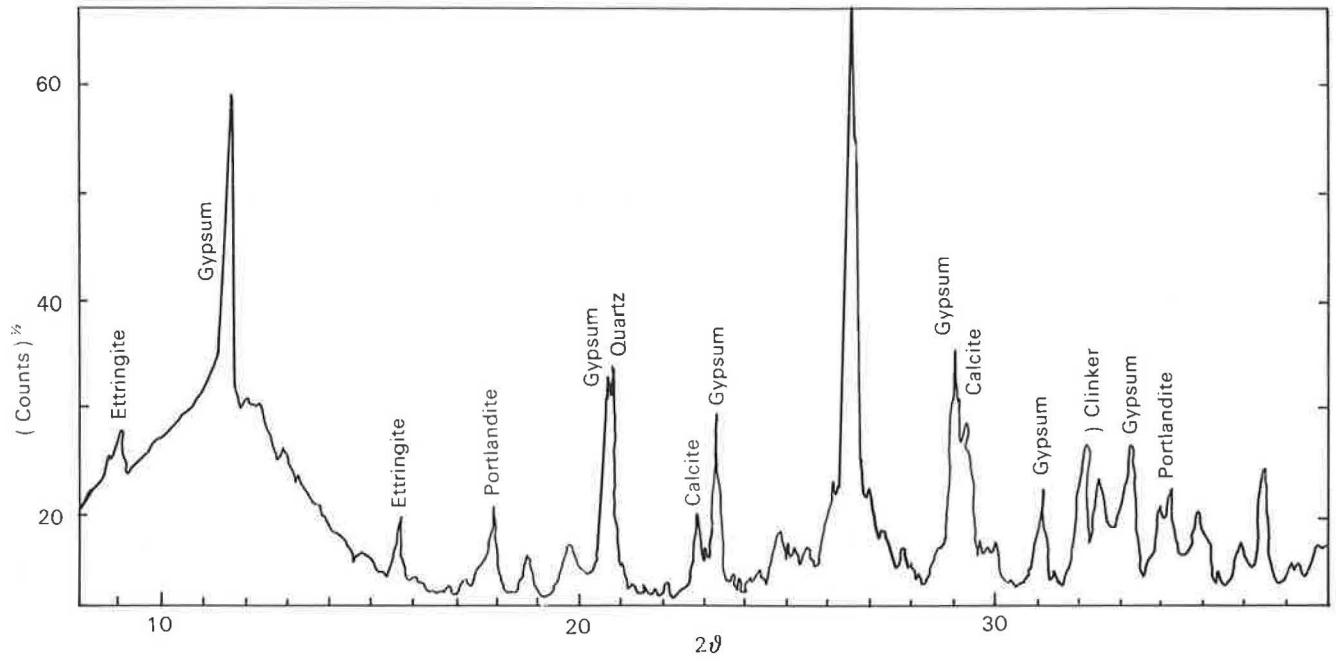

FIGURE 4 Diffractogram for crack infill material taken from car park, second phase.

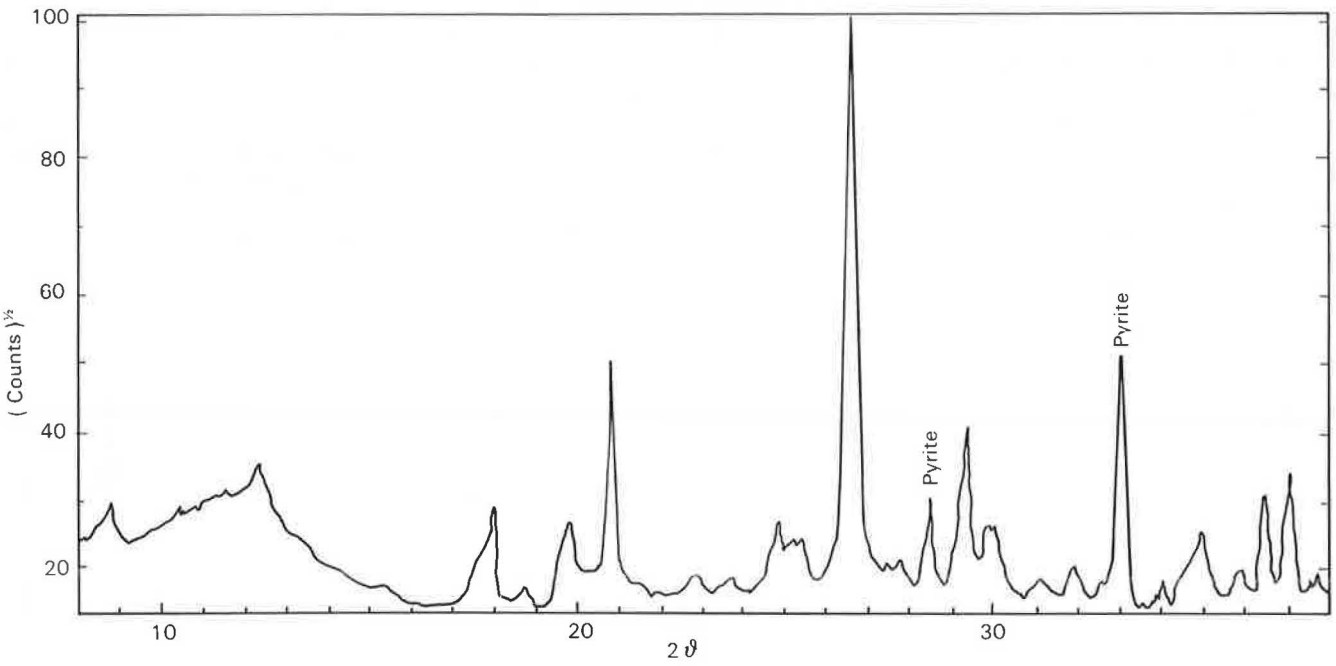

FIGURE 5 Diffractogram for disintegrated shale particle taken from school playground CSM.

the calcite and clinker mineral peaks. The minerals gypsum and ettringite were not always identified in association with one another, both minerals being separately identified in crack infill material.

The efflorescence from the Snowdown CSMs was also successfully removed and analyzed, the diffraction peaks corresponding mainly to the mineral thenardite (Na_2SO_4). Where disintegrating aggregate particles were detected, these were removed for analysis, and they invariably gave traces corresponding to highly pyritic shales (Figure 5). Attempts were made to remove the material between the laminations, and although no positive identification could be made, the presence of the mineral jarosite [$KFe_3(SO_4)(OH)_6$] is tentatively indicated in Figure 6. The peak around 29° in Figure 6 may not be assigned to gypsum in the absence of the principal gypsum peak at 11.7°. Many peaks on this trace are difficult to interpret, especially the large peak at 32°, although this may be partially due to siderite ($FeCO_3$).

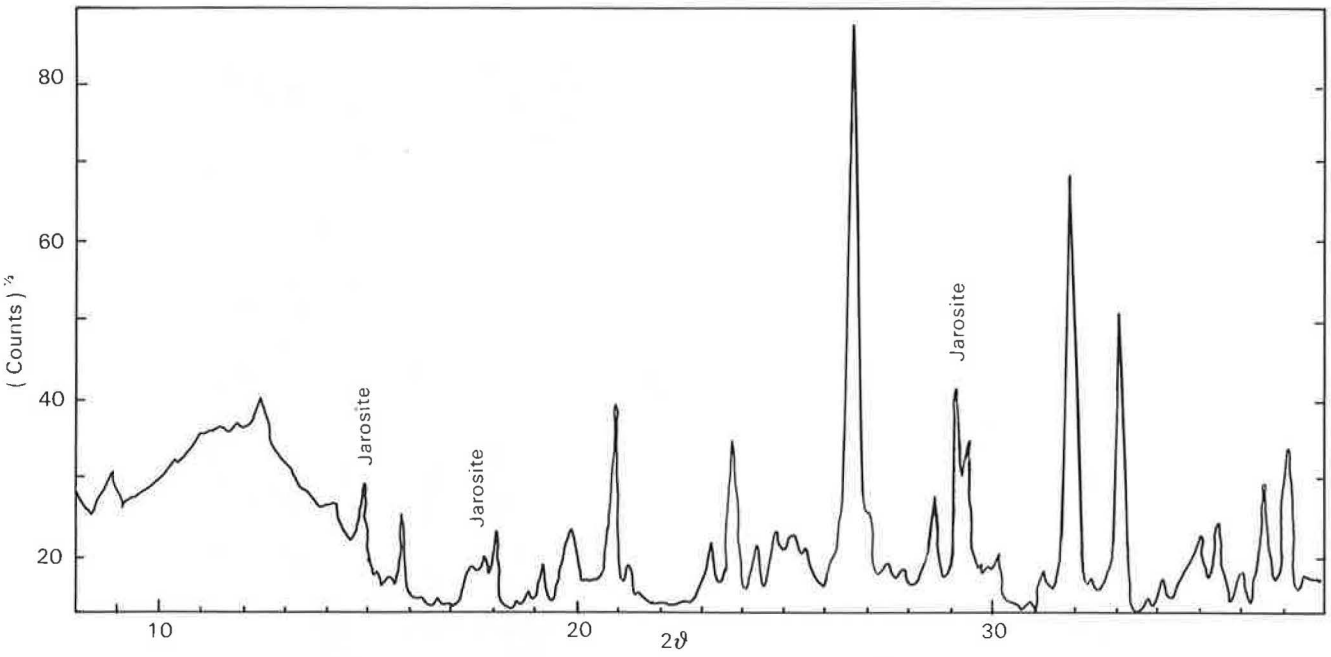

FIGURE 6 Diffractogram for material taken from between laminations of disintegrated shale particle.

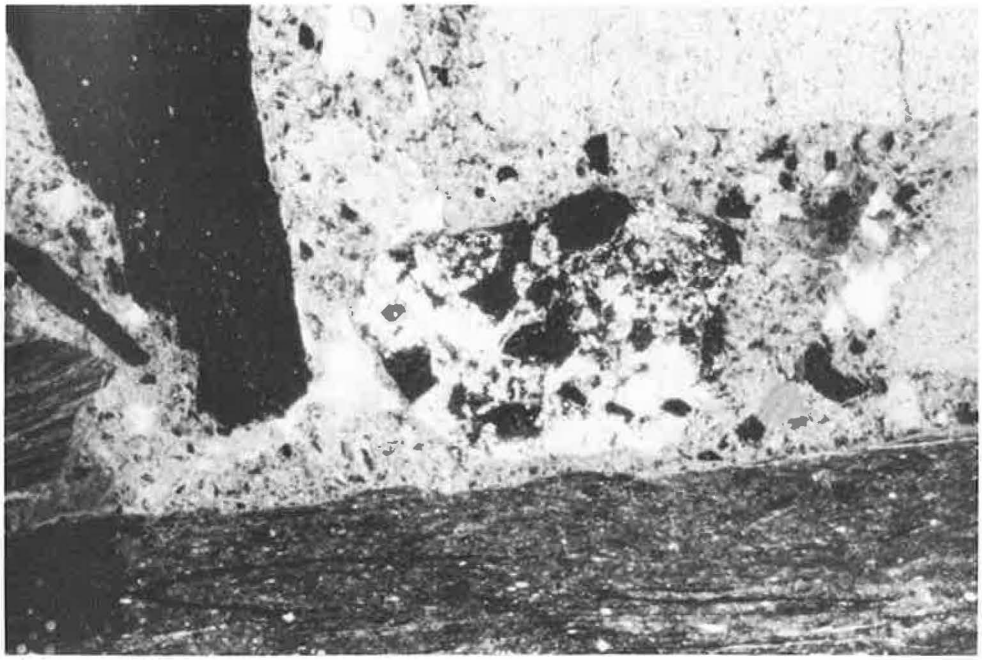

FIGURE 7 Photomicrograph of CSM from school playground (width of view 13 mm).

Examination of Thin Sections

Examination of petrographic sections taken from all three sites showed the materials to be extensively cracked. Because the preparation of material for thin sectioning requires it to be dried before resin impregnation, many of the cracks surrounding aggregate particles may result from the shrinkage of the aggregate. This suggests that much of the material in colliery shale is moisture sensitive. Coal was also identified in the CSM matrix.

Examination by reflected light revealed that many of the aggregate particles contained finely grained pyrite. In many cases these particles had undergone considerable deterioration and internal cracking. Figure 7 is a photomicrograph of a section through the CSM from the school playground, the center of which is dominated by a disaggregated particle of pyritic shale. The void spaces are a result of material loss during specimen preparation. However, there is some evidence of secondary mineral formation within the smaller cracks and surrounding some of the remaining shale particles. A

FIGURE 8 SEM photomicrograph (× 5,000) of pore infill material in Snowdown CSM.

small fraction of this mineral was resolved to be gypsum but the larger part remains unidentified.

Virtually no portlandite was detected in any of the sections. There was, however, an abundance of calcite as a result of the carbonation of portlandite. Gypsum was often found in association with the calcite. Hydrated cement minerals and cement clinker minerals were also present. In a few isolated cases, ettringite could be identified in close association with these minerals.

A comparison of the sections from the Wardley CSM and the three Snowdown CSMs showed the principal difference to be the abundance of quartz particles in the sections from Kent due to the addition of sand. These additional quartz particles tended to be in the size range of 150 to 425 microns. A point count was undertaken for the materials from the two phases of the car park. The first-phase material recorded approximately 10 percent more counts for quartz.

Scanning Electron Microscopy

Where crack infill material was removed for x-ray diffraction analysis, the associated crack surfaces were examined by scanning electron microscopy. Figure 8 shows such a crack surface taken from the CSM used in the construction of the school playground. The needle-shaped crystals are ettringite, which was confirmed by a dispersive x-ray analysis that measured calcium, sulfur, and aluminum as the most predominant elements (these being the elemental oxides of ettringite).

EXPLANATION OF IN SITU BEHAVIOR

At all three sites where failure of the pavement had occurred, the mode of failure was consistent with the expansion of the CSM layer. The expansion resulted in an overall strength loss throughout the CSM, with the materials from Kent failing to retain sufficient strength to satisfy the 7-day strength requirement specified by the Department of Transport (*11*) at the time of construction.

The examination of mineralogical slices suggests that much of the minestone fraction is susceptible to certain volume changes when subjected to fluctuations in moisture content. In particular, the expansive clay minerals and any residual coal may generate expansive movements. However, in view of the time scale and season during which the pavements failed (the CSM was in a dry state at all three sites), it seems unlikely that the disruption can be attributed to moisture movements.

The decrease in the pyritic sulfur content and the corresponding increase in the total sulfate content of the Wardley CSM imply that the oxidation of the pyrite present in minestone continues beyond cement stabilization and compaction. Although no such comparisons are available for the Snowdown minestone, the presence of deteriorated, sulfide-rich particles in the Snowdown CSM would suggest that similar geochemical changes are prevalent. These particles must have been intact at the time of mixing to avoid dispersion of the deteriorated fragments throughout the CSM matrix.

The oxidation of pyrite is initiated by contact with moist air, and the first products formed are ferrous sulfate and sulfuric acid:

$$2FeS_2 + 2H_2O + 7O_2 \longrightarrow 2FeSO_4 + 2H_2SO_4 \quad (1)$$

Further oxidation of the ferrous sulfate produces ferric sulfate:

$$4FeSO_4 + O_2 + 2H_2SO_4 \longrightarrow 2Fe_2(SO_4)_3 + 2H_2O \quad (2)$$

The ferric sulfate, a strong oxidizing agent, may reduce further pyrite:

$$7Fe_2(SO_4)_3 + FeS_2 + 8H_2O \longrightarrow 15FeSO_4 + 8H_2SO_4 \quad (3)$$

Reaction 2 cannot proceed chemically in the acidic environment normally associated with this process (*22*), and at low pH, the reaction is thought to occur because of the action of autotrophic bacteria of the *Ferrobacillus-Thiobacillus* type (*23*). Because of the presence of cement, the pH of CSM pore fluid is likely to remain alkaline, and thus the oxidation of ferrous sulfate may occur abiotically.

These reactions are common in coal mines (*24*) and on colliery spoil tips, although the extent to which they occur in CSM is not known. The oxidation of pyrite, even due to the occurrence of Reaction 1 alone, has serious engineering implications for CSM.

First, the production of sulfate salts of significantly lower density than pyrite leads to an increase in the volume of solids. If the crystallization of these minerals is confined, then considerable pressures are produced. These crystallization pressures are sufficient to degrade minestone particles and would undoubtedly lead to expansion of CSM.

The volume increase associated with the conversion of pyrite to jarosite, a process identified in the Snowdown CSM, is reported to be 115 percent and that of pyrite to ferric sulfate is 170 percent (*22*). The conversion of calcite to gypsum by reaction with the sulfuric acid released during pyrite oxidation is a known cause of heave in pyritic shale fills (*25,26*). With the exception of some of the Staffordshire minestones, most minestones contain insufficient calcite for this mechanism to prevail (*17*) in unbound minestone.

The second consequence of pyrite oxidation is the increase in the sulfate content of the CSM, which increases the potential for sulfate attack on the minerals of cement hydration. The combination of sulfate minerals with tricalcium aluminate to form ettringite and with calcium hydroxide to form gypsum is well established in concrete technology (*21*). The abundance of sulfuric acid that results from pyrite oxidation exacerbates the problem of sulfate attack. The acid will combine with either calcium hydroxide or calcite (resulting from the carbonation of calcium hydroxide) to form further gypsum. The formation of both ettringite and gypsum leads to considerable volume increase.

Both ettringite and gypsum have been detected in cracks in CSM. Gypsum often forms in association with calcite in CSM. This may result from the simultaneous action of sulfate ions and carbon dioxide on the calcium hydroxide released during cement hydration, forming gypsum and calcite, respectively. Alternatively, the gypsum may result from sulfuric acid attack on the calcite following carbonation.

Distress due to both pyrite oxidation and sulfate attack was detected in all the CSM samples tested, but was far more prevalent for the Snowdown CSM. The increased distress for these CSMs is due to the higher level of sulfur present, both as sulfide and sulfate minerals, in the constituent raw minestone. The survival of the CSM from the first phase of the Pfiser car park may be due to a combination of its reduced sulfur chemistry and increased sand addition. Continuing action of the sulfur-bearing mineralogy may eventually lead to failure.

It is worth noting that the Wardley CSM failed only at the site of a construction joint and that the CSM remote from this joint retained considerable strength. Other studies, both of site applications (*8*) and of laboratory-produced specimens (*17*), have shown Wardley CSM to be a durable material. There is little doubt that the presence of pyrite and sulfates in the raw minestone leads to an expansion of the CSM, but it is improbable that this expansion would have led to disruption without the assistance of a poorly finished construction joint.

The criteria currently used to assess the suitability of a particular minestone source for use in CSM make no allowance for its pyritic sulfur content. Many minestones have tolerable levels of sulfur-bearing mineralogy and can produce strong, durable CSMs (*17*). The need to establish effective criteria capable of identifying these minestones cannot be overemphasized.

ACKNOWLEDGMENTS

This work formed part of a research project financed by British Coal, and the authors wish to express their thanks for the support given and for permission to publish the paper.

REFERENCES

1. R. J. Collins. A Method for Measuring the Mineralogical Variation of Spoil from British Collieries: *Clay Materials*, Vol. 2, 1976, pp. 31–50.
2. *Report of Aggregates and Waste Materials*. Working Group, CP31/73, Building Research Establishment, 1973.
3. A. K. M. Rainbow, ed. *International Symposium on the Reclamation, Treatment and Utilization of Coal Mining Wastes*. National Coal Board, London, 1984.
4. R. J. Kettle and R. I. T. Williams. Preliminary Study of Cement Stabilised Unburnt Colliery Shale. *Roads and Engineering Construction*, Vol. 47, No. 559, 1969, pp. 200–206.
5. R. J. Kettle and R. I. T. Williams. Colliery Shales as a Construction Material. *Proc., International Conference on Use of By-Products and Wastes in Civil Engineering*, Vol. 2, Laboratoire Central des Ponts et Chaussées, Paris, 1978, pp. 475–481.
6. D. A. Tanfield. Construction Uses for Colliery Shale. *Contract Journal*, Jan. 1978, pp. 141–143.
7. A. K. M. Rainbow. Colliery Spoil—Its Production, Properties, and Use in a Cement Stabilized Form. Seminar on Waste Materials in Concrete. *Cement and Concrete Research*, 1982.
8. W. Sleeman. Practical Application of Cement Bound Minestone within the British Coal Mining Industry. In *Proc., International Symposium on Reclamation, Treatment, and Utilisation of Coal Mining Wastes*, National Coal Board, London, 1984, pp. 53.1–19.
9. R. J. Kettle. The Improvement of Colliery Spoil. *Quarterly Journal of Engineering Geology*, Vol. 16, 1983, pp. 221–229.
10. *A Guide to the Structural Design of Pavements for New Roads*. Road Note 29. U.K. Transport and Road Research Laboratory, Crowthorne, Berkshire, England, 1970.
11. *Specification for Road and Bridge Works*. Department of Transport, London, 1977.
12. *Methods of Test for Stabilised Soils*. BS1927. British Standards Institution, 1975.
13. D. Croney and J. Jacobs. *The Frost Susceptibility of Soils and Road Materials*. Report LR90. U.K. Transport and Road Research Laboratory, Crowthorne, Berkshire, England, 1970.
14. T. V. Byrd. The Sad Canterbury Tale. *New Civil Engineer*, Nov. 1980.
15. J. A. Morton, R. J. Kettle, and M. D. A. Thomas. Some Experimental Observations on the Potential Expansion of Cement Bound Minestone. In *Proc., International Symposium on Reclamation, Treatment, and Utilisation of Coal Mining Wastes*, National Coal Board, London, 1984, pp. 56.1–8.
16. A. T. McNulty. *Durability Criteria for Cement Bound Minestone*. Ph.D. thesis. University of Aston, England, 1985.
17. M. D. A. Thomas. *The Performance of Cement Stabilised Minestone*. Ph.D. thesis. University of Aston, England, 1986.
18. G. Berry. *Report on an Investigation into the Cement Stabilisation of Unburnt Spoil and Tip Washery Discard from the Former Wardley*

Colliery, Northeast Area. Report No. YRL13461. National Coal Board, London, 1981.
19. R. J. Kettle. The Use of Colliery Shale in Highway Construction. In *Proc., International Conference on Materials of Construction for Developing Countries*, Thailand, 1978.
20. M. D. A. Thomas. *Swelling Phenomena in Cement Stabilised Minestone*. Interim Report B. University of Aston, England, 1985.
21. A. M. Neville. *Properties of Concrete*, 3rd ed. Pitman Books Ltd., London, 1981.
22. E. Penner, J. E. Gillot, and W. J. Eden. Investigation of Heave in Billings Shale by Mineralogical and Biochemical Methods. *Canadian Geotechnical Journal*, Vol. 7, 1970, pp. 333–338.
23. K. L. Temple and E. W. Delchamps. Autotrophic Bacteria and the Formation of Acid in Bituminous Coal Mines. *Applied Microbiology*, Vol. 1, No. 5, 1970, pp. 255–258.
24. S. I. Kuznetsov, M. V. Ivonov, and N. N. Lyalikova. *Introduction to Geological Microbiology* (C. H. Oppenheimer, ed.), McGraw-Hill, New York, 1963.
25. A. B. Hawkins and G. Pinches. Timing and Correct Geochemical Testing of Soils/Weak Rocks. Presented at Engineering Group of the Geological Society 20th Regional Meeting on Site Investigation Practice: Assessing, University of Surrey, 1984.
26. P. J. Nixon. Floor Heave in Buildings Due to the Use of Pyritic Shales as Fill Material. *Chemistry and Industry*, Vol. 4, March 1978, pp. 160–164.

Publication of this paper sponsored by Committee on Soil-Portland Cement Stabilization.

The views expressed in this paper are those of the authors and not necessarily those of British Coal.

Field Measurement of Shrinkage Crack Depth in Expansive Soils

MIGUEL PICORNELL AND ROBERT L. LYTTON

The depths of surface cracks in expansive clay deposits control the depths of the active zone in many cases. Rainfall and surface runoff can fill these cracks, and the water in the cracks can travel, impelled only by gravity, wherever the crack goes. If the water travels beneath a pavement, it will remain there, soaking into the soil on each side of the crack, and cause swelling. Thus, the depth of the surface cracks determines the depth to which a vertical moisture barrier should be placed in order to control moisture beneath a pavement, and a means of determining this depth is needed. This paper describes such a method using wave propagation. A summary review of wave types is included—their generation, propagation, and alteration at a crack, and the feasibility of their detection and positive identification. This is complemented by the selection of several trial procedures for detecting surface cracks and estimating their depth. The results of field tests using several trenches excavated to different depths and at naturally occurring shrinkage cracks are presented. The testing setups are illustrated and the analysis performed with the field data is described. The best approach to determine the depth of the crack is from the increase in travel time of the surface wave caused by the crack.

This paper describes field tests and analysis methods for determining the depth of shrinkage cracks in expansive clay using wave propagation techniques. The major reason for determining crack depth is to design the depth of vertical moisture barriers that control moisture influx and efflux beneath a pavement.

During periods of extended drought, an expansive soil mass will gradually lose water to the atmosphere, which will cause the soil mass to shrink. In turn, vertical cracks will develop in the soil mass. The depth of the cracks will increase gradually as the desiccation of the soil deposit progresses. During wet periods, the water seeping into the cracks causes swelling of the soil on the crack walls, which will gradually close.

When a light structure, such as a pavement, is founded on one of these deposits, the moisture flow pattern is altered. Because the pavement is essentially impermeable, the soil conditions at the center will remain virtually unchanged through the year, and the soils near the edge will lose or gain moisture depending on the climatic season. These moisture changes will result in shrinking or swelling under the edges of the pavement, but the center will remain unchanged. These differential movements are then responsible for the progressive deterioration of the pavement structure.

M. Picornell, Department of Civil Engineering, University of Texas at El Paso, El Paso, Tex. 79968-0516. R. L. Lytton, Texas Transportation Institute, Texas A&M University, College Station, Tex. 77843.

For residential and light commercial construction, the differential movements are reduced to an acceptable level by increasing the stiffness of the foundation mat. However, this alternative is not economical in the case of pavements. For highway pavements, there is no widely accepted solution to eliminate this progressive damage. One method being tested by the Texas Highway Department in Districts 1 and 15 is to install a vertical moisture barrier, as shown in Figure 1, to delay the water flow in or out of the foundation soils beneath the edges of the pavement.

It is apparent that the effectiveness of a vertical moisture barrier will be readily affected by the presence of shrinkage cracks. If the cracks are deeper than the barrier (C_2 in Figure 1), they can render the barrier useless. Therefore, a procedure to design the depth of the barrier should consider the maximum depth of the shrinkage cracks in the area and the possible variations of crack depth with the seasons.

These considerations suggest the need for a site-exploration technique that is capable of detecting the depth of shrinkage cracks in expansive soil masses in the field. This paper presents the scope of such an investigation.

SITE INVESTIGATION

The ideal site investigation method should be a nondestructive test that is inexpensive, accurate, simple to operate, and capable of working rapidly. The test would be used to cover long stretches of roadway and would be convenient for making several surveys during different times of the year. It appears that the use of wave propagation techniques may be the best approach.

A common surface seismic energy source is an oscillator or an impact hammer that interacts with the soil through a circular plate. When a disturbance of short duration is created on the surface of a soil deposit, three wave types (*1*) are generated. Compression waves and shear waves are generated and propagate away from the point source with semispherical wave fronts. Rayleigh surface waves, the third type of wave generated, propagate on cylindrical wave fronts.

It has been shown (*2*) that the total energy input at the source is unevenly split among all three waves. Only 7 percent of the total energy is transmitted away as a compression wave. The shear waves account for 26 percent of the total energy input. The remaining 67 percent is transmitted away from the source as Rayleigh surface waves. Not only do the body waves (compression and shear waves) (*2*) account for less energy, but their geometrical damping is also higher. For the body waves, damping is proportional to the inverse of the distance

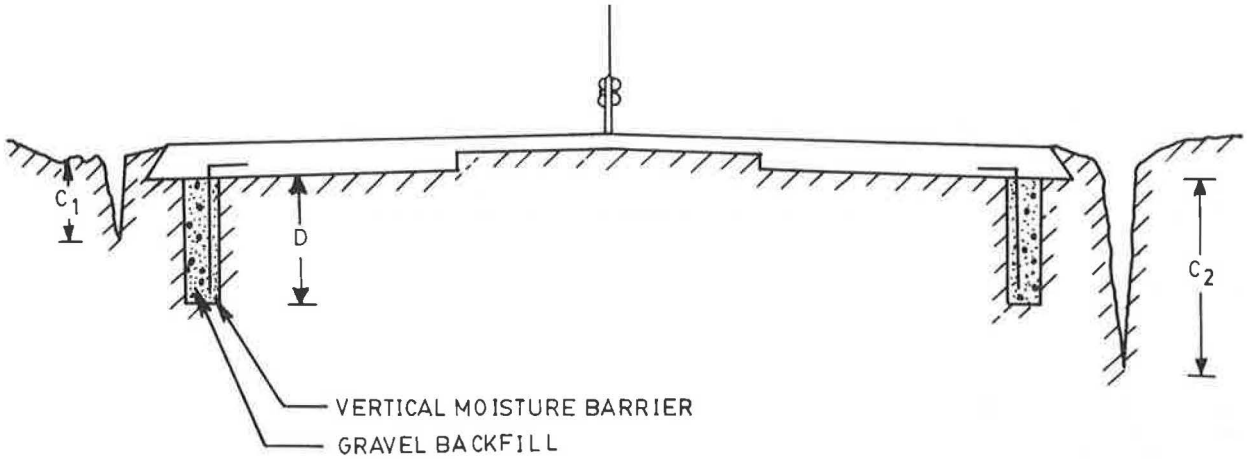

FIGURE 1 Sketch of a highway cross section with a vertical moisture barrier.

to the source, and on the ground surface, their damping is proportional to the inverse of that distance squared. For Rayleigh waves, the damping is proportional to the inverse of the square root of the distance.

Theoretically, it might be possible to use any of the three wave types in a field survey. However, because of the peculiar characteristics of soils, not all are considered adequate. Most of the energy that is transmitted through a Rayleigh wave is concentrated on the surface, and cracks are also local features in this zone; therefore a survey using Rayleigh waves is thought to be the most adequate method.

RAYLEIGH SURFACE WAVE SURVEY

A surface crack can be visualized as a succession of 90- and 270-degree surface corners. Published results (*3*) obtained by numerical iteration techniques are available for a right-angle corner of a material with a Poisson's ratio of 0.25. These indicate that, when the Rayleigh wave reaches the corner, 13 percent of the incident energy is reflected in another surface wave, a second surface wave travels down the vertical face of the corner transmitting away about 41 percent of the energy, and the remaining 46 percent is converted into bulk modes (compression and shear waves) that radiate into the solid.

If the incident pulse is split into its Fourier components, an amplitude ratio can be defined between the amplitude (perpendicular to the plane of propagation) of the surface wave transmitted, or reflected, and the amplitude of the same Fourier component in the incident wave. For the case under consideration, the transmitted wave will have an amplitude ratio of 0.64 and the reflected wave will have an amplitude ratio of 0.36.

If the Rayleigh wave strikes a 270-degree corner, the reflected surface wave is small (amplitude ratio of only 0.09), as is the transmitted surface wave that moves up on the vertical face (amplitude ratio of 0.28). When the wave reaches this corner, most of the incident energy (91 percent) is converted to bulk modes that radiate into the body.

In both of the cases mentioned above, the vertical faces were assumed to be infinitely long. Nevertheless, these solutions can be expected to be approximately true when the wavelength of the incident pulse is small compared with the length of the vertical face. A finite step change in elevation of the ground surface is equivalent to 90- and 270-degree consecutive corners, provided that the step change is large compared with the Rayleigh wavelength.

The theoretical solution (*4*) of the amplitude ratios for different wavelengths caused by a finite step change (Figure 2) displays two prominent features at scaled depths of 0.5 and 1.5. (The scaled depth is the ratio of the step change to the Rayleigh wavelength.) The first feature is a minimum in the amplitude ratio and the second is the point where the amplitude ratio is no longer dependent on the incident wavelength. Despite the fact that these results are for a step change, it seems reasonable to expect similar features on the corresponding curve for a finite surface crack.

Viktorov (*5*) determined the amplitude ratio versus scaled crack depth experimentally for a variety of metals. (The scaled crack depth is the ratio of the crack depth to the Rayleigh wavelength.) He found that this curve (Figure 3) was reproducible with only slight modifications for the different solids. Typically, he found the first minimum of the amplitude ratio at a scaled crack depth of 0.7 and the amplitude ratio ceases to depend on the Rayleigh wavelength for scaled crack depths larger than 1.5.

Woods (*2*) conducted field tests in which a circular trench of radius R and depth H surrounds the source of disturbance to measure the reduced vibration outside the trench. Woods concluded that a minimum ratio of trench depth to Rayleigh wavelength of 0.6 is required to achieve 75 percent reduction in vibration amplitude. Woods's tests were performed in trenches in silty sand.

From this discussion of the behavior of Rayleigh waves incident on a surface crack, it seems possible that some of the features of the amplitude ratio curve (Figures 2 and 3) might be used to identify the depth of the crack. In this way, a possible procedure to test for the depth of the crack would be to measure the amplitudes of vibration (before and after the crack) of a set of Rayleigh waves with an appropriate range of wavelengths. This would allow determination of the amplitude ratio curve. The crack depth would be determined from the wavelength at which the appropriate feature of the amplitude ratio curve occurred.

A second possibility would be to use Rayleigh waves as they are commonly employed in nondestructive testing to determine the size of surface cracks in fabrication products. For this purpose, Rayleigh waves of the appropriate wave-

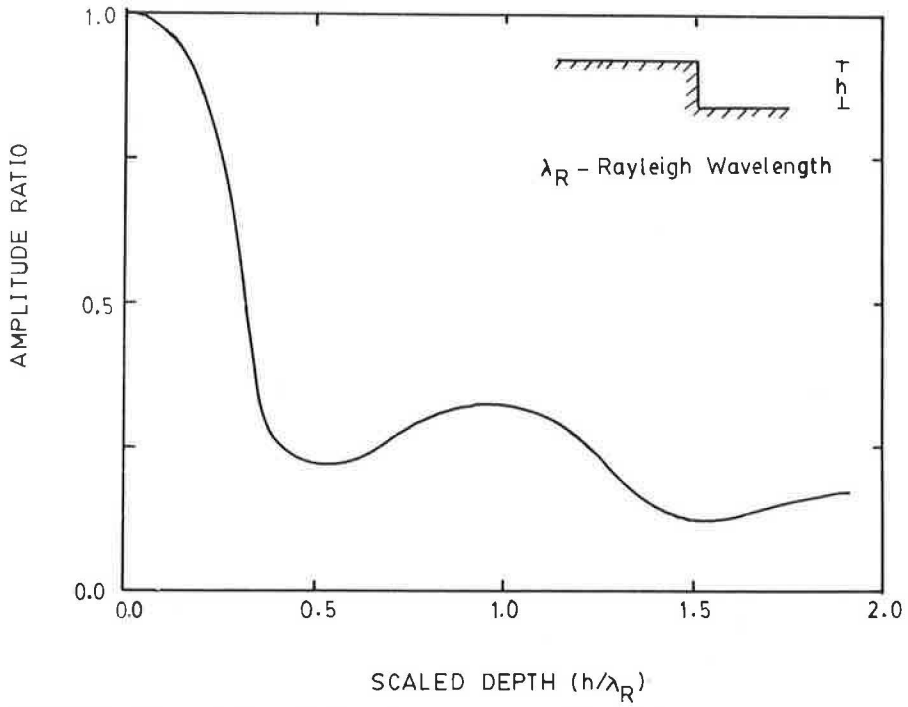

FIGURE 2 Theoretical amplitude ratio spectrum caused by a finite step change [redrawn from Farnell (*4*)].

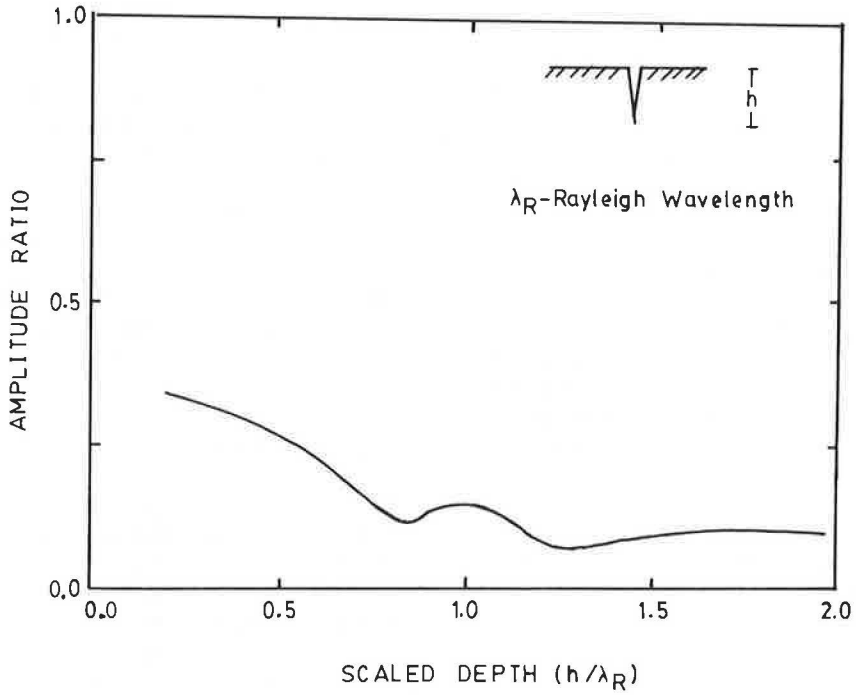

FIGURE 3 Experimental amplitude ratio spectrum caused by a surface crack [redrawn from Viktorov (*5*)].

length are excited. The crack forces the surface wave to travel down and back up the crack walls (*6*, *7*), increasing the transit time relative to the time expected from the unique Rayleigh wave velocity of the material. From this time delay and the assumption that the crack is vertical, the depth of the crack can be calculated. For this type of survey, it is necessary to measure the vibrations on both sides of the crack with an additional sensor to determine the travel time in the intact soil where no crack is present.

FIELD TEST PROGRAM

Field Trials

Two types of field tests were performed to check the capabilities of Rayleigh waves to measure the depth of shrinkage cracks. The first type of test consisted of exciting Rayleigh surface waves on one side of a preexcavated trench and recording with accelerometers the surface wave that reached

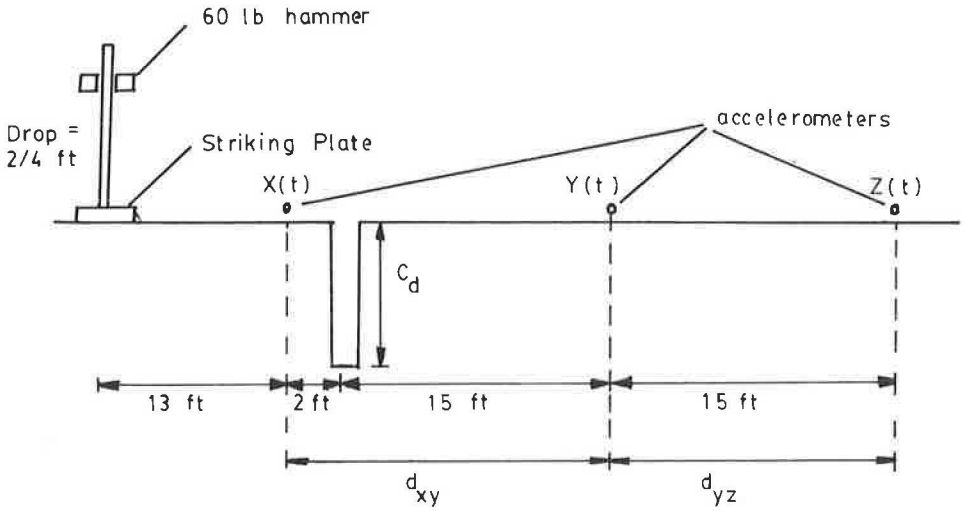

FIGURE 4 Field test setup for the accelerometer test.

both sides of the trench. The second type of test was basically identical, but geophones were used as the motion sensor. Both tests were performed at the Research Annex of Texas A&M University.

The tests of the first type were implemented first. A trenching machine was used to dig a trench 1 ft (0.3 m) wide and approximately 45 ft (14 m) long to different depths. Then a linear arrangement of a wave source and three accelerometers was placed. The relative positions of the source, the accelerometers, and the trench are shown in Figure 4.

The accelerometers were tied to stakes 6 in. (150 mm) long that had been driven 3 in. (75 mm) into the ground. The assemblage in each hole was covered with a rigid board to protect the accelerometer from picking up noise from the wind and to prevent the output from being affected by temperature changes.

The test itself consists in dropping a 60-lb hammer on a striking plate. Upon impact, a trigger mechanism causes the analog recorder to start recording at the three stations labeled *X*, *Y*, and *Z* in Figure 4. For each trench depth and drop height, the test is repeated five times and all five recordings are stored in analog form.

The test was first performed before the trench was dug; it was repeated for trench depths of 1.75 ft (0.5 m), 3.0 ft (0.9 m), and 4.0 ft (1.2 m). The drop height used in the tests was 4 ft (1.2 m). This drop was selected to obtain what seemed to be a noticeable signal/noise ratio in the farthest accelerometer labeled *Z* in Figure 4.

The second type of test was performed across naturally occurring shrinkage cracks in the expansive soils present at the Research Annex of Texas A & M University. The test setup was modified in an attempt to improve its accuracy. The first modification consisted of using geophones that were more sensitive than the accelerometers. Also to alleviate the problem of weak signals at the farthest recording station, the geophones were placed at 5 ft intervals.

The recording equipment used in these tests was a Nicolet oscilloscope that stored the recorded signal in digital form. This model can only record two channels simultaneously. Thus, each test had to be performed in two steps. The first consisted of recording in Stations X and Y only, as shown in Figure 5a. In the second step, the geophone at Station X was repositioned at the location of Station Z, and a new series of five blows was recorded for Stations Y and Z (Figure 5b).

A more detailed description of the equipment and layout used in the field tests is presented elsewhere (*9*).

Analysis of Field Data

The field data obtained in the first type of test were digitized at intervals of 1 msec. The field data obtained in the second type of test had been digitized at the time of recording at intervals of 0.05 msec. The total interval extended over 0.256 sec in the first type of test and over 0.1024 sec in the second type of test. Typical waveforms registered by all three geophones are shown in Figure 6.

For each trench depth or for each crack investigated, the test was repeated five times, and each time recordings were made at all three stations. These tests were repeated for identical drop heights of the hammer. After the signals were digitized, the five tests were averaged in an attempt (*8*) to reduce the random noise. The waveforms shown in Figure 6 are the average of five determinations.

The rest of the analysis was then performed on the average signal. In broad terms, this consisted of processing the signal with a fast Fourier algorithm. The amplitude spectra for the three stations were used to obtain the amplitude ratio spec-

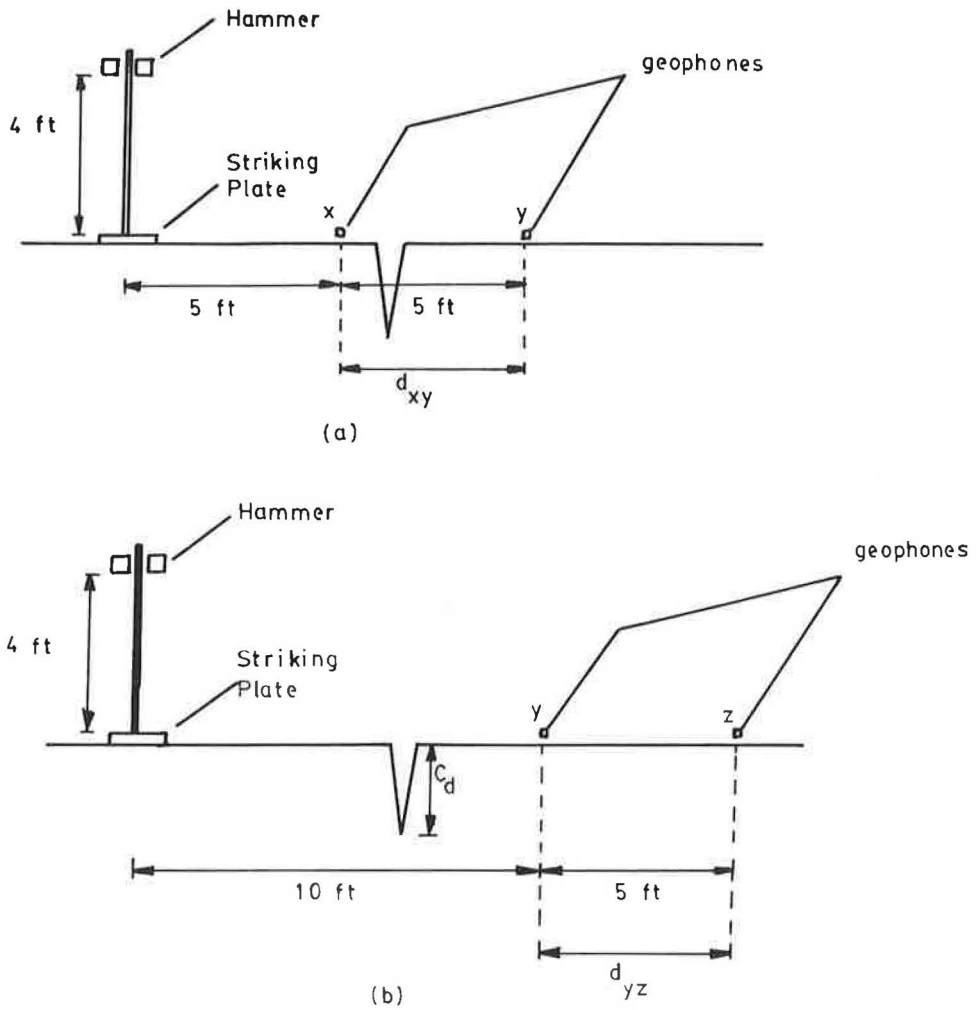

FIGURE 5 Field test setup for the geophone test.

trum and several other spectral measures. The most important were the phase spectra between Stations X and Y and Stations Y and Z. The amplitude spectra for the three stations obtained in the accelerometer test for a trench depth of 4.0 ft (1.2 m) are shown in Figure 7. The phase spectra X-Y and Y-Z for the same case are shown in Figures 8 and 9, respectively.

The phase spectrum is the phase angle lag that each frequency component exhibits between the two stations being analyzed. For a specific frequency component κ of frequency f_κ, $\phi_{xy}(\kappa)$ is the phase angle lag of the component between Stations X and Y, and $\phi_{yz}(\kappa)$ is the phase angle lag of the same component between Stations Y and Z. This phase angle lag allows the computation of the travel times between stations with the following expressions:

$$t_{xy}(\kappa) = \frac{\phi_{xy}(\kappa)}{360} \cdot \frac{1}{f_\kappa} \tag{1}$$

$$t_{yz}(\kappa) = \frac{\phi_{yz}(\kappa)}{360} \cdot \frac{1}{f_\kappa} \tag{2}$$

where $t_{xy}(\kappa)$ is the travel time between Stations X and Y of the frequency component κ, and $t_{yz}(\kappa)$ is the travel time between Stations Y and Z of the same frequency component κ. Because the distances between stations d_{xy} and d_{yz} are known, the apparent velocities of each frequency component κ can be calculated as follows:

$$v_{xy}(\kappa) = \frac{d_{xy}}{t_{xy}(\kappa)} \tag{3}$$

$$v_{yz}(\kappa) = \frac{d_{yz}}{t_{yz}(\kappa)} \tag{4}$$

The difference in apparent velocity between Stations X-Y and Stations Y-Z is used to calculate the crack depth, $C(\kappa)$, with the following expression:

$$C(\kappa) = \frac{t_{xy}(\kappa)}{2} [v_{yz}(\kappa) - v_{xy}(\kappa)] \tag{5}$$

The phase spectrum is calculated as the inverse function of a tangent. The phase spectrum angles are always calculated to be between $-180°$ and $+180°$. In reality, the phase lag of the frequency components is a monotonically increasing function. Therefore, it is necessary to unwind the calculated phase spectrum to construct the true phase spectrum. The process of unwinding the phase spectrum is shown in Figure 10. A hypothetical calculated phase spectrum is shown in the upper part of Figure 10. Every time there is a sharp drop of phase angle lag, the calculated phase angle lag has switched from

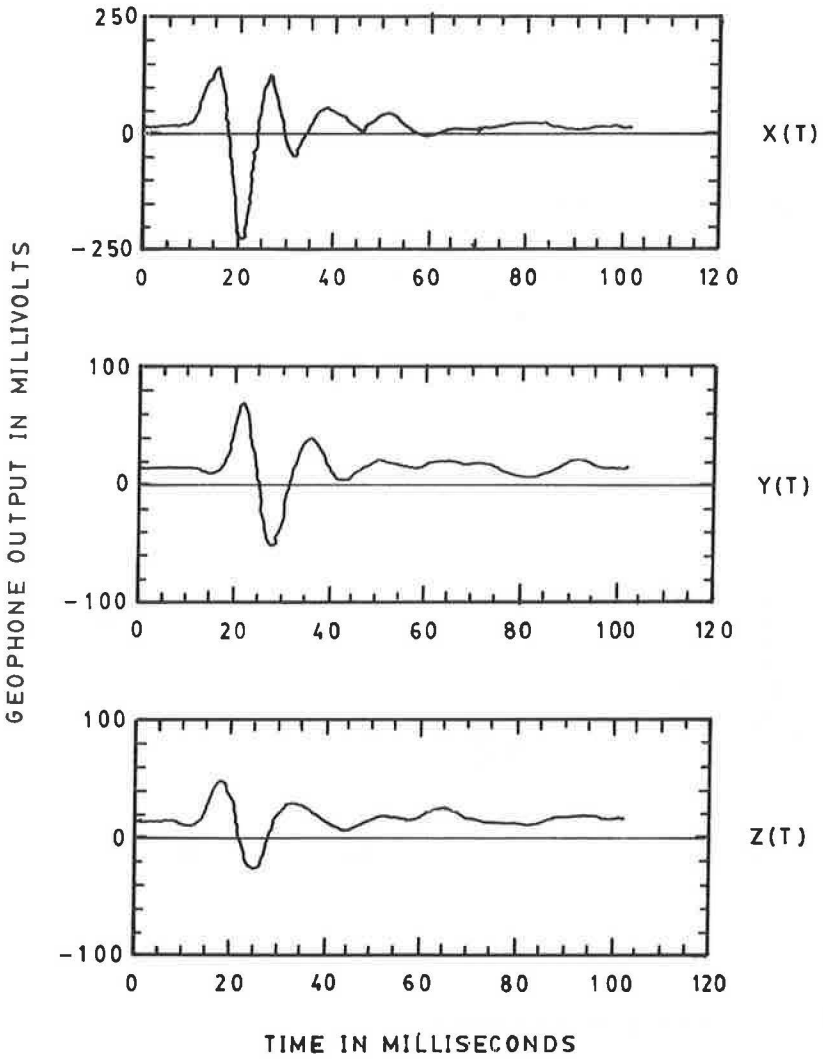

FIGURE 6 Typical average signals picked up by the geophones.

+180° to −180°. Each phase angle lag drop with increasing frequency is a candidate location for a cut. The actual accumulation process of phase angle is shown in the lower part of Figure 10. This plot is obtained by simply adding the segments of the calculated phase spectrum displaced vertically at the locations of the cuts.

The critical part of this analysis is the selection of the locations of the cuts. Some uncertainties are always associated with the selection of the cuts. Although these uncertainties cannot be eliminated completely, they can be reduced considerably if the phase spectrum can be defined at smaller frequency increments.

A more complete description of all the manipulations of the field data to determine the crack depth is presented elsewhere (*9*). All this analysis is performed with the computer program CROSSP. The FORTRAN listing of CROSSP is presented elsewhere (*9*). The only input necessary for CROSSP is the output of the sensor in millivolts versus time recorded at the three stations, such as that shown in Figure 6.

In short, the test consists of (a) recording the signal received at the three stations after striking the source plate and (b) digitizing the signal recorded in each geophone. This digitized signal (the average of five tests) is used as the input for CROSSP, which after the run prints the calculated crack depth. This program also prints all the intermediate results of different spectral measures.

DISCUSSION OF RESULTS

The first alternative considered to determine the crack depth from the Rayleigh wave measurements consisted of measuring the amplitude ratio of each frequency component between Stations X and Y to plot the amplitude ratio spectrum. The amplitude ratio spectra obtained from this survey did not exhibit shapes similar to the shapes observed by Viktorov (*5*) in solids, which are shown in Figure 3. The reasons for the different behavior were not apparent. Furthermore, the shapes of the amplitude ratio spectra obtained in this study were quite insensitive to crack depth. Because the amplitude ratio spectrum did not show the effects of crack depth, use of this alternative was ruled out. Thus, the results of this study indicated that the only alternative available was calculation of crack depth from increased travel time caused by the crack.

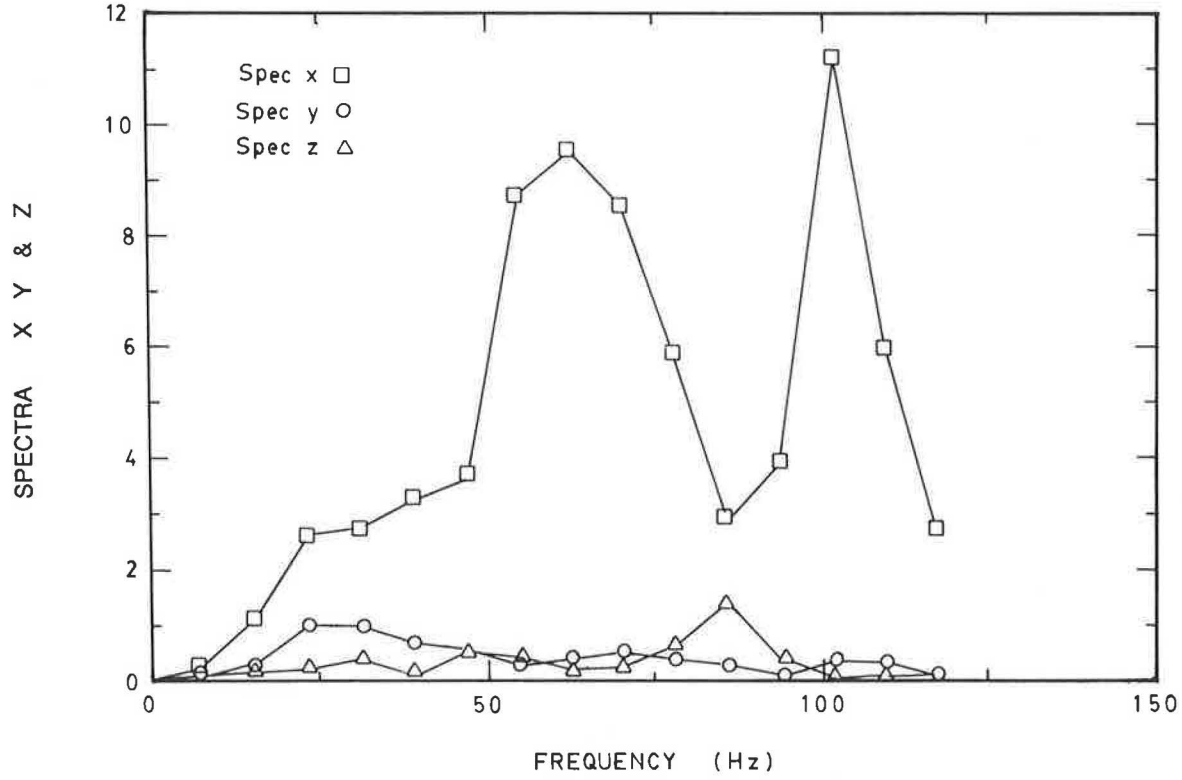

FIGURE 7 Amplitude spectra for a 4.0-ft trench depth.

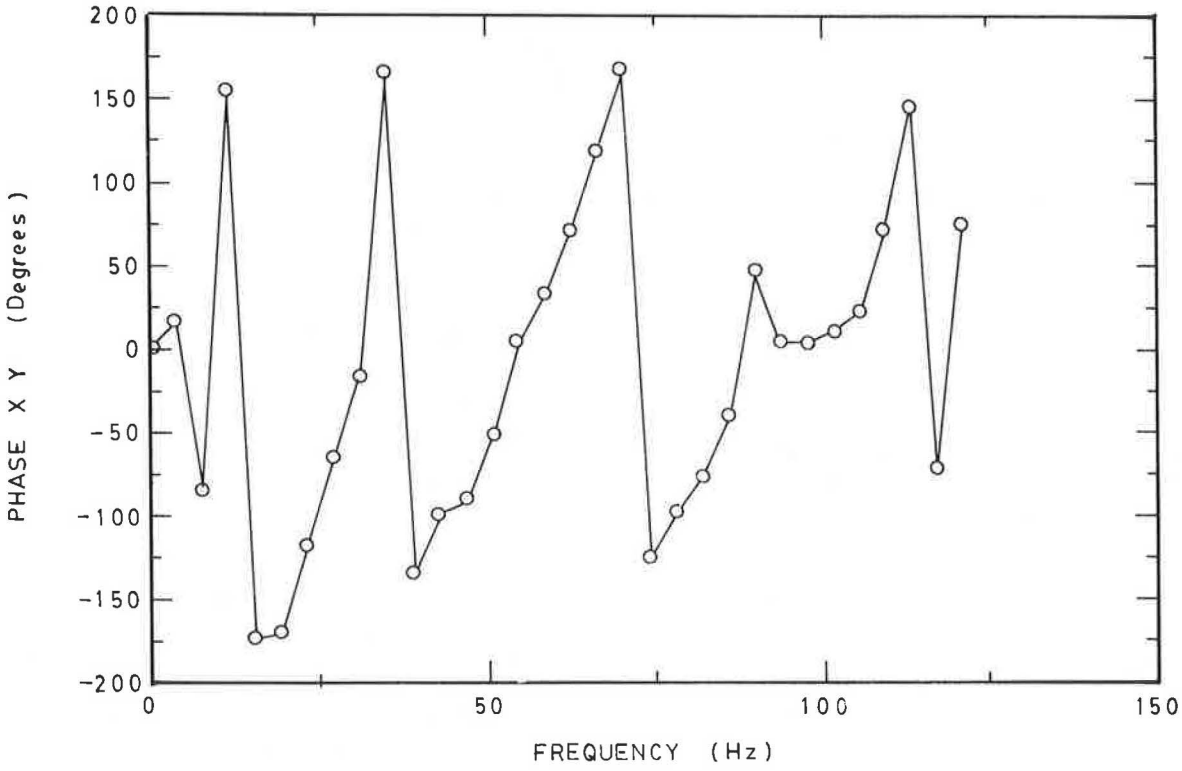

FIGURE 8 Phase spectrum (Stations X and Y) for a 4.0-ft trench depth.

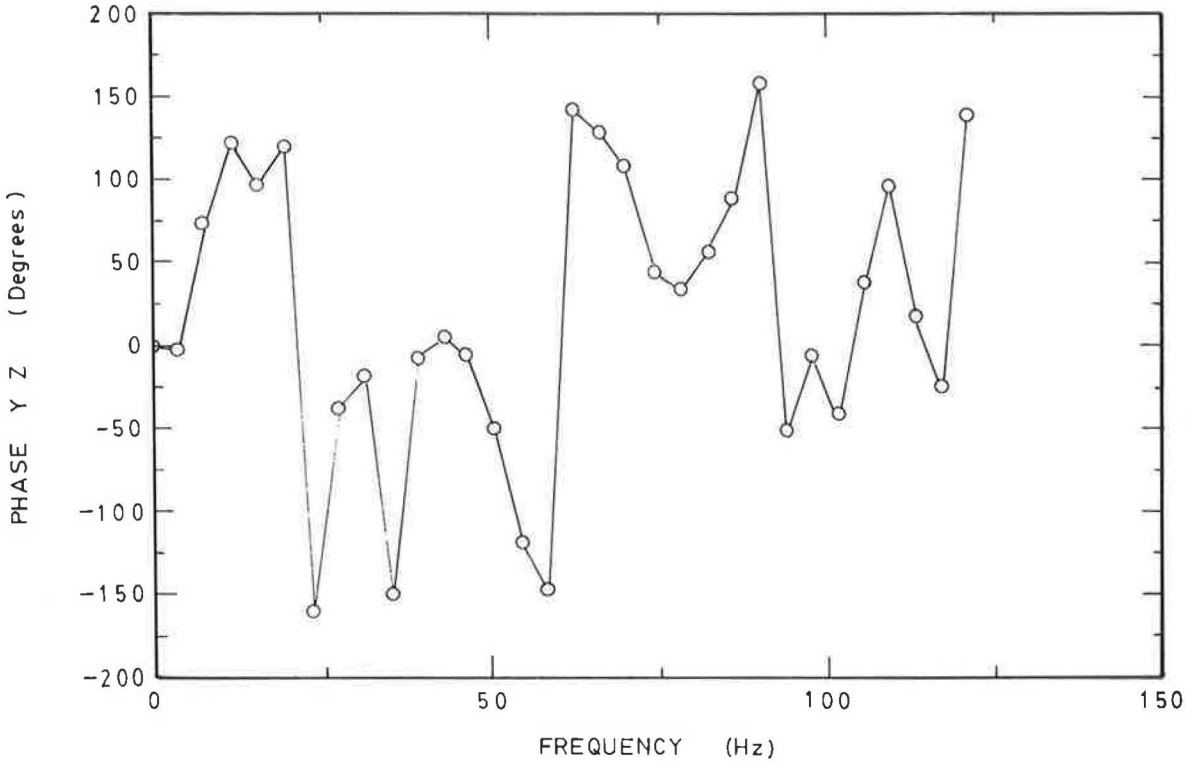

FIGURE 9 Phase spectrum (Stations Y and Z) for a 4.0-ft trench depth.

The trench depths calculated from the wave measurements in the accelerometer test are presented below:

Actual Depth		*Calculated Depth*	
Feet	*Meters*	*Feet*	*Meters*
0.00	0.00	12.11	3.69
1.75	0.53	2.55	0.78
3.00	0.91	2.76	0.84
4.00	1.22	4.07	1.24

Crack depths calculated from the geophone tests and measured depths obtained by inserting a measuring tape as far as possible into the crack are as follows:

Measured Depth		*Calculated Depth*	
Feet	*Meters*	*Feet*	*Meters*
1.25	0.38	2.35	0.72
2.66	0.81	2.48	0.76

The calculated depths for the two types of tests show a remarkable agreement when the crack depth is greater than about 2 ft (0.6 m). However, the results are clearly out of line for the smaller crack depths. The reason for this anomalous behavior is not clear. It is probably related to the wavelengths of the Rayleigh waves excited in the field tests. This effect will be discussed further in the next section.

Apparently, there is a reason for the large crack depth shown in the survey carried out before the trench was excavated. The most plausible explanation is that when the phase spectrum was unwound (ϕ_{xy}), some extra, inappropriate cut slipped in, causing an overestimation of the total phase lag. Equally probable is that some cut that should have been included in the phase spectrum (ϕ_{yz}) was overlooked. The result in both cases is a larger difference in phase lag for the two intervals, which would be responsible for the excessive crack depth calculated.

The difference between the measured and the calculated depths (shown above in the results of the geophone tests) for the case of a crack 1.25 ft (0.38 m) deep is probably due to some other reason. It is entirely possible that the measurement of 1.25 ft is in error. In fact, both shrinkage cracks surveyed were found close together, and they appeared to have similar crack widths on the ground surface. It seems reasonable to expect that both cracks would have similar depths, which is precisely what the wave survey indicated.

CONCLUSIONS AND RECOMMENDATIONS

The results shown in the previous section show remarkable agreement between measured and calculated trench or crack depths obtained by a survey of surface waves. The calculated depths were obtained using surface waves that were assumed to travel down and up the crack walls. The crack depth was calculated on the basis of the increased travel time caused by the presence of the crack. The results of this study show that the crack depth in soils can be accurately measured using this surface wave propagation technique. Nevertheless, it is believed that the testing procedure used in these field tests could be modified to improve the reliability and accuracy of the results.

The reliability could be improved by making sure that phase angle cuts do not slip by when the phase spectrum is unwound. To reduce this risk, the best solution is to increase the resolution of the phase spectrum, that is, to decrease the spacing between the discrete points that define this spectrum. This

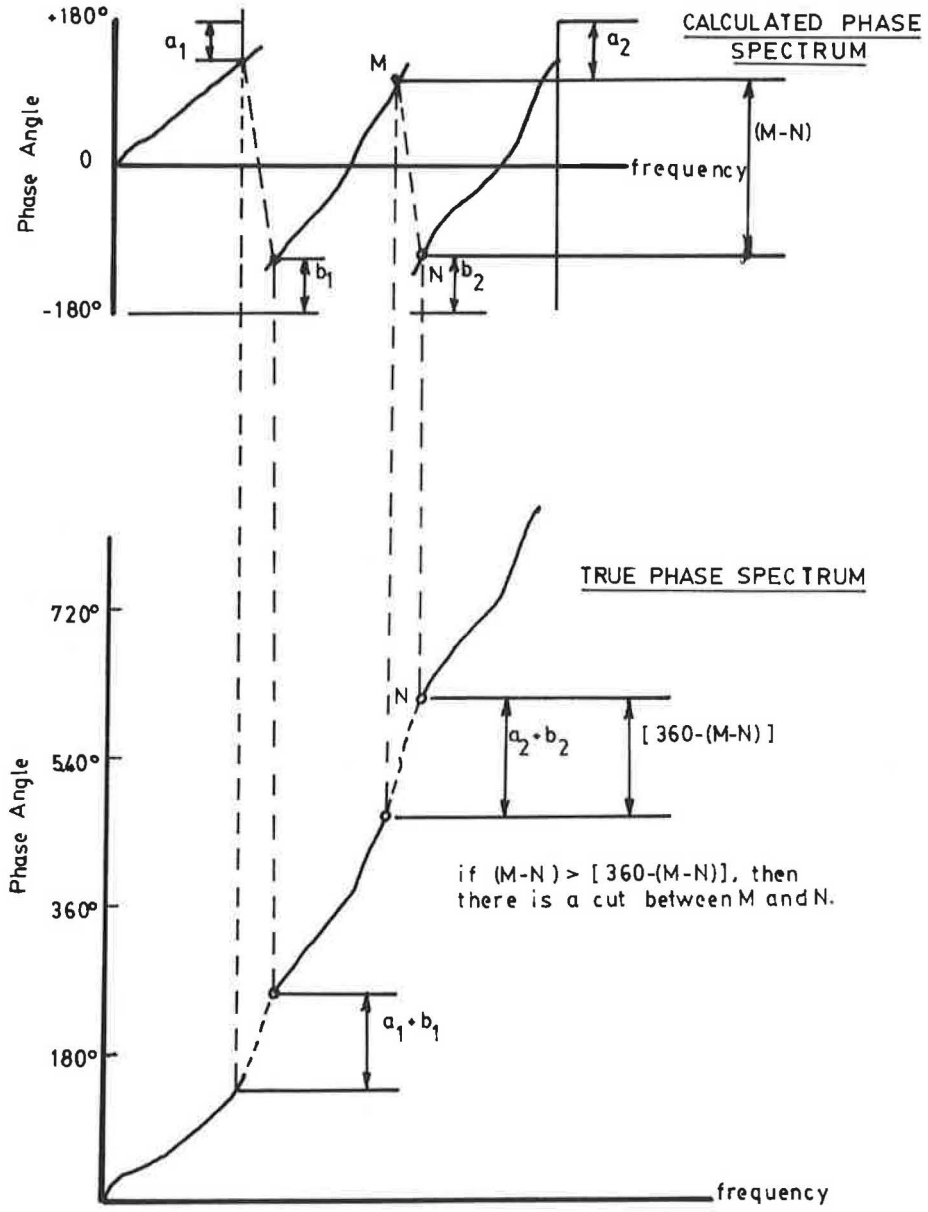

FIGURE 10 Unwinding of the phase spectrum.

means increasing the total length of the period of measurement for a fixed sampling rate. Keeping in mind that the signal caused by the drop hammer dies out at about 100 msec (see Figure 6), the increase in time of measurement implies the need for a longer-lasting surface wave source. Such a wave source would be a surface vibrator that could sweep a frequency range from 20 Hz to 1 kHz and that could also alter the total vibrating mass.

The accuracy of the measurements could be improved by exciting signals rich in harmonics of small wavelength. This is because the test procedure assumes that the surface wave harmonic travels down and up the crack faces. The wavelengths excited in the trial field tests are given in Table 1, along with the corresponding depths of the trench or crack.

Table 1 indicates that the calculated and measured depths agree much more when the wavelengths of the surface waves excited are the same size or smaller than the trench or the crack depth. The two cases that stand out are a trench 4.0 ft (1.2 m) deep and a crack 2.48 ft (0.81 m) deep.

These results are good evidence of the need to excite surface waves of short wavelengths. Furthermore, it is worth noting that the smaller spacing used in the accelerometer tests resulted in much smaller wavelengths of the harmonics that build up the surface wave signal. Therefore, a geophone spacing of 5 ft (1.52 m) or less favors the presence of harmonics of short wavelength and thus improves the accuracy of the measurements.

In summary, surface waves can be used to measure the depth of shrinkage cracks in expansive soils. The best method is to calculate the crack depth from the travel time delay caused by the crack. For this purpose, it is necessary to excite surface waves with wavelengths smaller than the depth of the cracks. This can be accomplished with drop hammers if the spacing between geophones is less than 5 ft (1.52 m).

TABLE 1 WAVELENGTHS OF SURFACE WAVES EXCITED IN THE FIELD TESTS

	Measured Depth		Calculated Depth		Wavelength Range	
	Feet	Meters	Feet	Meters	Feet	Meters
Trench	1.75	0.53	2.55	0.78	8.0–15.0	2.44–4.57
	3.00	0.91	2.76	0.84	7.0–10.0	2.14–3.05
	4.00	1.22	4.07	1.24	6.0–10.0	1.83–3.05
Crack	1.25	0.38	2.35	0.72	2.0–10.0	0.61–3.05
	2.48	0.81	2.42	0.76	1.3– 4.0	0.4 –1.22

REFERENCES

1. G. F. Miller and H. Pursey. On the Partition of Energy between Elastic Waves in a Semi-infinite Solid. *Proc., Royal Society, London Series A*, Vol. 233, 1955, pp. 55–59.
2. R. D. Woods. Screening of Surface Waves in Soils. *Journal of the Soil Mechanics and Foundation Division*, ASCE, No. SM4, July 1968, pp. 951–979.
3. J. C. De Bremaecker. Transmission and Reflection of Rayleigh Waves at Corners. *Geophysics*, Vol. 23, No. 2, April 1958, pp. 253–266.
4. G. W. Farnell. Types and Properties of Surface Waves. In *Acoustic Surface Waves*, A. A. Oliner, ed., Springer-Verlag, New York, 1978.
5. I. A. Viktorov. The Effects of Surface Defects on the Propagation of Rayleigh Waves. *Soviet Physics, Doklady*, Vol. 3, 1958, pp. 304–306.
6. M. G. Silk, B. H. Lidington, and G. H. Hammond. A Time Domain Approach to Crack Location and Sizing in Austenitic Welds. *British Journal of Non-Destructive Testing*, Vol. 22, No. 2, March 1980, pp. 55–61.
7. A. J. Slobodnik. Materials and Their Influence on Performance. In *Acoustic Surface Waves*, A. A. Oliner, ed., Springer-Verlag, New York, 1978.
8. J. S. Heisey, K. H. Stokoe II, and A. H. Meyer. Moduli of Pavement Systems from Spectral Analysis of Surface Waves. In *Transportation Research Record 852*, Transportation Research Board, Washington, D.C., 1982, pp. 22–31.
9. R. L. Lytton, M. Picornell, C. Garcia, and C. C. Huang. *Detection and Sizing of Surface Cracks in Expansive Soil Deposits*. Research Report 187-13. Texas Transportation Institute, Texas A&M University, April 1987.

Publication of this paper sponsored by Committee on Environmental Factors Except Frost.

Evaluation of AGWA-II Thermal Conductivity Sensors for Soil Suction Measurement

D. K. H. WONG, D. G. FREDLUND, E. IMRE, AND G. PUTZ

Several tests (both laboratory and full-scale) were conducted to assess the potential of AGWA-II thermal conductivity sensors to measure soil suction in geotechnical engineering applications. The tests conducted in the laboratory included examining the response of the sensors submerged in water, calibrating the sensors in a pressure plate, and measuring soil suction in undisturbed soil specimens. Initial tests conducted on the sensors indicated some inaccuracies associated with the linear calibration curves suggested by the manufacturer. The calibration results showed that the calibration curves for the sensors were bilinear with a breaking point at about 175 kPa. Reasonable agreement was found between the calibration curves obtained in this study and those provided by the manufacturer for matric suction ranging from 0 to 175 kPa. However, large deviations in the calibration curves were observed at suction above 175 kPa. With the calibrated sensors, a testing program was carried out by measuring soil suction in undisturbed soil specimens. Upon the completion of the laboratory tests, the sensors were installed in the subgrade soils of an indoor test track for long-term monitoring. The sensor outputs were found to be relatively consistent and stable with time.

The importance of reliable devices for measuring soil suction has long been recognized. The need for quantitative information on soil suction has led to the development of a number of suction-measuring devices. These include conventional tensiometers, thermocouple psychrometers, null pressure plates, and thermal conductivity sensors. The limitations of these devices have been reported by a number of investigators (*1*,2). Of these devices, the thermal conductivity sensor appears to be quite promising. It is unaffected by salts in the soil and can be used to measure suction over a fairly wide range (*3,4*).

In 1986 the University of Saskatchewan undertook a study, funded by the Saskatchewan Highways and Transportation Department, to evaluate the potential of thermal conductivity sensors to measure soil suction in the subgrade of pavements in Saskatchewan.

Thermal conductivity sensors have been evaluated by a number of investigators. Lee and Fredlund (*5*) used a commercial conductivity sensor, the MCS 6000 (manufactured by Moisture Control System Incorporated, of Finlay, Ohio) to measure matric suction in both plastic and nonplastic soil specimens. Curtis and Johnston (*6*) used this type of sensor in a major hydrological process evaluation. By 1984 the MCS 6000 sensor was no longer available commercially. A similar thermal conductivity sensor, the AGWA-II (manufactured by Agwatronics Incorporated, of Merced, California), was used in this study.

To accomplish the study objectives, a series of laboratory tests was conducted in three stages before a full-scale test was performed. The tests conducted in the laboratory included examining the response of the sensors submerged in water, calibrating the sensors in a pressure plate apparatus, and measuring soil suction on undisturbed soil specimens.

Initial tests conducted on the sensors indicated inaccuracies associated with the sensor calibration curves provided by the manufacturer. Each AGWA-II sensor is supplied with a linear calibration consisting of an intercept value and a slope. After difficulties were experienced in obtaining reasonable and consistent results, calibration tests were performed in an attempt to better define the relationship between the sensor output and matric suction. The recalibrated sensors were then used to measure soil suction in undisturbed specimens.

Upon completion of the laboratory tests, the AGWA-II sensors were installed in the subgrade soils of an indoor test track for long-term monitoring. The stability and reproducibility of the sensor output were evaluated throughout the period.

EQUIPMENT

The equipment used in this study included the AGWA-II thermal conductivity sensors, a hand-held Agwameter, and a data-acquisition system. A modified pressure plate extractor, along with a temperature control box, was also used during the calibration study.

AGWA-II Thermal Conductivity Sensor

The AGWA-II thermal conductivity sensor is a commercial development of the unit described by Phene et al. (*7–9*). The sensor consists of a miniature heater and a temperature sensor, which is embedded in a cylindrical porous ceramic block that forms the sensor tip. The lead wires for the miniature heater and the temperature sensor are sealed to the cylindrical block with a thermally conductive epoxy. Figure 1 shows a cross section of the thermal conductivity sensor.

D. K. H. Wong, D. G. Fredlund, and G. Putz, Department of Civil Engineering, University of Saskatchewan, Saskatoon, Saskatchewan S7N 0W0, Canada. E. Imre, Technical University of Budapest, H-1521, Budapest, Műegyetem-Rkp 3, Hungary.

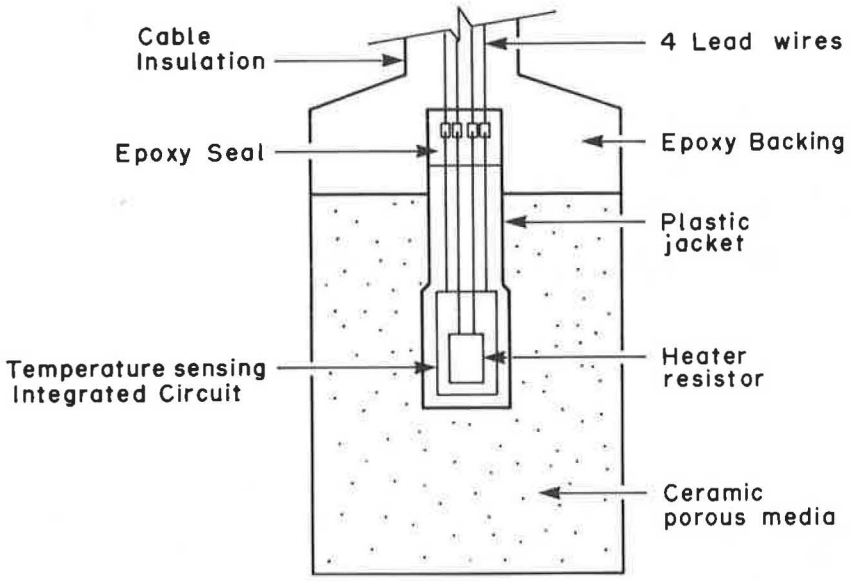

FIGURE 1 Thermal conductivity sensor (cross section).

The sensors indirectly measure the matric suction in a soil by measuring the heat-dissipation capacity of the water content in the sensor tip, which is a function of matric suction in the soil. Heat-dissipation capacity is, in turn, a function of water content; therefore, it may be related to soil matric suction. The heat dissipation by the water phase is measured by supplying a controlled amount of heat at the center of the porous medium and measuring the temperature rise at the same point after a fixed period of time. The change in temperature is a function of water content, and therefore it can be corrected to matric suction by means of a calibration procedure.

The water content of the sensor tip is sensitive to matric suction changes because the porous medium of the tip has a wide distribution of pore sizes. As a result, the sensor tip should commence desaturating or saturating in response to small changes in matric suction. The passage of air to the sensor tip is an important factor that can influence sensitivity at low matric suction values (i.e., below approximately one atmosphere). However, the sensors are generally installed in the bottom of holes augered into the soil, and ambient air pressure is close to the top of the sensor or may be indirectly in contact by passage along the interface between the sensor cable and the soil.

Hand-Held Agwameter

The hand-held Agwameter, which is also commercially available from Agwatronics, is a portable data display used to monitor AGWA-II sensors. The hand-held meter supplies a constant current source to the heater element within the sensor and measures the temperature change at the center of the ceramic block after the heating cycle. The measured temperature change, which is expressed in terms of a change in voltage, is shown on the liquid crystal display after the read cycle. The hand-held meter was used to monitor AGWA-II sensors for both the laboratory tests and the full-scale testing portion of the study.

Data-Acquisition System

The data-acquisition system comprises a Hewlett-Packard 3421A data-acquisition and control unit, a Hewlett-Packard 10-channel multiplexer assembly, board, a sensor interface and power supply (SIPS) unit, and a desktop microcomputer. Figure 2 shows the major components of the data-acquisition system.

The desktop microcomputer acts as a central controller for the entire data-acquisition system by dispatching commands to the data-acquisition and control unit. Commands, such as opening and closing the sensor internal heater circuits and measuring the temperature sensor voltages, are activated through the channel multiplexer that is housed inside the data-acquisition and control unit. The SIPS board provides power for the sensor heater circuits and conditions the temperature sensor voltage signals before input to the data-acquisition system.

The data-acquisition and control system with a 10-channel multiplexer can measure up to eight sensors in succession (two channels are used to control the heater circuits). The system can be enhanced to measure up to 16 sensors by installing an additional multiplexer. The data-acquisition system with a 10-channel multiplexer was used to monitor the AGWA-II sensors for the laboratory tests.

LABORATORY TESTS

The tests conducted in the laboratory are described in the following sections. The sensors were monitored by both the hand-held meter and the data-acquisition system.

Submergence of Sensors in Water

The following test was performed to verify the integrity of the sensors under saturated conditions. A total of 15 sensors were submerged in a small glass container of water at room

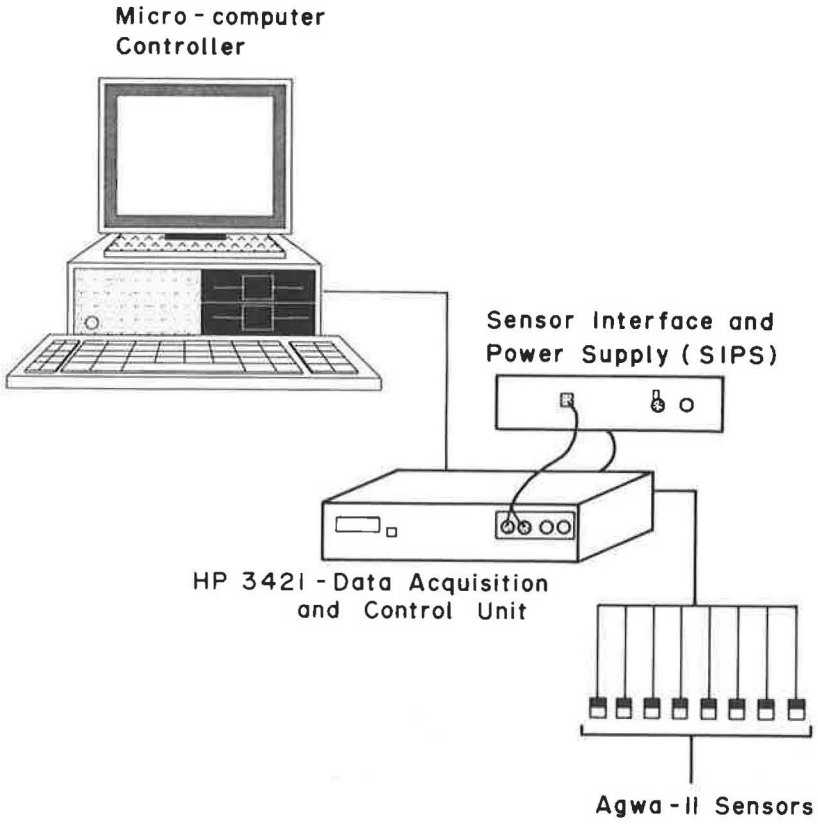

FIGURE 2 Major components of the data-acquisition system.

temperature for about a week. The sensors were then left to dry at room temperature and room relative humidity conditions. After they were air-dried for 1 day, the sensors were again submerged in water at room temperature until the test was completed. The temperature in the laboratory varied from 20°C to 24°C, and the sensors were generally monitored once or twice a day with the hand-held meter. The data-acquisition system was used occasionally to provide a continuous monitoring record.

The objective of the submergence test was to verify that the sensors responded to wetting and drying and to provide an indication of their output range. Air trapped in the sensor tip when the sensor is fully submerged may influence the saturation readings. However, it is difficult to ensure complete saturation, and for the purpose of response assessment, it was believed that water submergence was a reasonable simulation of in situ conditions.

Effect of Wetting and Drying

Typical behavior of the sensors under a drying and wetting cycle is shown in Figures 3 and 4. In general, the results show that the sensors that were submerged in water at room temperature for about a week indicated a matric suction ranging from ±10 to ±40 kPa according to the calibration equations provided by the manufacturer. After the sensors were air-dried at room temperature for one day, the measured matric suctions typically ranged from 175 to 475 kPa. Measurements converged back to between ±10 to ±40 kPa after the sensors were resubmerged in water.

Figures 3 and 4 demonstrate that the sensors were responsive to different applied suction conditions. Low suction values were obtained when sensors were subjected to a saturated condition, and high suction values resulted when sensors were allowed to dry. However, the sensors did not read zero suction according to the calibration equations provided by the manufacturer even though they were submerged in water for approximately 80 days. In some cases, they even read negative matric suction (i.e., a positive pressure). The fact that the sensors did not read zero suction at simulated saturation and zero suction conditions may be the result of air entrapment or minor inaccuracies associated with the calibration tests.

A summary of the sensor outputs read with the hand-held meter in both the water-submerged and air-dried conditions is presented in Table 1. The difference in the sensor outputs under these two conditions gives an indication of the measurable output range, which varied from 69 to 233 mV among the sensors. The implication is that sensors with the larger output range had a higher sensitivity to matric suction changes than those with a narrower output range.

Effect of Prolonged Submergence

Of the 15 sensors that were submerged in water for monitoring, two failed during the test. The typical response of a failed sensor is shown in Figure 5. The sensor initially responded to the drying and wetting cycle and reached complete equilibrium about 30 days after it was resubmerged in water. However, failure occurred soon after equilibrium was achieved. The sensor showed a dramatic response change, indicating an